Nanomaterials by severe plastic deformation: review of historical developments and recent advances

Kaveh Edalati, Andrea Bachmaier, Victor A Beloshenko, Yan Beygelzimer, Vladimir D Blank, Walter J Botta, Krzysztof Bryla, Jakub Čížek, Sergiy Divinski, Nariman A Enikeev, et al.

▶ **To cite this version:**

Kaveh Edalati, Andrea Bachmaier, Victor A Beloshenko, Yan Beygelzimer, Vladimir D Blank, et al.. Nanomaterials by severe plastic deformation: review of historical developments and recent advances. Materials Research Letters, 2022, 10 (4), pp.163-256. 10.1080/21663831.2022.2029779 . hal-03583326

HAL Id: hal-03583326

https://normandie-univ.hal.science/hal-03583326

Submitted on 21 Feb 2022

HAL is a multi-disciplinary open access archive for the deposit and dissemination of scientific research documents, whether they are published or not. The documents may come from teaching and research institutions in France or abroad, or from public or private research centers.

L'archive ouverte pluridisciplinaire **HAL**, est destinée au dépôt et à la diffusion de documents scientifiques de niveau recherche, publiés ou non, émanant des établissements d'enseignement et de recherche français ou étrangers, des laboratoires publics ou privés.

Materials Research Letters

ISSN: (Print) (Online) Journal homepage: https://www.tandfonline.com/loi/tmrl20

Nanomaterials by severe plastic deformation: review of historical developments and recent advances

Kaveh Edalati, Andrea Bachmaier, Victor A. Beloshenko, Yan Beygelzimer, Vladimir D. Blank, Walter J. Botta, Krzysztof Bryła, Jakub Čížek, Sergiy Divinski, Nariman A. Enikeev, Yuri Estrin, Ghader Faraji, Roberto B. Figueiredo, Masayoshi Fuji, Tadahiko Furuta, Thierry Grosdidier, Jenő Gubicza, Anton Hohenwarter, Zenji Horita, Jacques Huot, Yoshifumi Ikoma, Miloš Janeček, Megumi Kawasaki, Petr Král, Shigeru Kuramoto, Terence G. Langdon, Daniel R. Leiva, Valery I. Levitas, Andrey Mazilkin, Masaki Mito, Hiroyuki Miyamoto, Terukazu Nishizaki, Reinhard Pippan, Vladimir V. Popov, Elena N. Popova, Gencaga Purcek, Oliver Renk, Ádám Révész, Xavier Sauvage, Vaclav Sklenicka, Werner Skrotzki, Boris B. Straumal, Satyam Suwas, Laszlo S. Toth, Nobuhiro Tsuji, Ruslan Z. Valiev, Gerhard Wilde, Michael J. Zehetbauer & Xinkun Zhu

To cite this article: Kaveh Edalati, Andrea Bachmaier, Victor A. Beloshenko, Yan Beygelzimer, Vladimir D. Blank, Walter J. Botta, Krzysztof Bryła, Jakub Čížek, Sergiy Divinski, Nariman A. Enikeev, Yuri Estrin, Ghader Faraji, Roberto B. Figueiredo, Masayoshi Fuji, Tadahiko Furuta, Thierry Grosdidier, Jenő Gubicza, Anton Hohenwarter, Zenji Horita, Jacques Huot, Yoshifumi Ikoma, Miloš Janeček, Megumi Kawasaki, Petr Král, Shigeru Kuramoto, Terence G. Langdon, Daniel R. Leiva, Valery I. Levitas, Andrey Mazilkin, Masaki Mito, Hiroyuki Miyamoto, Terukazu Nishizaki, Reinhard Pippan, Vladimir V. Popov, Elena N. Popova, Gencaga Purcek, Oliver Renk, Ádám Révész, Xavier Sauvage, Vaclav Sklenicka, Werner Skrotzki, Boris B. Straumal, Satyam Suwas, Laszlo S. Toth, Nobuhiro Tsuji, Ruslan Z. Valiev, Gerhard Wilde, Michael J. Zehetbauer & Xinkun Zhu (2022) Nanomaterials by severe plastic deformation: review of historical developments and recent advances, Materials Research Letters, 10:4, 163-256, DOI: 10.1080/21663831.2022.2029779

To link to this article: https://doi.org/10.1080/21663831.2022.2029779

© 2022 The Author(s). Published by Informa UK Limited, trading as Taylor & Francis Group.

Published online: 17 Feb 2022.

Submit your article to this journal

Article views: 196

View related articles

View Crossmark data

Full Terms & Conditions of access and use can be found at
https://www.tandfonline.com/action/journalInformation?journalCode=tmrl20

MATER. RES. LETT.
2022, VOL. 10, NO. 4, 163–256
https://doi.org/10.1080/21663831.2022.2029779

MATERIALS RESEARCH LETTERS
Taylor & Francis
Taylor & Francis Group

PERSPECTIVE PIECE

OPEN ACCESS Check for updates

Nanomaterials by severe plastic deformation: review of historical developments and recent advances

Kaveh Edalati [a], Andrea Bachmaier [b], Victor A. Beloshenko[c], Yan Beygelzimer [c], Vladimir D. Blank[d], Walter J. Botta[e], Krzysztof Bryła[f], Jakub Čížek[g], Sergiy Divinski [h], Nariman A. Enikeev [i,j], Yuri Estrin [k,l], Ghader Faraji[m], Roberto B. Figueiredo[n], Masayoshi Fuji [o], Tadahiko Furuta[p], Thierry Grosdidier[q,r], Jenő Gubicza [s], Anton Hohenwarter [t], Zenji Horita[a,u,v,w], Jacques Huot[x], Yoshifumi Ikoma [y], Miloš Janeček[z], Megumi Kawasaki [aa], Petr Král[ab], Shigeru Kuramoto[ac], Terence G. Langdon [ad], Daniel R. Leiva[e], Valery I. Levitas [ae,af], Andrey Mazilkin[ag,ah], Masaki Mito[u], Hiroyuki Miyamoto[ai], Terukazu Nishizaki [aj], Reinhard Pippan[b], Vladimir V. Popov[ak], Elena N. Popova[ak], Gencaga Purcek[al], Oliver Renk[b], Ádám Révész[s], Xavier Sauvage[am], Vaclav Sklenicka[ab], Werner Skrotzki[an], Boris B. Straumal[ag,ah], Satyam Suwas [ao], Laszlo S. Toth[q,r,at], Nobuhiro Tsuji [ap,aq], Ruslan Z. Valiev [i,j], Gerhard Wilde[h], Michael J. Zehetbauer [ar] and Xinkun Zhu[as]

[a]WPI, International Institute for Carbon-Neutral Energy Research (WPI-I2CNER), Kyushu University, Fukuoka, Japan; [b]Erich Schmid Institute of Materials Science, Austrian Academy of Sciences, Leoben, Austria; [c]Donetsk Institute for Physics and Engineering named after A.A. Galkin, National Academy of Sciences of Ukraine, Kyiv, Ukraine; [d]Technological Institute for Superhard and Novel Carbon Materials, Moscow, Russia; [e]Departamento de Engenharia de Materiais, Universidade Federal de São Carlos, São Carlos-SP, Brazil; [f]Faculty of Mechanical Engineering, Cracow University of Technology, Cracow, Poland; [g]Department of Low Temperature Physics, Faculty of Mathematics and Physics, Charles University in Prague, Prague, Czech Republic; [h]Institute of Materials Physics, University of Münster, Münster, Germany; [i]Ufa State Aviation Technical University, Ufa, Russia; [j]Laboratory of Mechanics of Advanced Bulk Nanomaterials for Innovative Engineering Applications, Saint Petersburg State University, St. Petersburg, Russia; [k]Department of Materials Science and Engineering, Monash University, Clayton, Australia; [l]Department of Mechanical Engineering, The University of Western Australia, Crawley, Australia; [m]School of Mechanical Engineering, College of Engineering, University of Tehran, Tehran, Iran; [n]Department of Metallurgical and Materials Engineering, Universidade Federal de Minas Gerais, Belo Horizonte, Brazil; [o]Advanced Ceramics Research Center, Nagoya Institute of Technology, Tajimi, Japan; [p]Data-Driven Material Processing Research-Domain, Toyota Central R&D Laboratories Inc., Nagakute, Japan; [q]Laboratoire d'Etude des Microstructures et de Mécanique des Matériaux (LEM3 UMR 7239), Université de Lorraine, Metz, France; [r]Laboratory of Excellence on Design of Alloy Metals for low-mass Structures (DAMAS), Université de Lorraine, Metz, France; [s]Department of Materials Physics, Eötvös Loránd University, Budapest, Hungary; [t]Department of Materials Science, Montanuniversität Leoben, Leoben, Austria; [u]Graduate School of Engineering, Kyushu Institute of Technology, Kitakyushu, Japan; [v]Magnesium Research Center, Kumamoto University, Kumamoto, Japan; [w]Synchrotron Light Application Center, Saga University, Saga, Japan; [x]Hydrogen Research Institute, Département de Chimie, Biochimie et Physique, Université du Québec à Trois-Rivières, Trois-Rivières, Canada; [y]Department of Materials Science and Engineering, Kyushu University, Fukuoka, Japan; [z]Department of Physics of Materials, Faculty of Mathematics and Physics, Charles University in Prague, Prague, Czech Republic; [aa]School of Mechanical, Industrial and Manufacturing Engineering, Oregon State University, Corvallis, OR, USA; [ab]Academy of Sciences of the Czech Republic, Institute of Physics of Materials, Brno, Czech Republic; [ac]College of Engineering, Ibaraki University, Mito, Japan; [ad]Materials Research Group, Department of Mechanical Engineering, University of Southampton, Southampton, UK; [ae]Departments of Aerospace Engineering and Mechanical Engineering, Iowa State University, Ames, IA, USA; [af]Division of Materials Science & Engineering, Ames Laboratory, Ames, IA, USA; [ag]Russian Academy of Sciences, Institute of Solid State Physics, Chernogolovka, Russia; [ah]Karlsruhe Institute of Technology (KIT), Institute of Nanotechnology, Eggenstein-Leopoldshafen, Germany; [ai]Department of Mechanical Engineering, Doshisha University, Kyoto, Japan; [aj]Department of Electrical Engineering, Kyushu Sangyo University, Fukuoka, Japan; [ak]M.N. Miheev Institute of Metal Physics, Ural Branch of RAS, Ekaterinburg, Russia; [al]Department of Mechanical Engineering, Karadeniz Technical University, Trabzon, Turkey; [am]Groupe de Physique des Matériaux, Normandie University, UNIROUEN, INSA Rouen, CNRS, Rouen, France; [an]Institute of Solid State and Materials Physics, Dresden University of Technology, Dresden, Germany; [ao]Department of Materials Engineering, Indian Institute of Science, Bangalore, India; [ap]Department of Materials Science and Engineering, Kyoto University, Kyoto, Japan; [aq]Elements Strategy Initiative for Structural Materials (ESISM), Kyoto University, Kyoto, Japan; [ar]Physics of Nanostructured Materials, University of Vienna, Wien, Austria; [as]Faculty of Materials Science and Engineering, Kunming University of Science and Technology, Kunming, People's Republic of China; [at]Institute of Physical Metallurgy, Metal Forming and Nanotechnology, University of Miskolc, Miskolc, Hungary

CONTACT Kaveh Edalati kaveh.edalati@kyudai.jp WPI, International Institute for Carbon-Neutral Energy Research (WPI-I2CNER), Kyushu University, Fukuoka, Japan

© 2022 The Author(s). Published by Informa UK Limited, trading as Taylor & Francis Group.
This is an Open Access article distributed under the terms of the Creative Commons Attribution License (http://creativecommons.org/licenses/by/4.0/), which permits unrestricted use, distribution, and reproduction in any medium, provided the original work is properly cited.

ABSTRACT

Severe plastic deformation (SPD) is effective in producing bulk ultrafine-grained and nanostructured materials with large densities of lattice defects. This field, also known as NanoSPD, experienced a significant progress within the past two decades. Beside classic SPD methods such as high-pressure torsion, equal-channel angular pressing, accumulative roll-bonding, twist extrusion, and multi-directional forging, various continuous techniques were introduced to produce upscaled samples. Moreover, numerous alloys, glasses, semiconductors, ceramics, polymers, and their composites were processed. The SPD methods were used to synthesize new materials or to stabilize metastable phases with advanced mechanical and functional properties. High strength combined with high ductility, low/room-temperature superplasticity, creep resistance, hydrogen storage, photocatalytic hydrogen production, photocatalytic CO_2 conversion, superconductivity, thermoelectric performance, radiation resistance, corrosion resistance, and biocompatibility are some highlighted properties of SPD-processed materials. This article reviews recent advances in the NanoSPD field and provides a brief history regarding its progress from the ancient times to modernity.

Abbreviations: ARB: Accumulative Roll-Bonding; BCC: Body-Centered Cubic; DAC: Diamond Anvil Cell; EBSD: Electron Backscatter Diffraction; ECAP: Equal-Channel Angular Pressing (Extrusion); FCC: Face-Centered Cubic; FEM: Finite Element Method; FSP: Friction Stir Processing; HCP: Hexagonal Close-Packed; HPT: High-Pressure Torsion; HPTT: High-Pressure Tube Twisting; MDF: Multi-Directional (-Axial) Forging; NanoSPD: Nanomaterials by Severe Plastic Deformation; SDAC: Shear (Rotational) Diamond Anvil Cell; SEM: Scanning Electron Microscopy; SMAT: Surface Mechanical Attrition Treatment; SPD: Severe Plastic Deformation; TE: Twist Extrusion; TEM: Transmission Electron Microscopy; UFG: Ultrafine Grained

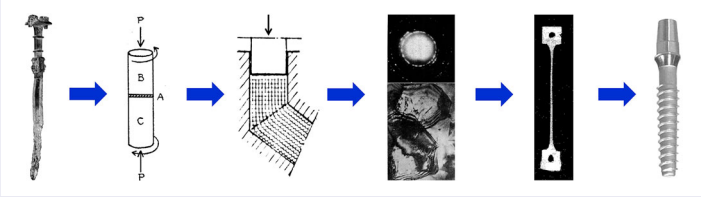

IMPACT STATEMENT

This article comprehensively reviews recent advances on development of ultrafine-grained and nanostructured materials by severe plastic deformation and provides a brief history regarding the progress of this field.

ARTICLE HISTORY
Received 3 December 2021

KEYWORDS severe plastic deformation (SPD); surface severe plastic deformation; ultrafine-grained (UFG) materials; mechanical properties; functional properties

1. Introduction

Severe plastic deformation (SPD) methods are becoming popular due to their capability for refinement of the grain size of materials to the submicrometer or nanometer scale [1]. Such grain refinement, which is accompanied with the formation of various kinds of lattice defects and unique microstructural features, leads to advanced mechanical and functional properties [2]. These properties are generally superior in SPD-processed materials when compared to their coarse-grained counterparts [1,2].

The SPD field owes its popularity to easy applicability to metallic materials, which results in enhanced mechanical properties [1,2]. Due to such enhancement of properties, there have been significant attempts to invent new SPD methods to produce metallic parts with large size or a special shape for future commercial applications [3]. Moreover, there are some trends to employ the SPD methods to other kinds of materials such as polymers [4], ceramics [5], glasses [6], carbon polymorphs [7], semiconductors [8], and so on. Moreover, nowadays, the SPD methods are used not only for the modification of existing materials, but they are also combined with theoretical studies and employed to design and synthesize new materials and metastable phases with advanced properties [9].

The SPD field has a long history for at least 2,700 years [10–12], although its written science first appeared in the twentieth century [13–16]. Such a long-lasting history confirms the high potential of the field in developing advanced materials. The promising results reported recently on the application of the SPD methods to meet energy-related challenges suggest that the NanoSPD field will continue its growth because energy is a significant issue in many countries due to the global warming crisis and scarcity of resources [17].

This review paper is a collective effort to the broad topics on NanoSPD, a field that deals with the science and art of production of advanced bulk nanostructured materials (BNM) by SPD techniques [2]. Both historical development and recent trends are reviewed by scientists active in the field and some terminological aspects are discussed. Since over 1,000 publications appear in the field of SPD every year (Figure 1) [18], this review endeavors to cover the most striking findings which can promote the science,

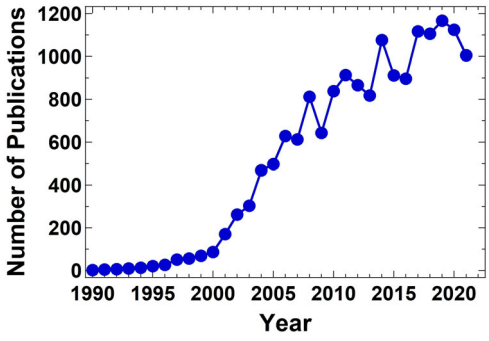

Figure 1. Number of publications per year on severe plastic deformation [Scopus, November 25, 2021]. Number of publications in 2020 and 2021 may have been negatively affected by the COVID-19 virus crisis.

technology, and commercialization of the SPD research in the future.

2. Terminology

According to the International NanoSPD Steering Committee, bulk nanostructured materials are typically defined as ultrafine-grained (UFG) materials that have grain sizes below 1 μm (i.e. sizes at the submicrometer or nanometer scale), with mostly high-angle grain boundaries [2]. These UFG materials usually contain other nanostructural features such as nanoprecipitates, nanoclusters, nanotwins, dislocation substructures, etc. The SPD technology is presently the most effective procedure to produce such nanomaterials and it includes different processing techniques and their modifications, namely, high-pressure torsion (HPT) [19], equal-channel angular pressing (ECAP) which was originally introduced as equal-channel angular extrusion (ECAE) [20], accumulative-roll bonding (ARB) [21], twist extrusion (TE) [22], multi-directional forging (MDF) which is also known as multi-axial forging (MAF) [23], and so on. These methods can realize heavy straining (equivalent strain > 6) under high pressure while maintaining the billet shape [1].

Despite this definition, there are still some arguments about the real threshold of strain, as in some materials, UFG structure can be achieved at strains lower than 6, while in some other materials, microstructural evolution continues to occur even at shear strains higher than 1,000. Although the term of *ultra-SPD* was recently suggested for introducing such extreme strains [9], it is hard to find rigid strain borders between conventional metal forming, SPD, and ultra-SPD. Another terminological issue is that some techniques, such as intensive rolling. intensive wire drawing, and intensive extrusion can induce extremely large strains to generate UFG structure [15]; however, there is no general agreement whether these methods should be classified as SPD because the dimensions of samples change during these processes. Some publications also suggest considering processes such as surface attrition or peening as *surface-SPD* methods [24].

3. History

The history of SPD can be divided into three parts: (i) ancient SPD, (ii) classic SPD and (iii) modern NanoSPD. It is not known when and where the first application of SPD appeared, but its history is probably as old as the history of metal forming. At the beginning of the twentieth century, scientists showed some interests in the application of SPD and the field experienced a turning point at Harvard University, where Percy W. Bridgman introduced several techniques to impose large plastic deformation in various materials [13,19]. Another turning point happened in 1988 in Ufa, where Ruslan. Z. Valiev and his co-workers reported the formation of UFG structures and resultant low-temperature superplasticity in an aluminum alloy [16]. Further development of this research into production of UFG materials by SPD processing, followed by the publication of a review paper in 2000 (which currently has over 5000 citations) [1], immediately attracted interest of materials scientists and heralded in the modern age of NanoSPD with a focus on the relation between advanced mechanical/functional properties and nanostructural features. Progress in the development of SPD processing was also assisted by the establishment of an International NanoSPD Steering Committee at the end of last century which supervised a series of international NanoSPD conferences which have been held at various locations around the world. The marked increase in the number of SPD-related publications since 2000 is shown clearly in Figure 1. Despite this well-known story about the evolution of the NanoSPD research, there were some significant historical activities in this field which are less known and need to be mentioned.

3.1. Ancient severe plastic deformation

The power of SPD was known at least during the transition from the Bronze Age to the Iron Age. Repeated hammering and folding (also known as repeated beating and twisting) was probably the first SPD technique that was used for processing tools [10–12]. Due to higher melting point of iron compared to bronze, its casting was a big challenge and thus metal forming received high attention for processing tools made from iron [12]. The iron ingot obtained from furnace required repeated hammering, heating, and folding to squeeze slag and remove carbon to make wrought iron with enhanced toughness. The application of this hard and time-consuming technique was mainly limited to fabricate simple but

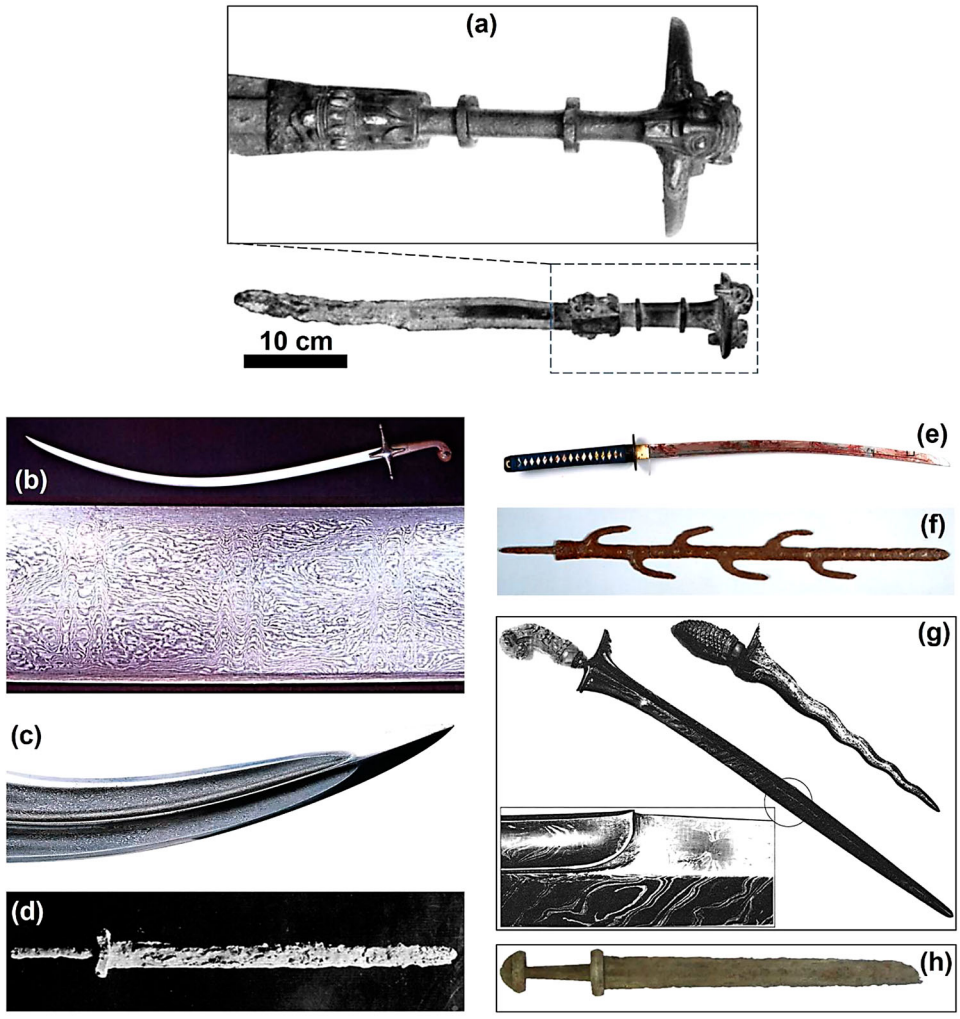

Figure 2. (a) Multipiece complex steel sword, fabricated in Lauriston, Iran, 750-650 BSE (The Metropolitan Museum of Art, New York) [11]. Patterned swords: (b) Persian Shamshir [31], (c) Indian blade [26], (d) Chinese sword [32], (e) Japanese Katana [33], (f) Korean seven-branched sword [34], (g) Indonesian Kris [35] and (h) Viking pattern-welded sword [30].

strategic tools such as weapons; however, skillful smiths could fabricate complex and multipiece tools, which are now available in some museums. Figure 2(a) shows a multipiece steel sword fabricated in 750-650 BCE in Luristan, an area in the southwest of Iran which experienced an early transition from the Bronze Age to the Iron Age (The Metropolitan Museum of Art, New York [11]).

The technique of repeated hammering and folding is historically connected to the production of patterned Damascus steel swords [12]. It is not still clear if Damascus refers to the historical capital city of Syria or to the patterned shape of these swords (known as damask or damascene pattern) [25,26]. To fabricate the Damascus steel swords, high-carbon wootz steels, which were known as Fuladh in Syria, watered Pulad in Persia, Bulat in Russia, and Bintie in China, were mainly shipped from Sri Lanka and India to Persia and other nearby countries and forged [12,25,26]. Due to repeated forging and folding, the structure of these swords became inhomogeneous consisting of low-carbon and high-carbon regions, and this gave a patterned shape to these swords [12]. The reason for high strength of these swords became a mystery in the eighteenth century, but it was shown in the last century that the strength of these swords was mainly due to their high carbon and dispersion of carbide particles in the microstructure [25,26]. Some studies within this century suggested that severe forging could result in the formation of carbon nanotubes to strengthen these swords [27], but some researchers raised doubt about the presence of carbon nanotubes in these swords [28].

The techniques of repeated hammering and forging to produce patterned swords was gradually employed by many ancient societies such as Egypt, Iran, China,

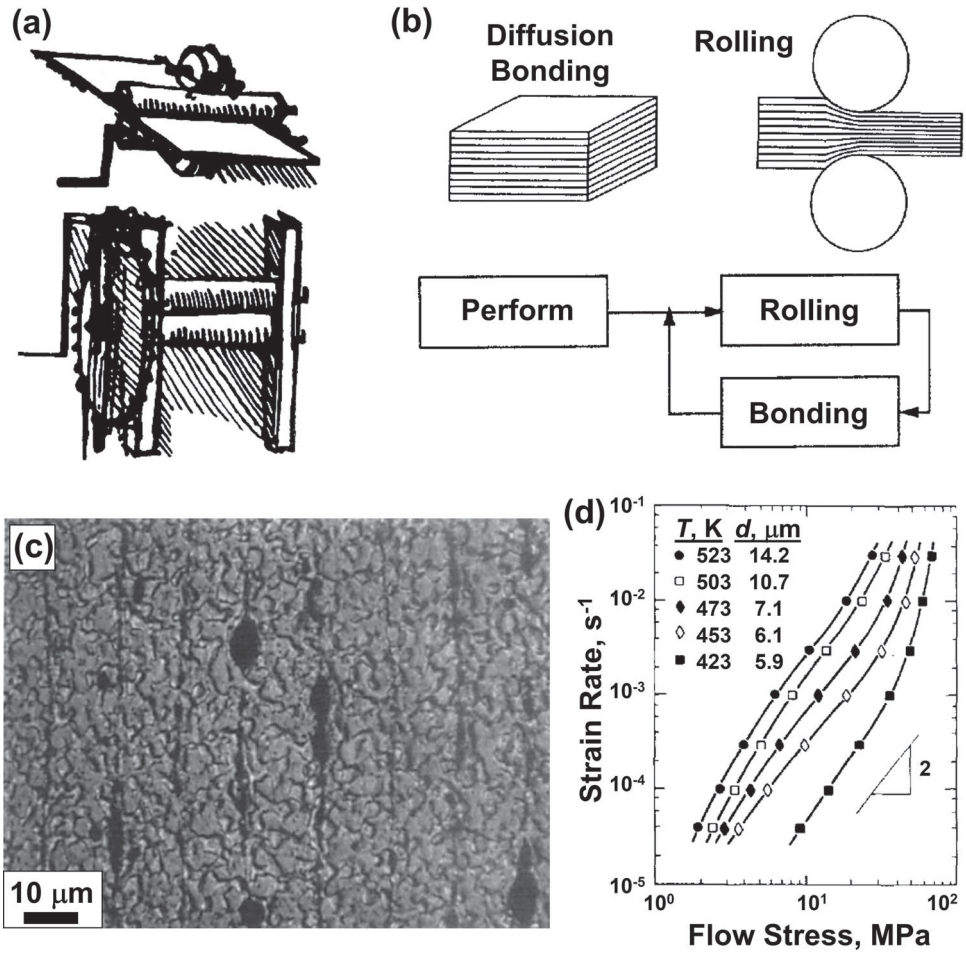

Figure 3. (a) Schematic illustration of rolling method by Leonardo de Vinci in 1495 [36]. (b) Illustration of foil metallurgy or superlamination method by Kikuchi *et al.* [45]. (c) Microstructure of Mg-Li alloy processed by foil metallurgy [46]. (d) Low-temperature superplasticity of Mg-Li alloy processed by foil metallurgy [46].

Russia, Korea, Japan, Turkey, Philippines, Indonesia, etc. [12,25,26]. European nations were apparently familiar with the repeated hammering and forging technique and Vikings widely used the method to produce their weapons [29]. The difference between the Vikings' early swords and Damascus steel swords was that the Vikings apparently forged different pieces of steels and iron together (a method which is known as pattern forging or pattern welding), while the Damascus steels were mainly fabricated from a piece of high-carbon steel by large numbers of forging and folding passes [12,29]. However, the famous Ulfberht Viking swords are believed to be fabricated from a single piece of imported steel similar to the Damascus swords [30]. Figure 2 shows some swords which apparently produced by repeated hammering and folding or pattern forging: (b) Persian Shamshir [31], (c) Indian blade [26], (d) Chinese sword [32], (e) Japanese Katana [33], (f) Korean seven-branched sword in Isonakami Jingu Shrine in Japan [34], (g) Indonesian Kris [35], and (h) Viking pattern-welded sword [30].

3.2. Transition from ancient repeated hammering and folding to modern accumulative roll-bonding

It is hard to mention when and where repeated rolling and folding was introduced. Rolling mills have over 2000 years history, but the first known written description about the rolling method, was presented by Leonardo da Vinci in the fifteenth century, as shown in Figure 3(a) [36]. Rolling mills were produced in Europe at least in the fifteenth century and they became popular during the Industrial Revolution [36]. A search in the available documents shows that the repeated rolling and folding was a known technique at least in the 1920s for processing polymers [37,38], in 1960s for fuel cell applications [39,40], in the 1960s for production of superplastic composites [41] and in the 1970s for production of superconductors [42,43]. In the late 1990s, the process of repeated rolling and folding was employed for grain refinement and it became popular as an SPD method with a new name of accumulative roll-bonding (ARB) [21].

The ancient pattern welding (pattern forging) process was also modified by replacing hammers with rolling machines in the foil metallurgy process [44]. As shown in Figure 3(b), in the foil metallurgy process, which is also known as lamination or super-lamination process [45], several sheets are rolled together, and the rolled sheets are cut and rolled again. In 1990, the foil metallurgy method was used to produce a fine-grained Mg-Li alloy with low-temperature superplasticity, as shown in Figure 3 (c and d) [46].

3.3. Bridgman's works on severe plastic deformation

Percy W. Bridgman, who won the Nobel Prize in physics in 1946, can be considered as one of the first scientists that could realize the application of high pressure and large plastic strain to a wide range of organic and inorganic materials including, metals, alloys, ceramics, glasses, polymers, etc. He published a book in 1952 and introduced some methods for introducing large strains and discussed about the effects of large plastic strain on the behavior of different materials [13]. He was the first scientist who could achieve pressures over 1 MPa in laboratory and he immediately noticed that high pressure is essential to induce large plastic strain [13]. The most striking findings of Bridgman in the field of SPD was achieved using a method, which is now known as high-pressure torsion (HPT) [19]. Since the HPT method is applicable to a wide range of materials, the method has made a significant contribution to different fields such as materials science, chemistry, physics, geology, and biology [47].

The principle of HPT, described by Bridgman, is shown in Figure 4(a) [19]. A thin disc is compressed between two anvils under high pressure, and large shear strain is induced by rotating the anvils with respect to each other. To realize the method in the laboratory, Bridgman made a facility schematically shown in Figure 4(b). His facility consisted of two cylindrical anvils with 6-3-12.7 mm diameter circular projections on the surfaces of the anvils. To introduce shear strain, he put a rectangular block between the two anvils and rotated the block manually using a lever, as shown in Figure 4(c) [48]. His main measurement was in-situ torque measurement and estimation of shear strength, as shown in Figure 4(d) for bismuth; however, he occasionally used the ex-situ methods. He found that breaks in the plots of steady-state shear stress against pressure like those observed in Figure 4(d) can correspond to pressure- or strain-induced phase transformations. Although Bridgman's main motivation to use the HPT method was to discover new polymorphs,

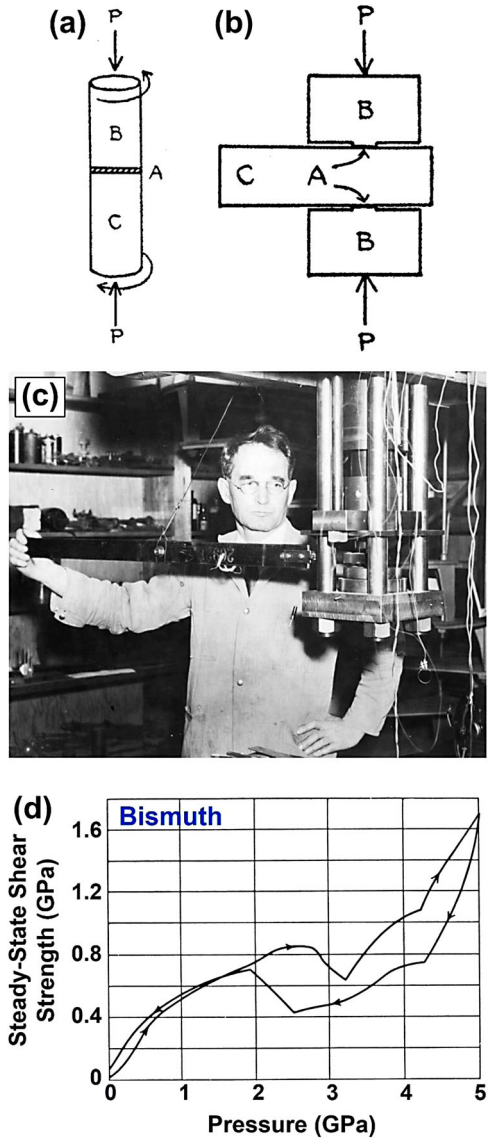

Figure 4. (a) Principles of high-pressure torsion described in 1935 (A: sample, B and C: cylindrical anvils) [19]. (b) Schematic illustration of the Bridgman method to conduct high-pressure torsion (A: sample, B: cylindrical anvils, C: rotating block) [19]. (c) Photograph of operation of first high-pressure torsion facility by Bridgman (rotation was manual) [48]. (d) Plot of steady-state shear strength versus pressure achieved by Bridgman anvils for bismuth (breaks in plot correspond to phase transformations) [50].

he reported various observations which can be considered as the first scientific building blocks of the SPD field. The details of Bridgman's works were reviewed in an earlier publication [47]. Here some of his key findings are briefly given.

- The idea of infinite strain hardening is not correct, and the flow stress of all materials finally saturates in a steady state [19].
- Some materials experience a paradoxical strain softening rather than strain hardening [49].

- Despite severe strain induced by SPD, amorphization is a rare phenomenon, indicating that also dynamic recrystallization should occur at large strains [49,50].
- The crystal size of materials decreases to the nanometer level by severe straining, but the severity of refinement depends on the material: it is more significant for metals with high melting points as well as for materials with low capacity for crystallization at room temperature such as minerals [48–51].
- Powders can experience cold consolidation and even mechanical alloying at large strains [19,52].
- New phases are detected by HPT processing which cannot be achieved by pure compression [13].
- Large plastic deformation can enhance the kinetics of phase transformations. Thus, chemical reactions: and phase transitions that occur within a geological timescale in nature can occur within a few minutes during the HPT process [51].
- Although minerals and ceramics are generally brittle at ambient temperature and pressure, with the application of HPT, they can be plastically deformed. The plastic deformation of these materials, which usually is accompanied by phase transformations and recrystallization, results in snapping of the HPT anvils suggesting a mechanism for deep-seated earthquakes under high pressure and plastic strain [53].

3.4. Transition from Bridgman anvils to modern high-pressure torsion

Bridgman's facility designed for HPT processing in 1935 had a central plate, and its rotation was manual [19]. Boyd and Robertson in 1945 employed an electric motor to rotate the central plate [54], and Vereshchagin *et al.* in 1960 used a hydraulic system for rotating the plate [55]. Griggs *et al.* in 1960 removed the central plate and rotated the upper anvil with respect to the lower one using large gears and an electric motor, as shown in Figure 5(a) [56]. The design of HPT facilities has not been significantly changed since 1960 to now, although some modifications were made by different groups to increase either the pressure, temperature or sample size or to modify the sample shape [57–60].

Within the last century, the HPT method gradually evolved from a tool mainly used to examine structural changes under high pressure to an SPD method for producing nanomaterials. Details on this less-known evolution can be found in an earlier review [47], but some major and less-known works on production of nanomaterials by HPT processing are briefly summarized below:

- In 1972, Jesser and Kuhlmann-Wilsdorf processed pure nickel by HPT and examined its microstructure by transmission electron microscopy (TEM) and clarified the formation of nanograins, as shown in Figure 5(b) [61].
- In 1976 and 1979, Erbel used TEM and reported the formation of ultrafine grains with high angles of misorientation in HPT-processed aluminum and copper [14,62].
- In 1984, Saunders and Nutting reported that the microstructures of copper and silver evolve from elongated subgrains at the early stages of straining to equiaxed submicrometer grains with lower dislocation density at large strains [63].
- In 1985, Zhorin *et al.* estimated the crystallite size of HPT-processed copper and Cu-Ni using X-ray diffraction (XRD) and reported crystallite sizes smaller than 50 nm [64].

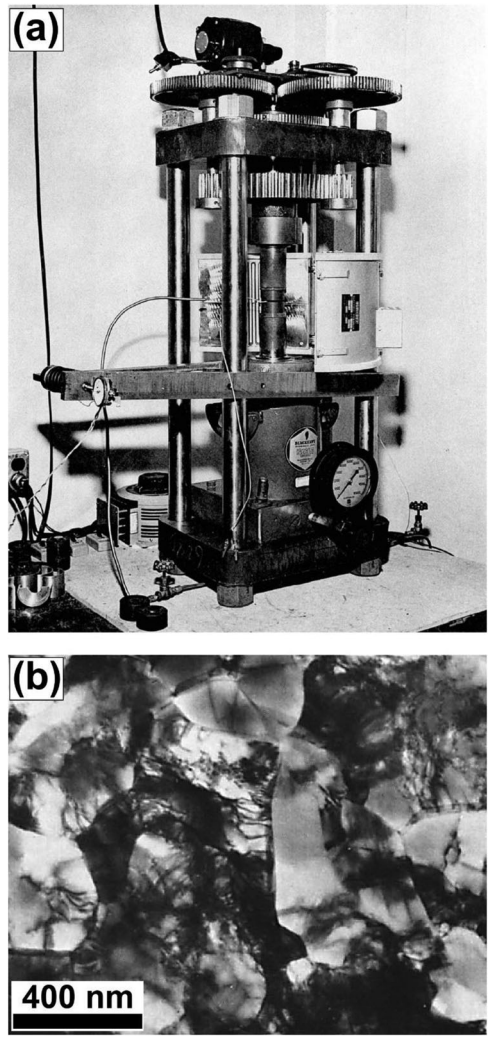

Figure 5. (a) Griggs's facility fabricated in 1960 for high-pressure torsion processing of geological materials (lower anvil was fixed and upper anvil was rotated by an electric motor and gears) [56]. (b) Transmission electron microscopy of ultrafine-grained pure nickel processed by high-pressure torsion in 1972 [61].

- In 1986, Smirnova *et al.* reported small nanocrystallite sizes and the occurrence of dynamic recrystallization in HPT-processed copper and nickel [65,66]. At this time, Russian scientists used the HPT method for processing various materials including iron alloys to achieve high strength and control phase transformations [67,68].
- In 1987, Gil Sevillano and Aernoudt reported the presence of ultrafine grains and low-energy dislocation structures in pure aluminum processed by HPT [69].
- In 1988, Aleksandrova *et al.* reported a significant grain refinement to an almost amorphous level in HPT-processed GaSb [70].
- In 1988, Teplov *et al.* reported the formation of nanograins in an HPT-processed austenitic steel [71].
- In 1988, Ivanov e*t al.* reported the formation of nanosized intermetallics in HPT-processed Ni-Al alloy [72].
- In 1988, Valiev *et al.* reported the formation of ultrafine grains and resultant low-temperature superplasticity in HPT-processed Al-4%Cu-0.5%Zr alloy [16]. This publication together with several other works appeared in the 1990s [73–75] and followed by a review paper in 2000 [1] made the NanoSPD field a popular research field worldwide.

3.5. Nanomaterials by other deformation methods

As discussed above, the ARB and HPT methods have made a large contribution to the historical development of the NanoSPD field. Since the ECAP, TE and MDF processes are newer SPD methods [20,22], their contribution to the SPD field became significant only at the end of the last century (forging from different axes has longer history than MDF in metal working and extrusion through a bended or twisted channel have longer history than ECAP and TE particularly in the food and polymer industries [76–78]). Conventional metal forming processes which are not considered as SPD methods in some classifications [2], extensively contributed to the generation of nanomaterials in the 1960s and 1970s. In 1982, Gil Sevillano *et al.* thoroughly reviewed the papers published in the 1960s and 1970s with regard to the effect of large plastic strain on microstructural evolution [15]. The methods used in these pioneering publications were conventional deformation methods such as severe rolling, severe drawing, and severe extrusion; and equivalent strains up to six were successfully introduced to a wide range of metals, alloys, and composites. For details of these results, the reader is referred to the original review paper, but some main points are indicated below. Here, it is worth mentioning that extrusion was first introduced by Joseph Bramah at the end of eighteenth century to fabricate lead tubes; however, wire drawing has a long history as rolling and it was at least 2500 years ago used by Persians to fabricate bronze and gold wires [79,80].

- The grain sizes in severely deformed metals such as aluminum, copper, nickel, iron, and chromium reach 100-500 nm, while grain sizes below 100 nm can be achieved in some alloys and composites.
- The grain size decreases with increasing the equivalent strain, but there is a saturation trend at large strains, as shown in Figure 6(a) for aluminum and in Figure 6(b) for copper.
- The rate of grain refinement depends on the deformation mode and the slowest grain refinement is achieved in the torsion mode. Similar conclusion was achieved in earlier studies by Bridgman [13].
- In addition to grain refinement, the dislocation density increases with increasing strain, while there are some saturation levels for some materials. In 1979, Rigney also showed that there are limitations for dislocation accumulation by straining and that the dislocation density finally saturates at a steady-state level [81].
- Grains can develop large angles of misorientation at large strains due to dynamic recrystallization, which can be confirmed by detailed TEM analysis. In 1972, Nutting conducted detailed TEM studies and observed that the dislocations generated during large deformation continuously move and get absorbed in low angle grain boundaries, and this gradually increases the misorientation angle until high-angle grain boundaries are formed (this is currently considered as continuous dynamic recrystallization). They reported a (discontinuous) dynamic recrystallization process also occurs when the stored energy reaches a critical level provided the grain boundaries are mobile enough [82].

In the 1970s, scientists at the Institute of Technical Physics, Minsk, USSR conducted significant theoretical and experimental works to develop a method that can apply simple shear uniformly and repeatedly in a large billet. The conclusion of these attempts, which was first appeared in the internal documents of the institute [83] was patented in 1977 [84]. This patent by Segal introduced the principles of a method which is now known as ECAE or ECAP method [84]. This method is still the most popular SPD process with high potential for industrial applications. Another important patent appeared in 1977 by Kopylov and Segal in which conform was combined with extrusion to make the extrusion technique continuous [85]. This extrusion-conform method was later combined with ECAP in Minsk and led to

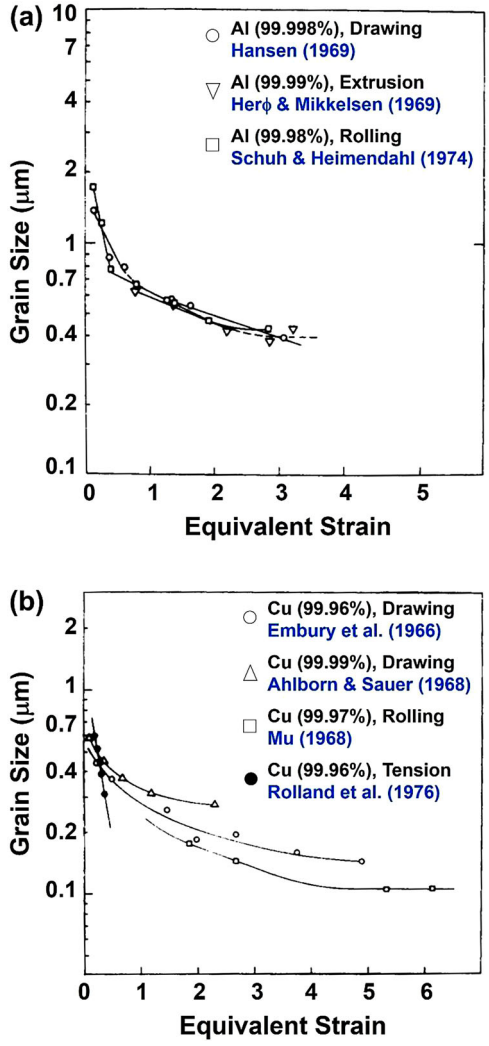

Figure 6. Grain refinement to submicrometer level in (a) aluminum and (b) copper with increasing equivalent strain through intensive drawing, extrusion and rolling [15].

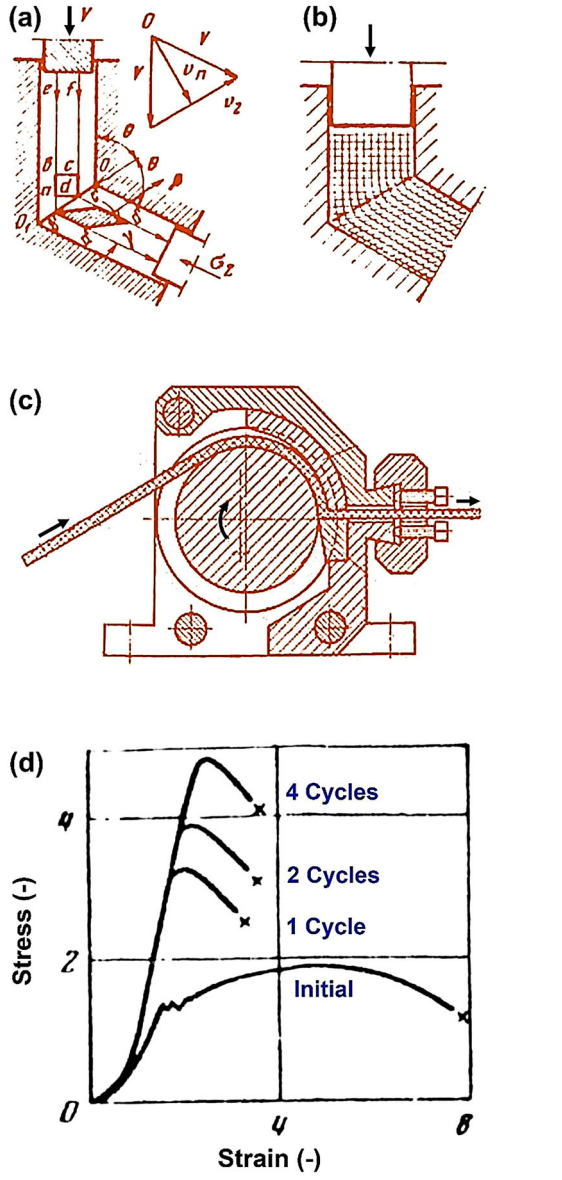

Figure 7. (a) Principles of equal-channel angular pressing (extrusion) developed by Segal *et al.* [20]. (b) Experimental visualization of simple shear in equal-channel angular pressing by Moire fringes and coordinate grids [20]. (c) Combination of equal-channel angular pressing with conform developed in Minsk [86]. (d) Stress-strain curves for iron processed by equal-channel angular pressing, showing combination of high strength and good ductility (units for X and Y axes were not given in paper, but it seems each unit in X and Y axes roughly correspond to strain of 2-3% and stress of 200-250 MPa, respectively) [20].

a continuous method which is now known as ECAP-conform [86]. In 1978, Segal *et al.* submitted a paper about the principles of ECAP method which was finally published in 1981 [20]. The paper not only introduced the principles of the method, but also highlighted the possibility to achieve high strength and good ductility in severely deformed materials. There were significant activities in Minsk to apply the ECAP method to control strength, elasticity, superconductivity, and magnetic properties [3], but very limited publications were released from these studies. In 1994, details of some activities conducted in Minsk appeared in a book, which covered the principles of both ECAP and ECAP-conform methods and presented some experimental data achieved using the methods [86]. In the 1990s, the capability of the ECAP method in production of UFG materials was reported [75,87] and this resulted in quick spread of the ECAP method in Western and Asian countries [88]. Figure 7 shows (a) the principles of ECAP [20], (b) experimental visualization of simple shear in ECAP by using Moire fringes and coordinate grids [20], (c) principles of ECAP-conform [86] and (d) high strength and high ductility reported after processing by ECAP [20].

In 1986, Rigney and co-workers examined the effect of sliding on microstructure of copper [89]. They found

that the material experiences large plastic deformation at the surface during sliding, but the strain decreases with increasing depth, as shown in Figure 8(a). Examination of the material by TEM confirmed that nanograins clearly form in the upper surface layer. With increasing depth, a gradient structure from nanograins to coarse grains is observed, as shown in Figure 8(b). They also found similar features in other materials including aluminum, as schematically shown in Figure 8(c) [90]. These studies provided clear evidence for the formation of a gradient (graded) microstructure by surface-SPD. Such, a concept was later used to develop new approaches to induce intense plastic strain on the surface to achieve gradient microstructures [91].

3.6. Erbel's book on severe plastic deformation

Although the history of the HPT technique has been presented in a recent review [47], some historical studies on producing UFG materials by SPD methods are less known in the NanoSPD community and were missed in Ref. [47]. The research work of the Polish scientist Stanisław Erbel, and especially his book 'Mechanism of change of properties of metals subjected to large deformations' written in 1976 (Figure 9a) are among these less-known studies [14]. Despite the fact that Bridgman published a book earlier on the principles of SPD in 1952 [13], Erbel's book is probably the first one dedicated to the formation of UFG materials by SPD processing, as discussed in a recent paper [92].

In this book, Erbel presented details of an HPT device for obtaining large strains in rings and tubes (Figures 9b and c). He explained the cause for cracking of a few metallic materials such as iron and brass under the action of high hydrostatic pressures ($\sim$1.2 GPa) and large stain. He reported the formation of voids in some grain boundaries, a fact that was reported in recent years in severely deformed copper [93].

He investigated the mechanical properties (Figure 9d) and microstructure by means of TEM for severely deformed pure aluminum processed to equivalent strains up to 400 (Figure 9e). He reported that despite strengthening of aluminum at the early stages of straining, a softening occurs at large strains which is consistent with numerous reports about aluminum in recent years [94,95]. Furthermore, he found a high strain-rate sensitivity and suggested that this can be considered as an interesting indication for grain boundary sliding and superplastic behavior at low temperature. Recent studies also suggested that grain boundary sliding can partly contribute to the deformation of SPD-processed aluminum at room temperature [96]. The potential of SPD to achieve low-temperature superplasticity was clearly confirmed several years after Erbel's publication [16,46].

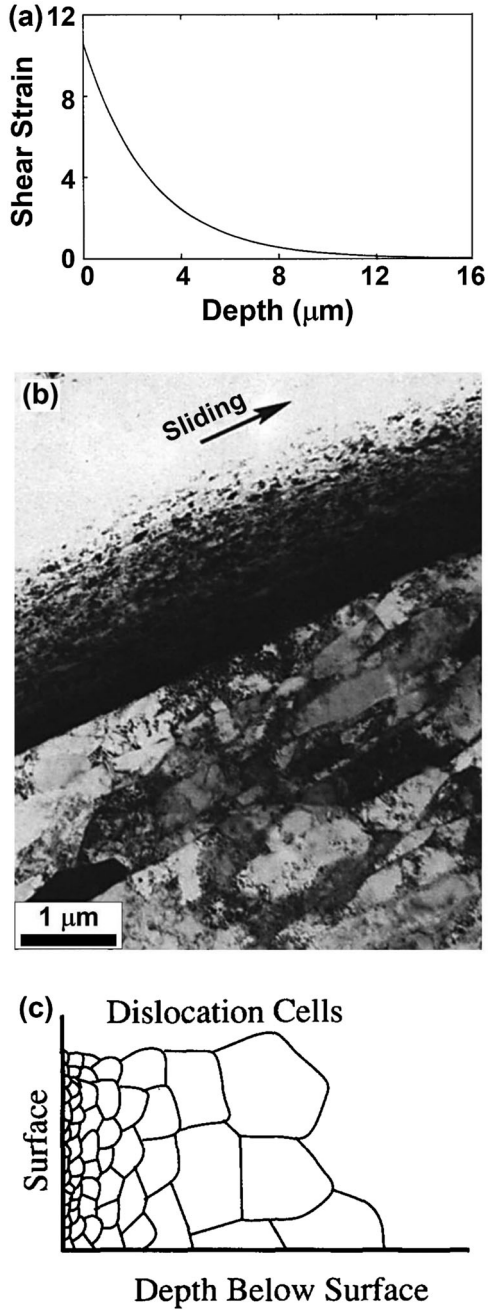

Figure 8. (a) Estimation of surface severe plastic deformation by sliding reported by Rigney *et al.* [89]. (b) Gradient microstructure in copper processed by sliding [89]. (c) Schematic illustration of gradient microstructure formation in aluminum by sliding [90].

He reported the formation of a UFG structure and discussed its formation mechanism. He confirmed the formation of grains with high-misorientation angles using time-consuming electron diffraction method (Figure 9f), although quantitative analysis of misorientation angles in SPD-processed metals is much faster and

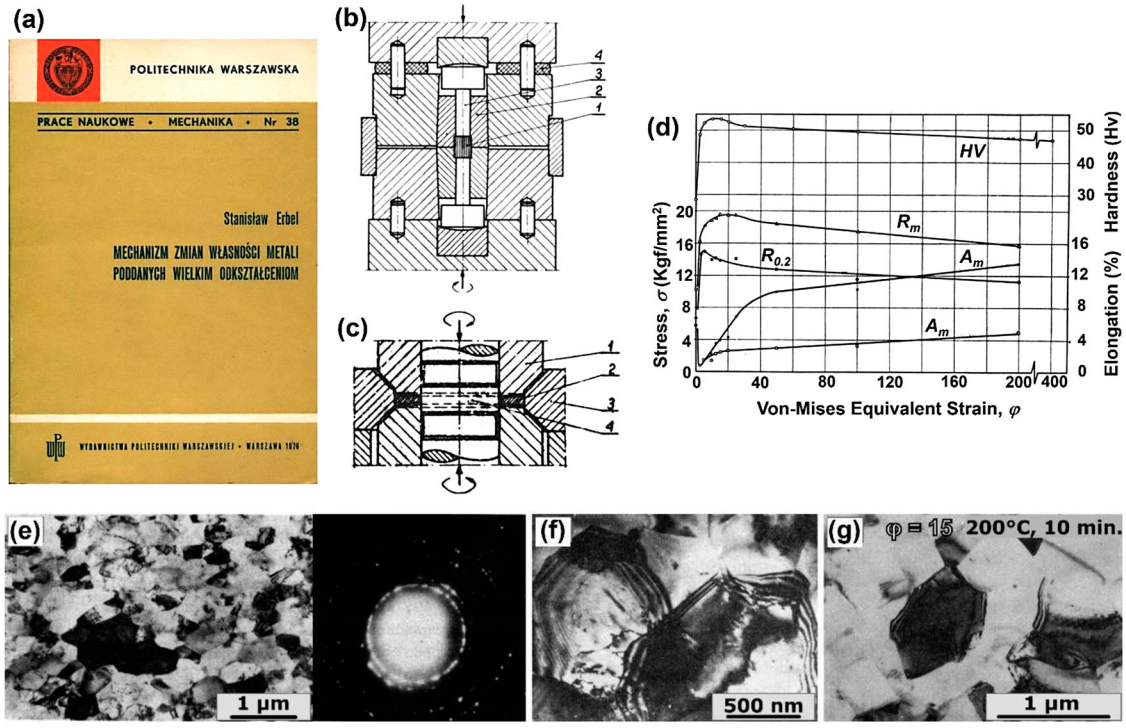

Figure 9. (a) Cover image of Erbel's book published in 1976. (b) and (c) Erbel's high-pressure torsion devices for processing tubular and ring samples, respectively (1: toothed punch, 2: ring or tube specimen, 3: external ring, 4: pin). (d) Change of mechanical properties of aluminum versus equivalent strain φ (*HV*: Vickers microhardness; $R_{0.2}$: yield stress, R_m, ultimate tensile strength, A_r: uniform elongation, A_m: maximum elongation). (e) Transmission electron micrograph and corresponding electron diffraction pattern of aluminum sample after torsional straining under an equivalent strain of $\varphi = 100$. (f) Transmission electron micrograph of equiaxed ultrafine grains with high misorientation angle in aluminum under severe plastic deformation. (g) Transmission electron micrograph taken during in-situ heating for aluminum after deformation under equivalent strain of $\varphi = 15$ [14].

easier in these days using electron backscatter diffraction (EBSD) method in scanning electron microscopy (SEM) [97,98]. Detailed microstructural observations conducted by Erbel and particularly the saturation of grain refinement are consistent with detailed observations conducted in recent years [99]. Here, it should be noted that although Erbel attributed the formation of high-angle grain boundaries to grain boundary rotation and sliding in his book, he revised his opinion in 1979 and commented that dynamic recrystallization should play an important role at very large strains [62]. It should be noted that the occurrence of dynamic recrystallization at large strains was originally suggested by Bridgman [19]. Detailed studies conducted in recent years also suggest similar mechanisms for the formation of high-angle grain boundaries [99].

Erbel's TEM studies were not limited to ex-situ observations but he also conducted advanced in-situ observations to examine the dislocation motion and thermal stability [14]. The in-situ observations of dislocation movement in SPD-processed metals by Erbel showed both emission and absorption of dislocations from grain boundaries. These findings are quite interesting for that time because it is well-known now that the grain boundaries in UFG materials can act as both source and sink for dislocations [100]. Erbel carried out in-situ observations of the thermal stability by heating the thin foils of UFG aluminum samples in the TEM (Figure 9g) and came to the conclusion that the UFG structures are thermally stable. Although Erbel's conclusion is acceptable for UFG aluminum, the thermal stability of many other UFG metals can be weak after SPD processing due to large stored energy in the form of dislocations or non-equilibrium grain boundaries [101,102].

4. Severe plastic deformation methods

Classic SPD methods such as HPT [19], ECAP [20], ARB [21], TE [22] and MDF [23] are still the most popular techniques to produce UFG metallic materials. In addition to these techniques, there are now over 100 SPD methods or their modifications, including friction stir processing (FSP) [103], repetitive corrugation and strengthening [104], hydrostatic extrusion [105], cyclic extrusion and compression (or expansion) [106], KOBO extrusion [107], constrained groove pressing [108], high-pressure sliding [109], etc. [3,110]. There are recent

trends to scale up the sample size, modify the sample shape, and develop new continuous or semicontinuous processes for possible industrial applications [111], which resulted in some successes in commercialization of SPD-processed materials [112]. In this section, the progress on different SPD methods is discussed.

4.1. High-pressure torsion

As explained earlier, in the HPT method, the material (usually in the form of disc) is torsionally strained under high pressure between two anvils. The shear strain in this method is calculated as $\gamma = 2\pi rN/h$, where r is the distance from the disc center, N is the number of turns and h is the thickness of the disc [47,113]. Since strain hardening in torsion is slower than in other SPD processes, there are suggestions to use the logarithmic or Hencky equivalent strain for this process [113], although the von Mises method is considered the most reasonable physical method to calculate the equivalent strain [47]. The HPT method is undoubtedly the best SPD method for fundamental studies because of two main reasons. First, the processing parameters such as strain, strain rate, pressure and temperature can be easily controlled. For example, the shear strain can be increased to 1,000 or even more in very small steps by changing the rotation angle [114]. In contrast, with other methods such as ECAP, ARB or TE, it is quite difficult to change the strain in small steps by increasing the number of passes [2]. Second, the pressure applied in HPT is quite high and offers a unique opportunity to handle almost all types of materials including hard and brittle ones such as silicon or diamond [115]. Despite these advantages of HPT for fundamental studies, the size of samples severely deformed with HPT are smaller than those deformed with other methods. This causes significant drawbacks to use the method for industrial applications. Moreover, the HPT facility itself is more complicated and expensive compared to the facilities required for ECAP, ARB, TE and MDF. Some important progresses regarding the HPT method are discussed below.

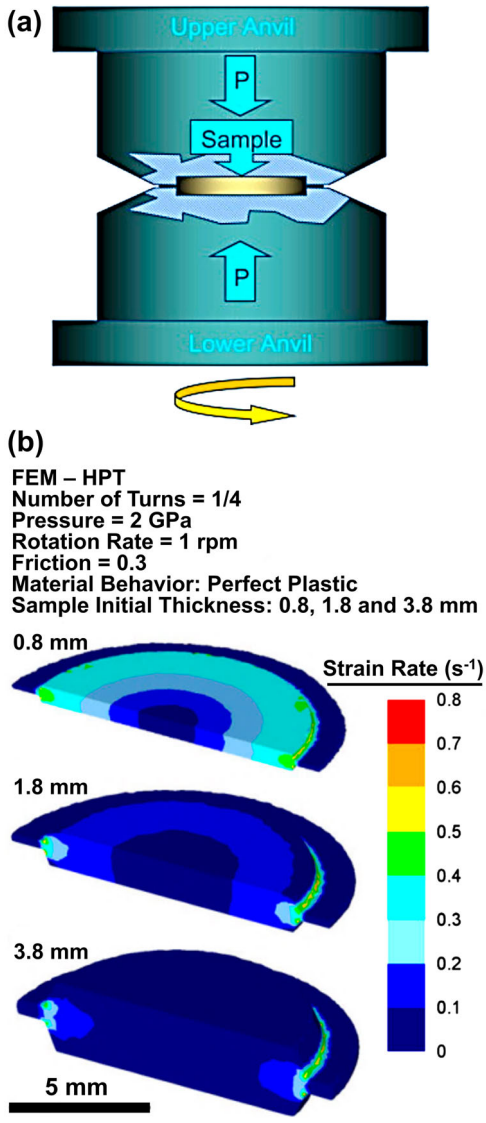

Figure 10. (a) Schematic illustration of quasi-constrained high-pressure torsion processing [116]. (b) Distribution of effective strain rate along cross-sectional planes of discs having initial thicknesses of 0.8, 1.8 and 3.8 mm during quasi-constrained high-pressure torsion under steady-state conditions [124].

4.1.1. Quasi-constrained high-Pressure torsion

The HPT method has attracted increasing attention of the materials science community due to its exceptional ability to impose extremely large strains in virtually any kind of material [113]. The unique combination of high compressive hydrostatic stresses and continuous shear straining in HPT is beneficial not only for grain refinement but also for powder consolidation and solid-state reactions [113]. To produce bulk samples with reasonable thickness, the HPT method practically is conducted under quasi-constrained condition by introducing flat-bottomed holes on the surface of both anvils, as shown in Figure 10(a) [116]. This quasi-constrained condition makes some complications in the flow behavior of materials during the HPT process compared to the basic description of the method. The basic description of HPT considers that the compressive stress acting on the sample is the axial load divided by its initial cross-sectional area. It is also considered that the effective strain increases with increasing distance from the disc center, and it is considered constant along the axial direction. There are some attempts to clarify the material behavior during quasi-constrained HPT conditions by theoretical modeling and simulations [117].

The finite element method (FEM) has been a powerful modeling tool to understand the plastic flow during quasi-constrained HPT and the distribution of stresses and strains [117]. For example, it has been shown that the outflow of material processed under quasi-constrained condition increases the load bearing area and effectively reduces the hydrostatic compressive stress [118]. Furthermore, this stress is higher near the center and decreases along the sample radial direction [119–121]. Consequently, the material near the center is processed under higher hydrostatic compressive stress than the material near the edge. The distribution of strain also differs from the basic description which is built on a similarity with torsion deformation. The friction with the anvil's lateral surface significantly affects the plastic flow around the edge of the discs [122]. Thus, an early attempt to scale up the sample thickness in quasi-constrained HPT resulted in pronounced strain localization [123]. FEM can accurately predict this effect. Figure 10(b) shows the distribution of strain rate during steady-state processing of samples of different initial thicknesses [124]. As the thickness-to-diameter ratio increases, the volume of the sample with inhomogeneous strain rate distribution also increases. The deformation zone concentrates near the mid-plane of the disc reducing the deformation imposed near the top and the bottom surfaces. Such strain and flow stress behaviors were also shown in some experimental studies [125–128]. These simulation and experimental studies suggest that the thickness-to-diameter ratio should be kept constant in any attempt to scale up the sample dimensions.

It is widely known that over 90% of plastic work imposed to the material in metal forming operations is converted into heat. This amount of heat can increase the sample temperature in the absence of heat conduction to the anvils in quasi-constrained HPT. FEM has been used to predict the temperature rise during this SPD process considering heat generation by plastic deformation, temperature rise in the sample and heat transfer to the anvils [129–131]. It was shown that the sample heating rate is higher in the beginning of the process, but it tends to decrease until reaching a steady-state temperature in which the heat generated is equal to the heat loss to the environment. This steady-state temperature depends strongly on the anvil volume, rotation rate and the strength of the material.

4.1.2. Upscaled high-pressure torsion

The HPT process [19] is very promising for grain refinement of metallic materials to sizes that are usually finer than those achieved by other SPD methods [2] such as ECAP [20] and ARB [132]. Another advantage of using the HPT process is its applicability to less-ductile (or even brittle) materials including intermetallics [9], ceramics [133,134] and semiconductors [8]. However, the limitation of the HPT process is small dimensions of the sample size which is typically 10 mm in diameter and 1 mm in thickness for quasi-constrained processing condition. Several strategies were employed to scale up the sample size in the HPT process: HPT using bulk cylindrical samples as shown in Figure 11(a) [123], HPT using ring samples as shown in Figure 11(b) [135], continuous HPT using sheet samples [136], continuous HPT using wire samples [137], and incremental HPT [138,139]. Motivated by attempts to scale up the sample size in the HPT process, some new methods were also introduced such as high-pressure torsion extrusion [140], incremental high-pressure sliding [141], and friction-assisted lateral extrusion [142]. Upscaling of the HPT process was extensively discussed in a recent overview paper [143].

Despite all previously used strategies for upscaling the sample size in the HPT process, increasing the press load still seems to be a viable approach for upscaling the sample size on an industrial scale. Thus, in a recent study [144], the machine capacity was increased to 500 tons so that the sample size could be extended to discs with 30 mm in diameter. This scaled-up HPT machine was applied to magnesium alloys, which are little ductile at ambient temperature. Discs with 30 mm diameter were prepared from commercially extruded AZ31 (Mg-3%Al-1%Zn in wt%) and AZ61 (Mg-6%Al-1%Zn in wt%) and processed at room temperature under 6 or 7 GPa and their grain sizes were well refined to $\sim$150 nm and $\sim$100 nm, respectively, as shown in Figure 11(c) [144]. Superplastic elongations of more than 400% were then attained in the corresponding alloys when tested in tension at elevated temperatures because of grain boundary sliding controlled by grain boundary diffusion.

It is emphasized that the magnesium alloys were successfully processed by the upscaled HPT at room temperature without breaking the samples. Such upscaling is important not only for future commercialization of the HPT method, but also for understanding the behavior of materials during the HPT process. For example, it was shown that, enlargement of the disc sample enables tensile samples to be taken at different radial distances within the same disc and therefore the effect of the equivalent strain on the superplastic elongations can be effectively evaluated, as demonstrated in Figure 11(d) [19].

4.1.3. High-pressure tube twisting

The high-pressure tube twisting (HPTT) process is a variant of HPT, introduced in 2009 by the SPD group of Metz, France [145]. In the HPTT method, a tube is fully constrained between an internal and external mandrel, an axial pressure is applied on the tube, then the external

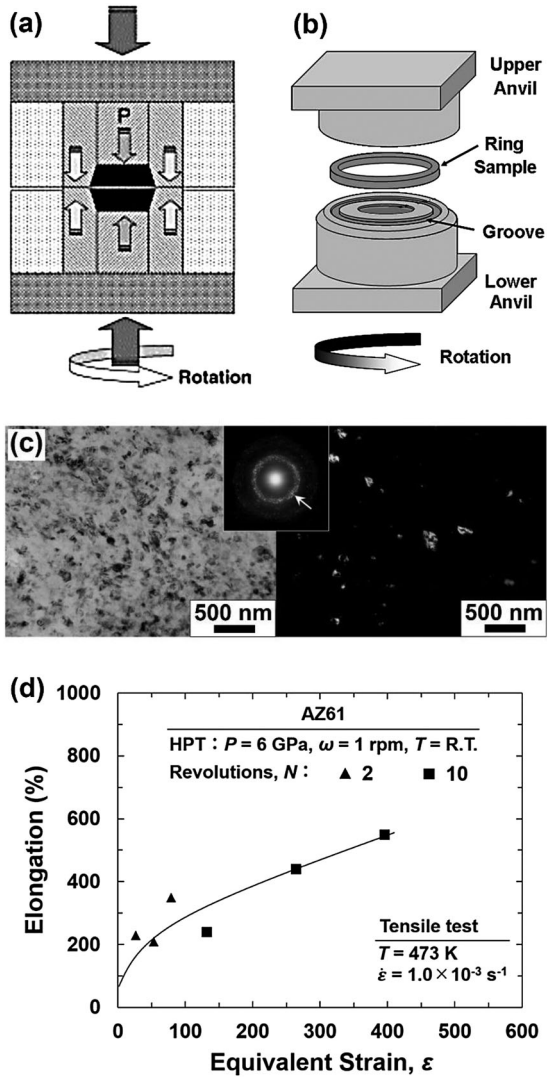

Figure 11. Schematic illustration of high-pressure torsion using (a) bulk cylindrical sample [123] and (b) ring sample [135]. (c) Transmission electron microscopy after high-pressure torsion processing of upscaled AZ61 sample through 10 turns: bright-field images (left), dark-field images (right) and selected area electron diffraction (inset) [144]. (d) Plots of elongation to failure with respect to equivalent strain after deformation with initial strain rate of 1×10^{-3} s^{-1} at 473 K for upscaled AZ61samples processed by high-pressure torsion through 2 and 10 turns [144].

mandrel is rotated (Figure 12a). The shear direction is the same as in the HPT method, but the shear plane is very different: it is the plane tangent to the tube wall. One can also derive HPTT from the cone-cone shearing process [146] by making the cone angle zero. The HPTT method was developed with the hope that by shearing a thin-walled tube, the shear strain can be homogeneous within the tube, which would have been an advantage compared to the HPT process where the shear strain increases proportionally with the radial position. However, it was realized already in the first study [145] that there is a strain gradient also in the HPTT method: the shear strain being much larger in the internal part of the tube wall (about five times). Thus, the gradient is in the opposite sense with respect to the gradient in the HPT method. This can be explained and modeled with the stress gradient within the tube wall inherent in the HPTT process [147,148]: the shear stress is larger near the internal tube surface compared to the external one (Figure 12b). HPTT induces the strain continuously, so it is readily possible to reach the steady state where grain fragmentation is balanced with the continuous dynamic recrystallization process. Therefore, despite the strain gradient, the steady state can be finally reached also at the outer radius of the tube [149].

It is important that no slippage takes place between the mandrels, which is assured by the high friction forces generated by the axial force-induced hydrostatic pressure. Another variant of SPD processing for tubes was proposed in Ref. [150] for longer tubes, where slip can take place between the internal mandrel (which is moving in the axial direction) and the tube wall. The consequence of slip is that the shearing force is not fully circumferential, so the texture deviates from a simple shear texture [150]. The advantage of imposing simple shear deformation mode on the material is a higher rate of grain fragmentation (see experiment and modeling in Ref. [151]).

The HPTT method was applied for processing of aluminum, copper, IF (interstitial free) steel, and magnesium in three thesis studies in Metz [149,152,153]. The most efficient grain fragmentation process was documented in HPTT processing of commercially pure aluminum by reaching a tensile yield strength of 350 MPa [154]. In addition to grain refinement and strengthening, another feature of HPTT is the possibility of material architecturing. The SPD group of Nanjing obtained a layered structure within the tube with different grain sizes of the layers by HPTT processing of two different purities of aluminum [155]. The full cohesion between the layers indicates the possibility of architecturing the tube using dissimilar metals. See a review article on HPTT in Ref. [156].

4.1.4. Shear (rotational) diamond anvil cell

Shear diamond anvil cell (SDAC), which is also known as rotational diamond anvil cell was introduced by Russian scientists in 1980s [59,157] by combining the Bridgman method for shearing under high pressure (developed in 1935) [19], and the concept of diamond anvil cell (DAC developed in 1959) [158]. The SDAC method not only provides opportunity to increase the pressure by two orders of magnitude compared to conventional HPT, but also can be used for in-situ examinations under high

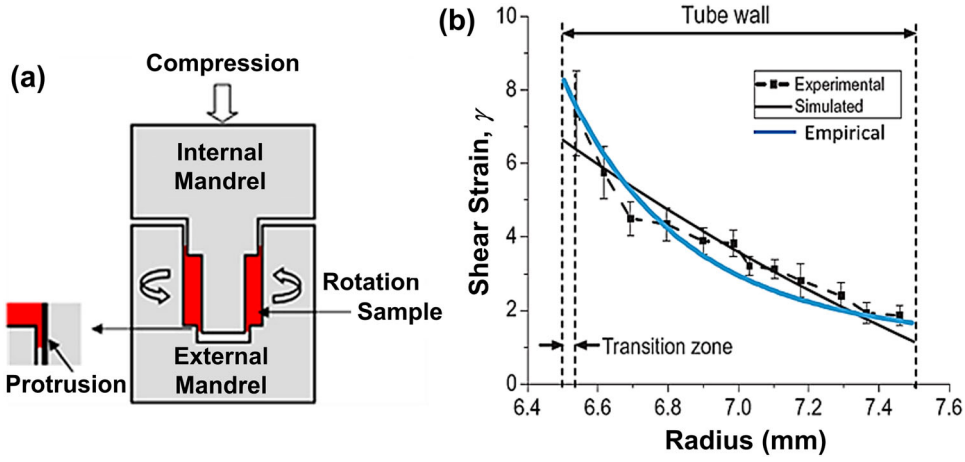

Figure 12. (a) Schematic illustration of high-pressure tube twisting process [154]. (b) Shear strain gradient within tube wall examined by experiments and simulation for IF (interstitial free) steel tube processed by high-pressure tube twisting [156].

pressure using X-ray diffraction, Raman spectroscopy, etc. [115]. Moreover, the SDAC method has very good precision for calibration of pressure and this is of significance for examination of phase transformations. Figure 13(a) shows a SDAC facility which can be used for increasing the pressure up to 150 GPa [115].

Some recent findings using the SDAC are summarized in a recent review [115]. Carbon shows new phase transformations by application of shear under high pressure: graphite transforms to diamond under 20-40 GPa and it transforms to carbon onions at pressures higher than 55 GPa, as shown in Figure 13(b) [159,160]. The carbon onions transform to diamond again at pressures higher than about 100 GPa at ambient temperature. Analysis of these in-situ experimental data in combination with theoretical calculations gives the opportunity to construct a new temperature-pressure phase diagram under shear for carbon up to 130 GPa, as shown in Figure 13(c) [115]. Examination of silicon, fullerene (C60) and zirconium also show clear phase transformations, although their deformation behavior is different [115]. In fullerene and zirconium, transformation-deformation bands are formed together with high-pressure phases. However, shear bands are not formed in silicon, but only high-pressure Si-III and Si-IV phases are detected.

4.2. Equal-channel angular pressing (extrusion)

The ECAP method, as schematically shown in Figure 14(a), is an SPD technique leading to refinement of the grain size of polycrystalline metals to submicron- or even nano-size length scales depending on the material [20,84,161]. As a result, ECAP-processed materials simultaneously possess high strength and moderate ductility and therefore have a high potential for technical applications. Because of this, much work has been devoted to the evolution of microstructure and texture and their relation to the mechanical properties. Moreover, there have been successful attempts to scale up the sample size or make the technique continuous for commercialization.

Pressing materials through an angled channel is a complicated deformation process leading to deformation heterogeneities across the billet cross-section [162–166]. Within the vast amount of research done on ECAP during the last three decades, only a quite small fraction of publications systematically deals with the heterogeneities in microstructure, texture and mechanical properties developing in the billets. Based on the results published, the following short overview can be given.

In the ideal case of ECAP (sharp die corners, no friction and rigid plastic material behavior), deformation is by simple shear in a narrow zone along the die intersection plane. Deviations from this behavior arise when these conditions are not fulfilled. In this case, deformation takes place in a much broader zone, the shape of which depends on die design, processing conditions and material properties. By varying these factors, it turned out that the shearing of the sample is most homogeneous when using a friction-reduced die and applying a back pressure. Nevertheless, there exists an increase in strength from top to bottom of the billet, except in the lowest section where the material is softer. This section can be almost eliminated by increasing the back pressure. The strength increase from top to bottom is smaller than 10% and decreases with the number of passes (Figure 14b). It is the same for laboratory and industrial-scale samples [166]. Consequently, the strength gradient is smaller in bigger samples. Thus, upscaling improves

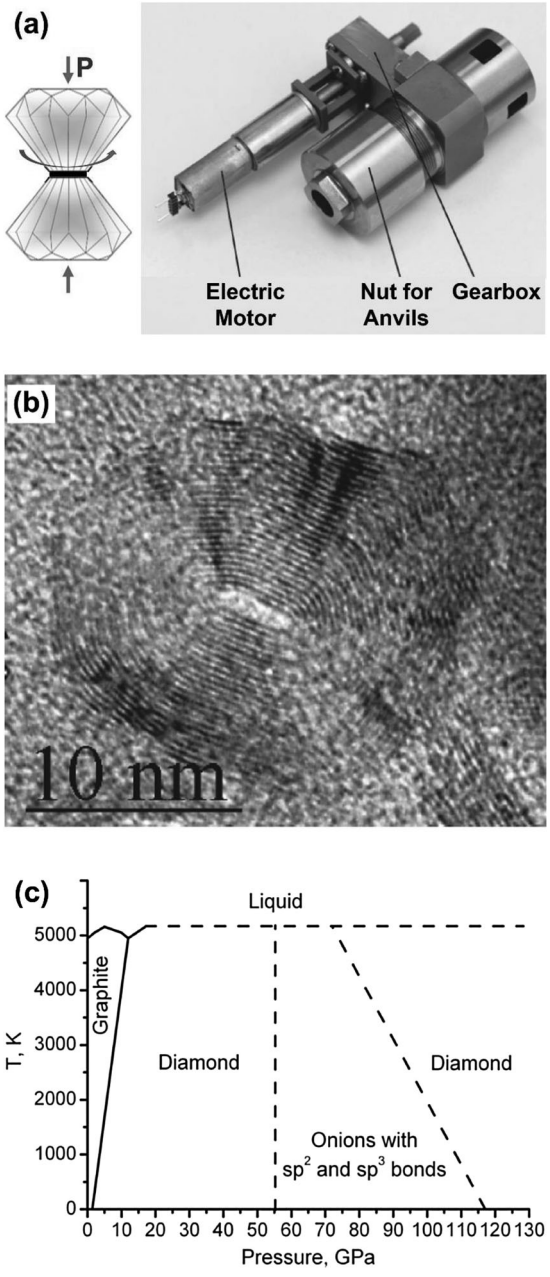

Figure 13. (a) General view of shear (rotational) diamond anvil cell [115]. (b) Formation of carbon onions from graphite by processing through a shear diamond anvil cell [159,160]. (c) New temperature-pressure phase diagram for carbon by considering shear effect [115].

the homogeneity in a comparable volume and therefore favors technical applications. The strength gradient via Hall-Petch relation and Taylor factor may be related to the gradient in microstructure and/or texture generally observed. However, because of the experimental scatter in grain size and texture measurements, it is difficult to unambiguously separate their contribution to the relatively weak inherent strength heterogeneity in ECAP [167].

4.3. Accumulative roll-bonding

The ARB process is an SPD technique of which principle is schematically illustrated in Figure 15(a) [21]. The ARB process was developed by Saito *et al.* [21,132,168] in late 1990s, in order to establish an SPD process applicable to continuous production of bulky materials with UFG structures. At that time, most of the SPD techniques were batch processes treating small specimens in a non-continuous way. ARB uses the rolling deformation, which is the most advantageous metal working process for fabricating plates, sheets, bars, and pipes continuously. However, it is difficult to apply equivalent strain above $4\sim5$ (which is necessary for obtaining uniform UFG structures [169]) in conventional rolling, since the dimension of the materials, such as thickness of sheets, decreases with increasing total strain applied. For instance, one needs to start with a 76 mm thick plate for obtaining a UFG or nanostructured sheet having 1 mm thickness after total equivalent strain of 5 in conventional plate/sheet rolling. Cold rolling of such thick plates is unrealistic. When the thickness of starting plate is reduced to realistic size, final products would become thin foils. In ARB, a plate of 2 mm thick, for example, is rolled by 50% reduction in thickness at the first step. The rolled plate with a thickness of 1 mm is cut into two, stacked to become the initial dimension before the first rolling, and then rolled by 50% reduction again. Such procedures can be repeated unlimitedly in principle, so that one can apply SPD to get plates (1 mm thick) having UFG or nanostructures. For obtaining one-body solid materials, rolling in ARB is not only a deformation process but also a bonding process, which has been known as roll-bonding for fabricating clad sheets. In order to achieve good bonding, contact surfaces of the sheets are degreased carefully and wire-brushed in ARB. Since bonding by one-pass deformation is the most critical issue in the ARB process, the surfaces should be cleaned from harmful contaminations and oxides. Contaminations on the surfaces are removed by degreasing, while wire-brushing is used to remove oxide layers to reveal fresh surfaces of metals. Wire-brushing also introduces roughness of micrometer scale on fresh metallic surfaces, which would be beneficial for good bonding. It has been found that wire-brushing acts also as a surface-SPD process to introduce nanocrystalline structures in surface areas [170]. Large one-pass rolling is necessary for achieving good bonding. A critical rolling reduction to realize bonding exists which depends on the material, processing temperature and roll geometry [171,172]. Roll-bonding in ARB can be carried out at elevated temperature for making both deformation and bonding easier, but the rolling temperature must

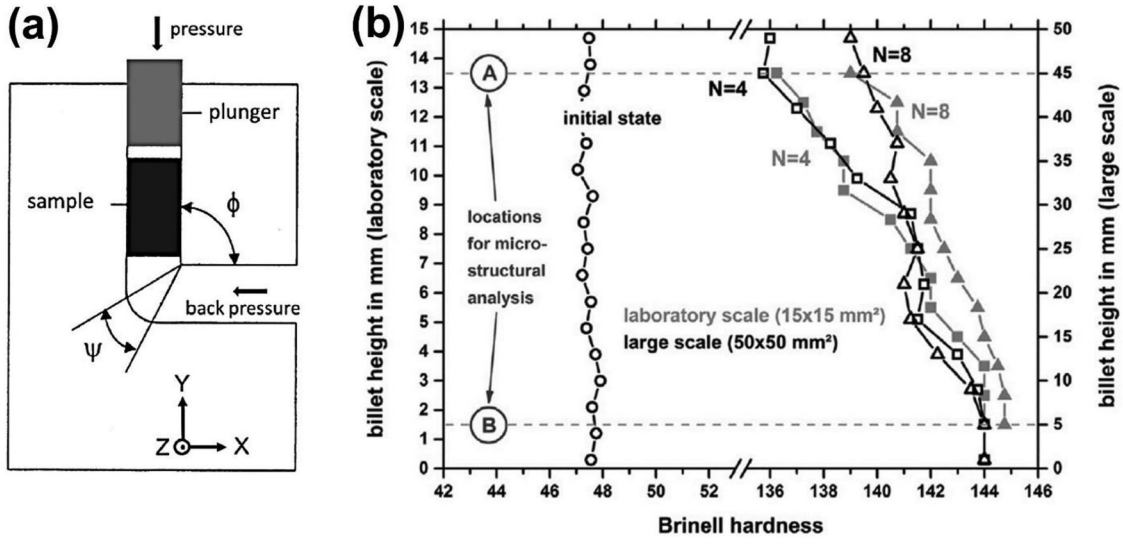

Figure 14. (a) Schematic illustration of equal-channel angular pressing (extrusion) [167]. (b) Distribution of average hardness from a set of longitudinal indents plotted as a function of billet height for copper after 4 and 8 passes of small and large scale equal-channel angular pressing. The results for the initial state are included for comparison [166].

be lower than the recrystallization temperature of the materials to avoid coarsening of microstructures during the process. It should be noted that the critical temperature for recrystallization and grain growth decreases with decreasing grain sizes. Larger roll diameter would be favorable for realizing roll-bonding by one-pass large reduction, although it would increase rolling force. Large one-pass rolling might cause cracking of sheets, but there are several techniques to avoid such cracks [173].

The von Mises equivalent strain (ε_{eq}) after n cycles of ARB is expressed as,

$$\varepsilon_{eq} = -\frac{2n}{\sqrt{3}} \ln\left(\frac{t}{t_0}\right) = -\frac{2n}{\sqrt{3}} \ln(1-r) \qquad (2)$$

where t_0, t, and r are the initial thickness of the sheets before stacking, the thickness after roll-bonding, and the reduction in thickness per cycle, respectively. Here, redundant shear strains introduced by large friction between rolls and material [174] are ignored, although roll-bonding is often carried out under high friction conditions in the ARB process for realizing large one-pass rolling and good bonding. Such redundant shear strains play an important role in grain refinement [169,175]. Assuming 50% rolling reduction per cycle ($r = 0.5$ in Equation (1), corresponding to rolling from 2 mm to 1 mm in thickness), Table 1 summarizes geometrical changes of materials processed by ARB. As the equivalent strain corresponding to 50% rolling reduction is approximately 0.8, total strain applied after n cycles of ARB is simply $0.8n$. On the other hand, it is interesting that the number of initial sheets included in the final product after n cycles becomes 2^n. Thus, 1024 initial sheets are included within the final sheet with 1 mm thickness after 10 ARB cycles. This means that the thickness of the initial sheet (not the grain size) becomes less than 1 μm after 10 cycles.

ARB is basically applicable to all kinds of metals and alloys deformable in rolling, and UFG structures are achievable in such bulky metals and alloys. Figure 15(b) shows a TEM micrograph and corresponding grain boundary misorientation map obtained by Kikuchi-line analysis for a commercial purity aluminum processed by ARB for 6 cycles ($\varepsilon_{eq} = 4.8$) [176]. The TEM image observed from the transverse direction (TD) of the sheet represents a homogeneous UFG structure with grains elongated to the rolling direction (RD). Numbers shown in the boundary map indicate misorientation angles of each boundary in degree. It is confirmed that most of observed boundaries (especially lamellar boundaries parallel to RD) have large misorientations. As bulky samples can be fabricated even in the laboratory, ARB is beneficial for studying microstructure evolution and mechanical properties of nanostructured materials systematically. Careful observations on materials processed by ARB to various strains have clarified that the formation of UFG microstructures during SPD can be understood in terms of *grain subdivision* [176–178], as will be described in Section 6.1. Figure 15(c) indicates the effect of equivalent strain applied by ARB on the average spacing of high-angle grain boundaries and their fraction in an ultra-low carbon IF steel [169]. This investigation clearly showed that the equivalent strains of 4 ~ 5 are necessary

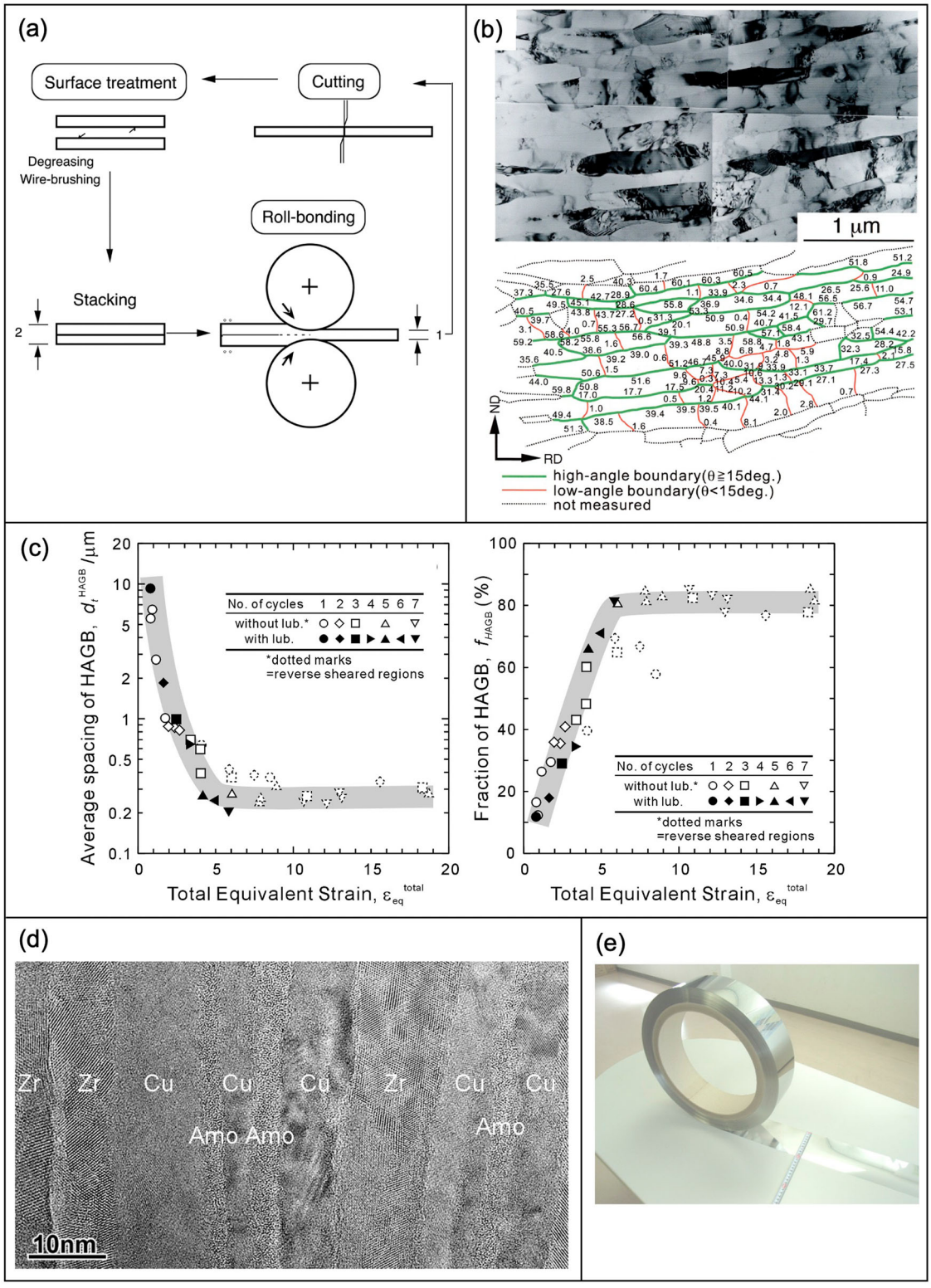

Figure 15. (a) Schematic illustration of accumulative roll-bonding [21]. (b) transmission electron micrograph and corresponding boundary misorientation map of commercially purity aluminum (Al-1100) processed by accumulative roll bonding at 473 K. Misorientation angles (in deg.) of each boundary indicated in the boundary misorientation map were measured by Kikuchi-line analysis in transmission electron microscope [176]. (c) Effect of equivalent strain applied by accumulative roll-bonding on average spacing of high-angle grain boundaries and their fraction in an ultra-low carbon IF (interstitial free) steel [169]. (d) High-resolution image of Cu + Zr multi-stacks processed by accumulative roll-bonding for 9 cycles (equivalent strain of 13.7) at room temperature. Nano-layered structure of amorphous (Amo), copper (Cu) and zirconium (Zr) is formed [183]. (e) Appearance of an ultrafine-grained thin strip of austenitic stainless steel (SUS 304) fabricated through repetition of deformation induced martensitic transformation in cold rolling and reverse transformation to austenite (Courtesy of Tokushu Kinzoku Excel Co., Ltd.) [195,196].

Table 1. Change of strain (ε_{eq}), rolling reduction (r), number of sheets in product (N), thickness of each sheet in the product (t) and geometry as a function of the number of cycles (n) in accumulative roll-bonding process with 50% rolling reduction per cycle, starting from stack of two sheets with 1 mm thickness.

n	1	2	3	4	5	6	7	8	9	10	n
ε_{eq}	0.8	1.6	2.4	3.2	4.0	4.8	5.6	6.4	7.2	8.0	$0.8n$
r (%)	50	75	87.5	93.8	96.9	98.4	99.2	99.6	99.8	99.9	$100(1\text{-}0.5^n)$
N	2	4	8	16	32	64	128	256	512	1024	2^n
t (μm)	500	250	125	62.5	31.3	15.6	7.81	3.91	1.95	0.977	$1000/2^n$

to obtain metals having homogeneous UFG structures by SPD. Grain size dependence of mechanical properties, such as strength, ductility [179] and toughness [180], were systematically studied using specimens with a wide range of average grain sizes fabricated by ARB and subsequent annealing. From such studies, it was clearly shown that UFG metals exhibit very high strength 3 ~ 4 times higher than the same materials having conventionally coarse grain sizes [181], but their tensile ductility (especially uniform elongation) is limited due to early plastic instability [179]. After this understanding, various kinds of nanostructured metallic materials managing both high strength and large tensile ductility have been found [178,181,182]. Fully recrystallized nanostructured metals [176] are typical example of such new nanostructured metals.

ARB can be also applied to bulk mechanical alloying, and nano-layered structures composed of amorphous and nanostructured metals, as shown in Figure 15(d) [183]. ARB has been also used to fabricate heterostructured materials [184–193], since it has been found that heterostructured materials show excellent mechanical properties [194]. ARB is still one of the limited SPD processes that can be applied to continuous production of large bulky materials. Since large-scale metal productions are restricted by huge facility installed, it is still difficult to adapt SPD (even ARB) to mass productions, such as those in steel industries. In small-scale industries, on the other hand, the concept of ARB has been already applied to commercial production of thin strips of ~ 0.1 mm thick of stainless steels (Figure 15e), for instance [195,196]. Even in university laboratory, scaling up of the ARB process has been successfully achieved [193]. It is expected that ARB can contribute to the progress of fundamental research as well as commercial production of nanostructured metals and alloys in future.

4.4. Twist extrusion

The TE process is schematically illustrated in Figure 16(a). The idea of this processing method was proposed by Beygelzimer in 1999, on the margins of the conference on Multiscale Phenomena in Plasticity (Greece), prompted by an inspiring conversation with Valiev about

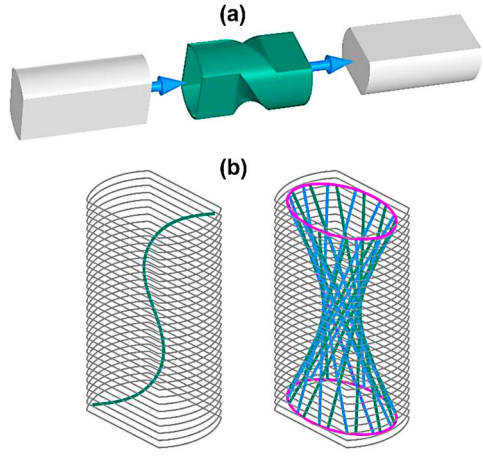

Figure 16. (a) Schematics of twist extrusion [200]. (b) Hybrid material containing inclined fiber (left) and embedded Shukhov tower-type armor (right) produced by several passes of twist extrusion [218].

the emerging research area on SPD. In the same year, the process was trialed at the Donetsk Institute for Physics and Engineering of the National Academy of Sciences of the Ukraine. The institute had a great expertise in hydroextrusion technology, and thus, in the first TE experiments, the samples were extruded under high pressure using a fluid [22]. Subsequent research showed, however, that the process is more stable when a sample is pressed through the die by means of a dummy billet, which can be made from various materials, including metals and alloys, mixtures of lubricants with flake graphite, or polymers. The choice of the dummy material is dictated by the deformation conditions and may vary from case to case. The results of first studies of TE were reported at a TMS meeting in 2002 [197,198] and were published in a monograph [199].

Research on TE was conducted initially in Ukraine, but it was later taken up in several countries, notably in China, France, India, Iran, and South Korea. Various modifications of TE have come up, and combinations of TE with other SPD techniques, and particularly with ECAP, were proposed (see literature compiled in [200–206]). At present, the following characteristic features of TE can be considered as firmly established.

(i) The process is viable for a broad range of cross-sectional shapes of billets, including convex and concave ones and those containing hollow spaces. In the latter case, a supporting insert needs to be employed. TE of billets with a circular cross-section is realized by using a helical die [207], in some cases by an eccentric one [208].

(ii) For rigs with a sharp transition from straight to helical parts of the die channel, straining occurs mainly in narrow zones at the boundaries of helical parts. The character of deformation is simple shear, which has the opposite sense at the entry and the exist sides of the helical die. Introduction of simple shear opens up new possibilities with regard to microstructure formation in the processed materials [209,210]. The shear plane is normal to the extrusion axis, and the magnitude of the shear strain varies from ~ 0.5 near the axis of the helical channel to ~ 1 at its bounds. The strain distribution can be controlled by shifting the axis of the TE die with respect to the symmetry center of its cross-section [208].

(iii) To prevent failure of the billets and achieve complete filling of the die channel, TE needs to be carried out under back pressure, at a level of about the yield strength of the material to be processed [200, 211].

(iv) TE is accompanied with cross flow of the material with a varying magnitude of vorticity [212, 213].

The mentioned aspects of TE were described in detail in earlier review papers [200,214].

The TE technology has proven itself as an efficient tool for solving various problems. These include producing metals and alloys with UFG microstructure; deformation-induced homogenization of various materials such as aluminum alloys and consolidation of powder materials [200,214,215]. Further development of TE will certainly be guided by the needs of industry. An exemplary case of potential applicability of TE technology is the process of titanium and iron-nickel alloys for aerospace industry [216,217]. To that end, a pilot rig was established at Motor Sich JSC, one of the world leading manufacturers of aircraft engines and gas turbines. Another emerging area in which the TE method can be used efficiently is the design and manufacture of novel materials, whose local UFG microstructure in combination with a special internal architecture on a macroscopic level gives the material exceptional mechanical characteristics [218–220]. This feature of TE offers additional possibilities to give the material a multi-scale structure as well as to produce hybrid materials, as shown in simulated images of Figure 16(b).

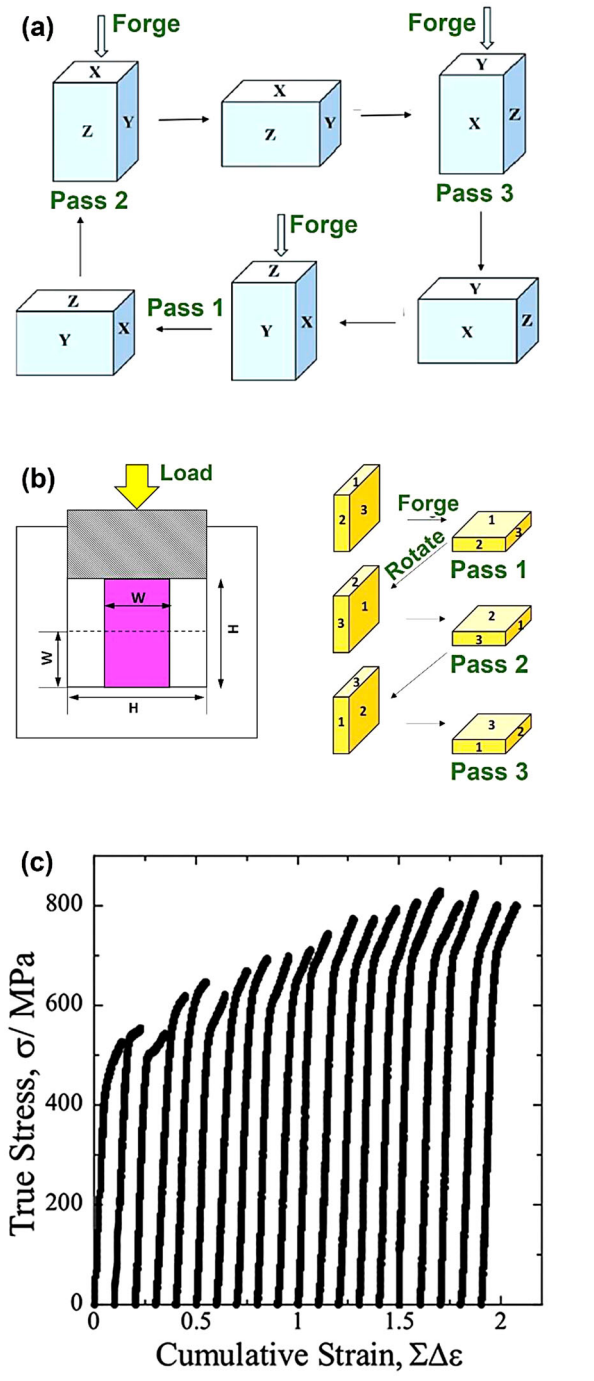

Figure 17. (a) Principles of the multi-directional forging method [226]. (b) Principles of the cyclic closed die forging method [228]. (c) Stress-strain curves for titanium processed by multi-directional forging for 20 passes at room temperature [233].

4.5. Multi-directional (-axial) forging

Forging from different directions has been of interest to metal forming since the ancient times. Scientists also employed this concept as an effective strategy for accumulation of plastic strain. Bridgman developed a two-directional forging facility to introduce large plastic

deformation in metallic materials [13]. The MDF was occasionally used to improve the homogenization of forged products within the past century [221]. The MDF method, in the form used todays, has been employed as an SPD technique since the 1990s at the latest [23]. In the 1990s and the beginning of this century, the process was successfully used by different research groups for the production of UFG materials [222–225]. In the MDF process, the sample is forged repeatedly along three orthogonal axes by rotating the sample by 90° between passes. The easiest MDF method is forging without using any particular dies (Figure 17a) [226], but it can be also conducted using a die in constrained condition (Figure 17b which is known as cyclic closed die forging) [227,228]. The total strain in MDF is the accumulation of strains achieved in each cycle and this results in a large plastic strain ($\varepsilon = \ln(h_0/h)$, ε: strain, h_0, initial height of billet, h: final height of billet) [228].

The main advantage of MDF is that it can be carried out with large hydrolytic presses that are already available in the industry, which makes the method attractive for commercial applications for producing large bulk samples. The presence of tensile stresses at the free surfaces and low hydrostatic pressure are the main disadvantages of the MDF process, which lead to the formation of cracks and a limited number of passes that can be applied at low temperatures. Another disadvantage of MDF is the heterogeneity of microstructure, as in other forging process. To avoid these limitations, the MDF method is usually carried out at high temperatures in order to achieve sufficient formability and homogeneity, but this can lead to the formation of coarser grains [229–231]. Despite all these limits, the process has been successfully used not only for grain refinement of easy-to-deform materials such as aluminum and copper, but also for processing of titanium, magnesium alloys, steels, etc. [224,229–232]. Figure 17(c) shows the enhancement of mechanical properties of titanium processed by several MDF cycles at room temperature [233]. In addition to its high strength, the MDF-processed titanium has good biocompatibility [234], which indicates the high potential of the process for the production of functional UFG materials.

4.6. Continuous severe plastic deformation methods

The SPD processes have been extensively studied over the last two decades to enable the manufacturing of UFG materials with unique properties. Most of the efforts, however, has been limited to the laboratory-scale studies, which do not meet the requirements for industrial-scale applications. One of the main challenges in SPD processing is to upscale the sample size including the length and the cross-sectional area. The SPD processes may be categorized into three main groups of continuous, semicontinuous, and discontinuous techniques [111]. The semicontinuous operations are attributed to the techniques that can process large-scale products with UFG structure, while the continuous methods can process sample with almost unlimited length. The criterion is that both ends of the samples are stress-free in the continuous process, while in the discontinuous process, only one side end or none of them is stress-free [111]. The semicontinuous processes are similar to the discontinuous process except that the stresses are lower on one or both sides of the sample length.

Incremental equal-channel angular pressing [161], single-task incremental high-pressure torsion [235], porthole equal-channel angular pressing [236], hydrostatic cyclic expansion extrusion [237], hydrostatic tube cyclic expansion extrusion [238], and equal-channel angular drawing [239,240] are important semicontinuous processes where one side of the deformed sample is almost stress-free and the other side is not, as shown in Figure 18. In most of the semicontinuous processes, the possibility of punch or sample yielding or buckling constitutes the main processing limitation, while the potential for buckling/yielding rises with increasing the deformation load. Therefore, any measure that decreases the deformation load can improve the conditions for the manufacture of larger industrial products. A good example was shown in the hydrostatic cyclic expansion extrusion process in which the friction force and, accordingly, the total load were reduced to increase the workable sample length from $\sim$40 mm for regular cyclic expansion extrusion to over 100 mm in hydrostatic cyclic expansion extrusion [241].

ECAP-conform [86,242], continuous confined strip shearing [243], continuous high-pressure torsion [136,137], and ARB [132] are considered as continuous SPD techniques, which were adopted from main SPD techniques. In these processes, both sides of the specimen are stress-free, as shown in Figure 18. In addition to these three techniques, there are several other processes in this category, including cone shearing [244], single roll angular rolling [245], continuous frictional angular extrusion [246], continuous severe plastic deformation [247], continuous cyclic bending [248,249], asymmetric rolling (also known as differential speed rolling) [250], caliber rolling [251], repetitive corrugation and straightening [104], constrained groove rolling [227], and repetitive corrugation and straightening by rolling [252].

There are some factors that influence the effectiveness of these techniques and should be considered in developing any new semicontinuous or continuous processes: the level of hydrostatic compressive stress, the level of strain,

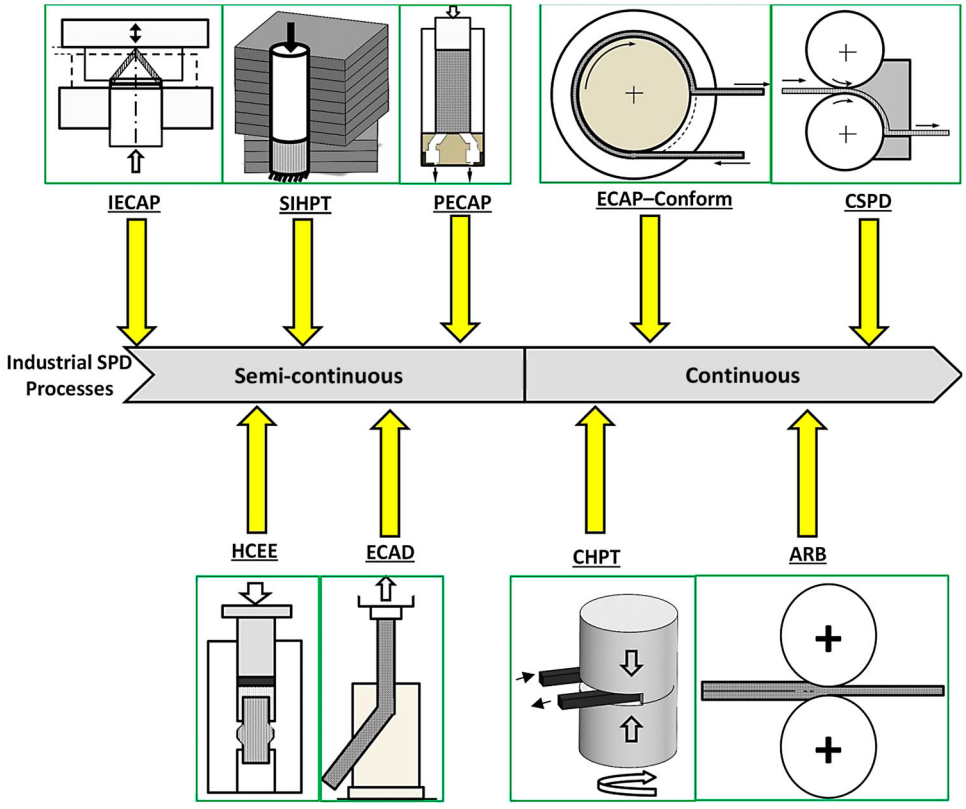

Figure 18. Schematic illustration of continuous and semicontinuous SPD methods with high potential for industrial applications: incremental equal-channel angular pressing (IECAP) [161], single-task incremental high-pressure torsion (SIHPT) [235], porthole equal-channel angular pressing (PECAP) [236], hydrostatic cyclic expansion extrusion (HCEE) [237], equal-channel angular drawing (ECAD) [239,240], equal-channel angular pressing - conform (ECAP-Conform) [86], continuous high-pressure torsion (CHPT) [136,137], accumulative roll-bonding (ARB) [132], and continuous severe plastic deformation (CSPD) [247].

homogeneity of stress and strain, the maximum processable sample size, the expected mechanical properties of final product, the complexity of the process, etc. [111].

4.7. Surface severe plastic deformation

As failure is often initiated from the surface, various surface treatment techniques have been developed to induce SPD on the surfaces of parts to generate gradient structures and, thus, to improve mechanical properties such as fatigue or tensile strength. Some of these techniques are derived from shot peening and use shots to induce SPD. For some, the shots are accelerated via compressed air such as in the air blast shot peening process [253], or by rotating paddles for the rotationally accelerated shot peening technique [254]. In these cases, the incidence angles at a given time as well as the shot velocities have rather narrow ranges of distribution. For other processes, the shots are set in motion within a confined chamber either mechanically, by a rotating eccentric at low frequency (~ 50 Hz) or at much higher frequency using a resonating part called sonotrode (~ 20 kHz). These techniques are found in the literature under various names such as surface mechanical attrition treatment (SMAT) [91,255–257] or ultrasonic shot peening (USP) [258,259] and, despite different acronyms, share the same concept. Using ultrasonic SMAT, the surface is treated by shots impacting multi-directionally the surface at velocities up to 10 m/s [260,261]. Schematic description of these method is shown in Figure 19(a). Instead of using shots, other surface-SPD techniques use the direct mechanical action of a peening tip—eventually set in motion by an ultrasonic wave—to modify the surface microstructure [262–265].

Taking into account the structure of the grains and their misorientation, as quantitatively observed by EBSD [266] coupled with TKD (transmission Kikuchi diffraction) [267] or with TEM [268], the microstructure in the gradient layer is generally depicted as the succession of three different zones: (i) an 'UFG zone', which also contains a nanostructured zone present at the extreme top surface - containing randomly oriented grains separated by high-angle grain boundaries; (ii) a 'transition zone', where grains have been fragmented under heavy deformation; and finally, (iii) a 'deformed zone', where initial grains are simply deformed. Using the SMAT-type

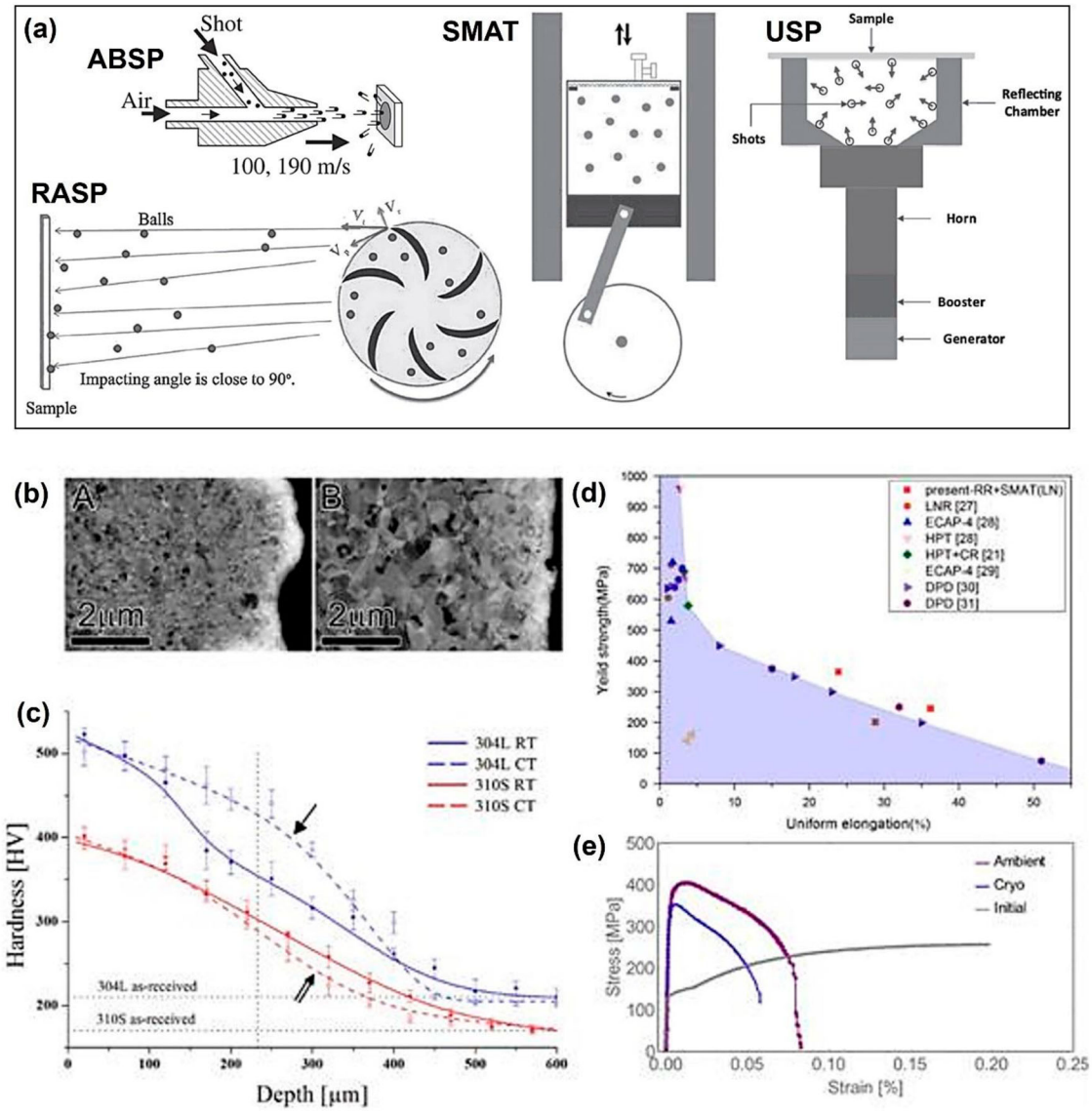

Figure 19. (a) Schematic illustration of surface severe plastic deformation methods: air blast shot peening (ABSP) [253], rotationally accelerated shot peening (RASP) [254], surface mechanical attrition treatment (SMAT) [257], and ultrasonic shot peening (USP) [259]. Effect of SMAT carried out at cryogenic temperature on (b) modification of top surface grain size in copper (A: processing at cryogenic temperature, B: processing at room temperature) [293] and (c) modification of sub-surface hardness in austenitic stainless steels with (blue lines) and without (red lines) stress/strain-induced martensitic transformation [298]. (d) Enhanced mechanical properties in Cu-Zn alloy processed by SMAT [295]. (e) Lower strength and ductility of pure iron after SMAT processing at cryogenic temperature (blue curve) compared with SMAT processing at room temperature [297].

techniques, the mechanical performance of the overall material can be significantly enhanced through the formation of these gradient structures. Considering steels for example, besides conventional use to harden the surface [256] and modify wear [269] and fatigue [270] properties, tensile properties of the 316L [271] and 304 [260,272] stainless steels were also improved, while multi-layered laminate composites were created by SMAT and subsequent roll bonding [273]. These different aspects have been reviewed in several manuscripts [274–278]. The high fraction of structural defects in UFG materials also leads to a significant increase in stored energy which, inevitably, increases the material reactivity in comparison to coarse-grained materials. Therefore, SMAT has been used within duplex treatments to enhance the kinetics of diffusion for several chemically assisted industrial processes such as nitriding [279], pack boronizing [280], aluminizing [281,282], etc.

The gradient structures created by SMAT can also have their own advantages for hydrogen storage materials used for automotive and energy applications. Since the earlier works by Skripnyuk *et al.* using ECAP and

high-energy ball milling [283], it is well established that a fine grain structure obtained by SPD can enhance the hydrogen storage kinetics [284]. Since the activation for hydrogenation is mainly a surface-related issue involving the separation of H_2 molecules at the surface to create H atoms which subsequently diffuse from the surface towards the bulk [285], surface-SPD by ultrasonic SMAT has been used for activation on the Ti-V-Cr system [286,287]. It was shown that the nanostructure and cracks present at the top surface can act as shortcuts for hydrogen diffusion and transport through the oxide layer and ease the activation of the material, while the hydrogen atoms can be stored in the defect-free subsurface with good reversibility [286]. However, as illustrated for the corrosion resistance, the higher reactivity may not always be suitable or lead to a dual behavior depending on the material environment. In the case of stainless steels for example, a decrease in corrosion resistance was reported in depassivating electrolytes while the higher reactivity of the SMAT-processed surface helps to create a passivating (i.e. protective) film faster in many aqueous environments [288–290]. In fact, the improvement in properties requires a perfect control of the various processing parameters in order to tailor precisely both (i) the gradient structure that controls the mechanical properties and (ii) the top surface that can react with the exterior atmosphere.

Several research works have investigated the effects of processing parameters on the nature of the in-depth microstructure gradient [266,291,292]. For example, Chen *et al.* [291], using two sets of SMAT processing parameters (vibrating frequency, type and diameter of balls) to treat the 304 stainless steel, showed that for similar surface hardness different sub-surface hardness gradients were obtained. This resulted in different mechanical behavior for thin (1 mm) plates processed by SMAT on both sides [291]. The temperature at which the SMAT treatment is carried out is another important processing parameter that has been recently investigated. Examples are illustrated in Figures 19(b–e). To prevent dynamic recovery and/or stimulating mechanical twinning, cryogenic SMAT can result in further surface grain refinement for a wide variety of metals such as pure copper (Figure 19b) [293,294], brass [295], Cu-Al alloys [296], pure iron [297] and stainless steels [298,299]. The subsurface hardness can also be positively affected in cases where twinning or martensitic transformation is more easily triggered [298,299]. As shown in Figure 19(c) [298], an increase of the subsurface hardness is clearly visible along the first 300 μm for the unstable 304L austenitic stainless steel when processing is done at cryogenic temperature. This is due to the easier subsurface formation of stress/strain-induced martensite [298,299]. On the contrary, as for the case of pure iron [297], because the strength of the material increases at cryogenic temperature, the size of the subsurface-affected region decreases for the same given set of processing parameters for the stable 310L steel (Figure 19d) [298]. The detailed analysis of the effect of various processing parameters, including cryogenic temperature, on the 304L steel also revealed that the gradient structure is, in fact, the superimposition of differently graded microstructures: one in terms of grain size, the other in terms of phase distribution [299]. The formation of a gradient structure with finer grains on the surface by SMAT at cryogenic temperature led to enhanced mechanical properties in the Cu-Zn [295] (Figure 19d) and Cu-Al [296] alloys. Comparatively, despite the finer surface grain size, both tensile strength and elongation were reduced after cryogenic SMAT in the case of pure iron (Figure 19e) [297].

Some cracking and contamination are also important factors that can potentially affect the surface reactivity as well as the integrity of the treated parts. The presence of contamination at the surface of SMAT-processed samples is now clearly established and depends on the exact way the surface attrition is done [277]. For example, the corrosion resistance of magnesium [300,301] and that of aluminum alloys [302,303] has been proved to be significantly affected by iron contamination from the peening tools. The work by Wen *et al.* [302], for example, demonstrated that the corrosion resistance of a 2024 aluminum alloy was directly affected by the nature of the shot peening media. In order to compensate or at least weaken the possible effect of surface contamination, Murdoch *et al.* [304] introduced a pre-processing step (pre-coating of the shot media and chamber) to reduce the resulting impact on corrosion properties. The surface contamination also has a significant effect on the tribological properties as wear is affected by the exact nature of the oxide formed during processing and subsequent rubbing [305]. Finally, although SMAT is sometimes performed under vacuum, chemical etching [306] or mechanical polishing [267,307,308] was used as an intermediate stage during SMAT and nitriding duplex treatment process to reduce the surface contamination and, thereby, further improve the quality and thickness of the nitrided layers.

Considering fatigue, superficial refined microstructure and high compressive residual stress gradient allow to delay crack initiation and impede crack propagation [270]. However, excessive peening treatments deteriorate the fatigue properties of the C-2000 [309], Ti-based [310,311] and Al-based [312,313] alloys due to surface contamination, micro-damage or enhanced roughness/cracking induced by the impacting balls acting as stress raisers. For example, several publications have

shown that the correct selection of SMAT parameters is extremely important to obtain good surface integrity, and a softer roughening can be useful for this purpose [314]. Also, fatigue lifetime analysis indicated that SMAT could decrease the fatigue lifetime of an austenitic stainless steel under cyclic loading with high strain amplitude [315]. Finally, as the damage and failure mechanism may change, contrary to the beneficial effect of SMAT under low and high cycle fatigue regimes, SMAT was found to have a negative effect for very high cycle fatigue of a titanium alloy [316]. With regard to the peening temperature, as experimental results on steels [317,318] and magnesium alloys [319] showed, a slight increase in the peening temperature (473-573 K) can be useful in order to improve the fatigue life or fatigue strength.

Finally, it should be noted that the modified surfaces, produced by SPD techniques like ECAP or HPT [320–322] or by various types of surface-SPD [323–325], are now receiving increasing interest for various biomedical applications. It is expected that the gradient-structured materials produced by various surface-SPD methods in the future will be employed for an extended range of functional applications.

5. Materials processed by severe plastic deformation

In 1935, when the principles of HPT were introduced, the method immediately was applied to a wide range of materials such as metals, minerals, glasses, and various kinds of organic and inorganic materials [19]. This capability of the HPT method to process any kinds of materials was well appreciated by geologists and physicists at the time [47]. However, this capability was virtually overlooked by materials scientists for many years, and the research in the NanoSPD field was mainly remained in the framework of metallic materials. Currently, a wide range of metals and metallic alloys with different crystal structures such as bod-centered cubic (BCC), face-centered cubic (FCC) and hexagonal close-packed (HCP) are processed by various SPD methods [110]. There are also new trends to use the SPD process to various kinds of intermetallics and non-metallic materials such as glasses, carbon polymorphs, semiconductors, ceramics and polymers [18], as will be discussed in this section. Although most of these materials are the materials that have been designed and optimized for conventional processing methods in the industry, there are now some attempts to develop novel materials by SPD processing which are inaccessible by any other processing technique [326,327]. These novel materials offer new fields of applications, but they require optimization of compositions and technical strategies for the SPD processing conditions.

5.1. Composites versus metals

In the last two decades various SPD methods have been applied for obtaining UFG metals and alloys with an attractive combination of properties [2]. The most popular SPD process is still ECAP [161], but the HPT method has been used for processing a wider range of metals and alloys [47]. So far, over 30 pure metals/elements and over 1000 metallic alloys have been processed by various SPD methods. Significant grain refinement and a large proportion of lattice defects lead to interesting properties of these materials. However, thermal stability within long period of time is a main concern regarding the severely deformed metals and alloys [2,47,161]. In addition, SPD-processed metals typically have grain sizes in the submicron range, but nanograins are desirable for many mechanical and functional properties. There are some recent trends to use less pure metals or composite materials to not only improve thermal stability, but also to achieve smaller grain sizes and enhance mechanical and functional properties. Despite numerous publications on the behavior of metals and composites under SPD processing, many problems are still debatable and not completely solved. The different behaviors of niobium and Cu-Nb composites are discussed here as an example.

Niobium, a refractory but plastic metal, is of great scientific and practical importance in multifilamentary superconductors and Cu-Nb is a high-strength composite used for wires [328–330]. These two materials can show different microstructural evolution and thermal stability after SPD processing. During ECAP processing, the microstructure of niobium gradually refines to non-uniform submicrocrystalline sizes (Figure 20a) with both equilibrium and non-equilibrium grain boundaries, which can be evidenced by emission Mössbauer spectroscopy [331]. Processing niobium by HPT at room temperature enables smaller microstructures in the border area between nano- and submicro-crystalline with an average grain size of 120 nm (Figure 20b) [332]. Combination of ECAP and HPT does not result in further grain refinement, confirming that the initial state (single crystalline, polycrystalline or first ECAP-processed) does not affect the final grain sizes in the saturation state of metals after HPT processing. To refine the grain size further, SPD processing at cryogenic temperature (e.g. in liquid nitrogen) is effective, but it results in lower thermal stability. For example, a uniform nanocrystalline structure with high hardness of 4800 MPa was reported in niobium after HPT processing at cryogenic temperature (Figure

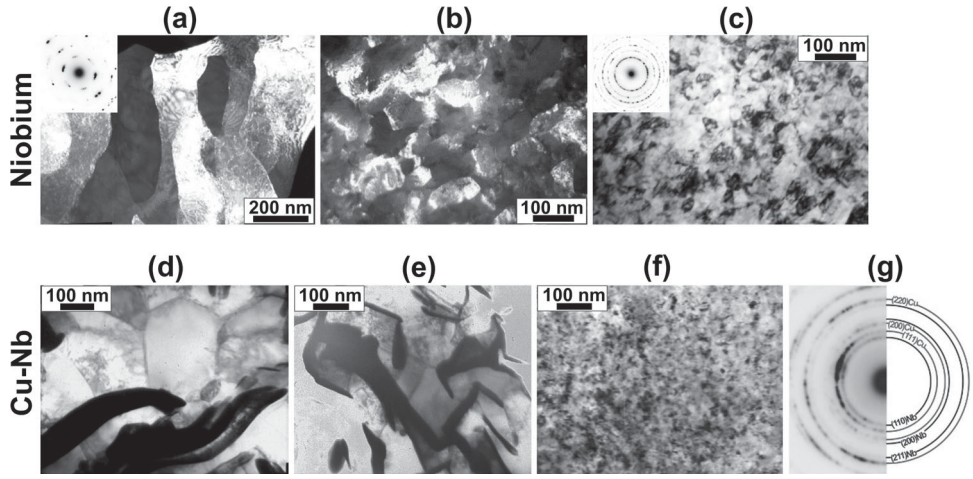

Figure 20. (a-c) Microstructure of niobium after (a) 5 passes of equal-channel angular pressing, (b) 5 turns of high-pressure torsion at room temperature, and (c) 3 turns of high-pressure torsion at cryogenic temperature. (d-g) Ribbon-like niobium filaments in Cu-Nb composites after drawing to strains of (d) 5.4 and (e) 10.2, and their transformation into (f, g) equiaxed nanograins after 5 turns of high-pressure torsion at room temperature. a, b: dark-field images, c-f: bright-field images, g: selected area electron diffraction pattern [339].

20c) [333]. The thermal stability of HPT-processed niobium depends on strain and processing temperature. After HPT processing at room temperature for 5 turns, the structure is stable up to 873 K; however, grain growth starts at 773 K after 10 turns [334]. The structure of niobium processed at cryogenic temperature is stable at room temperature for at least several months [333]; however, recrystallization starts at low temperatures of 473-573 K [335].

In conventional Cu-Nb composites that are produced by wire drawing, niobium filaments have a ribbon-like shape and a sharp $<110>$ fiber texture. In addition, a limited texture with $111<110>$, $100<110>$ and $311<110>$ components is formed, which probably is due to the ribbon formation (Figures 20d and e) [336]. The Cu/Nb interfaces are semi-coherent, and the niobium lattice is distorted (the d_{110} spacing is extended along the strain axis and compressed in the perpendicular direction to it) [337]. Coagulation of the niobium filaments begins during annealing at 573-673 K, and a complete recrystallization and disappearance of niobium lattice distortion is observed at 973-1073 K [337]. When this composite is processed by HPT at room temperature, the ribbon-like niobium filaments are replaced by equiaxed niobium nanograins with sizes of 10-20 nm (Figures 20f and g) [338]. This structural refinement is accompanied by a remarkable strengthening of more than 1.5 times. After annealing in the temperature range of 673-1073 K, grain coarsening is observed, but the nanocrystalline structure with grain sizes smaller than 100 nm is retained. Moreover, even after annealing at 1073 K, the microhardness is higher than that in the as-drawn composites. Thus, the general thermal stability of severely deformed Cu-Nb composites is higher than that of the as-drawn composite wires and of SPD-processed pure niobium [338].

The comparison of the behavior of niobium, in pure form and in the composite, under different deformation modes confirms the high potential of SPD-processed composite materials for industrial applications, where thermal stability of nanostructured components is an essential requirement. However, revealing the specific features of grain and interface boundaries is necessary for a deeper understanding of the processes providing the basis for the production and optimization of various advanced nanocomposites by SPD processing [339].

5.2. High-entropy alloys

High-entropy alloys or multi-principal element alloys, which contain a solid-solution mixture of at least five principal elements (fraction of each element in the range of 5-35 at%), are a new group of materials with interesting properties [340,341]. The presence of five elements with different atomic diameters and different electronic structures leads to a distorted structure with high configurational entropy and enhanced properties [342]. Although high-entropy alloys have usually high flow stress [343,344], it was shown that the hardness of these materials can be further enhanced by processing through SPD [345–348]. It was reported that the HPT method is quite effective to improve hardening of CoCrFeMnNi [349,350], CoCrFeMnNi + C [351]. CoCrFeNiMo [352], AlFeCoNiCu [353], $Al_{0.3}$CoCrFeNi [354,355], AlCrFeCoNiNb [356], $Al_{0.5}$CoCrFeMnNi [357], TiAlFeCoNi [358], TiAlFeCoNi + C [359], $CrFe_2NiMnV_{0.25}$ [360], and

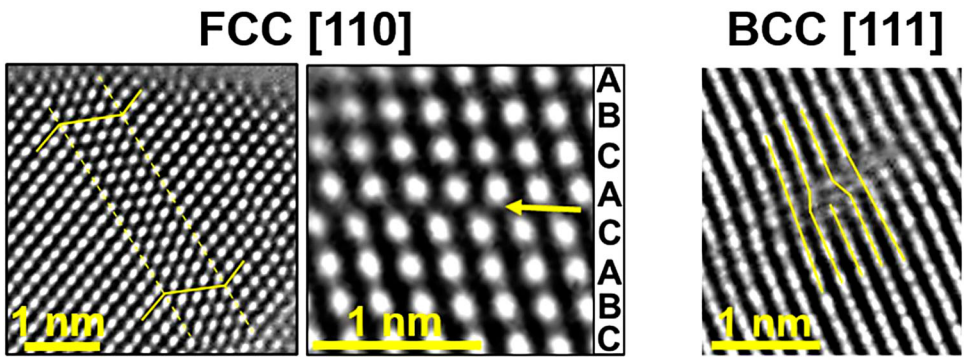

Figure 21. High-resolution electron microscopy images showing formation of twins (left), stacking faults (center) and dislocations (right) in dual-phase high-entropy alloy AlFeCoNiCu processed by high-pressure torsion [353].

$V_{10}Cr_{15}Mn_5Fe_{35}Co_{10}Ni_{25}$ [361,362]. Hardness levels of up to 1,000 Hv were reported in HPT-processed high-entropy alloys, which are some of the highest reported hardness levels for metallic alloys [356]. These hardness levels are not only due to the formation of nanograins, but also due to the generation of various kinds of defects such as dislocations, twins and stacking faults, as shown in Figure 21 [353].

The SPD process has been used not only to improve the mechanical properties of high-entropy alloys but also to control their functional properties such as hydrogen storage [363]. Moreover, SPD processing via the HPT method has been used for cold consolidation of powders of high-entropy alloys [364], to fabricate their particle-reinforced composites [365], and to produce their lamellar composites with other alloys [366]. Very recently, the SPD process has been employed as a synthesis path to produce hard CoCrFeMnNi [367] and biocompatible TiNbZrTaHf [368]. By considering the attractive functional properties of high-entropy ceramics [369,370], there have been also some attempts to employ the HPT process to synthesize new functional high-entropy ceramics: MgTiVCrFe-H high-entropy hydride for solid-state storage of hydrogen [371], $TiZrHfNbTaO_{11}$ high-entropy oxide as an active photocatalyst for production of hydrogen from water [372], $TiZrHfNbTaO_{11}$ high-entropy oxide for conversion of CO_2 to CO [373], and $TiZrHfNbTaO_6N_3$ high-entropy oxynitride for photocatalytic water splitting [374]. These results confirm that SPD is not only an effective processing tool to enhance the mechanical properties of HEAs, but also a potent synthesis method to produce totally new functional high-entropy materials.

5.3. Glasses

The first application of SPD methods to glasses goes back to 1935, when Bridgman processed some non-metallic glasses using the HPT method [19]. The investigation of the effect of high pressure and shear on the behavior of non-metallic glasses was later extended in some other studies [375–378]. These studies showed that crystallization at room temperature is rarely observed in SPD-processed glasses, but compaction to denser forms frequently takes place. The occurrence of densification was also reported after HPT processing of silica glass in recent years [379]. Within the past two decades, the research direction in the NanoSPD field has moved from non-metallic glasses to bulk metallic glasses.

Bulk metallic glasses, which exhibit a disordered amorphous structure and lack of long-range atomic order [380,381], have been attracting remarkable attention in the last decades due to their extraordinary mechanical properties [382,383]. Generally, they are brittle, which restricts their broad application [380,384]. Limited plastic deformation of bulk metallic glasses occurs in two different modes. Below the glass transition temperature, the deformation is highly inhomogeneous accompanied by the formation and propagation of sharp shear bands [385,386]. These very narrow bands ($\sim$ 10 nm) are characterized by high atomic mobility and local temperature rise [387,388]. At elevated temperatures, the deformation becomes homogenous over the entire volume of the material [384]. The mechanical properties, especially the ductility, of bulk metallic glasses can be significantly improved by dispersing the applied macroscopic deformation among competitive shear bands either by introducing structural or compositional inhomogeneity into the structure [389,390] or by the application of SPD [391]. Among the large variety of the SPD techniques, the HPT method can significantly improve the plasticity of metallic glasses due to the application of high concentrated pressure on the material [1,113,392].

The SPD process usually creates structural anisotropy in bulk metallic glasses [393]. Small distortions of the amorphous phase were clearly detected with high brilliance and high stability monochrome synchrotron X-ray radiation by analyzing the diffraction halo [394].

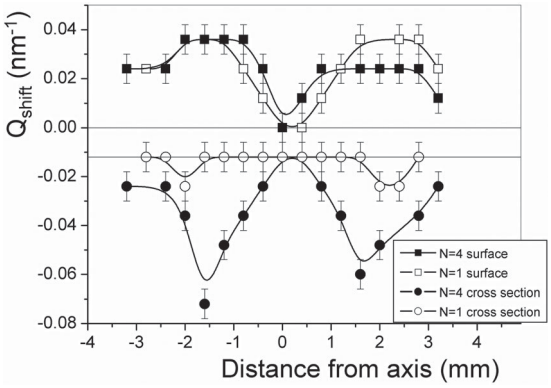

Figure 22. Shift of the halo positions (Q_{shift}) for a Zr-based bulk metallic glass processed by high-pressure torsion for $N = 1$ and $N = 4$ turn. Shifts were measured along the diameter on the surface and along a cross-section of discs [395].

Although anelasticity is not anticipated at low temperatures, a difference was obtained in the integrated halo positions between diffractions taken at different positions on the surface and a cross-section of a Zr-based amorphous alloy after HPT processing [395]. The shift of this position indicates that, even at room temperature, anisotropy can be generated by SPD processing (Figure 22) [395]. It was also found that the variation of the pair distribution function due to HPT deformation was opposite to the changes observed for structural relaxation, indicating a significant increase of the fictive temperature of the glass [396]. A detailed review on SPD processing of glasses was published elsewhere [6].

5.4. Semiconductors

When SPD processing is applied to semiconductor materials, not only grain refinement but also phase transformations are expected to occur. Among various SPD techniques, the HPT method is useful for processing semiconductors because it is applicable to brittle materials [1,47,113]. HPT processing of semiconductor materials was first reported by Bridgman [19] and later investigated by several other researchers [397–400]. There are some recent studies about HPT processing of semiconductor materials (e.g. silicon, germanium, SiGe and GaAs) and examination of their crystal structures and functional properties, as will be discussed below.

When silicon is subjected to HPT, metastable phases such as Si-III with bc8 cubic structure and Si-XII with rhombohedral r8 structure are formed from the Si-I phase with diamond cubic structure (through a high pressure Si-II phase), as shown in Figure 23(a) [401,402]. Moreover, during HPT processing the grain size is refined to the submicrometer and nanometer levels [401,402]. The metastable Si-III and Si-XII phases transform to Si-I during annealing at 873 K [401–403]. Annealing at lower temperatures ($\leq$ 473 K), however, leads to the transformation of Si-III to the Si-IV phase with hexagonal diamond structure [404]. Examination of the optical properties of these materials confirmed that no appreciable photoluminescence appears after HPT processing, while a broad photoluminescence peak appears in the visible light region after annealing [401,402]. Examination of electrical properties showed that the electrical resistivity decreases with increasing torsional strain due to the formation of metastable phases, especially semimetallic Si-III [405]. Photoemission spectroscopy using synchrotron radiation further confirmed the changes in the electronic structure by the formation of Si-III and Si-XII phases [406]. In addition to these optical and electrical properties, the HPT-processed silicon shows low thermal conductivity due to the formation of nanograins and metastable phases [407,408].

In the case of germanium, the samples deformed by HPT at room temperature consist of a metastable Ge-III phase with a tetragonal st12 structure and a Ge-I phase

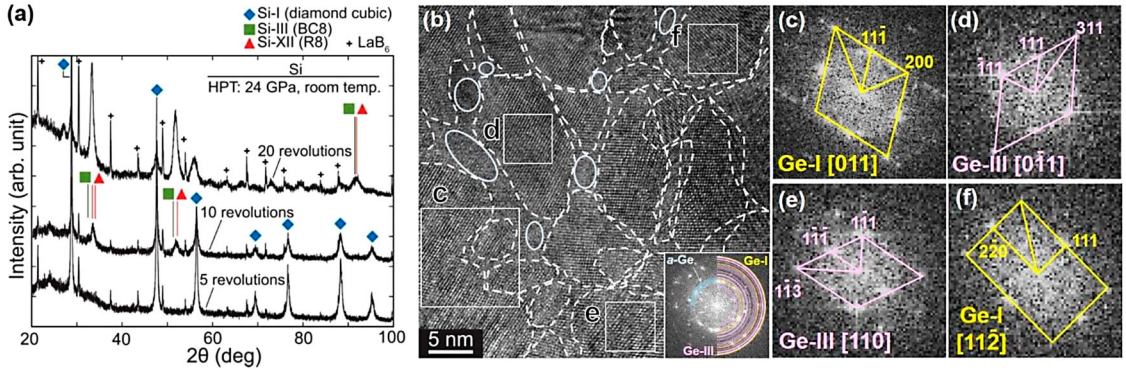

Figure 23. (a) X-ray diffraction profiles of silicon processed by high-pressure torsion for 5, 10 and 20 revolutions [402]. (b) High-resolution transmission electron microscopy images of germanium processed by high-pressure torsion at room temperature, where fast Fourier transformations in (c-f) were obtained from square regions (c-f) in (b). Ellipses in (b) show amorphous regions [410].

with a diamond cubic structure [409]. TEM observations confirmed the presence of nanograins in the Ge-I and Ge-III phases as well as an amorphous phase after HPT processing at room temperature, as shown in Figures 23(b–f) [410]. A broad photoluminescence peak is observed after annealing the HPT-processed germanium at 573 K [409]. When the HPT process is carried out at cryogenic temperature, the formation of Ge-III is considerably suppressed and a small amount of Ge-IV phase with bc8 structure appears [411].

The formation of a metastable phase was also reported in the SiGe semiconductor after HPT processing [412]. It was confirmed that the electrical behavior of the metastable phase of SiGe with bc8 structure is similar to that of Si-III [412]. In the case of GaAs, no metastable phases were reported after HPT processing [413]. A strong photoluminescence peak corresponding to the bandgap energy of GaAs (1.42 eV) disappears after HPT processing, while a weak photoluminescence peak centered at ~700 nm appears after annealing at 673 K [413]. There are also reports on phase transformations from graphite to diamond-like carbon [414], carbon onions [159] and diamond [160] by SPD processing via the HPT and SDAC methods. Taken altogether, these reports indicate that the SPD process has a high potential to create new functionalities in existing semiconductors by controlling microstructure and phase transformation, as discussed in more detail earlier [8,415].

5.5. Ceramics

The processing of ceramics by SPD has a close connection with the history of the HPT method. In 1915, Boeker tried to combine high pressure and torsion for deformation of oxide ceramics; however, the range of pressure was not high enough at that time to induce SPD in these hard materials [416]. Bridgman made a significant progress in increasing the range of achievable pressure from the sub-gigapascal level to several gigapascals, and this progress finally led to the birth of HPT in 1935 [19]. Bridgman found that the high pressure in HPT makes the method unique to induce plastic strain in hard and/or brittle materials such as ceramics. Since plastic deformation under high pressure has been an important issue in geology for many decades, the HPT method was immediately applied to minerals, rocks, and ceramics in 1935 [19]. Bridgman recognized that unlike the plastic behavior of metals, minerals, oxides, and ceramics experience snapping and noisy shocks during plastic deformation. He highlighted the idea that such snapping behavior should be a possible mechanism for deep-seated earthquakes. Therefore, the first press release on the HPT method appeared with the title 'scientist makes miniature earthquake' [47]. Bridgman's studies on ceramics continued for years, although his big target was to find new phases or to accelerate phase transformations by shearing [49,51].

After Bridgman's pioneering studies, some other geologists and physicists continued the application of the HPT method to ceramics and minerals. Griggs first used Bridgman's facility with manual rotation in 1936 [417] and later made a modern facility with an electric motor for processing rocks in 1960 [56]. These kinds of facilities were later used to process various ceramics by different groups. Bates *et al.* [418], Bell [419], Dachille and Roy [420], Miller *et al.* [421], and Vereshchagin *et al.* [422] reported the acceleration of phase transformations by shearing under pressure. In 1990s, Mozoroca *et al.* found that oxides can be reduced by shearing under high pressure [423,424], a fact that was also reported by Bridgman and can be an evidence of oxygen vacancy formation [19,47,49,51]. Despite large efforts on SPD processing of ceramics by geologists and physicists [47], SPD processing of ceramics was surprisingly overlooked by materials scientists for many years. In 2010, a Japanese group started the examination of SPD-processed ceramics from the materials science point of view to control the microstructure and achieve advanced properties [133]. Table 2 summarizes the materials examined by this group, including the microstructural features, phase transformations and reported functional properties [379,425–436,438–443]. Reviews of some functional properties of these ceramics can be found elsewhere [5,134,444].

Ceramics show SPD-induced grain refinement like metals, but the achievable grain size of ceramics is much smaller than those of metals [5]. Lattice defect formation (such as oxygen vacancies, dislocations) and phase transformation are frequently observed in HPT-processed ceramics [5]. As given in Table 2, these structural and microstructural features lead to enhancement of functional properties of ceramics such as dielectric performance, electrocatalysis for hydrogen production, luminescence, photovoltaics, and photocatalytic activity for dye degradation, water splitting, and CO_2 conversion. A limited number of scientists is currently working on SPD processing of functional ceramics. Because of a wide range of functional properties of ceramics, these materials have a high potential for various applications and, therefore, should be studied in future more extensively. The HPT method is used not only as a process tool for existing ceramics but also as a synthesis method to fabricate new ceramics such as high-entropy oxides ($TiZrHfNbTaO_{11}$) [372,373] and high-entropy oxynitrides ($TiZrHfNbTaO_6N_3$) [374].

Deformation behavior and the mechanisms of formation of lattice defects in ceramics are not yet so clear, although some theoretical studies have shed light on

Table 2. Microstructural features, phase transformations and functional properties of ceramics processed by severe plastic deformation via high-pressure torsion.

Ceramics	Microstructural features	Polymorphic transformations	Functional properties	References
α-Al_2O_3	Strained lattice		High hardness	[133]
γ-Al_2O_3	Grain coarsening, Vacancies	$\gamma \rightarrow \alpha$	Photocatalyst	[425,426]
MgO	Nanocrystals, Vacancies, Dislocations		Photocatalyst	[427]
ZrO_2	Nanocrystals, Vacancies, Dislocations	Tetragonal → Monoclinic	Photocatalyst	[428,429]
TiO_2	Nanocrystals, Vacancies, Dislocations	Anatase → Columbite	Visible-light photocatalyst, Photovoltaics	[429–433]
Nano-TiO_2	Grain coarsening	Anatase → Columbite + Rutile	Electrocatalyst	[434,435]
ZnO	Nanocrystals, Vacancies	Wurtzite → Rocksalt	Visible-light photocatalyst	[436]
VO_2	Nanocrystals	Monoclinic → Triclinic	—	[379]
SiO_2 Glass	Not crystallized	Transition to denser glass	—	[379]
SiO_2 Quartz	Nanocrystals, Vacancies	Quartz → Coecite + Amorphous	Photocatalyst	[437]
Y_2O_3	Nanocrystals	Cubic → Monoclinic	Luminescence	[438]
Bi_2O_3	Nanocrystals, Vacancies		Photovoltaics	[439]
$BaTiO_3$	Nanocrystals	Tetragonal → Cubic	Dielectric	[440]
$LiTaO_3$	Nanocrystals, Vacancies		Photocatalyst	[441]
$CsTaO_3$	Nanocrystals, Vacancies	Orthorhombic → Amorphous	Photocatalyst	[441]
TiO_2-ZnO	Nanocrystals, Vacancies	Anatase → Columbite Wurtzite → Rocksalt	Photocatalyst	[442]
GaN-ZnO	Nanocrystals, Vacancy clusters, Dislocations		Photocatalyst	[443]
$TiZrHfNbTaO_{11}$	Nanocrystals	Synthesized by HPT + Oxidation	H_2 production, CO_2 conversion	[372,373]
$TiZrHfNbTaO_6N_3$	Nanocrystals	Synthesized by HPT + Oxidation + Nitriding	H_2 production	[374]

these questions [445–449]. However, as discussed in a recent paper [5], despite differences in the atomic bonding of metallic materials and oxides, their deformation mechanisms are reasonably similar depending on the deformation conditions. While ceramics generally fracture at room temperature, they plastically deform under high hydrostatic pressure during HPT. Like in metals, dislocation activity is a common observation in ceramics, but because of the covalent and ionic bonding, dislocation mobility is more difficult in ceramics. Similar to metals, grain refinement and polymorphic transformations frequently occur at the early stage of straining and an apparent steady state is observed at high strains. Although future studies are needed to clarify the mechanisms underlying the appearance of a steady state for ceramics, a combination of dynamic recovery, dynamic recrystallization and grain-boundary migration can be assumed as responsible mechanisms [99,450,451]. Compared to metals, dynamic recovery and dynamic recrystallization are more difficult in ceramics due to their covalent and ionic bonding leading to smaller grain sizes and higher dislocation densities. The formation of vacancies in HPT-processed ceramics is basically similar to metals [452–454].

5.6. Polymers

SPD processing of polymers was first conducted by Bridgman [455,456]. In his seminal study performed using the HPT method, he demonstrated that the SPD process accelerates both polymorphic transformations and chemical reactions in solid organic compounds. Bridgman hypothesized that these effects may be caused by ruptures of individual bonds in the molecules of organic compounds, caused by high pressure acting in concert with shear stress. In a later work, Larsen and Drickamer observed a decrease of the molecular weight of various polymers under similar deformation conditions [457]. These results gave them a reason to believe that the mechanism underlying the changes is rupture of covalent bonds under shear with high pressure.

In-depth research into SPD of polymers was carried out mainly by Russian researchers for over three decades since the 1960s [458–461]. In numerous publications summarized in [462,463], it was shown that monomers or monomer mixtures which do not react even under pressures of several thousand atm, polymerize when deformed by HPT. In this process, nearly full transformation of monomers to polymers occurs, and the rate of transformation is thousand or even tens of thousand times greater than that typical for liquid-phase polymerization of the same monomers at comparable temperatures and pressures. A most prominent feature of the HPT-induced polymerization reactions is a sigmoidal shape of the curve representing the fraction of transformed material as a function of shear stress.

Further developments in the SPD of polymers focused on the use of various versions of solid-state extrusion [464]. The first attempts to use ECAP were made at the end of the last century [465,466]. The process was

Table 3. Influence of severe plastic deformation by twist extrusion on Young's modulus, yield stress and ductility (elongation to failure) of polymers [4].

	Young's modulus (GPa)		Yield stress (MPa)		Elongation to failure (%)	
Polymers	Initial	SPD	Initial	SPD	Initial	SPD
Polyamide-6	0.87	1.35	68	100	14	9
Polyethylene	0.21	0.27	22	27	25	23
Polytetrafluoroethylene	0.40	0.51	26	34	27	25

shown to cause a substantial change in the polymer morphology both at the micro scale and the molecular level. These changes influence the characteristic properties of polymers such as elastic modulus, strength, fracture toughness, resistance to solvents, and optical properties. New developments in SPD processing of polymers by different techniques such as twist extrusion, equal-channel multiple angular extrusion, planar twist extrusion, and T-shape equal-channel extrusion aim at creating novel multi-scale inner architectures in semi-crystallized, amorphous and hybrid polymers [467–471]. These studies showed that architecturing polymers by means of SPD has the potential to improve their mechanical properties in a significant way and to achieve new functionalities that are not attainable by other methods. As shown in Table 3, SPD processing can increase both elastic modulus and yield strength of polymers without significantly deteriorating their ductility [4].

6. Microstructural features of severely deformed materials

The SPD methods introduce large strain in a piece of material under usually high pressures, and this naturally leads to significant microstructural changes. Grain refinement to the submicrometer or nanometer level is the most well-known microstructural change during the SPD process [1]. It is well established that such a grain refinement finally saturates to a steady-state level at large strains. Understanding the mechanism of grain refinement as well as the physical phenomena underlying the saturation of grain refinement are still of critical significance in the NanoSPD field [178,472]. In addition to the formation of ultrafine grains with large fraction of high-angle grain boundaries, various kinds of defects such as twins, dislocations, stacking faults and vacancies [452,473] as well as some unique microstructural features including grain boundary segregation, precipitate formation/dissolution [474] and texture development [475,476], are characteristics of SPD processing. As mentioned above, these microstructural features are not limited to SPD-processed metallic materials and similar features can be observed in many oxide ceramics [5]. The salient microstructural features that lead to improved mechanical and functional properties of SPD-processed materials are covered in this section.

6.1. Formation mechanism of ultrafine grains

Metallic materials with UFG structures, having average grain sizes smaller than 1 μm, have been vigorously studied all over the world in the last decades, for which SPD gave a great breakthrough. It was found that SPD can realize UFG structures in most metals and alloys. However, it is still not entirely clear why and how UFG structures are formed by SPD processing. In conventional metallurgy, recrystallization taking place during annealing after plastic deformation is the main way to refine the grain size of metallic materials [477]. In the case of SPD-processed materials, however, UFG structures are already observed in the as-deformed (as-SPD-processed) states without annealing.

Figures 24(a and b) shows TEM microstructures in IF steel and pure Al (99%), respectively, both processed by ARB for 6 cycles (total strain: $\varepsilon = 4.8$) [478]. Both materials show ultrafine lamellar structures with an average lamellar spacing of about 200 nm. After carefully studying the microstructure evolution during SPD by SEM-EBSD and Kikuchi-line analysis, it is concluded that the formation of UFG structures by SPD can be understood in terms of the *grain subdivision* mechanism [177,178,479,480], which is schematically illustrated in Figure 24(c) [177,178]. In grains of polycrystalline materials, due to the constraints by neighboring grains not only the primary slip system with the highest resolved shear stress is activated, but also other slip systems become active. The activation of different slip systems in different grain areas causes different local crystal rotations. This leads to the evolution of misorientation between neighboring areas resulting in geometrically necessary boundaries (GNBs) [479,480]. Many dislocations are also stored within each domain divided by GNBs, and they tend to form low-energy configurations that are called incidental dislocation boundaries (IDBs) [479,480]. With increasing plastic deformation, original grains are subdivided by GNBs and IDBs, and eventually, finer subdivided structures in the nanometer scale are formed during SPD. The ultrafine lamellar structures

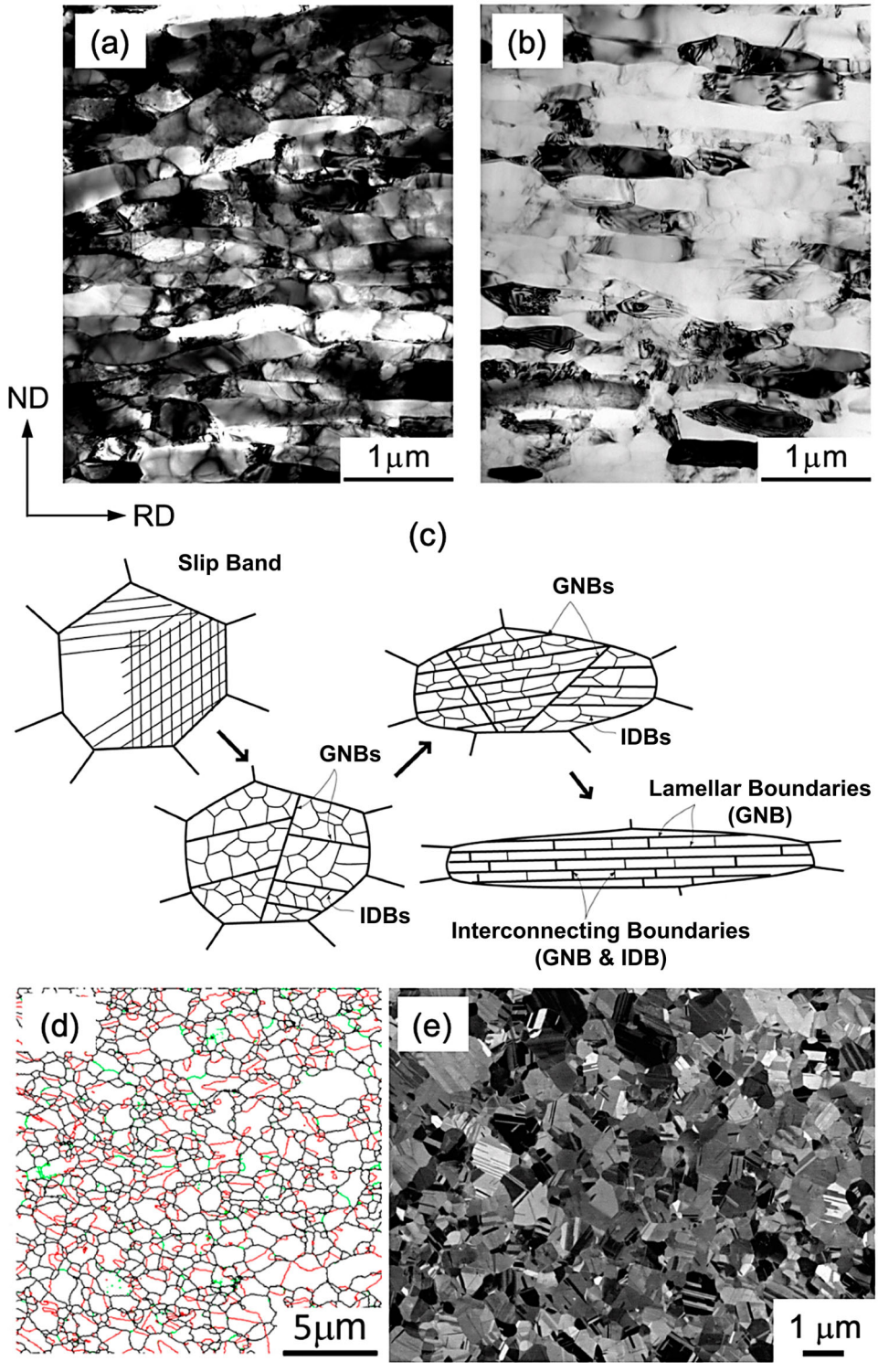

Figure 24. (a, b) Typical ultrafine-grained microstructures obtained by severe plastic deformation: (a) IF (interstitial free) steel and (b) pure aluminum (99%) processed by accumulative roll-bonding for 6 cycles at 773 K and room temperature, respectively [478]. (c) Schematic illustration of the formation of an ultrafine lamellar structure by the grain subdivision mechanism [177,178]. (d) Recrystallized ultrafine-grained structures of Fe-22Mn-0.6C (wt%) steel with average grain size of 580 nm processed by repeated cold rolling and annealing [487]. (e) Recrystallized microstructure of CoCrFeNi equiatomic medium-entropy alloy with average grain size of 163 nm, processed by high-pressure torsion and annealing [493].

shown in Figures 24(a and b) are elongated along the major deformation direction and contain high densities of dislocations. This indicates that the UFG structures obtained by SPD are also a kind of highly deformed microstructures.

The characteristic UFG structures formed by SPD can affect the mechanical properties in both positive and negative ways [178,179,481]. Recently, it also has been found that fully recrystallized UFG structures keeping submicrometer grain sizes during annealing treatment could be realized in certain metals and alloys such as copper [482,483], magnesium [484], titanium [485], high-manganese steels [486–488], Cu-based alloys [489], Mg-based alloys [490,491], Ti-based alloys [492], and medium-entropy alloys [493,494]. Figures 24(d and e) indicate examples of such fully recrystallized UFG structures in Fe-22Mn-0.6C (wt%) steel [487] and CoCrFeNi equiatomic medium-entropy alloy [493]. Both alloys show fully recrystallized structures with grain sizes of several hundred nanometers. It has been also clarified that such fully recrystallized UFG metals show a good balance of high strength and large ductility [495,496].

6.2. Saturation of grain refinement

Heavy plastic deformation of single-phase metals transforms the initial coarse-grained material into UFG structures. This grain refinement saturates at sufficiently high strains, resulting in minimum grain sizes at the nanometer or submicometer levels. Further straining does not alter average microstructural features, hence a dynamic equilibrium between the generation of deformation-induced defects (vacancies, dislocations and boundaries) and their recovery or annihilation is required. While vacancies and dislocations may easily annihilate at numerous grain boundaries, grain size and grain shape were found to be maintained by migration of grain boundaries and triple junctions [497,498]. Their migration causes local coarsening and fragmentation, allowing microstructural features to be in equilibrium with the imposed refinement (Figure 25a). Although thermally facilitated, these migration processes become athermal below a certain deformation temperature. Lowering the processing temperature beyond this transition point does not allow to reduce the grain size any further, (Figure 25b) [499]. (Thermo)mechanically driven grain-boundary migration occurs by movement of disconnections (i.e. grain-boundary line defects associated with a step height and a Burgers vector [500]) within the boundary due to their coupling with the imposed load, realizing grain growth by the step height [500,501]. It should be emphasized that disconnections cannot only be nucleated in the grain boundaries [502], but can originate more easily from lattice dislocations impinging the boundaries [503]. The latter is in line with recent experiments, providing evidence that mechanically-induced growth is amplified in highly strained regions [504,505]. As long as dislocation slip prevails, mechanically-induced boundary migration may thus be considered as a strain-driven rather than a stress-driven phenomenon [472].

In the cases of limited disconnection mobility (e.g. disconnections with out-of-plane Burgers vector and low temperatures), individual steps may accumulate to macro-steps [501], potentially inducing grain fragmentation and limiting their length. Accordingly, the disconnection mobility strongly affects the resulting grain size and shape, reflected in the evolution of grain aspect ratios with deformation temperature. For intermediate temperatures below 0.30 T_m (T_m: melting point), the grain length increases faster with temperature than the thickness, causing increasing grain aspect ratios (Figure 25c) [472,506,507]. The enhanced disconnection mobility at elevated temperatures may avoid macro-step formation, and thus limit the grain fragmentation. For sufficiently high temperatures, the increasing role of triple junctions in structural restoration effectively reduces the aspect ratio again. Although this description allows for a general understanding of temperature and strain rate effects, quantitative differences between individual metals appear [472,507], which need to be understood to establish physically-based models for microstructural evolution. Similarly, the effect of alloying or impurity elements needs to be investigated, as already small amounts of impurity atoms can cause tremendous effects on the saturated grain structure [472,508]. Since the migration of grain boundaries and triple junctions occurs not only in the saturation regime but also at comparably low strain levels (often during mechanical testing of nanoscaled specimens), in-depth understanding of this phenomenon is essential to describe grain evolution during the SPD process as well as to predict the mechanical properties of nanomaterials.

6.3. Linear and planar lattice defects

Lattice defects, such as vacancies, dislocations, stacking and twin faults as well as grain boundaries, significantly influence the mechanical properties of metallic materials. SPD leads to the development of high amounts of defects. Therefore, the study of the evolution of lattice defects during the SPD process and understanding the influence of defects on the mechanical behavior is essentially important for developing materials with improved mechanical performances. Quantitative analysis of lattice defects is a key factor to address the property-microstructure relations. Some of the first attempts on

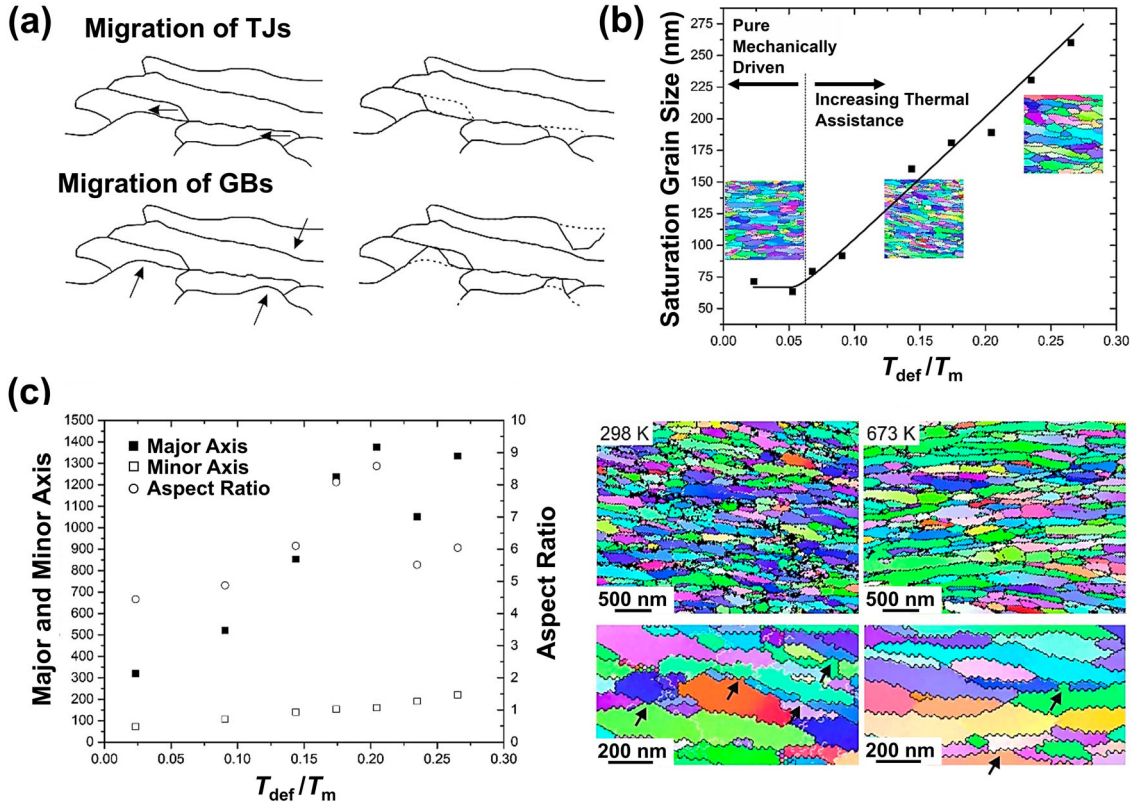

Figure 25. (a) Schematic illustration of principles of restoration mechanisms leading to local coarsening and fragmentation of microstructure. (b) Minimum grain dimensions of pure tantalum (99.999%) as a function of homologous deformation temperature, showing that grain size becomes temperature-independent below a certain deformation temperature. (c) Major and minor grain dimensions, resulting grain aspect ratio and corresponding inverse pole figure maps for tantalum (99.95%) processed by high-pressure torsion at various temperatures: up to 673 K, aspect ratio continuously increases as grain fragmentation events (indicated with arrows in inverse pole figures) [472,506,507].

quantitative description of SPD-induced defects were published at the end of the 1990s and the early 2000s using the X-ray diffraction method [509–511], although there were earlier attempts on this issue even in the 1970s [61]. Very soon, it became clear that indirect methods such as positron annihilation spectroscopy [512] and X-ray line profile analysis [513] are very effective in measuring densities of vacancies, dislocations and planar faults in SPD-processed materials. These techniques revealed that the vacancy concentration and the dislocation density after SPD can reach high values of 10^{-4}-10^{-3} and 10^{16} m^{-2}, respectively [514–517].

Considerable research effort was invested in the determination of the effect of material physical parameters (e.g. melting point and stacking fault energy) and processing conditions (e.g. deformation mode and processing temperature) on the type and densities of lattice defects [518]. It was found that the higher the melting point and the lower the stacking fault energy, the larger the saturation dislocation density in FCC metals (see Figure 26a) [473]. Increased solute concentration and secondary phase content also result in an enhanced dislocation density. Therefore, very high dislocation densities can be achieved in high-entropy alloys with low stacking fault energy [519]. The higher solute content and the lower stacking fault energy result in a less clustered dislocation structure. It was found that a smaller value of the stacking fault energy also causes a higher twin fault probability, however, the grain size also influences the occurrence of twinning (see Figure 26b) [473]. It was also revealed that the fraction of high-angle grain boundaries at the saturation state was as high as 60-80% for SPD-processed materials which was slightly influenced by the solute content [520,521]. Among the SPD techniques, the HPT method yields the highest vacancy concentration, dislocation density, twin fault probability and grain boundary area (i.e. the smallest grain size) because large applied hydrostatic pressure can hinder the annihilation of defects during the HPT process [452,516].

To achieve desired mechanical and functional properties of bulk UFG materials, the defect structure can be tailored with an appropriate selection of SPD conditions and post-SPD treatment. Recent studies have shown that annealing at moderate temperatures may yield additional

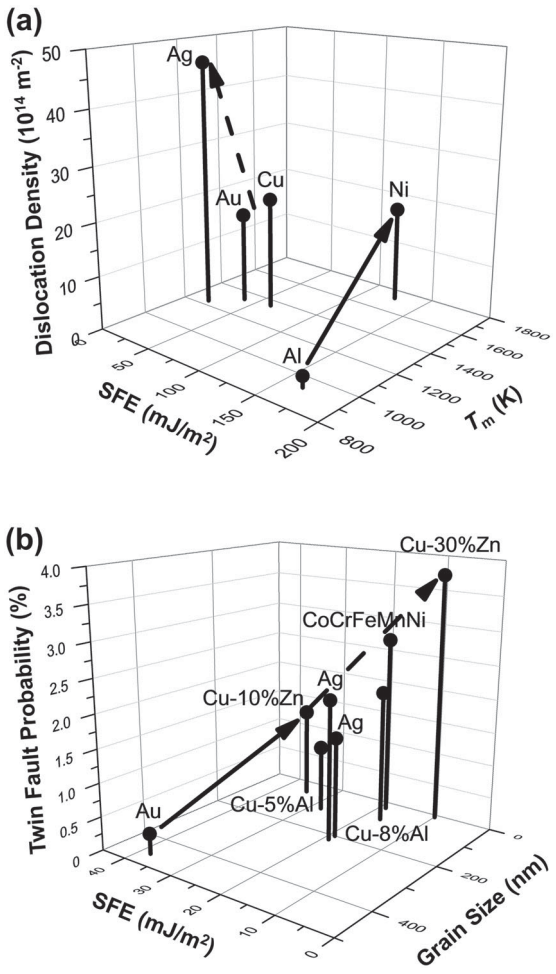

Figure 26. (a) Maximum dislocation density as a function of melting point (T_m) and stacking fault energy and (b) twin fault probability as a function of stacking fault energy and grain size for pure FCC metals processed by equal-channel angular pressing at room temperature. Dislocation density is higher for metals with higher melting point and lower stacking fault energy, and twin fault possibility is higher for metals with low stacking fault energy and smaller grain size [473].

hardening of SPD-processed materials [483,522,523]. This effect can be explained by the annihilation of mobile dislocations and the rearrangement of remaining dislocations into a more clustered configuration. The increase of solute content in SPD-processed materials reduces the effect of annealing-induced hardening, mainly because solute atoms can hinder the annihilation and rearrangement of dislocations [523]. Details of lattice defect evolution during SPD processing and post-SPD treatment were reviewed in an earlier publication [524].

6.4. Vacancies

As discussed in the previous section, lattice defects introduced by SPD represent an intrinsic feature of UFG materials [116] and they are responsible for many outstanding properties and unique features such as significantly enhanced diffusion [525,526]. Numerous experimental techniques, in particular electron microscopy, and X-ray, electron and neutron diffraction, etc. have been employed to characterize the evolution of microstructure and defects with strain [99,113]. These techniques concentrate mainly on the investigation of planar (grain boundaries) and line defects (dislocations). On the other hand, point defects, namely vacancies and their agglomerates, have been investigated in less detail. Positron annihilation spectroscopy proved to be an effective method for the investigation of point defects in UFG materials [513]. Positron annihilation spectroscopy was successfully employed for the characterization of lattice defects created by SPD in UFG metals with FCC (aluminum, nickel, copper), BCC (iron, niobium, tungsten) and HCP (magnesium, titanium) structure processed by HPT [513].

Positron annihilation spectroscopy investigations revealed that the HPT process not only introduces dislocations but also a high concentration of vacancies. The concentration of vacancies introduced by SPD approaches the values close to that at the melting point of materials [473]. A significant fraction of deformation-induced vacancies disappears by diffusion to sinks at grain boundaries, but remaining vacancies agglomerate into vacancy clusters which persist in the UFG materials. The average size of vacancy clusters was determined by comparison of experimental data with *ab-initio* calculations of lifetimes of positrons trapped in vacancy clusters of various sizes. The mean size of vacancy clusters differs in various metals: aluminum and titanium contain large clusters consisting of 40-50 vacancies; iron, nickel and tungsten contain smaller clusters consisting of 13-14 vacancies; copper and niobium contain small clusters consisting of 4 vacancies only. The size of vacancy clusters is affected by the activation energy for vacancy migration in the given material. The size distribution of vacancy clusters can be well described by the positron distribution [454,527,528]. An example of size distribution of vacancy clusters determined by positron annihilation spectroscopy in UFG copper deformed by HPT is shown in Figure 27.

The analysis of homogeneity of UFG structure showed that spatial distribution of dislocations becomes uniform after sufficient number of HPT revolutions. On the other hand, the lateral distribution of vacancy clusters remains non-uniform even in the samples subjected to a high number of HPT revolutions. As shown in Figure 27, the average size of vacancy clusters is higher in the periphery of the sample than in the center (corresponding to the torsion axis). This effect is caused by increasing strain and strain rate with increasing the radial distance from

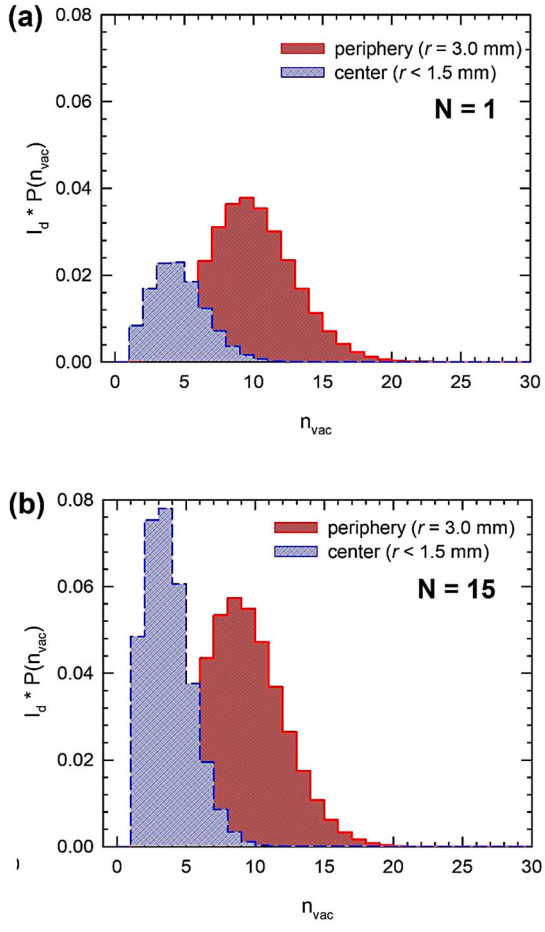

Figure 27. Size distribution of vacancy clusters in ultrafine-grained copper deformed by high-pressure torsion using (a) $N = 1$ revolution and (b) $N = 15$ revolutions, at central region (radial distance from center $r < 1.5$ mm) and periphery (radial distance from the center $r = 3.0$ mm) of disc samples. The size distribution of vacancy clusters $P(n_{vac})$ was determined by positron annihilation spectroscopy. The size distribution of vacancy clusters in the figure was multiplied by the intensity I_d of positrons trapped at vacancy clusters which is a measure of the concentration of vacancy clusters [454,528].

the center, which results in a higher production rate of vacancies in the periphery compared to the central region [528].

6.5. Grain boundary segregation

The interaction between solutes (or impurities) and grain boundaries might significantly affect UFG structures resulting from SPD processing. It not only affects the dynamic recovery mechanisms during SPD processing and thus the steady-state grain size but also leads to grain boundary segregations [529,530]. Such segregations are indeed a frequent feature in metallic alloys processed by SPD which is partly connected to the specificity of the 'non-equilibrium' state of the grain boundaries obtained

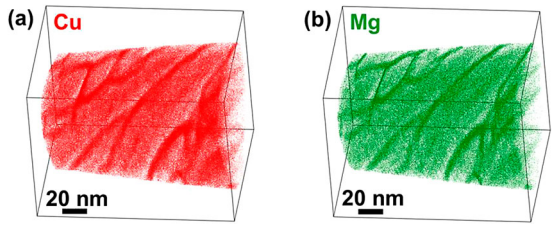

Figure 28. Three-dimensional reconstruction of a volume ($88 \times 88 \times 110$ nm^3) analyzed by atom probe tomography: atom maps of (a) copper and (b) magnesium in aluminum alloy 2024 processed by high-pressure torsion at room temperature (shear strain: ~ 300) and aged to achieve hardness peak. It exhibits intensive grain boundary segregation and stabilization of the ultrafine-grained structure resulting from severe plastic deformation [534].

during grain refinement by SPD [531]. Such grain boundary segregations have been observed in commercial aluminum alloys [532–536] (Figure 28), model binary systems [474,537,538], steels [539,540] or titanium [541]. The atom probe tomography technique is a key instrument for the investigation of grain boundary segregations [542] and it has been applied only when SPD processes became relatively mature.

All crystalline defects created during SPD processing may influence the atomic mobility and promote grain boundary segregations: dislocations can drag solutes or act as diffusion pipes, grain boundaries are also fast diffusion paths and can drag solutes when they move during the deformation, and at last, strain-induced vacancies can directly enhance the atomic diffusion [474,538,543]. Strain-induced grain boundary segregations may also promote phase separation in super-saturated solid solutions under SPD conditions, such as dynamic precipitation in the Al-Zn or Al-Cu systems [536,544]. Indeed, since grain boundaries are fast diffusion paths, these segregations provide a strong flux of solutes toward particles that nucleate at triple lines.

Strain-induced grain boundary segregations may lead to a significant extra mechanical strength, as reported for aluminum alloys and stainless steels [539,545,546]. This specific feature is attributed to an increase of the critical stress necessary to nucleate dislocations from boundaries covered by solutes. However, grain boundary segregations do not only affect the yield stress, but they may also have a significant impact on superplastic properties as demonstrated for Al-Zn [537] and Mg-Li [547] alloys. Grain boundary sliding which is directly linked to grain boundary structures and grain-boundary diffusion coefficients can be indeed very sensitive to grain boundary segregations.

The thermal stability is a major concern for the application of UFG alloys and it is important to note that it

can be significantly enhanced thanks to grain boundary segregations. The segregations can first reduce the boundary mobility and thus the grain growth. The equilibrium grain boundary segregations are driven by minimization of the grain-boundary energy, and thus they can eventually reduce the driving force for grain growth.

6.6. Texture

It is now well established that characteristic texture evolution is one of the most important features of SPD processing. Texture is defined as the orientation distribution of crystallites in polycrystalline aggregates. Texture plays a major role in the grain refinement process during the SPD process. It also influences the properties of severely deformed materials. Texture changes are produced by the rotation of grains. During deformation, small regions within a grain start rotating by the activity of different slip systems, which leads to the formation of substructures.

Among different SPD processes, the ECAP process, in which the shear plane is the plane of intersection of the two channels of the die, has been the most extensively investigated technique for texture development. Early studies on texture of ECAP-processed materials revealed that the ECAP method leads to the formation of simple shear-type textures with some deviation in the location of components from their ideal position [475]. Texture evolution during ECAP has been extensively investigated for various FCC and HCP materials as a function of processing routes, number of passes, degree of deformation, and material variables like purity, stacking fault energy, initial texture, etc. The overall conclusion of these investigations is that the simple shear texture is maintained irrespective of processing route applied and number of passes [162]. The intensity of individual texture components may change as a function of either material or process variables. Another important observation is the through-thickness heterogeneity of texture in ECAP processing [163], which is manifested in intensity and deviation of texture components from the ideal simple shear location. It was also observed that with increasing the number of passes, texture tends to saturate. The number of passes after which texture saturates depends on the material. Saturation of texture is reported in materials with different crystal structures including BCC, FCC and HCP. In the case of materials with the HCP structure, for example in magnesium alloys, a clear dependence of mechanical properties on the ECAP-induced texture was reported [548].

In the other shear-based SPD processes such as HPT and FSP, shear texture forms; however, texture strength is weakened much faster [549,550]. Heterogeneity of texture is very well manifested in the HPT- and FSP-processed materials. It should be noted that texture is significantly influenced by large strain induced in the HPT method and by the temperature rise during the FSP process. The temperature rise during the HPT process was reported to be of minor influence on texture and microstructure evolution [551].

The SPD processes with non-shear deformation such as ARB and MDF also lead to a characteristic texture formation, however, the type of texture is different in these processes. In the ARB method, textures broadly resemble those developing in rolling with some modification in the first passes, but the texture strengthens in the subsequent passes and attains saturation [552]. These ARB-induced textures are stable even after annealing [553]. On the contrary, in the MDF process, where there is a substantial change in the strain path, texture starts weakening after the first cycle itself. The resulting texture, after a few MDF cycles, becomes reasonably weak.

Overall, there is a clear influence of strain path, material type, and microscopic phenomena associated with deformation on texture formation in various SPD processes. Textures of SPD-processed materials are usually heterogeneous and tend to weaken after imparting large deformation, but they have a clear effect on the properties of the final product [554]. Table 4 summarizes the texture components for metallic materials with different crystal structures after processing with different SPD methods [554].

7. Phase transformations during severe plastic deformation

Polymorphic phase transformations are frequently obser ved during the application of SPD methods and particularly for the HPT method because of high processing pressure. It has been well established for several decades that severe straining under high pressure can significantly enhance the kinetics of phase transformations [19]. The SPD-induced phase transformations, which are sometimes irreversible, are either strain-induced, pressure-induced or strain/pressure-induced [446,447]. Among pure elements, titanium [555,556], zirconium [557,558], hafnium [559,560], cobalt [561,562], carbon [159,160], silicon [115,404], germanium [8,409] and phosphorous [555] show phase transformations to metastable phases. Many other elements including bismuth [118,555] can show pressure-induced phase transformations, but their transformations are reversible after releasing the pressure. Phase transformations in metallic alloys are also frequently observed and various metastable phases in binary and ternary systems were reported using SPD processing [563]. Phase transformations to polymorphs that

Table 4. Texture components for metallic materials with FCC, BCC and HCP structures after severe plastic deformation by various methods including equal-channel angular pressing (ECAP) accumulative roll-bonding (ARB), high-pressure torsion (HPT), multi-directional forging (MDF) and friction stir processing (FSP) [554].

Crystal structure	Material	Processing		Texture
FCC	Pure Al	ECAP	Route A	A_1 and C components
			Route B_C	$B/\bar{B}$ components
			Route C	A_1 and C components
	AA5109	ECAP	Route A – 3N	(Cube $\rightarrow A_1^*$) or ($A_2^* \rightarrow$ B $\rightarrow A_1^*$) depending on initial orientation
	AA2014	ECAP	Route A – 5N	$B/\bar{B} \rightarrow A_1 \rightarrow A_2 \rightarrow C$
			Route B_A – 5N	$B/\bar{B} \rightarrow A_1 \rightarrow A_2 = C$
			RouteB_C – 5N	$A_1 \rightarrow B/\bar{B} \rightarrow \bar{A} \rightarrow A_2 = A = C$
			Route C – 5N	$A/\bar{A} \rightarrow C \rightarrow A_2 \rightarrow A_1 \rightarrow B/\bar{B}$
	AA2195	ECAP	Route A; N $\leq$ 3	A_1, A_2, $B/\bar{B}$
			N = 4	A_2, C
	Pure Ni	ECAP	1 pass	Strongest C $\rightarrow$ A1 = $B/\bar{B}$
			Route A – 3N	$B/\bar{B} \rightarrow$ Oblique Cube $\rightarrow A_2$
	Ni Single crystal	ECAP	1 pass	TD-RC and C components
			Billet top	C_1 and C_2 Cube
			Billet middle	
			Billet bottom	
	Pure Cu	ECAP	1 pass	Strongest C $\rightarrow A_1 \rightarrow B/\bar{B}$
			Route A – 3N	$A_1 \rightarrow B/\bar{B}$
	OFHC Cu	ECAP	1 pass	C, $A/\bar{A}$, $B/\bar{B}$ components
	Cu	ECAP		$<110>$ ||SD
	Cu	ECAP	Route A	A_1^*, C strongest after N = 1
				A_1^*, B after N = 2,3
	OFHC Cu	ARB		RD rotated cube, Cube, S, Bs, Cu
	Pure Ag	ECAP	1 pass	Strongest $B/\bar{B} \rightarrow$ A
			Route A - 3N	Stronger $B/\bar{B} \rightarrow A_2$
	Pure Al	MDF	1 pass	$\{111\}<110>$ A $\rightarrow \{001\}<110>$ C $\rightarrow \{111\}<112>$ A$* \rightarrow$ $\{100\}<001>$ Cube
			7 passes	$\{001\}<110>$ C $\rightarrow \{111\}<110>$ A
	Al-4Mg	MDF	1 pass	$\{111\}<112>$ A$* \rightarrow \{123\}<634>$ S $\rightarrow \{001\}<110>$ C $\rightarrow$ $\{100\}<001>$ Cube
			7 passes	Brass $\rightarrow$ S
	CP-Al	HPT		B$\rightarrow$ C$\rightarrow$ A$\rightarrow$ A$*$
	AA5086	FSP		C $\rightarrow B/\bar{B}$
	AA2024	FSP		A_1^*/A_2^*, and C
	AA2219	FSP		C
	AA7075	FSP		A fiber
	Al-Mg-Mn	FSP		(111)[1$\bar{2}$1], (011)[100]
	AA5086	ARB	< 8 passes	Cu, Bs, S, Dillamore, Cube Goss
	AA6016	ARB	< 8 passes	β fiber, Cu strongest
	Pd-10at.% Au	HPT		B $\{\bar{1}12\}<110>/\bar{B}\{1\bar{1}\bar{2}\}<\bar{1}\bar{1}0>$
BCC	IF Steel	ECAP	1 pass	Partial $<111>$ and {110} fibers
	IF Steel	ECAP	Route A	Strong $<111>$ fiber
			Route B_A	Strong $<111>$ fiber
			Route B_C	Complete b1 fiber seen to pass through D_2-$\bar{E}$-D_1; $\bar{E}$ strongest
			Route C	D_1 strongest
				Nearly complete {110} and $<111>$ fibers for all passes
				Strongest components are:
				F, D_2 for N = 2
				F, $J/\bar{J}$ for N = 3
				F, D_1 for N = 4
	IF Steel	ARB	Center	α fiber
			Surface	$\{110\}<001>$ $\{110\}<112>$
	Pure Fe	ECAP	Route B_C	{110} fiber || ED
	Pure Va	HPT		{110} fiber
	$Ni_{50}Mn_{29}Ga_{21}$	HPT		Rotated cube$\{001\}<100>$
				F$\{110\}<100>$
HCP	Mg	ECAP	Multi-pass by routes A, B_C and C	B fiber CCW rotated about the TD axis by varying degrees, which is characteristic to the processing route
	AZ_{31}, AZ_{80}, ZK_{60},WE_{43}, MgLi	ECAP	Route A	$<10\bar{1}0>$ fiber
	Cp-Ti	ECAP	Route A	B fiber
	Mg	HPT		B fiber
	Mg-Dy-Al-Zn-Zr	HPT		P_1 and B fibers
	CP-Ti	FSP		Partial P fiber, P_1
	Zr	ARB		Split TD basal texture

can remain metastable after SPD processing are often reported in ceramics such as hydrides (MgH_2 [564], $MgTiH_4$ [565]), nitrides (BN [447]), and oxides (Al_2O_3 [425], TiO_2 [430], VO_2 [379], ZnO [436], Y_2O_3 [438], ZrO_2 [428], $BaTiO_3$ [440]). Although there are now some trends to employ the metastable phases produced by

SPD for different applications, understanding the direction of phase transformation (i.e. metastable→stable or stable→metastable) as well clarifying the mechanisms underlying these phase transformations are two fundamental issues in predicting and stabilizing new phases by the SPD methods [563,566]. Here, these fundamental issues are analyzed from the experimental and theoretical points of view as well as by in-situ studies.

7.1. Experimental aspects of phase transformation

The frequent observation of phase transformations during SPD processing is mainly due to the nature of this process. The SPD process permits to experimentally apply an extremely high strain to the material without its failure, while this is hardly possible with conventional metallurgical methods. After SPD processing, not only the grains in the material become extremely fine (the material even sometimes becomes amorphous), but also phase transitions frequently occur [567,568]. Allotropic and martensitic transitions, mass transfer, formation of grain boundary phases, dissolution/precipitation of a second phase, and amorphization/crystallization are some reported SPD-driven phase transformations [568]. It was shown that the phases in a material after SPD processing differ from those before SPD and are often similar to those that are observed if a sample was annealed at an elevated temperature, which is known as effective temperature T_{eff} [568]. In this way, SPD allows one to tailor the microstructure and properties of materials by phase transformations. However, it is essential to clarify the direction of the phase transformations, e.g. second phase dissolution or precipitation.

To discuss the direction of a phase transformation, it is beneficial to recall the sequence of microstructural evolution events. As mentioned earlier, when straining starts, the amount of lattice defects (like vacancies, dislocations, and grain boundaries) increases; however, the fraction of defects does not increase indefinitely. Thus, after a certain level of strain, the rate of defect production becomes equal to the rate of their annihilation (relaxation) and a steady state is reached. Therefore, if one starts to deform a material with a grain size in the range of several millimeters, the grain size quickly drops down to a few hundred nanometers until the grain size reaches the steady state. It should be noted that in the same material, the steady-state grain size depends on the SPD mode, as shown in Figure 29(a) [516,568–579]. However, if one starts to deform the nanocrystalline sample with grain sizes below the steady-state value the grains do not become smaller, but they rather grow during SPD up to the same steady-state value. Therefore, the direction of grain refinement

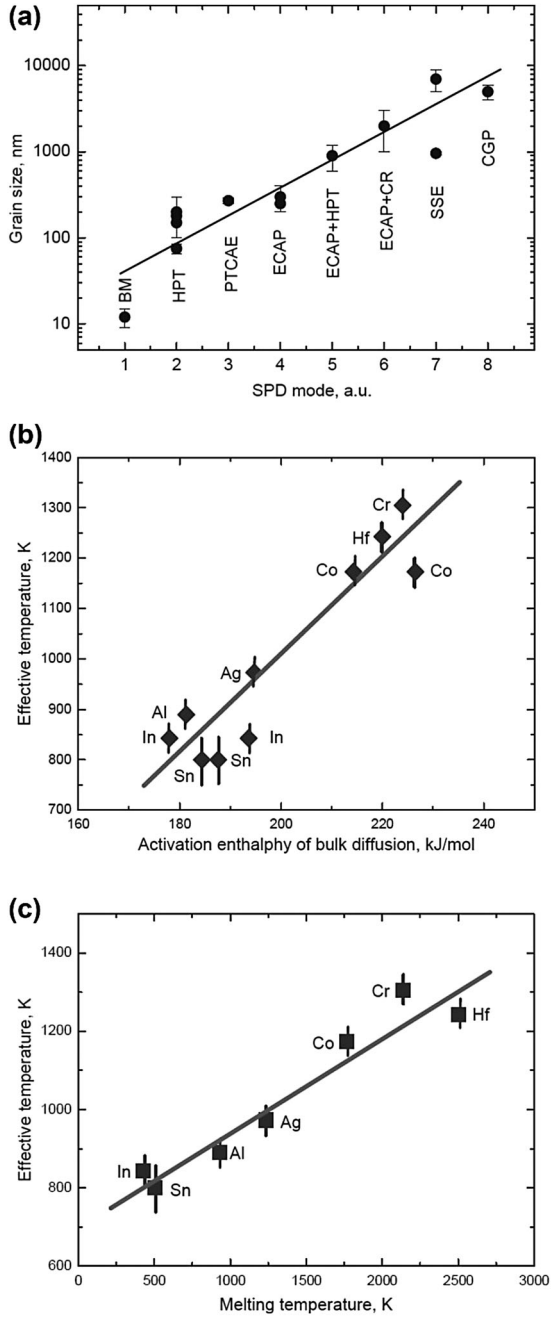

Figure 29. (a) Steady-state grain size in copper subjected to different SPD modes: 1- ball milling (BM) [567], 2- high-pressure torsion (HPT) [516,568–570,573], 3- planar twist channel angular extrusion (PTCAE) [574], 4- equal-channel angular pressing (ECAP) [572,575], 5- ECAP + HPT [572], 6- ECAP with following cold rolling (ECAP + CR) [576], 7- simple shear extrusion (SSE) [577,578], and 8- constrained groove pressing (CGP) [579]. Effective temperature for phase transformations during HPT plotted versus (a) activation enthalpy of diffusion and (b) melting temperature for various solute elements in Cu-based alloys [563,572].

or grain growth depends on the initial size. This is also true for the SPD-induced hardening/softening [563,572].

The situation is similar with the SPD-induced dissolution/precipitation process. In the steady state, a certain

concentration in the solid solution, c_{ss}, establishes. Its value is controlled by the dynamic equilibrium between competing processes of dissolution and precipitation. If the initial concentration in a solid solution, c_{init}, is below c_{ss}, it increases during the SPD process and the second phase dissolves. Otherwise, if $c_{init} > c_{ss}$, holds, the concentration of second component in a solid solution decreases and new precipitates appear (so-called dynamic ageing). Physically, it is the steady-state concentration in the solid solution, c_{ss}, which establishes during the SPD. To compare different binary alloys with different maximal solubilities of a second phase, an idea of T_{eff} is very useful. Thus, after SPD the concentration c_{ss} of a second phase in the matrix solid solution is as high as if the sample had been annealed at a certain (elevated) temperature T_{eff}. In other words, c_{ss} is equal to the solubility of a second phase at T_{eff}. The solubility can be defined by the solvus line in the equilibrium binary phase diagram [563,572].

The SPD process can also drive the amorphization in some crystalline materials and (nano)crystallization in some amorphous materials, which can be explained by considering the concept of T_{eff} as well [563]. In order to predict the phase transformation direction, it is then essential to estimate T_{eff} for an alloy system. The variation of T_{eff} for Cu-based alloys processed by HPT is shown in Figure 29 with respect to (b) the activation enthalpy of bulk tracer diffusion and (c) the melting point [563]. Figures 29(b and c) show that T_{eff} increases linearly with increasing activation energy and melting temperature. This correlation is important because it allows to estimate T_{eff} and accordingly predict the phase transformation direction in the Cu-based alloys during HPT processing.

7.2. Theoretical aspects of phase transformation

Numerous experiments have documented that combinations of SPD and high mean pressure during the HPT process in rotational metallic, ceramic, or diamond anvils (Figure 30a) produces various important mechanochemical effects including phase transformations [19,47,49,566,580,581] and chemical reactions [582,583]. Theoretical aspects of these effects are of importance to predict the kinetics of phase transformations and microstructure evolution during the SPD process and utilization of SPD to produce new phases. In this section, four experimental observations and their underlying theoretical mechanisms are discussed.

(a) Plastic deformation significantly reduces the pressure for initiation and completion of phase transformations [7,449,584,585] and chemical reactions [582,583]. The largest transformation pressure drop, from 52.5 to 6.7 GPa, was obtained for hexagonal BN to superhard wurtzitic BN [584], and from 70 to 0.7 GPa for the graphite to cubic diamond transformation [7].
(b) Intensive plastic strain leads to the discovery of hidden metastable phases and compounds [7,19,47,49,449,486,566,580–583].
(c) Plastic deformation reduces the phase transformation pressure hysteresis [445,448,580].
(d) Plastic deformation substitutes a reversible phase transformation with an irreversible phase transformation [7,445,448,580].

Recent overviews [566,587,588] summarized the current understanding of the underlying phenomena based on multiscale atomistic and continuum theories and computational modeling. Initially, processes in rotational anvils have been considered theoretically as pressure- or stress-induced [589,590]. The main first step was done in [445,448], where phase transformations in the phenomena mentioned above were classified as strain-induced rather than pressure-induced under high pressure and a three-scale analytical approach was suggested. Currently, much more developed four-scale theoretical and computational approaches use both atomistic and continuum studies. Recent atomistic (first principles and molecular dynamics) simulations provide conditions for the initiation of phase transformations in a defect-free lattice as a function of the general stress tensor (Figure 30b) [591–593]. These conditions (i) allow one to determine stress states that significantly decrease the transformation pressure and (ii) determine whether the given phase can, in principle, be preserved at ambient pressure.

The main physics is related to the nanoscale mechanisms of phase nucleation at plastic-strain-induced defects (mostly at dislocation pileups against grain boundaries), which are suggested and studied analytically [445,448], by utilizing advanced phase field theory and simulations (Figure 30c) [446,447,594,595], as well as by molecular dynamics simulations [596]. It is demonstrated that the concentration of all components of the stress tensor near the tip of the dislocation pileup may decrease the nucleation pressure by one to two orders of magnitude, as in the experiments. Similar results are obtained for a microscale polycrystalline sample using a scale-free phase field approach [597–599]. When dislocations slip through the grain boundaries and cannot produce pileups, this mechanism cannot work, and a reduction in phase transformation pressure is not expected [600]. These findings are incorporated into the microscale analytical kinetic equations for strain-induced phase transformations (Figure 30d)

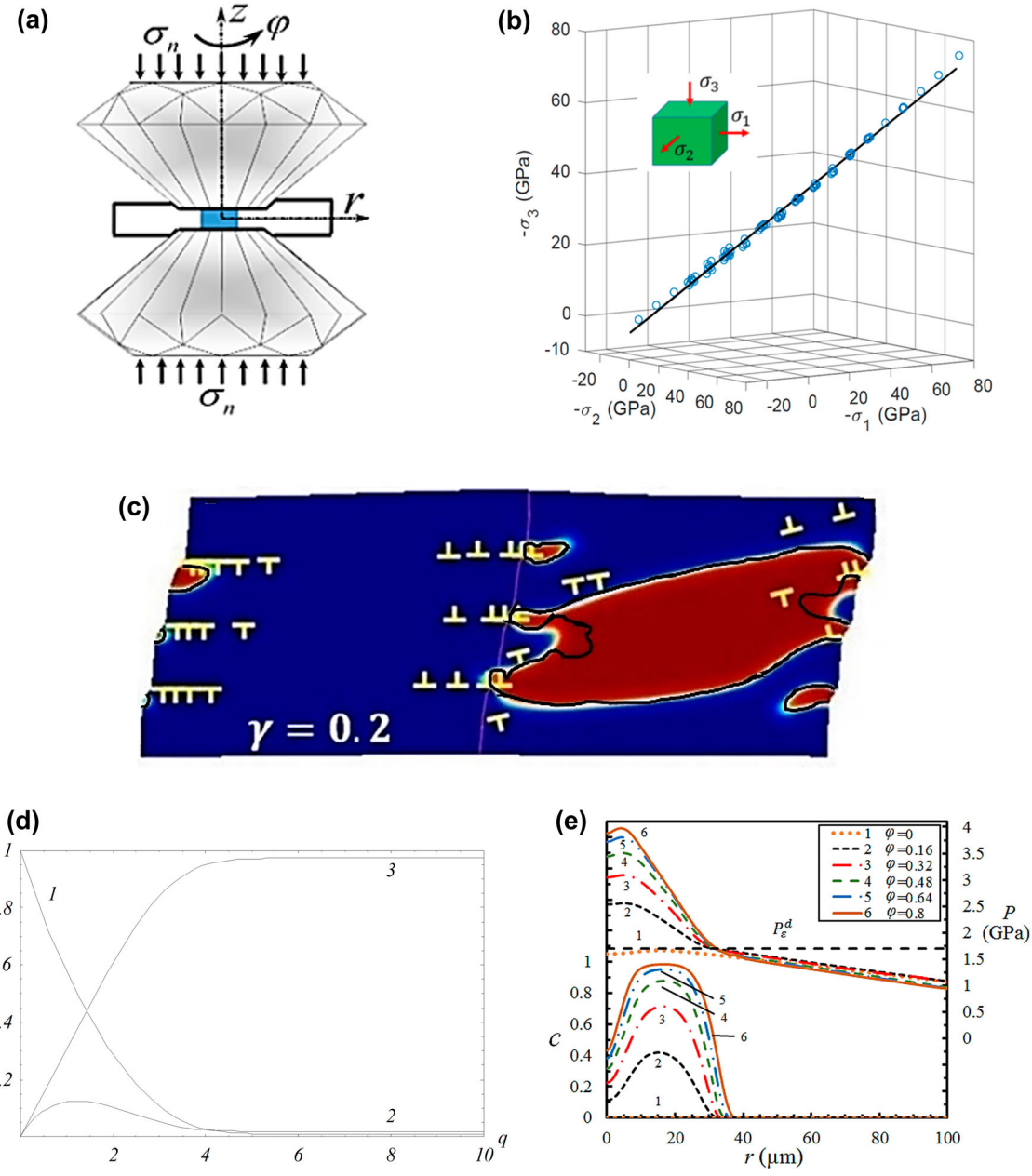

Figure 30. (a) Schematics of shear (rotational) diamond anvil cell, in which a sample within a gasket is compressed and twisted by diamond anvils [566]. (b) The crystal lattice instability criterion in the space of normal-to-cubic-faces stresses (σ_i) for Si-I→Si-II phase transformation obtained within the phase field approach (plane) [607] and confirmed by the first-principles calculation (points) [593]. (c) The high-pressure phase (red) obtained under compression and shear of a bicrystal at the stress concentrators produced by dislocation pileups [595]. (d) Evolution of the volume fraction of Si-I (1), Si-II (2), and Si-III (3) under plastic straining at a pressure of 7 GPa obtained from solution of the theoretical strain-controlled kinetic equation [601]. (e) Distributions of the pressure (*P*) and concentration (*c*) of the ω phase at the contact surface between a zirconium sample and diamond anvil during twisting under the fixed axial force [604].

[445,448,601]. These equations are part of a macroscale geometrically-nonlinear theory for coupled plastic flow and phase transformations, first with simplified plasticity [602–604], then utilizing strict large-strain plasticity [605] and combing it with phase transformations [606]. The macroscale models are currently used for FEM simulations of plastic deformations and phase transformations in a sample under torsion in a rotational cell (Figure 30e) [602–607]. Numerous experimentally-observed phenomena are reproduced by simulations, and new effects are predicted and experimentally confirmed. Combination of the results on all four scales suggests novel routes for strain-induced synthesis of new or known high-pressure phases at low pressures and

methods of an experimental characterization of strain-induced phase transformations under high-pressure during torsion.

7.3. In-situ studies of phase transformation

As mentioned in an earlier section, utilization of an SDAC facility for compression and HPT processing allows one to study the occurring processes in situ [580,608–611]. Some of the first in-situ measurements were related to the radial pressure distribution at the boundary between a diamond and a sample [580,608,609]. They were based on measuring the shift of the R_1 ruby fluorescence line utilizing ruby particles spread over the sample surface [580,608,609]. Since pressure is very heterogenous during the HPT process, this method leads to a much more precise characterization of the phase transformation pressure than in terms of the total force divided by area that is commonly used for the conventional HPT method. These examinations led to the discovery of the pressure self-multiplication effect in SDAC (i.e. phase transformation-assisted pressure multiplication under a constant force) and the steps on the pressure distribution corresponding to the transition zone between the phases [580], which were confirmed in [608], described analytically in [585,586], and simulated with FEM in [563,612]. Displacements of ruby particles were used to characterize displacements of material particles, qualitatively in [613] and quantitatively in [614]. Measurements in [614] quantify quite large relative sliding of a sample with respect to an anvil.

Utilization of X-ray diffraction with synchrotron radiation and scanning along the diameter opened new opportunities for in-situ studies of phase transformations. Experiments on hexagonal BN during its transformation to the superhard wurtzitic BN [449,615–617] reported the evolution of volume fraction of the high-pressure phase and the concentration of turbostratic stacking faults, averaged over the sample thickness, at the center and periphery of a sample. In these studies, an unknown superhard phase was detected, and phenomena of transformation-induced plasticity and cascading structural changes were revealed. The theoretical description of these phenomena led to a quantitative resolution of the main puzzles of the deep-focus earthquakes [618]. Reversible phase transformation from the α to the ε phase in iron [619], from the crystalline to a new amorphous phase of SiC [584], and from graphite to hexagonal diamond [7] could be studied in-situ only. The transformation from the disordered hexagonal BN to the wurtzitic BN was detected at 6.7 GPa under shear but did not occur under hydrostatic compression of 52.8 GPa [448]. The phase transformations to hexagonal and cubic diamonds were obtained at pressures of 0.4 and 0.7 GPa, which are 50 and 100 times lower than the transformation pressures under hydrostatic compression and well below the phase equilibrium pressure of 2.45 GPa [7]. A new orthorhombic diamond phase was also found in carbon [7].

The most informative measurements were performed on the $\alpha \rightarrow \omega$ transformation in SPD-processed pure zirconium (Figure 31) [620]. A strongly pre-deformed sample reaches a critical microstructure and the maximum yield strength, which practically do not evolve during further deformation. In these experiments, radial distributions of pressure in each phase and in the mixture, and concentration of ω-Zr, all averaged over the sample thickness, as well as thickness profiles, were measured using X-ray diffraction and absorption. The minimum pressure for the strain-induced $\alpha \rightarrow \omega$ transformation, 1.2 GPa, was smaller than under hydrostatic loading by a factor of 4.5 and smaller than the phase equilibrium pressure by a factor of 3 [620].

In-situ Raman spectroscopy was utilized in [621,622] to detect different phase transformations in SDAC. In [621], the normal stress distribution at the boundary of sample and diamond was evaluated using Raman spectra of diamond. The distributions of all stress tensor components were determined in a diamond cell at the boundary with a sample using nitrogen-vacancy color centers and in the entire diamond using FEM [623]. A coupled experimental-theoretical-computational approach is developed in [624] (based on experiments [625]). The approach allowed to refine, calibrate, and verify models for elastoplastic behavior and contact friction with tungsten in diamond anvil cell up to 400 GPa, as well as to reconstruct fields of all components of stress and large plastic strain tensors in tungsten and diamond. These kinds of combined approaches are considered promising future direction in in-situ phase transformation studies.

8. Design and synthesis of new materials by severe plastic deformation

Rational design of new materials, including metallic alloys, has accompanied the development of mankind ever since the ancient civilizations started to improve materials beyond what was found in nature. In fact, a look into the history books shows that important periods in the development of civilization are often connected with the disruptive appearance of the use of a specific material that acted as game-changer, such as bronze or iron [11]. In many cases, metastability in terms of processing pathways or microstructure elements were strongly involved and still are involved, when new materials, such

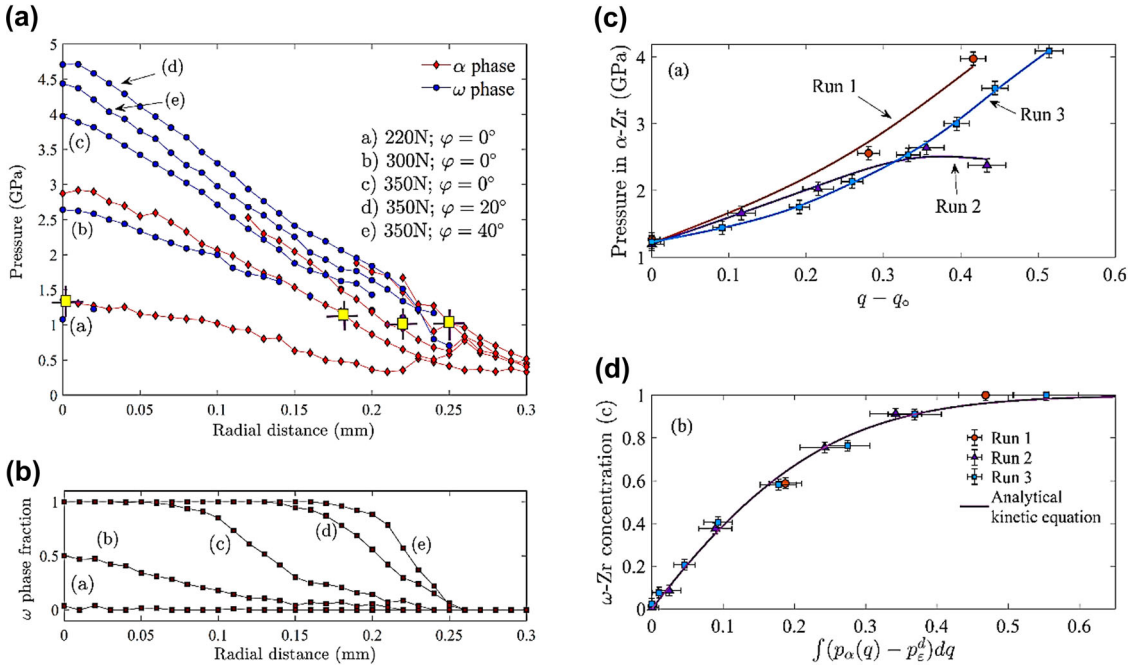

Figure 31. (a) The radial profile of pressure in α and ω phases of strongly pre-deformed zirconium and (b) phase fraction of ω phase at different load/shear conditions of shear (rotational) diamond anvil cell. Yellow squares correspond to the minimum pressure of 1.2 GPa at which ω-Zr was first detected at the center and periphery of the sample [620]. (c) Pressure in α-Zr accumulated plastic strain q - q_0 loading paths for three experimental runs and (d) kinetics of strain-induced α-ω phase transition [620]. Theoretically predicted plastic strain-controlled kinetic equation shown by solid line in (d) confirms that the kinetics is independent of the pressure-plastic strain loading path and plastic deformation q_0 at pressures below 1.2 GPa [449,617].

as, e.g. new high-strength steels or multi-principal element (high-entropy) alloys are designed [340,341]. However, many of the design rules as well as the processing strategies applied for materials design follow pathways that are close to local equilibrium, i.e. equilibrium thermodynamics is applied to assess the available phase space. With mechanical metallurgy, a new pathway was opened up to access regions of microstructures and alloy constitution that no-longer are restricted to states that are close to equilibrium. Powder processing and specifically so-called high-energy ball milling and later the use of evaporation-condensation methods have shown that highly unstable states, e.g. given by instable solid solutions deep in the spinodal regions of thermodynamically immiscible systems can be synthesized and retained for extended times even at temperatures well above ambient. Another example is given by the multitude of amorphous metallic materials that extend the regions accessible for glass formation by any method that employs rapid melt quenching [380,381].

Compared to these methods for creating materials that are not to be found in equilibrium phase diagrams, SPD processing provides specific advantages concerning the volume of materials that can be synthesized, concerning the shape and—also associated with that aspect—concerning the purity and concerning the amount of control of the relevant processing variables such as temperature, total strain or strain rate [1,20]. In addition to synthesis, SPD processing also serves to include grain boundary features and all defects of the crystal lattice into the materials design process. In this section, some aspects on material design and synthesis are reviewed with a focus on four recent trends: defect and grain boundary engineering by SPD, mechanical alloying by SPD, diffusion bonding by SPD, and metallurgical alchemy by ultra-SPD.

8.1. Grain boundary engineering by severe plastic deformation

Defect engineering via SPD processing significantly extends well-known concepts such as grain boundary engineering [626], since in addition to the total amounts of defects and their distributions, the local structures on the atomic scale are also susceptible to, and at least partially controllable by the SPD processing conditions. This concept has been brought forward early on by the authors of the earliest experimental results in the NanoSPD field suggesting that—concomitant to grain refinement—the atomic structure of grain boundaries is modified by SPD [1]. A theoretical model for the modified grain boundary structures based on the absorption of lattice dislocations

has been proposed [627], and the resulting high-angle grain boundaries with additional excess free energy density have been termed 'non-equilibrium' grain boundaries. According to these early works [1,627], these 'non-equilibrium' grain boundaries should be responsible for the enhanced mechanical properties of materials processed by SPD that exceed the property advances which are expected just on the basis of grain size changes alone. Since all grain boundaries in a single-component material represent non-equilibrium defects, this nomenclature is not fully appropriate [531], and these grain boundaries with enhanced excess energy densities [628] are better to be referred to as 'grain boundaries in a deformation-modified metastable state' or 'deformation-modified grain boundaries'.

Recently, structural and kinetic properties of deformation-modified grain boundaries and microstructures have been reviewed [629]. The high rates of defect creation during SPD at low homologous temperatures in combination with the intrinsic heterogeneity of deformation-induced processes and transformations creates complex hierarchies of microstructure elements and can be used for creating multi-modal microstructures [630] or instable states of matter [631] with very high kinetic stabilities and unique property combinations. The available data also substantiate the intrinsic heterogeneity of defect production and defect-induced modifications of the local interface structures in SPD-processed materials [632]. A fraction of high-angle grain boundaries attains a metastable, deformation-modified state which is characterized by enhanced atomic transport [633], increased (but localized to interfaces) elastic strain fields [93] and corresponding stresses.

Well-dedicated measurements of tracer diffusion using cobalt and silver atoms as sensitive probes of local structure modifications in ECAP-processed α-Ti revealed unambiguously the presence of localized excess volume in such boundaries [634]. The deformation-modified state occurred to be relatively stable—given that the room temperature conditions correspond to a relatively low homologous temperature. The key feature is the above-mentioned heterogeneity of excess volume localization inside deformation-modified grain boundaries, as schematically visualized in Figure 32, that enables highly enhanced rates of atomic transport and relatively reduced rates of relaxation of the deformation-induced modifications [628].

Co-deformation of dissimilar alloys opens up new perspectives into alloy design and grain boundary engineering, especially when multi-principal element alloys are co-processed [635]. Recently, a new composite material has been produced by HPT processing of equiatomic FCC CoCrFeMnNi and BCC HfTiZrNbTa alloys and

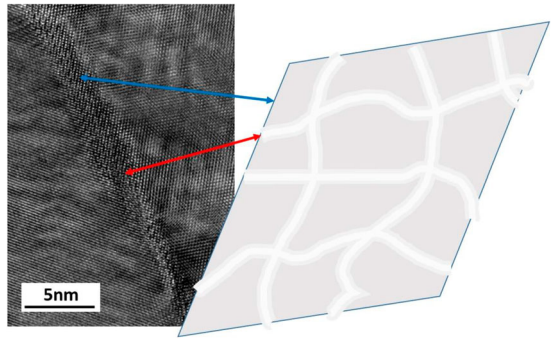

Figure 32. Schematic plane-view of a heterogenous distribution of the excess free volume in a deformation-modified high-angle grain boundary. The deformation-induced distortion is localized to channels (light gray) where the excess free volume exceeds the values typical for a relaxed high-angle grain boundary. The undistorted (relaxed) regions are colored in gray. Such areas in a high-angle grain boundary of copper processed by equal-channel angular pressing are specified for its cross-section view [628].

a mixture of nano-scale phases (the original, but now nanocrystalline FCC and BCC alloys, an amorphous phase and a BCC alloy strongly alloyed by 3d elements, mainly by Ni) has been formed. The interphase boundaries were found to play a critical role in the partial amorphization of the microstructure, since similar processing of solely FCC or BCC alloys never resulted in the appearance of amorphous regions [635]. All these observations together with the occurrence of grain boundary segregation, which was discussed in an earlier section, confirm that the SPD processing can be used for engineering the fundamental properties of the boundaries and their impact on microstructure and phase evolution.

8.2. Mechanical alloying by severe plastic deformation

The SPD process enables the generation of innovative metastable nanomaterials and nanocomposites with compositions and phase constituents beyond the equilibrium phase diagram and with fewer thermodynamic restrictions. These novel metastable materials and nanocomposites can be synthesized by inducing a multitude of different phase transformations and phase formation reactions during deformation. This includes the dissolution of phases [636,637], amorphization of crystalline phases [638], crystallization of nanocrystals in amorphous matrices [639], and the synthesis of metastable phases such as supersaturated solid solutions or phase separations [640–642]. The HPT method is a promising SPD process for mechanical alloying. As initial materials for HPT processing, coarse-grained multiphase alloys, powder blends of different elements or any other combination of solid materials can be used. One

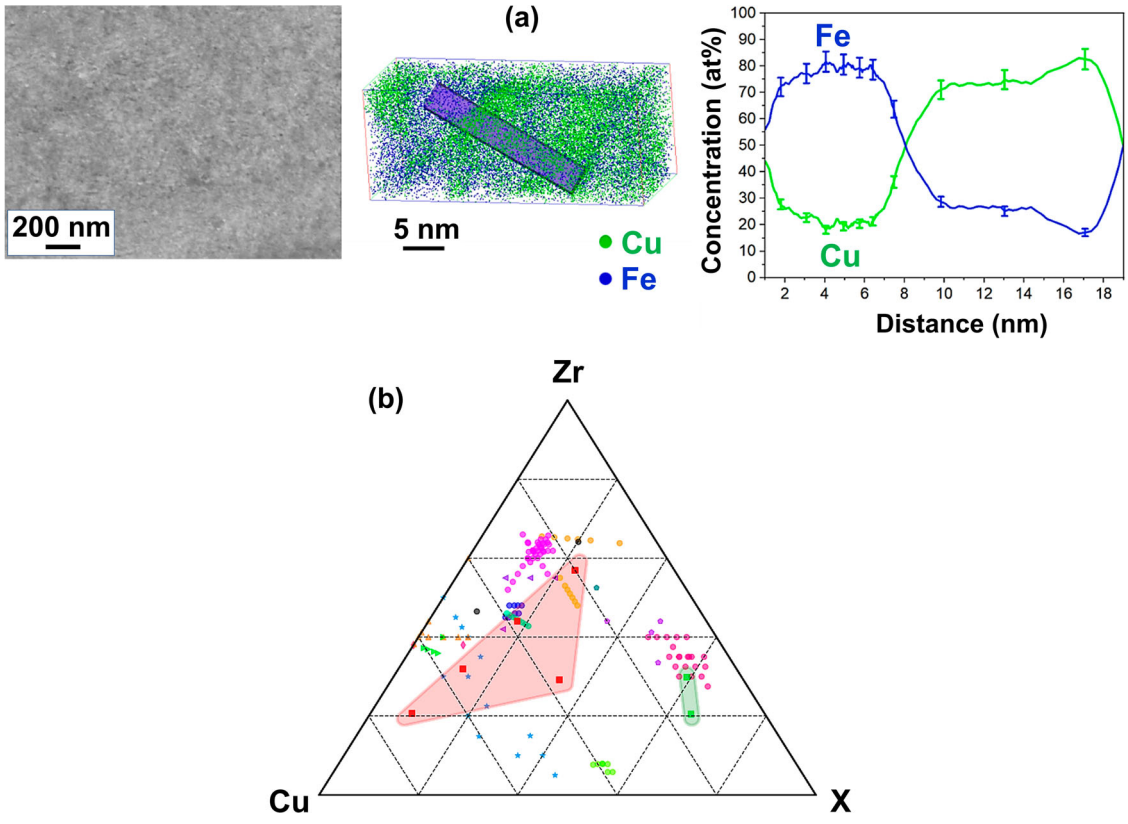

Figure 33. (a) Scanning electron microscopy image of a nanocrystalline Cu - 53 at% Fe material after high-pressure torsion deformation (right) and three-dimensional reconstructed volume by atom probe tomography (center) with copper and iron concentration profiles across a Cu/Fe interface (left) [641]. (b) Chemical composition of bulk metallic glass composites (composites of Zr-based metallic glasses with copper: red field; and composites of Zr + Ni metallic glass: green field) obtained by high-pressure torsion processing [326] in comparison with data points reported in literature [645–659]. All elements except copper and zirconium are summed up as X in (b).

advantage of mechanical alloying by HPT is that the finally obtained microstructures are not producible by classical metallurgical ways. Another advantage is that bulk materials are readily obtained by cold consolidation.

One example is shown in Figure 33(a) for the Cu - 53 at% Fe nanocomposite synthesized by the HPT process [641]. Despite immiscibility of the Fe-Cu system, about 25 at% of copper are dissolved in the iron phase and about 20 at% of iron are dissolved in the copper phase [641]. In other recent studies, the generation of bulk metallic glass composites from starting powders was reported by the HPT process, in which atomic mixing between the constituent phases takes place [326,644,645]. Moreover, direct synthesis of bulk nanocrystalline high-entropy alloys from the constituent powders using deformation-induced mechanical alloying was reported [643–645]. As an example, the chemical compositions of different bulk metallic glass composites synthesized by the HPT process are shown in Figure 33(b) compared to compositions from the literature [326,645–659].

During the past 20 years, although the mechanisms of strain-induced mechanical mixing, metastable phase formation, and amorphization or crystallization during the HPT process have been investigated, the detailed mechanisms are not yet fully explained [326,367,568,644,660–662]. However, the synthesis of metastable materials and nanocomposites by HPT leads to materials with extraordinary mechanical and physical properties. The nanocrystalline or UFG microstructures of these materials result in advanced mechanical properties. Equally important is a high microstructural stability of these materials at elevated temperatures. The thermal stability of supersaturated solid solutions has been found to be significantly higher compared to pure metals because decomposition or phase separation is thermodynamically favored before grain growth sets in [663]. Additional annealing of these HPT-synthesized supersaturated alloys can lead to phase separation and formation of nanocrystalline composites with a high thermostability [663].

A current main research trend is to investigate the physical properties (i.e. magnetic, electric, radiation resistant, etc.) of these novel HPT-synthesized materials. An overview on the properties of these novel materials and nanocomposites can be found in [664]. It has been shown that the magnetic properties of hard magnetic and

soft magnetic materials can be tailored using the above-mentioned phase transformations/formations. Furthermore, materials with good electrical conductivity in combination with excellent strength for electrical applications can be processed. A new approach is to use the HPT method to synthesize porous materials and nanocomposites with efficient resistance to radiation. Deformation-induced mixing and phase formations have also been used to design innovative hydrogen storage materials with unique compositions and microstructures as well as enhanced kinetics.

To summarize, the SPD process can be used as an innovative solid-state processing route for the synthesis of novel materials and nanocomposites with tailored mechanical and physical properties with high potential for a wide range of future applications.

8.3. Diffusion bonding by severe plastic deformation

In response to current demands for light-weight materials, introducing functionality in bulk metals, and developing efficient manufacturing processes, general metal processing techniques invariably experience an upper limit on the enhancement in mechanical properties for both functional and structural materials. This urges innovative approaches of achieving superior physical and mechanical properties in bulk solids. Bonding dissimilar metals is one approach to achieve both enhanced mechanical properties and functionality.

Cladding-type metal working was utilized earlier by pressing or rolling dissimilar sheet metals together under a high pressure as in the roll-bonding process [665–668]. Further extension of the approach was made by applying the ARB process for producing multi-layered microstructures with grain sizes finer than after conventional rolling [669–675]. However, metal processing by rolling involves an essential drawback of the anisotropic mechanical responses depending upon the rolling direction and the sample thickness direction [676]. The FSP technique was used as another solid-state bonding technique for high-quality welding of dissimilar aluminum and magnesium alloys [677].

The HPT method was actively used in the past years as an alternative approach for the synthesis of nanograined bulk hybrid metal systems by direct mechanical bonding of dissimilar metal discs. In practice, this diffusion bonding process was simply developed by modifying the sample set-up procedure in HPT [526,631,678,679] with applying several different metal combinations as shown in Figure 34(a) [679]. This type of HPT processing was conducted on Al/Cu, Al/Mg, Al/Fe, Al/Ni, Al/Ti, Al/Mg/Cu/Fe/Ti, Ag/Cu, Ag/Ni, Cu/Ta, Cu/ZnO, Fe/V, V-Ti-Cr/Zr-Nb, Zn/Mg, and Zr/Nb systems [678–683]. Microstructural evaluations of these systems confirmed the capability of the HPT method for rigid bonding with severe mixing of the dissimilar metals and ultimately the formation of metal matrix nanocomposites [680] or metastable alloys [681,682]. An example is shown in Figure 34(b) for an Al/Mg/Al system which shows high hardness [683]. Demonstrating several improved functionalities including specific strength, the HPT process can provide a significant contribution to current developments not only in diffusion bonding, but also in welding and mechanical joining technologies.

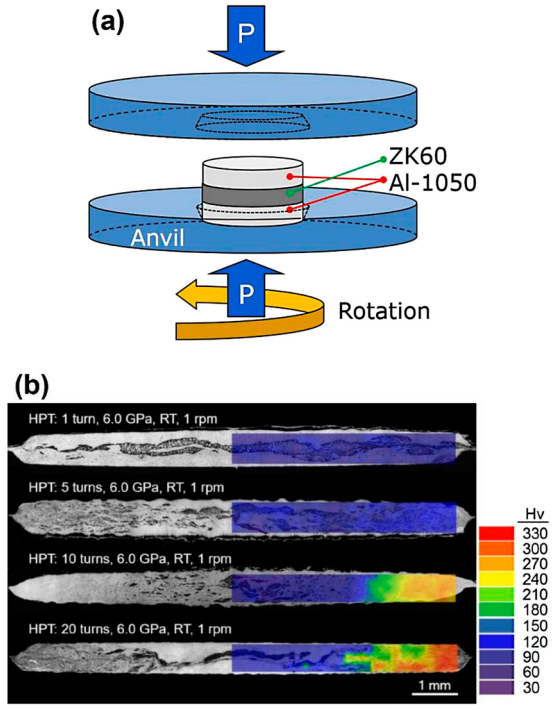

Figure 34. (a) Schematic illustration of the sample set-up for diffusion bonding through high-pressure torsion processing to produce an Al/Mg/Al composites [679]. (b) Optical micrographs and hardness distribution for an Al/Mg/Al system after high-pressure torsion for 1, 5, 10 and 20 turns [683].

8.4. Metallurgical alchemy by ultra-severe plastic deformation

It is now well established that the structural and microstructural features of severely deformed materials finally saturate to the steady after initial changes at the early stages of straining [99,451,460,684]. As mentioned in earlier sections, the first reliable experimental evidence for the occurrence of steady state at large strains was reported by Bridgman using the HPT method [19]. Despite the current agreement on the occurrence of steady state, the SPD processes are mainly conducted for

strains in the range of 10 or shear strains in the range of 100 [1–3]. Several studies, however, focused on the application of extremely large shear strains up to 100,000 using the HPT method and found that new phenomena can occur at such large strains [9,114]. Since several materials started showing new behaviors at strain levels over 1,000, a new terminology of ultra-SPD was defined for the SPD processes in which the shear strains over 1,000 are introduced to a work piece [9,114]. Some of the main findings reported by the application of ultra-SPD are summarized below.

- Appearance of new levels of steady-state microhardness in a few metals [9] and several multiphase alloys [114]. The absence of a real steady state at large strains in a few pure metals has led to a suggestion that some new deformation mechanism may exist beyond the stage V of deformation [685].
- Low-temperature atomic-scale elemental mixing in miscible systems or immiscible system with low heat of mixing and the formation of bulk nanostructured binary alloys (e.g. superconductors [686], hydrogen storage materials [687] and biomaterials [688]), binary intermetallics [689–691] and ternary intermetallics [692].
- Atomic-scale elemental mixing in the binary [693–696] and ternary [114,327,697] immiscible systems with high heat of mixing and formation of new BCC, FCC and HCP phases. Some of these immiscible systems such as Mg-Ti, [693], Mg-Zr [695] and Mg-Hf [696] are thermodynamically immiscible even in the liquid form.
- Continuous grain refinement below the apparent steady-state grain sizes, particularly in the immiscible systems [114,698].
- Achievement of ultrahigh strength and high plasticity, which critically depends on the chemical composition and microstructural features [690,692].
- Room-temperature superplasticity in a two-phase Mg-Li alloy [547] as well as in a two-phase Al-Zn alloy [699] at low homologous temperatures of 0.35-0.36.
- Development of new age-hardenable Al-based alloys with high thermal stability from immiscible system such as Al-Fe [698], Al-Ca [535], Al-Zr [700] and Al-La-Ce [701].
- Development of advanced superconductors [686].
- Development of new materials for hydrogen storage [327,696,697,702].
- Development of new functional high-entropy alloys for mechanical applications, biomedical applications, hydrogen storage and photocatalysis [703].

Figure 35 shows the microstructure of several materials synthesized from elemental powders by ultra-SPD: (a) nanotwinned TiAl (binary miscible system) [690], (b) Ni_2AlTi with $L2_1$ ordering (ternary miscible system) [692], (c) Nb-Ti with BCC structure and nanoclusters of BCC-Ti (immiscible binary system with low heat of mixing) [686], (d) MgZr with new BCC and FCC phases (immiscible binary system even in the liquid form with high heat of mixing) [695] and (e) Mg_4NiPd with new BCC-type phase (ternary immiscible system) [327]. The TiAl and Ni_2AlTi materials in Figures 35(a and b) exhibit high strength and high plasticity [690,692]; the Nb-Ti alloy in Figure 35(c) shows high strength and superconductivity [686] and new MgZr and Mg_4NiPd phases in Figures 35(d and e) exhibit hydrogen storage performance at room temperature [327,695]. These results suggest that processing of materials by ultra-SPD not only provides new insights into the behavior of materials at extremely large shear strains, but also provides a new route to synthesize advanced materials with exceptional mechanical or functional properties.

9. Mechanical properties of materials processed by severe plastic deformation

Mechanical properties are the most investigated properties of severely deformed materials. The effect of deformation strain on hardening has been a well-known fact since the birth of ancient metal forming. There are scientific descriptions about the strain hardening at least in the eighteenth century, when the German-Russian scientist Bulffingeri (Bilfinger) proposed a power-law relationship between strength and strain similar to the well-known Hollomon equation [704,705]. In the 1930s, Bridgman examined the shear strength by torque measurements during the HPT process and reported that the power-law stress-strain relationship is not valid at high strains and the strength finally saturates to a steady state [19]. He also reported that pure lead shows unusual strain softening rather than expected strain hardening [49]. The occurrence of steady state at large strains was confirmed later by other scientists by measuring the hardness and tensile properties [14,15].

Nowadays, microhardness measurement is a quick mechanical characterization test to examine the severity of deformation and the occurrence of steady state in metals and alloys processed by SPD [706]. Three main hardness-strain behaviors were reported for pure metals, although their behaviors depend on the purity level and processing temperature [707,708]. (i) For metals with low melting temperatures such as indium, lead, tin and zinc, hardness decreases with increasing strain (despite grain refinement) and saturates at large strains. The steady-state hardness of UFG aluminum with an ultrahigh purity of 99.9999% is also below the

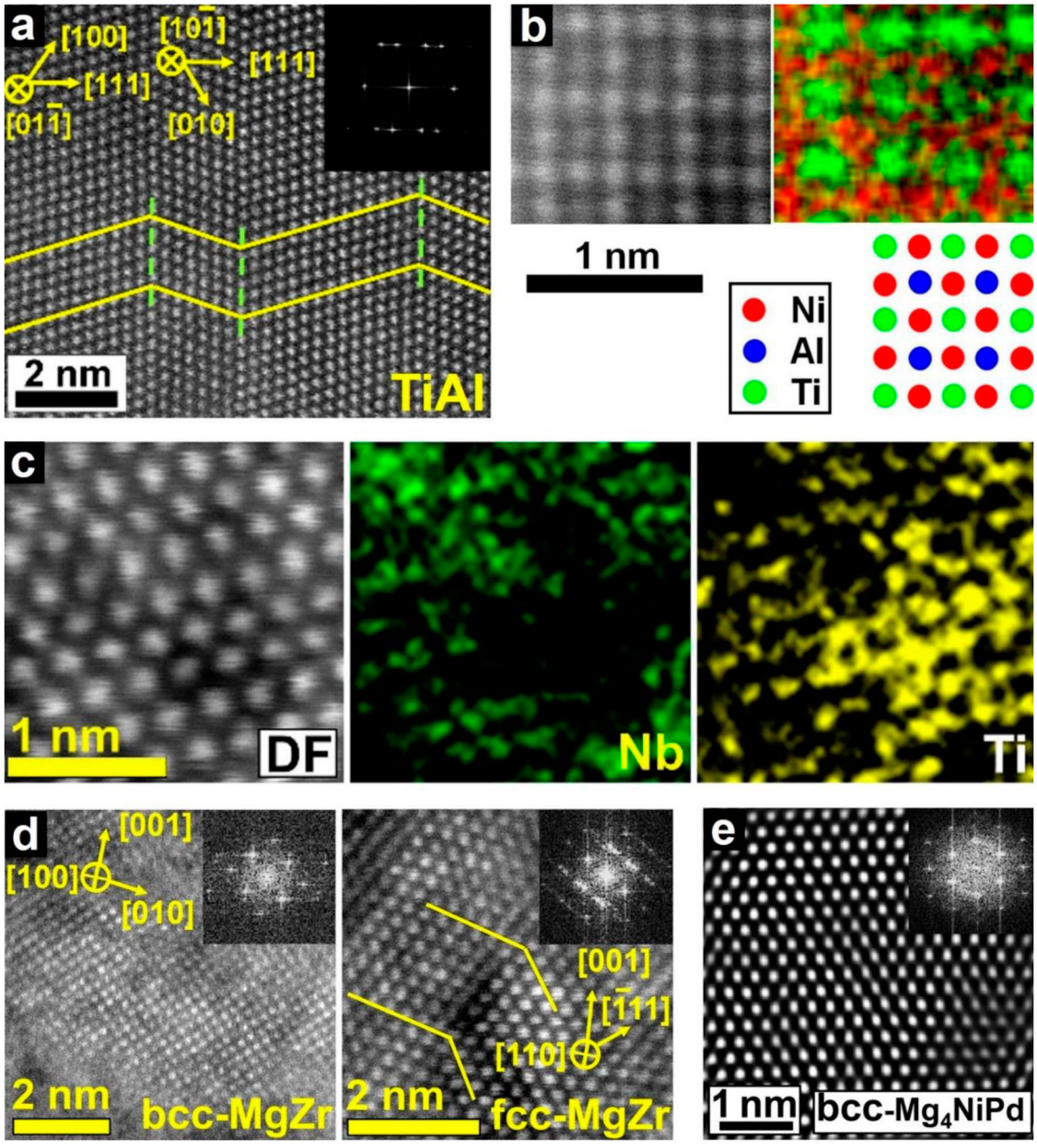

Figure 35. High-resolution lattice mages of several functional materials synthesized by ultra-severe plastic deformation via high-pressure torsion method: (a) nano-twinned TiAl with FCC structure [690], (b) Ni_2AlTi with $L2_1$ ordering [692], (c) Nb-Ti superconductor with BCC structure [686], (d) MgZr hydrogen storage material with BCC and FCC structures [695], and (e) Mg_4NiPd hydrogen storage material with BCC structure [327].

hardness of coarse-grained sample material [709]. (ii) For metals with moderate melting temperatures such as pure aluminum and pure magnesium, the hardness increases at the early stages of straining and, after passing through a maximum, decreases to a steady-state value above the hardness level for coarse-grained materials. (iii) For metals with high melting temperatures, the hardness typically increases until it saturates at large strain. The latter hardness-strain behavior is observed in most of the SPD-processed metals and alloys [707, 708].

In addition to hardness measurements, examination of severely deformed materials by bending, compression and tensile tests shows that these materials usually exhibit superior strength due to the presence of large fractions of lattice defects as well as due to small grain sizes (causing the Hall-Petch effect) [1,2]. Beside a high strength, the plasticity of these materials is usually within an acceptable range [710], although there are numerous attempts to enhance the uniform ductility of these materials [711] or even to achieve room-temperature superplasticity [712]. Fracture toughness [713], wear resistance

[714], fatigue resistance [715] and creep resistance [716] are other mechanical properties of these materials which have been investigated in recent years. In this section, some of the main findings on mechanical properties are summarized.

9.1. High strength and high ductility

Nanomaterials show high strength, but their uniform elongation (i.e. ductility) is usually limited due to their poor strain hardening capability. In 1981, Segal *el al.* reported that metals severely sheared by ECAP can show a good combination of high strength and high ductility [20]. Similar issue was later reported by Valiev *et al.* as a paradox of strength and ductility [710]. Despite these interesting reports, nanomaterials processed by SPD usually show low uniform elongation. There have been significant attempts in recent years to enhance the strength of nanomaterials without reducing their ductility by introduction of nanotwins [717] and stacking faults [718], formation of bimodal structures [719], controlling precipitation [720], grain-boundary engineering [721], development of heterostructures [194], lattice softening [722], generation of gradient structures [723], etc. Details of these strategies were reviewed in an earlier publication [711], but two strategies are described below: (i) lattice softening, which resulted in some of the best combination of ultrahigh strength and high ductility ever reported [724], and (ii) introduction of gradient structure by surface-SPD which has a high potential for commercialization [725].

9.1.1. High strength and high ductility in lattice-softened ultrafine structures

Generally, high-strength metallic materials have poor strain hardenability, which leads to plastic instability at early stage of plastic deformation, poor ductility and premature failure. It was reported that a lattice-softened Ti-based alloy, which is known as Gum Metal, also has poor strain hardenability, which leads to intense strain localization [722]. However, such strain localization is accommodated by local plastic deformation in Gum Metal and does not result in premature failure. The origin of this ductile mechanism has been attributed to lattice softening, where the elastic constant C' goes to a very small value [722]. Recently, several reports have been made on lattice-softened Fe-Ni-based alloys with high strength and good ductility processed with SPD [726–734]. These alloys were designed based on the knowledge obtained from SPD and Gum Metal [722,724].

The SPD-processed Fe-Ni-Co-Ti and Fe-Ni-Al-C alloys were reported to have ultrahigh strength along with good tensile ductility and their balance of strength and ductility is better than that in conventional high-strength steels [726–732]. The phase stability of γ phase in these alloys has an important role on the microstructural development during the SPD process as well on the deformation behavior in the subsequent mechanical testing. The untransformed γ phase has a potent capability for plastic deformation where strain-induced transformation and deformation twinning can be expected to occur during mechanical tests after SPD processing. Simultaneous activation of these deformation mechanisms during plastic deformation is a common feature in the lattice-softened alloys [733,734], although the exact mechanism underlying the effects of phase stability on the deformation behavior and ductility have not been well understood yet.

The relation between the ultimate tensile strength and tensile elongation in several SPD-processed Fe-Ni-Al-C alloys is plotted in Figure 36(a) [724]. Some of the alloys have ultimate tensile strengths over 2 GPa and total elongations up to 26%. It is worth to compare the performance of these lattice-softened alloy with famous steels with high strength and large uniform elongation, in which the capacity of strain hardening is improved by transformation-induced plasticity, TRIP, or twinning-induced plasticity, TWIP. Figure 36(a) compares the strength and ductility of SPD-processed Fe-Ni-Al-C alloy with the reported trade-off curve for steels with high strength and high ductility. The lattice-softened Fe-Ni-Al-C alloy shows excellent combination of the strength and ductility compared to the TRIP and TWIP steels.

Figure 36(b) shows the effect of equivalent strain during the SPD process on the ultimate tensile strength of Fe-Ni-Al-C alloy [724]. Here, the equivalent strain of around 2 can lead to a strength of 2 GPa, and the further increase in equivalent strain gradually improves the strength up to 2.5 GPa. This gradual increase in UTS might be attributed to the strain-induced transformation from γ to α' which can be achieved only in the heavily-strained specimens after 50 turns of HPT. Taken together, these results show that combination of SPD process and lattice softening concept can be an effective solution to overcome the problem of poor ductility of nanomaterials.

9.1.2. High strength and high ductility in gradient structures

Poor uniform elongation (i.e. ductility) of nanocrystalline and UFG metallic materials greatly hinders their applications, despite their high strength [735,736]. In most cases, material failures usually start from surface, and thus, surface modification is crucial to improve the mechanical properties of metallic materials. K. Lu and J. Lu proposed the SMAT process in 1999, which is one of the most effective surface modification methods [91]. As

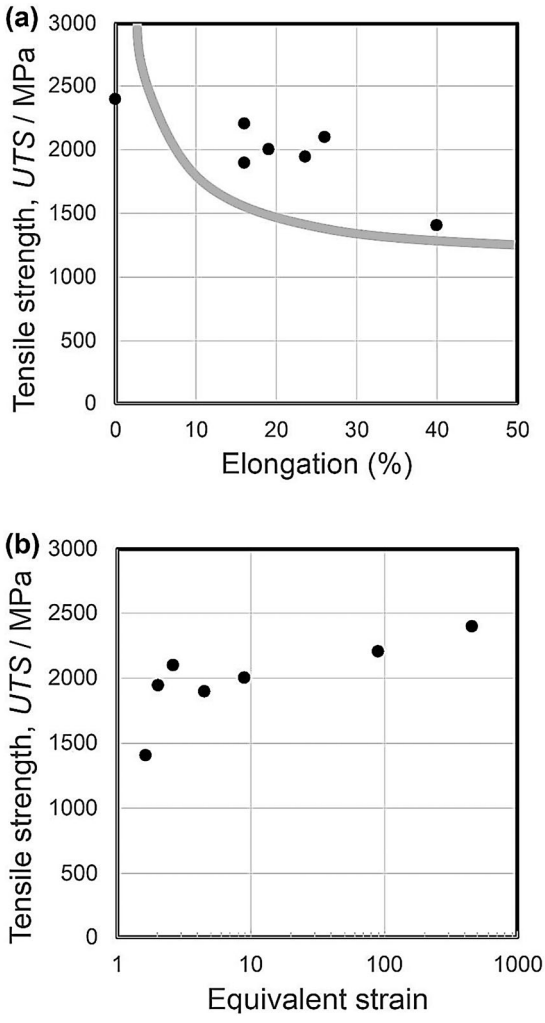

Figure 36. (a) Ultimate tensile strength versus uniform elongation for severely deformed Fe-Ni-Al-C alloy in comparison with trade-off curve reported for steels with high strength and high ductility [724,731]. (b) Effect of equivalent strain on ultimate tensile strength of Fe-Ni-Al-C alloy processed by severe plastic deformation [724].

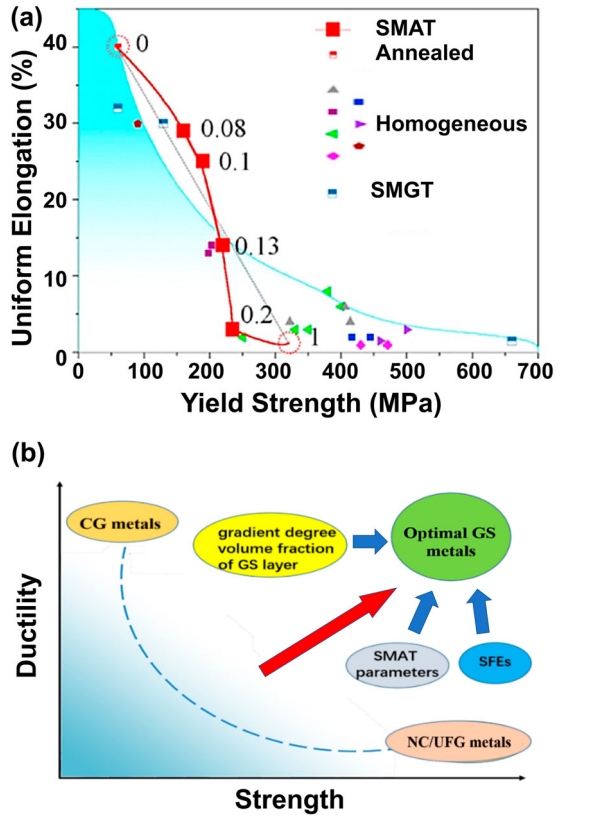

Figure 37. (a) Strength and ductility of gradient-structured copper processed by surface mechanical attrition treatment (SMAT) and surface mechanical grinding treatment (SMGT) compared with copper samples with homogenous structure [725]. (b) Basic factors affecting correlation between strength and ductility of gradient-structured materials [711,725,741–743].

discussed in an earlier section, the method can be used to manufacture gradient-nanostructured materials with no interfaces between the surface and the coarse-grained matrix [737]. The gradient-nanostructured metallic materials fabricated by SMAT exhibit a superior combination of strength and ductility compared with conventional homogeneous materials [271]. It is generally believed that the high strength of the SMAT-processed metallic materials owes to the surface fine-grain strengthening [738]. Whereas the improved ductility can be attributed to coarse-grained matrix and the superior work hardening ability of the gradient-structured materials [737].

Figure 37(a) compares the correlation of strength and ductility for gradient-structured copper processed by SMAT and surface mechanical grinding treatment in comparison with homogenous copper samples [725]. The gradient-structured copper shows a better combination of strength and ductility compared to the trade-off trend for homogenous copper. In general, the main factors affecting the mechanical properties of gradient-structured materials include processing parameters [260,294], volume fraction of gradient-structured layer [739], gradient degree [723] and stacking fault energy [295,740]. As schematically summarized in Figure 37(b), the key point to obtain an excellent combination of strength and ductility in gradient-structured materials is how to control and optimize the above factors further rationally [711,741–743].

9.2. Fracture toughness

Possible applications of SPD-processed nanostructured materials can be found in the mechanical, biomedical or energy sectors [744–746]. The reliability of these nanostructured materials in service is strongly determined by the resistance against crack growth, which can be

described by their fracture toughness [747]. Flaws and crack-like defects are permanently present in engineering materials and therefore threaten the structural integrity. This is widely known in materials science and has led to a damage tolerant design especially for safety critical structural components. However, the fracture toughness has also great significance apart from designing components. During manufacturing of components made from SPD-processed materials, a sufficient fracture toughness is also required in order to prevent failure during the machining. The same issue arises for functional applications, where materials are not primarily subjected to high mechanical loads but still require a certain mechanical integrity during production or later use. Lastly, the fracture resistance is even an issue during SPD processing. The formation of cracks, which often defines the deformability of a materials in a certain SPD process, is controlled not only by the characteristic stress state of the process but also by the resistance of material against crack propagation, i.e. by fracture toughness. Therefore, the fracture behavior has always great significance in the NanoSPD field.

Compared to other research topics in the NanoSPD community, the research into the fracture behavior is quite young. Only within the last 15 years, several research groups have started to investigate the fracture behavior of SPD-processed materials in detail [748–753]. One major problem why this research area is quite small is connected with the limitations of the well-established fracture mechanics concepts. For example, linear elastic fracture mechanics requires certain minimum specimen dimensions.

The most cohesive insights into the fracture behavior of UFG materials can be gained by materials processed by HPT. At the first sight, one can think that this SPD technique is fairly unsuitable for such studies; however, the HPT method bears some insuperable advantages for fracture mechanics questions compared to other techniques. One main advantage of HPT is that the high hydrostatic compressive stress can prevent the formation of cracks or pores during deformation. In addition, it can be also proven that the general tendencies that were found in the HPT-processed materials can also be found in materials processed by other SPD processes showing a high potential for future industrial use [754].

One of the main observations of numerous studies is that the fracture toughness can show pronounced differences among SPD-processed materials [713]. A basic classification into ductile and brittle SPD-processed materials can be principally made by considering the behavior of the coarse-grained counterparts. However, it is impossible to identify any grain-size dependent trends covering a large grain size regime, as for example, it is well established for the yield strength of materials. This can be related to the fact that the fracture properties display quite often a highly anisotropic behavior and a transition in the fracture type when the grain size become very small [750,755]. The extent of anisotropy clearly depends on the principal fracture type and is more pronounced for the brittle type in which one crack propagation direction exists where primarily intercrystalline fracture along the elongated microstructure is found (Figures 38a and b) [756]. In contrast, for the same crack propagation direction in the ductile type, micro-ductile fracture prevails [757]. Up to now, there is still a gap in understanding the occurrence of intercrystalline fracture. So far, intercrystalline fracture seems not necessarily to be the sole effect of grain boundary embrittlement and could also have intrinsic reasons [750].

The fracture anisotropy in SPD-processed materials, however, has also beneficial effects. It enables exceptional combinations of fracture toughness and strength in some testing directions (Figure 38c), which are difficult to be achieved in conventional high-strength materials [756]. A recent example for this fact was found in steel wires possessing with almost 7 GPa strength (one of the highest achievable strength of engineering materials) and high fracture toughness at the same time [758]. Analogies to this observation can be found in nature designed materials such as wood where exceptional properties are only enabled by having a distinctive anisotropy in the mechanical properties [759]. An intelligent design of components by adapting the anisotropy of the material properties in the design, can allow to exhaust the full potential of these ultra-strong and damage tolerant SPD-processed materials in the future.

9.3. Superplasticity

Superplasticity is now well established as a flow mechanism in polycrystalline materials where the elongations to failure in tensile testing are at least 400% [760]. The first example of true superplastic flow was in classic experiments conducted in England over 80 years ago when elongations of up to 1950% were recorded in a Bi-Sn alloy [761]. Recent experiments showed that superplasticity occurs in this alloy through grain boundary sliding with maximum sliding occurring on the Bi-Bi interfaces [762]. It is now established that superplastic flow requires a very small grain size, typically below $\sim 10\,\mu m$, and a testing temperature of at least $\sim 0.5\ T_m$ where T_m is the absolute melting temperature [763]. Processing by SPD provides opportunities for achieving exceptional grain refinement, often to the submicrometer or even the nanometer range, and this suggests the

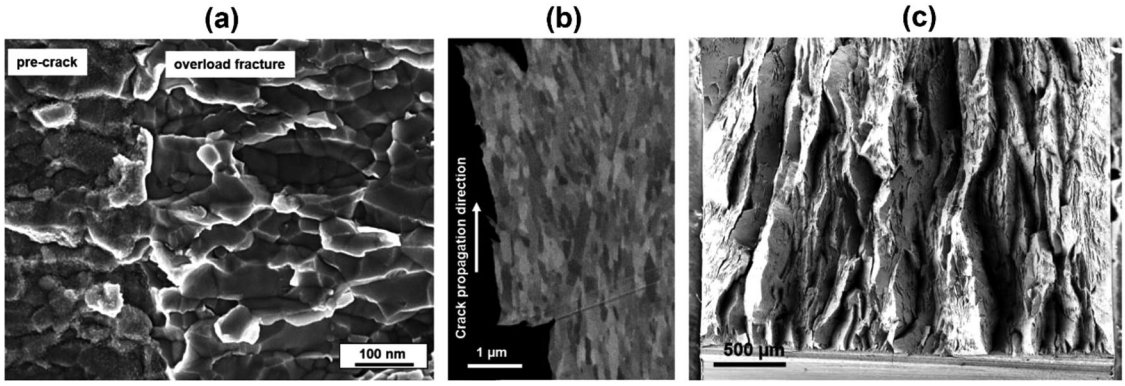

Figure 38. Typical fracture features of nanostructured metals exemplified with iron processed by severe plastic deformation. (a) Intercrystalline crack propagation which is the prevalent failure type in many severely deformed metals. (b) Crack runs along the elongated grain structure. (c) Perpendicular to crack plane, totally different failure type with numerous delaminations is found, inducing a substantially higher fracture toughness [756].

potential for using SPD in order to obtain excellent superplastic behavior [764].

9.3.1. Enhanced superplastic elongation

The first example of the use of SPD for the processing of superplastic alloys was in 1988 where it was shown that the materials contained arrays of boundaries having high angles of misorientation [16] and this contrasts with other processing techniques, such as extrusion or rolling, where the microstructure consists of subgrains having boundaries with low angles of misorientation. Since the strain rate in superplasticity varies inversely with the grain size raised to a power of 2, it appears that SPD-processed materials may exhibit superplastic flow at exceptionally high strain rates. This was first demonstrated in 1997 where the measured tensile elongations corresponded to high strain rate superplasticity as shown in Figure 39(a) for an Al-based alloy [765]. Later experiments provided many excellent examples of superplastic flow after SPD processing including an exceptional elongation of 3050% in a commercial magnesium alloy as shown in Figure 39(b) [766]. If SPD processing is used in superplastic forming operations, the materials should form rapidly at elevated temperatures. This was first confirmed in 2000 where an Al-Mg-Sc alloy was inserted in a gas-pressure forming facility and successfully formed into a uniform dome in a time of 60 s [767].

By collecting large numbers of results on aluminum and magnesium alloys, and then plotting the grain size and temperature compensated strain rate against the normalized stress, it was shown that the results are in excellent agreement with the strain rate predicted from the theory for conventional superplastic flow [768]. Therefore, new models of sliding are not required [769].

Very recent experiments used the processing procedure of tube high-pressure shearing [148] in order

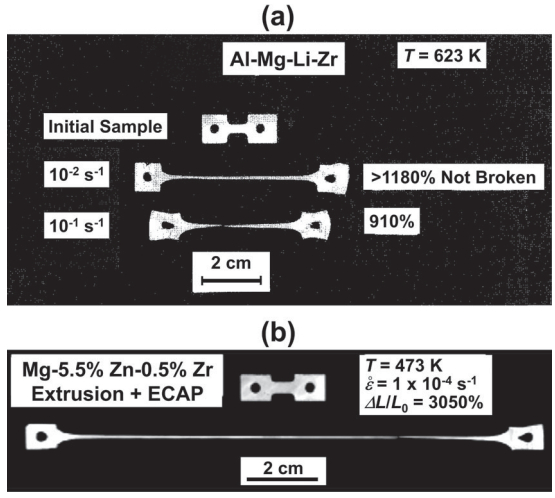

Figure 39. (a) The first example of high strain rate superplasticity in an Al-based alloy processed by equal-channel angular pressing [765]. (b) Exceptional superplasticity in a Mg-based alloy processed by equal-channel angular pressing [766].

to prepare Pb-Sn alloys for subsequent tensile testing. The results demonstrated the ability to achieve remarkable superplastic elongations at room temperature even when testing at a reasonably rapid initial strain rate of 1.0×10^{-3} s^{-1} [770]. Thus, the tests gave a tensile elongation of $\sim$1870% which exceeds, by more than three times, the earlier maximum elongation of 600% recorded for Pb-Sn alloys under these testing conditions [771].

9.3.2. Room-temperature superplasticity

Achieving superplasticity at high temperatures and at very low strain rates is the most important disadvantage of superplastic forming for industrial applications [772]. For example, superplastic behavior at low strain rates means that each part can be produced in a long

time (such as 30 min) by superplastic forming technology [773,774], which increases the manufacturing cost. Superplastic forming at high temperature also increases the cost and can negatively influence the properties of the final product. Therefore, it is important to achieve superplastic behavior at low temperature and high strain rates in order to enhance the applications of superplasticity, and to reduce the cost of superplastic forming.

High-temperature plastic flow, including superplasticity, can be expressed by the constitutive creep equation in the following form [775]:

$$\dot{\varepsilon} = \frac{ADGb}{kT}\left(\frac{b}{d}\right)^{p}\left(\frac{\sigma}{G}\right)^{n} \quad (2)$$

where $\dot{\varepsilon}$ is the strain rate, A is a dimensionless constant, D is the diffusion coefficient ($D = D_o\exp(-Q/RT)$, where Q is the activation energy, D_o is a frequency factor, R is the gas constant and T is the absolute temperature), G is the shear modulus, b is the Burgers vector, σ is the flow stress, k is the Boltzmann's constant, d is the grain size, n is the stress exponent and p is the inverse gran size exponent. This equation indicates that any decrease in the grain size of the material increases the strain rate and decreases the temperature at which the superplastic behavior occurs [776,777]. The SPD methods like ECAP, HPT and FSP have been efficiently used to attain significant grain refinement to achieve low-temperature superplasticity in some classes of materials [778–781]. Furthermore, The SPD-induced formation of UFG microstructure with special grain boundary features resulted in decreasing the temperature for superplastic behavior to room temperature, as an extreme example of low-temperature superplasticity [712].

Excellent room-temperature superplasticity was reported in severely deformed Zn-Al alloys including the eutectoid Zn - 22% Al [782–786], eutectic Zn - 5% Al [787] and quasi-single phase Zn-Al alloys having aluminum content up to 1.1% (all in wt%) [788], as shown in Figure 40(a). Superplastic elongation of these alloys was stated to be dependent on some microstructural parameters like size and shape of the grains, homogeneity of the phase distribution throughout the microstructure and chemical composition of the phase/grain boundaries. Particularly phase composition has a significant effect on the room-temperature superplastic elongation in these alloys. Although Zn - 0.3% Al had the largest grain size among all Zn-Al alloys, the highest superplastic elongation was achieved in this alloy due to the effective grain boundary sliding mainly in the boundaries of Zn-rich η phase grains. The lowest superplastic elongation was reported in the Zn - 22% Al alloy, while the Zn - 5% Al alloy showed a moderate superplastic elongation (Figure 40a).

It was recently shown that decreasing the superplasticity temperature is also possible by enhancing the grain boundary diffusion of difficult-to-slide boundaries with modification of the chemical composition of the boundaries via SPD processing [547,699]. Processing of an Al - 30 at% Zn alloys for large number of HPT turns resulted in high zinc concentration at the α/α boundaries (α: Al-rich phase). Formation of a few layers of zinc atoms at the α/α boundaries enhanced the grain-boundary diffusion in these boundaries and made them favorable for grain boundary sliding at room temperature. Hence, the HPT-processed alloy exhibited a high superplastic elongation of 480% at room temperature (Figure 40b) [699]. Similarly, for a dual-phase Mg - 8 wt% Li alloy with Mg-rich α phase and Li-rich β phase, large number of HPT turns maximized the segregation of lithium atoms at the α/α boundaries and lowered their grain-boundary diffusion to levels comparable with the β/β and α/β boundaries [789,790]. Such a segregation of lithium atoms at the α/α boundaries enhanced the grain boundary sliding and resulted in high superplastic elongation of 440% at room temperature (Figure 40c) [547]. All these studies confirm the potential of SPD methods in fabrication of new room-temperature superplastic materials, as discussed in detail in a recent review paper [712].

9.4. Creep behavior

Creep is the time-dependent component of plastic deformation which occurs usually under conditions of constant load and/or stress and at a constant temperature. Although creep can occur at all temperatures, it becomes important at elevated temperatures (usually higher than $\sim 0.4T_{\mathrm{m}}$, T_m: absolute melting temperature) where diffusional processes occur fairly fast. An investigation of high temperature creep in metallic materials was initiated early in the last century [791], however, very extensive theoretical and experimental research of creep started after World War II. Many dislocation models and theories of creep have been proposed to explain creep behavior observed experimentally [792]. At the present, it is generally accepted that materials with conventional grain sizes may be strong or ductile but there are rarely both. Nevertheless, the various published results of creep behavior in relation to mean grain size differ significantly and are frequently contradictory.

Processing through the application of SPD is now an accepted procedure for producing bulk UFG materials (grain sizes $<$ 1μm) [793]. The UFG materials are characterized by enormous extension of internal interfaces giving an opportunity to study new areas that were not feasible in earlier creep studies. Some of the first

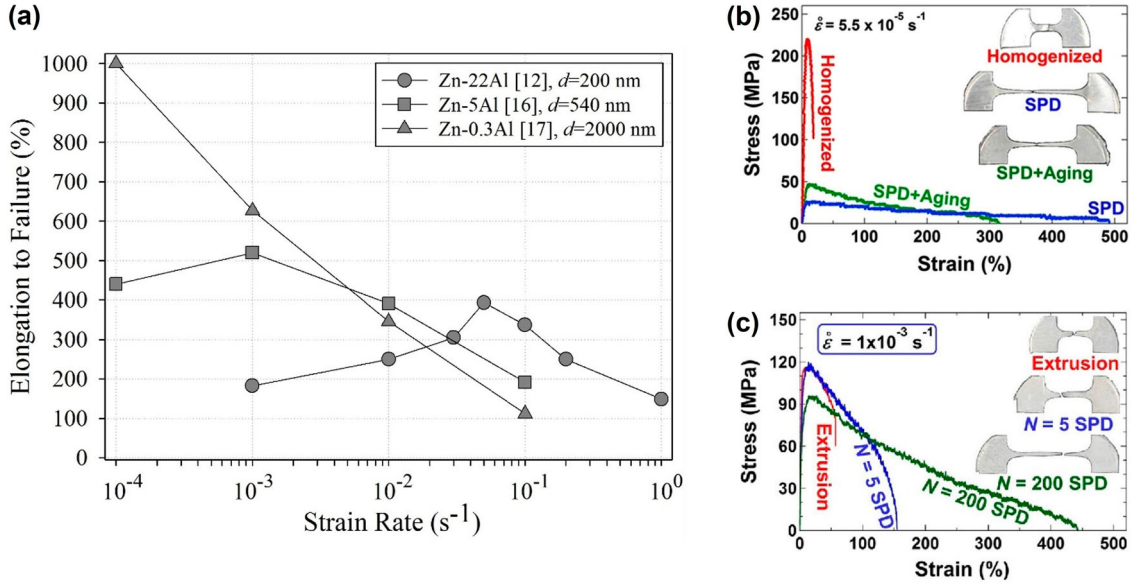

Figure 40. (a) Variations of elongation to failure with strain rate in severely deformed Zn - (0.3, 5, 22) wt% Al alloys having different grain sizes (*d*) [712,783,787,788]. Stress-strain curves of (b) Al - 30 at% Zn [699] and (b) Mg - 8 wt% Li [547] alloys, showing room-temperature superplasticity.

creep experiments on SPD-processed UFG pure metals or binary alloys were carried out in the beginning of this century [794–796]. Later experiments continued on more complex materials using different SPD processing methods [797–799]. All effort to understand creep processes in SPD-processed materials has been rewarded with a considerable success, though numerous details of this complex phenomenon still await a satisfactory explanation. It should be stressed that it may be difficult to reveal new creep mechanisms in SPD-processed materials because grain growth occurs easily during high temperature creep tests.

The important conclusion from the creep experiments on SPD-processed materials with unstable microstructure is that the creep behavior and operating mechanisms are similar to those recorded in conventional coarse-grained materials without processing by SPD. The different creep resistance between coarse-grained and SPD-processed materials is mostly influenced by the SPD processing routes (Figure 41), grain size, fraction of high-angle grain boundaries, creep conditions and testing modes [716]. A higher thermal stability of UFG microstructure was observed in precipitation-strengthened alloys. Recent works have shown that a reduction of grain size to ultrafine size level and a high fraction of high-angle grain boundaries increase the contribution of boundary-mediated processes to the total creep deformation [797–799]. However, the important conclusions from extensive series of experiments show that regardless of thermal stability, SPD-processed materials exhibit no substantial beneficial creep response. In comparison with the creep behavior of the counterpart coarse-grained materials tested under identical creep conditions, SPD-processed materials exhibit an increase in the minimum creep rate and a decrease in creep life. By contrast, an application of SPD leads to a remarkable increase of creep fracture plasticity.

10. Functional properties of materials processed by severe plastic deformation

Nanomaterials produced by SPD exhibit interesting functional properties due to their microstructural features and particularly small grain size and high density of lattice defects. The SPD technique has been used not only to process existing functional materials but also to synthesize new materials for a specific functional property. Since the materials processed or synthesized by SPD can usually exhibit more than one functional property, the term 'multifunctional properties' is sometimes used to describe the properties of these materials. For some functional properties (particularly in energy applications), since these nanomaterials show much better performance compared to conventional materials, the term 'superfunctional properties' is sometimes used. These materials have been studied for various functional properties including, shape memory effect [800], acoustic properties [801], hydrogen embrittlement [802], hydrogen storage [283], catalytic activity [803], photocatalytic hydrogen production [431], photocatalytic CO_2 conversion [433], photocurrent generation [432],

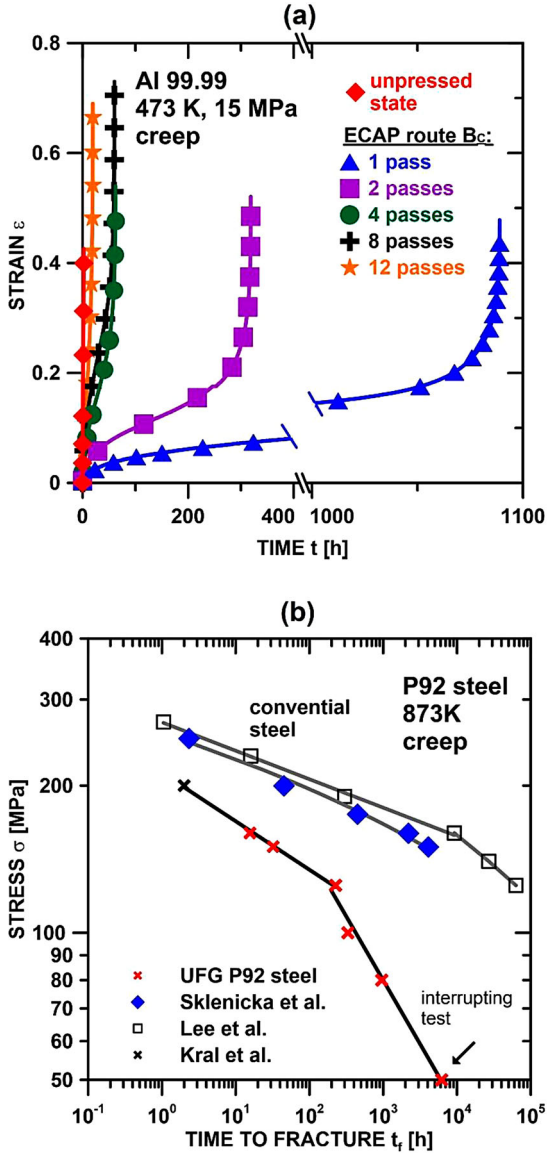

Figure 41. (a) Standard creep curves for aluminum before and after processing with equal-channel angular pressing for 1-12 passes [796]. (b) Stress versus time to fracture for ultrafine-grained and conventional creep-resistant P92 steel [799].

photoluminescence [409], electrocatalytic hydrogen production [804], electrocatalytic oxygen production [805], magnetic properties [806], electrical conductivity [807], superconductivity [808], dielectric performance [440], thermoelectric performance [809], thermal conductivity [407], radiation resistance [810], corrosion resistance [811], tribocorrosion resistance [812], biocompatibility [813], etc. Some significant functional properties of SPD-processed materials are discussed below.

10.1. Hydrogen storage performance

Metal hydrides can store hydrogen in the solid-state form in a compact and safe way under low pressures [814]. MgH_2, for instance, has a high hydrogen storage capacity of 7.6 wt% in addition to very good hydrogen absorption/desorption reversibility and cyclability. However, due to the slow kinetics of the reaction between magnesium and hydrogen and high thermodynamic stability of the hydride phase, absorption and desorption temperatures are usually too high to allow intensive practical applications [815]. Such limitations were the driving force for the development of novel materials, such as the nanostructured MgH_2 powders produced either by high-energy ball milling of MgH_2 under argon atmosphere [816–819] or by ball milling of magnesium under hydrogen atmosphere [820,821].

Processing of hydrogen storage materials by SPD techniques has come as an alternative to avoid the complexity of handling highly reactive ball-milled powder. The SPD-processed materials are in the bulk form and do not suffer from surface contamination/oxidation which is usually associated with the nanocrystalline ball-milled powders. The HPT [822–824] and ECAP [283,825–829] methods are the main SPD processes used to produce bulk hydrogen storage alloys with refined microstructures containing high density of defects and interfaces. The same type of microstructure can also be produced by heavy straining with conventional methods, such as fast forging [830–832] and intensive cold rolling [833–835], in which an important texture feature is developed for magnesium [833–837] and magnesium alloys [838,839].

10.1.1. High-pressure torsion of hydrogen storage materials

The HPT method can significantly improve the hydrogen absorption/desorption properties of hydrogen storage materials based on magnesium or titanium [840]. The HPT procedure is used to enhance the kinetics by means of the intense grain refinement and introduction of high-angle grain boundaries [822]. In the case of magnesium systems, strong (002) fiber-type texture is introduced, which is known to improve activation (first hydrogenation) kinetics [822]. TiFe-based intermetallics can exhibit improved activation properties and air resistance by HPT processing [841,842]. While commercial as-cast TiFe cannot store hydrogen without a heating process under vacuum, the HPT-processed sample can reversibly store hydrogen at room temperature even after long-time storing the material in air atmosphere [841,842]. Easy activation by HPT processing was attributed to hydrogen diffusion through grain boundaries [843], amorphous regions [844] or stacking faults [845]. The HPT process is not only effective to enhance the hydrogen storage kinetics and activation, but it can be used as a synthesis method to produce hydrogen storage materials such as TiFe [846] and Mg_4NiPd [327].

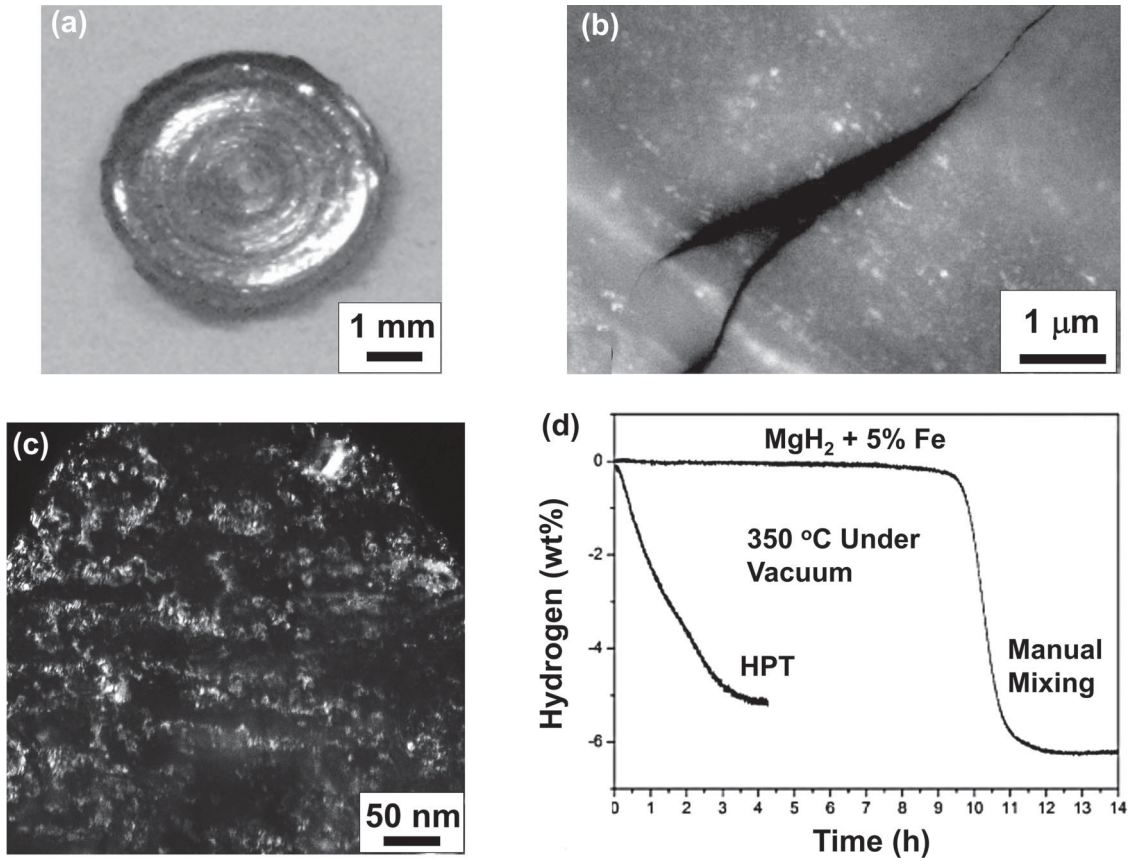

Figure 42. (a) Disc shape, (b) back-scattered image by scanning electron microscopy, (c) dark-field image by transmission electron microscopy and (d) desorption kinetic curves of $MgH_2 + 5$ wt% Fe with and without processing by high-pressure torsion under 5 GPa with 5 turns [822].

The HPT method is also applicable to make composites of hydrogen storage materials and a catalyst to improve the kinetic properties. Figure 42(a) shows an HPT-processed disc from the mixture $MgH_2 + 5$ wt% Fe, which resulted in a nanostructured hydride with good distribution of the iron particles after 5 HPT turns under 5 GPa (Figure 42b). The detailed microstructural modification after HPT processing of MgH_2 is shown in the dark-field TEM image in Figure 42(c). Important improvement in desorption kinetics was observed after HPT processing, as shown in Figure 42(d) [822]. Such improvement was associated with the fine grains, uniform distribution of iron particles and extensive cracking (and thus, free surfaces) after HPT processing. Taken altogether, the HPT method is considered as an effective technology to process/synthesize hydrogen storage materials with high activity and fast kinetics, as discussed in a recent review paper [702].

10.1.2. Intensive cold rolling of hydrogen storage materials

Cold rolling is a well-known metal forming technique that is extensively used in industry. Upon cold rolling, the effects on a material typically include texture formation, increased defect density, reduction in crystallite size, increased microstrain, etc. All these effects could potentially be beneficial for metal hydrides to enhance the hydrogen storage properties and kinetics. Therefore, *prima facie* cold rolling can be an interesting technique for the development of metal hydrides for hydrogen storage. Despite this, the investigation of the effects of intensive cold rolling on metal hydrides is relatively new and the number of studies is still small. Some of the first investigation was reported by Zhang *et al.* who studied the Ti-22Al-27Nb (wt%) alloy [847,848]. Cold rolling improved the first hydrogenation of the alloy, but after a few hydrogenation/dehydrogenation cycles, the kinetics were the same as the unprocessed samples.

Intensive cold rolling can also be used to synthesize alloys. For hydrogen storage applications, the Mg-based alloys are one of the most interesting system. One of the first attempts to report on synthesis of Mg_2Ni by cold rolling was made by Ueda *et al.* [849]. They obtained a laminated structure of magnesium and nickel by repetitive rolling. The intermetallic Mg_2Ni was then obtained by heat treating the laminated structure at 673 K for

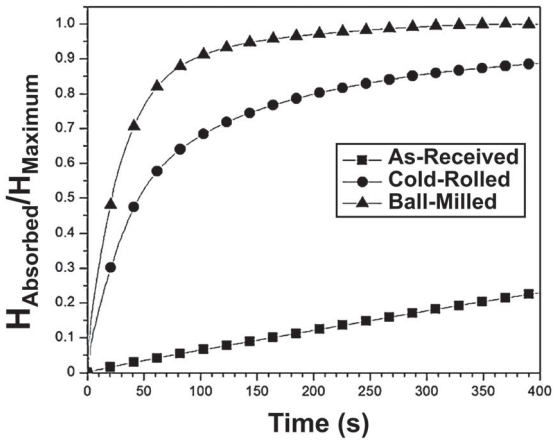

Figure 43. Normalized kinetic of hydrogen absorption at 623 K and under 2 MPa hydrogen pressure for MgH_2 hydrogen storage material in as-received, intensively cold-rolled, and mechanically milled states. [850].

4 hours. The resulting sample could then be completely hydrogenated to Mg_2NiH_4 [849].

Intensive cold rolling can also be performed on the hydride phase as was shown for MgH_2 [822,833,850]. Figure 43 shows the comparison of hydrogenation kinetics, normalized to the maximum capacity, for MgH_2 in the as-received, cold-rolled (five times in air) and ball-milled (for 60 minutes under argon) states [850]. A comparison between the behavior of cold-rolled and as-received samples indicates that cold rolling greatly enhances the hydrogenation kinetics compared to the as-received sample. The ball-milled sample has the faster kinetics, but it should be pointed out, that milling was done in the argon atmosphere, while cold rolling was performed in air. Therefore, the processing by cold rolling was much simpler and quicker than ball milling. For this reason, intensive cold rolling can be considered as an attractive mechanochemistry method for processing and synthesis of metal hydride for hydrogen storage applications [851,852].

10.2. Photocatalytic activity

Photocatalysis (chemical reaction under light in the presence of a semiconductor catalyst) is considered as a clean chemical technology with zero CO_2 emission [853]. Photocatalysis has been used for various chemical reactions including production of hydrogen from water, conversion of CO_2 to fuels or active CO and decomposition of toxic dyes. Metal oxides are promising materials for photocatalysis due to their high stability even under crucial environments [853]. However, the large band gap of metal oxides restricts their application to photo-excitation under ultraviolet (UV) light. Since the UV light accounts for only 5% of the solar spectrum, it has been the goal of many researchers to design metal oxide semiconductors with low bandgap and a capability of absorbing visible light [854]. Doping with cations or anions is the main strategy for band gap narrowing, but this strategy may not necessarily result in enhanced photocatalytic activity due to the defect-induced recombination losses [855,856]. Defect engineering through the introduction of vacancies and interphase junctions as active sites for photocatalysis is another main strategy to enhance the photocatalytic activity [854–856].

The SPD processing has been recently used to improve the photocatalytic activity. Since photocatalysts are hard and brittle at ambient condition, the HPT method has been used for their process. Five main strategies have been employed to improve the photocatalytic activity using the HPT method.

- Stabilization of low band gap high-pressure phase at ambient pressure, as will be discussed further below. This strategy was used to stabilize high-pressure TiO_2-II (columbite) phase for hydrogen production [431] and CO_2 conversion [433] as well as to stabilize high-pressure rocksalt ZnO phase for toxic dye degradation [436].
- Introduction of oxygen vacancies as active sites for photocatalysis as well as effective defects for reducing the optical band gap. It was shown that the introduction of oxygen vacancies by HPT processing can make new photocatalysts from oxides that are not originally photocatalyst such as Al_2O_3 for dye degradation [426], and ZrO_2 for hydrogen production [429]. It was also shown that photocatalytic hydrogen production can be improved by introduction of oxygen vacancies in perovskites [441].
- Introduction of nitrogen vacancy clusters as active sites for photocatalytic hydrogen production in oxynitrides such as Ga_6ZnON_6 [443].
- Introduction of large fraction of interphase boundaries as effective sites for charge carrier separation and enhancement of photocatalytic hydrogen production. The HPT method was applied for mechanical mixing of TiO_2 and ZnO and formation of large fractions of strain-induced interphases [442].
- Synthesis of new high-entropy photocatalysts with high stability and good activity for photocatalysis. The HPT method was used to synthesize high-entropy oxide $TiZrHfNbTaO_{11}$ for photocatalytic hydrogen production [372] and CO_2 conversion [373] as well to synthesize high-entropy oxynitride $TiZrHfNbTaO_6N_3$ for hydrogen production [374].

TiO_2 is the first photocatalyst discovered in 1970s [853]. Three major crystal structures of TiO_2 are rutile, anatase, and brookite, all of which have the band gaps larger than 3 eV in the UV region. Under high pressures, TiO_2 undergoes a phase transformation from anatase to TiO_2-II, as shown in Figure 44(a) [857]. Theoretical studies showed that the band gap of TiO_2-II can be as small as 2.59 eV [858]. Motivated by the theoretical studies, the HPT method was applied to the anatase phase and it was shown that the strain and grain size effect can stabilize the TiO_2-II phase after releasing pressure [430]. The band gap was reduced from 3.2 eV to 2.4 eV due to the TiO_2-II phase formation. In addition, as shown in Figure 44(b), the HPT-processed TiO_2 after annealing (to annihilate some defects) was able to split water and produce hydrogen under visible light illumination, while anatase TiO_2 showed no activity under visible light [431]. The TiO_2-II phase also showed high photocatalytic activity for CO_2 to CO conversion under the UV light, as shown in Figure 44(c) [433]. In a similar way, ZnO with a crystal structure of wurtzite at ambient pressure was transformed to high-pressure rocksalt phase by HPT processing [436]. The rocksalt phase, which remained metastable for years after decompression, led to the band gap reduction from 3.4 eV to 1.8 eV. Rocksalt ZnO was able to decompose toxic dyes under visible light, while wurtzite ZnO was not active under visible light. Taken altogether, these studies suggest the high potential of the SPD process in producing active photocatalysts to address the future demands for carbon-neutral energy production and CO_2 reduction.

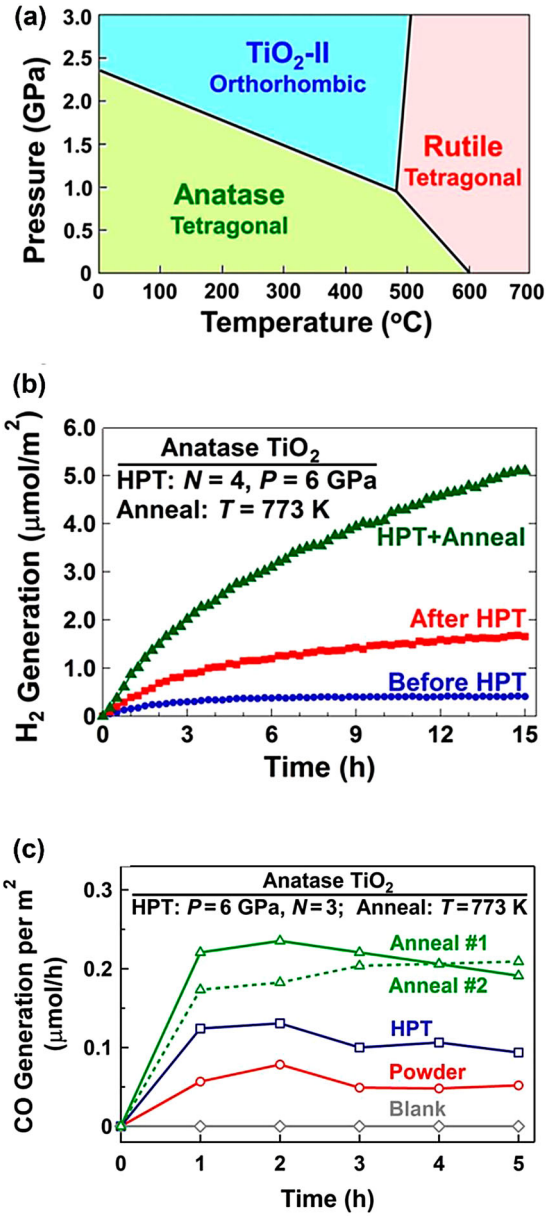

Figure 44. (a) Pressure-temperature phase diagram of TiO_2 [431,857]. (b) Photocatalytic hydrogen production from water under visible light on TiO_2 before and after HPT processing and after annealing [431]. (c) Photocatalytic CO_2 to CO conversion under UV light on TiO_2 before and after high-pressure torsion processing followed by annealing [433].

10.3. Superconductivity

Superconductivity is characterized by the zero electrical resistivity and perfect diamagnetism below a critical temperature T_c [859–861]. In 1911, H. Kamerlingh Onnes discovered superconductivity in mercury at the critical temperature of $T_c = 4.2$ K [862–864]. Since that time, superconductivity has been found in many metallic elements, alloys, and intermetallic compounds [859–861]. Nowadays, metallic superconductors can be used for various applications such as sensitive magnetometers based on superconducting quantum interference device (SQUID), sensitive detectors, low-loss power cables, and superconducting magnets used in maglev trains and magnetic resonance imaging (MRI), and so on. These applications of superconductors are based on the thin film or wire technology. However, applications of bulk superconductors have not widely been developed, because the control of the superconductivity is not easy in bulk superconductors. The SPD process has been used successfully in recent years to produce bulk superconductors for potential applications under ambient pressure [865] and high pressure [866].

10.3.1. Superconductivity under ambient pressure

The bulk nanostructured superconductors generated by SPD are unique materials to control superconducting property, because UFG structures with high density of grain boundaries, dislocations, and other crystalline defects modify the superconducting order parameter. Recently, the HPT method has been applied to niobium

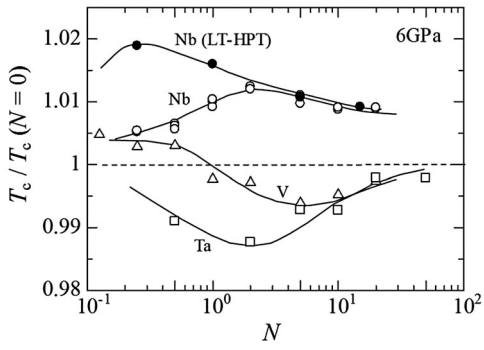

Figure 45. Critical temperature T_c normalized by T_c of as-received materials as a function of high-pressure torsion turns (N) for vanadium, niobium and tantalum. LT-HPT refers to processing in liquid nitrogen [865].

[808], rhenium [867], and the Nb-Ti alloys [686] and the enhancement of critical temperature T_c, upper critical field H_{c2} and critical current density J_c has been reported. Figure 45 shows T_c variation versus the number of HPT turns for niobium, tantalum and vanadium processed at room temperature as well as for niobium processed at cryogenic temperature in liquid nitrogen [865]. In niobium processed at room and cryogenic temperatures, T_c increases with the evolution of grain refinement through increasing the number of HPT turns. In vanadium and tantalum, on the other hand, T_c decreases at a certain HPT turn number.

The different behavior of T_c for different SPD-processed materials can be explained by the competition between quantum size effect and disorder effect. These effects are characterized by the parameters of grain size $2r_{av}$, electron mean free path l, and the superconducting coherence length ξ_0 [865]. Under the condition of clean superconductors (i.e. $l > \xi_0$) such as in niobium, the quantum size effect becomes remarkable when r_{av} is reduced close to ξ_0 (for example, $r_{av}/\xi_0 \sim 3$ for niobium processed with HPT for 2 turns at room temperature). However, in vanadium and tantalum, the disorder effect, which results from the electron scattering by the crystalline imperfection (i.e. $l < \xi_0$), reduces superconductivity.

As mentioned above, the UFG structure with the comparable grain size to ξ_0 and the clean superconductivity (i.e. $l > \xi_0$) inside the grains provides a new method of T_c enhancement. Therefore, the SPD process has an advantage to produce bulk nanostructured superconductors with higher T_c, J_c, and H_{c2} [686,808,865,867].

10.3.2. Superconductivity under high pressure

Bulk superconductivity exhibits macroscopic phase coherence in the Josephson arrays composed of superconducting grains. In the late 1950s to the early 1970s, the superconductivity at zero magnetic field (superconducting at critical temperature T_c) was found to depend on both the sample purity and the residual strain in single-element superconductors, such as rhenium [868], tantalum [869], and vanadium [870]. Generally, the shear strain reduces crystallinity, and it is not usually favorable for macroscopic phase coherence. It has been shown that it rarely works toward favorable manner in rhenium [868] and in thin film and amorphous aluminum [871]. Motivated by these backgrounds and motivated by the effect of the HPT method in inducing strain [19,47,872,873], the improvement of functionality in superconductors was successfully achieved in recent years [686,808,867]. As mentioned in the preovious section, it was reported that HPT processing is effective in increasing T_c of superconductors such as niobium [808] and rhenium [867] under ambient pressure.

In the periodic table containing 118 elements, there are 29 superconductors at ambient pressure, and 11 elements of them exhibit the increase in T_c under hydrostatic pressure [874,875]. Three fifth-element superconductors such as vanadium, niobium and tantalum have nominal T_c of 5.3 K, 9.2 K, and 4.5 K, respectively. All of three are considered to belong to a group that exhibits an increase in T_c under the hydrostatic pressure circumstances [874,875], although smooth linear increase in T_c is observed only in vanadium. The compression under hydrostatic pressure is thus considered as an approach to shift T_c to higher temperatures [874].

Mito *et al.* attempted to increase Tc for the above fifth-element superconductors by conducting the compression under quasi-hydrostatic pressure (using a DAC facility) on materials severely deformed by the HPT method, as illustrated in Figure 46(a) [866,876]. Here, it is noted that both the HPT apparatus and the DAC facility commonly use the same route of Bridgman's pioneering studies [19]. The HPT process was used to achieve grain refinement and strain accumulation in the samples. The additional compression using DAC on severely strained superconductors triggers strengthening intergrain contact and/or structural deformation in the unit-cell level. The significance of the above two effects depends on the kind of elements. First, in vanadium, there is no prominent effect of HPT, comparing to the hydrostatic compression effects on the non-strained material. Next, in tantalum, the effect of strengthening intergrain contact appears at small hydrostatic compression, resulting in a temporal increase in T_c. Finally, as shown in Figure 46(b), niobium exhibits a prominent increase in T_c by both effects (i.e. by structural refinement via HPT processing and by hydrostatic pressure application via DAC processing). In particular, the structural deformation in the unit-cell level significantly promotes the increase in T_c [876]. Thus,

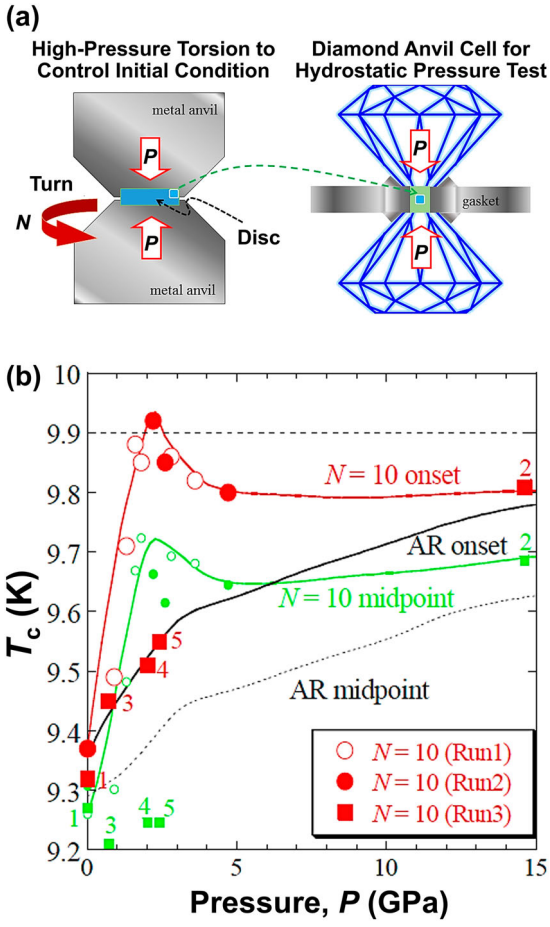

Figure 46. (a) Schematic illustration of two-step procedure for examination of superconductivity of severely deformed superconductors under hydrostatic pressure: high-pressure torsion using metallic anvils is used for controlling initial structure and diamond anvil cell is used to introduce quasi-hydrostatic pressure. (b) Variations of critical temperature for superconductivity (T_c) versus hydrostatic pressure for niobium in the as-received state (AR) and after proceeding by HPT for $N = 10$ turns. Critical temperature increases by both severe plastic deformation and hydrostatic pressure [866].

the accumulation of residual strain by SPD processing can be a promising approach to manipulate T_c to high temperatures under hydrostatic pressure.

10.4. Thermoelectric performance

Since recently, it is known that SPD processing of thermoelectrics can provide values of the figure of merit (ZT) higher than 1.2, and thus gets highly attractive for materials which enable sustainable generation of electric power [877]. These high values arise from the UFG microstructure in combination with a high level of point, linear and surface lattice defects which significantly enhances the scattering of the phonons, thus leading to a minimum of thermal conductivity and therefore to exceptional values

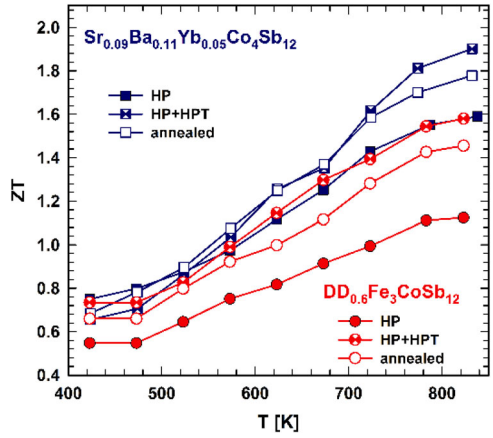

Figure 47. Response of the figure of merit (ZT) values of n-type (blue curves) and p-type (red curves) skutterudites to high-pressure torsion processing and additional annealing. The curves with empty symbols represent the thermally stable states of the samples [878].

of ZT. The SPD processing has been applied so far mainly to high-temperature thermoelectric materials such as skutterudites, clathrates, and recently even to Heusler phases, but far less to low-temperature thermoelectrics such as bismuth tellurides [878].

For all skutterudites, the HPT method, as one of the most efficient techniques of SPD processes, proved to be very effective to either enhance ZT of hot-pressed samples [878], or to directly produce bulk samples of high-ZT thermoelectrics [879,880]. Recently, by use of an upscaled HPT facility, bulk samples from powders of n-type [881,882] and p-type [883] skutterudites $DD_{0.7}Fe_3CoSb_{12}$ with sizes as large as 30 mm in diameter and 1-8 mm in thickness could be directly achieved by HPT, with ZT $\approx$ 1.3 at 856 K. These studies introduce a cheap and energy-saving production route for thermally stable p- and n-legs for thermoelectric modules with the good compatibility and contact.

Still all-time records are the enhancements of ZT for n-type skutterudites from 1.6 to almost 2, and for p-type skutterudites from 1.15 to almost 1.5 at 825 K by HPT processing [878,884,885] (see Figure 47). However, HPT processing of Heusler and half-Heusler phases can rise ZT only slightly, e.g. from 0.22 to 0.3 ($VTa_{0.05}Fe_2Al_{0.95}$) [886], or from 0.68 to 0.75 (p-type $Ti_{0.15}Nb_{0.85}FeSb$) [887]. The increases in ZT achieved in clathrates were found to be almost negligible [888]. Nevertheless, low-temperature thermoelectrics like bismuth tellurides of type $V_1(VI)_1$ and/or $V_2(VI)_3$ (with V, VI representing the group elements) show more potential in the SPD-induced increases of ZT. Already with high temperature and pressure after ball milling, ZT could be enhanced from $\sim$1.0 up to 1.4 at 373 K [889], at least by ensuring a high electrical conductivity with respect to the strong

anisotropy in these materials. This value was reached by many ECAP experiments published so far (see e.g. [890]), but the first applications of HPT did not reach that ZT level as either the texture was not optimal, or the processing rates and/or temperatures were too high. By using low-rate HPT processing and achieving optimum textures, Ashida *et al.* [891] found promising power factors of around 6 $mWm^{-1};K^{-2}$. Recent investigations underline the importance of the lattice defects' specific phonon scattering efficiencies - especially those of dislocations - and their generation in sufficiently high densities, thus reaching the enhancement of p-type Bi-tellurides up to ZT = 1.9 [892,893].

As concerns the mechanical properties of SPD-processed thermoelectric materials such as skutterudites and half-Heusler alloys, the application of SPD methods significantly raises the strength while the elastic moduli remain unchanged unless new phases are formed (for more details, see [878,894]).

10.5. Radiation resistance

The progress in increasing reliability and safe functioning of existing and future nuclear reactors demands development of new materials with the improved radiation tolerance (resistance) and the outstanding mechanical performance [895]. Fluxes of high-energy particles result in generation of point defects, which agglomerate and form clusters, voids, dislocation loops and so on, leading to the notable degradation of mechanical and functional properties [895,896]. Radiation resistance can be improved by introducing additional sinks for point defects into the microstructure of materials, for instance, by drastic increasing the fraction of interfaces via grain refinement. Pioneering experimental works on irradiation behavior of materials with refined grain size produced by gas condensation [897–899] as well as numerical simulations [900,901] provided the first evidences that promoted grain boundary networks can effectively prevent agglomeration of radiation-induced defects. Tremendously increased number of the subsequent irradiation studies of various nanomaterials, including thin films, multi-layers, nanocomposites, coatings, nanoporous and electrodeposited metallic materials, confirmed their improved radiation resistance (see reviews in [902,903]). However, these materials are often characterized by redundant porosity, contamination and limited dimensions. This occasion complicates both precise systematical studies of such materials (especially from the viewpoint of mechanical performance) and evaluation of their potential application.

The SPD techniques not only refine grain structure of metals and alloys and produce bulk UFG billets [1,904], but they also can be modernized and upscaled to fabricate pore-less and full-density billets with commercially attractive dimensions for applications under irradiation. The effect of proton and ion irradiation on nickel and Cu-0.5%Al_2O_3, produced by ECAP followed by HPT, was reported in [905,906]. It was demonstrated that grain refinement by SPD can effectively suppress the damage of microstructure and reduce hardening induced by irradiation, though accompanied with the grain growth. Later investigations of HPT-produced shape memory alloys and steels used in nuclear engineering revealed their high resistance to disordering of microstructure [907] and accumulation of intragranular solute clusters or dislocation loops [810,908] after heavy ion bombardment. Recent model irradiation studies [909–917] revealed many phenomena occurring in various alloys produced by different SPD methods. Together with confirming the previous findings, grain boundary segregation in SPD-processed alloys under irradiation (Figures 48a and b) were shown to be different from the redistribution of alloying elements caused by HPT [909,910]. Such elemental distribution can modify the corrosion resistance as well [910]. The question if the reduction in grain size should always enhance radiation tolerance [902,911] was experimentally challenged in [912,913], where ECAP-processed ferritic-martensitic steels showed poorer swelling resistance at huge ion irradiation doses (up to 1000 dpa). At the same time unprecedented radiation tolerance of SPD-processed alloys was demonstrated in [914–917].

However, ion irradiation experiments do not fully reproduce changes in microstructure and properties in conditions of a nuclear reactor core. Studies of the performance of SPD-processed materials under neutron irradiation at elevated temperatures are of the great interest of nuclear engineering scientists, yet significantly less numerous since the equipment for such experiments and subsequent investigation of specimens with redundant radioactivity is available at few laboratories in the world. The experiments on the ECAP-processed stainless steel, irradiated by neutrons in a research fission reactor, suggested a positive effect of nanostructuring on its radiation tolerance [918]. Investigations of the neutron irradiated steel-10 produced by ECAP [919] showed less radiation hardening in UFG materials (examined by hardness measurements and tensile tests) and smaller irradiation-induced dislocation density, while the tendency for cluster formation was lower in a conventional steel. Authors of [920] reported excellent resistance of UFG microstructure to neutron irradiation in the HPT-processed 321 stainless steel, but its corrosion resistance seemed to be affected with thermal-induced precipitation. Authors of [921] reported on less pronounced

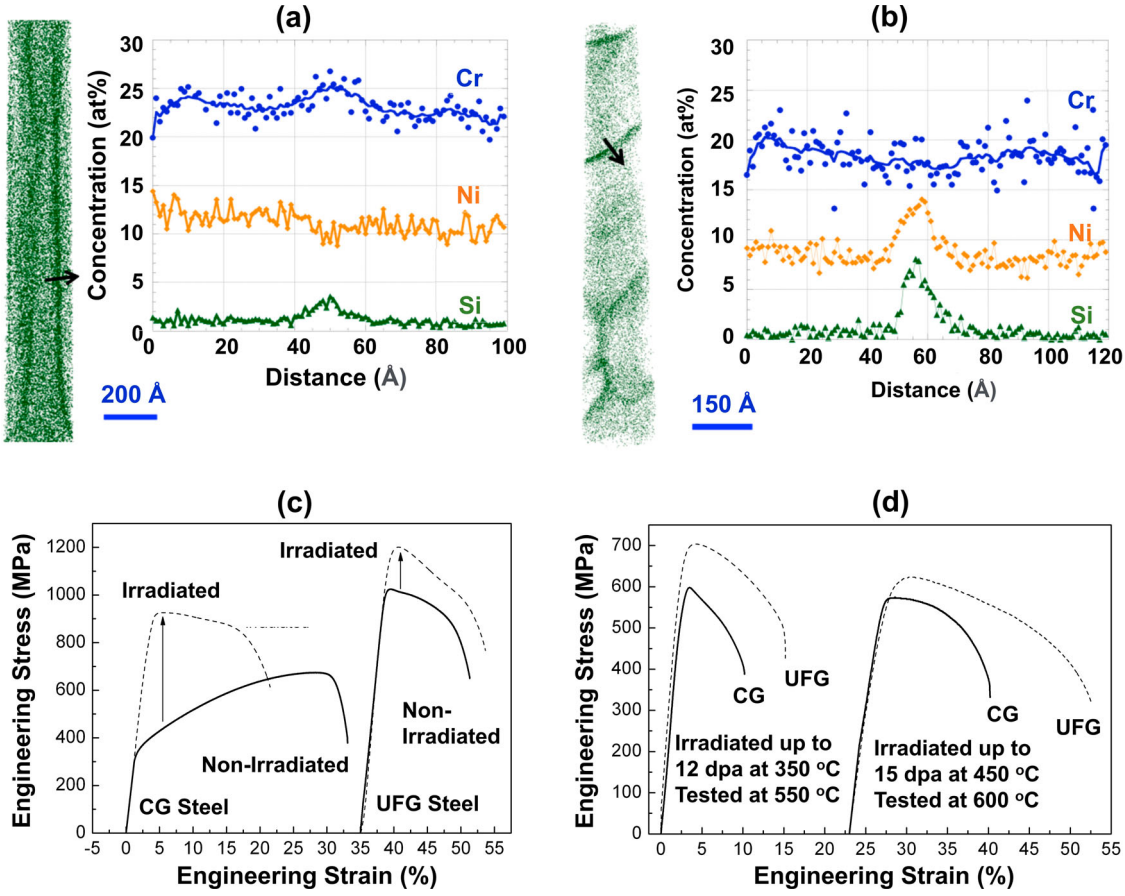

Figure 48. Atom probe tomography images of (a) un-irradiated and (b) self-ion irradiated 316 steel produced by high-pressure torsion, showing different tendency in grain boundary segregation with no irradiation-induced intragranular clusters and Franc loops [909]. (c) Engineering stress-strain plots of irradiated ultrafine-grained and conventional 321 steel irradiated at 723 K to 15 dpa and tested at room temperature [921]. (d) Illustration of simultaneously enhanced strength and plasticity of severely deformed steel as shown by tensile tests at elevated temperatures after irradiation in different conditions [921].

irradiation strengthening in a metastable austenitic stainless steel produced by ECAP and neutron irradiated to 12-15 dpa (Figure 48c). In addition, mechanical tests at elevated temperatures showed that UFG structures provided a combination of both high strength and good plasticity (Figure 48d), indicating an improved ability of the SPD-processed steel to resist high-temperature radiation embrittlement typical to conventional Cr-Ni steels.

Thus, grain refinement proved to be a powerful pathway to design high-performance radiation-tolerant materials. The importance of the related research is being proved by the most recent results on the enhanced tolerance of the microstructure of SPD-processed ferritic/martensitic [922] and austenitic [923] steels to ion irradiation. Investigation of the impact toughness of a neutron irradiated UFG stainless Cr-Ni steel demonstrated its higher resistance to the onset of evolving cracks, compared to the coarse-grained material [924]. It can be concluded, that bulk UFG metals and alloys produced by SPD can demonstrate excellent mechanical performance and improved resistance to model and neutron irradiation, as reviewed in detail in [925], while there still is a number of open questions which require further intensive studies in the field.

10.6. Corrosion resistance

The effect of cold working, or, more generally, plastic deformation, on the corrosion resistance of metallic materials has long been an important issue from both practical and scientific perspectives [926]. With the advent of SPD to fabricate UFG structures in bulk form, the effect of plastic deformation on corrosion has received more considerable attention. The pioneering work by Vinogradov *et al.* and the majority of subsequent published studies on the corrosion behavior of SPD-processed materials have been conducted by using ECAP [927]; however, there are studies on other techniques such as ARB [928], HPT [929], hydrostatic extrusion [930] and modified types of rolling [931]. Surface nanocrystallization by the surface-SPD methods such

as SMAT [932] and FSP [933] is emerging as a relatively new strategy to enhance corrosion and tribological performance.

The majority of the lattice defects generated during SPD contribute to increasing the internal energy in materials. Thermodynamically, the stored energy (ΔG) reduces the electrode potential of materials (ΔE) according to the relation $\Delta E = -\Delta G/nF$, where n is the oxidation number of metals and F is the Faraday's constant [934]. The potential drop in pure copper is estimated to be only 0.1 mV due to the excess energy of grain boundaries for a grain size of 0.1 μm, and only 0.1 mV with the extremely high dislocation density of 10^{15} m^{-2}. However, the alteration observed experimentally in the corrosion potential of UFG and coarse-grained copper is usually much larger [935], and this indicates that corrosion kinetics are enhanced by the introduction of high-density lattice defects.

The effect of SPD on corrosion is very complicated because the corrosion behavior is affected not only by dislocations and grain boundaries, but also by the alteration of other metallurgical variables such as second phase, solute segregation and texture. Therefore, comprehensive understanding of the corrosion behavior of SPD-processed materials is far behind that of other properties, such as the mechanical properties. From an exhaustive survey of the literature [936], SPD appears to mostly improve the corrosion resistance of major commercial metallic materials, although there are contradictory results for the same materials and environments: 128 out of 228 surveyed papers reported or claimed a positive effect, 28 papers reported a negative effect, while the others reported a marginal effect or an effect that depended on the testing condition. If the survey is limited to pure metals (copper, titanium, magnesium and aluminum), 43 out of 63 papers reported a positive effect, and only 8 reported a negative effect. The major reason for the positive effect is the development of a protective passivation layer due to the high kinetics at active sites such as high-density grain boundaries and dislocations. Plastic deformation has a negative effect on corrosion due to the enhanced kinetics of anodic dissolution in environments where the passivation is not stable or protective. Galvanic coupling by fragmented cathodic precipitations, defective passive films, residual stress and surface roughness can be other negative effects and causes of the apparent contradiction. Despite the complex effect of SPD processing on corrosion resistance, many attempts have been made to find a general rule of corrosion behavior, and in most cases, grain size is seen as a key parameter that governs the corrosion resistance. Ralston and Birbills reported a general trend that the corrosion resistance of UFG materials is superior to coarse-grained materials in passive environments, whereas it becomes opposite in non-passivating environments [288]. They also proposed a Hall-Petch-type universal law, that expresses the relationship between the grain size and the corrosion rate and showed that it can be applied to aluminum and magnesium within a reasonable dispersion [937].

On the other hand, the anomalous change in the corrosion behavior at high plastic strain was observed in pure copper [928,938] and Fe-Cr alloys [939–941] from systematic studies of the dependence of corrosion on plastic strain. One prominent example was reported by Rifai *et al.*, who found that the corrosion resistance to pitting of Fe-Cr alloys in NaCl solution was significantly improved after 8 ECAP passes [939,940]; however, this improvement disappeared after post-ECAP annealing with no apparent microstructural change [939]. This was attributed to the formation of a UFG structure or more specifically to the introduction of non-equilibrium high-angle grain boundaries [939]. Surprisingly, UFG Fe-8%Cr and Fe-10%Cr alloys exhibited spontaneous passivation in the neutral NaCl solution, as shown in Figure 49 [940,941], which goes against the established notion that a critical chromium content of 11% is required to attain passivity for stainless steels [942]. The reduction of required chromium by passivation of steels is perhaps one of the most beneficial effect of SPD on the corrosion behavior. These anomalous behavior of corrosion during SPD and subsequent annealing indicate that the structural modification has a significant impact on corrosion kinetics due to the closely spaced configuration of lattice defects despite the negligible change in the stored energy [943].

10.7. Biomedical applications

Presently, over 70% of implant devices are constructed from metals because of their strength, toughness and durability [944]. At the same time, their biofunctionality establishes certain requirements for the type and quality of metals and this, in turn, justifies the application of corrosion-resistant materials, mostly such as stainless steels, Co-Cr-Mo alloys, commercial pure titanium (CP-Ti) and Ti-based alloys, and more recently - bioresorbable magnesium and iron alloys. New alloys with the optimized chemical composition, manufacturing processes and surface modifications undergo continuous research and development to satisfy the clinical demands for medical devices [944,945].

Recently, nanostructuring of metals to improve their properties using SPD processing [1] is becoming a new and promising area for medical applications [322]. The first works in this regard were applied to CP-Ti because of its highest biocompatibility with living tissues among

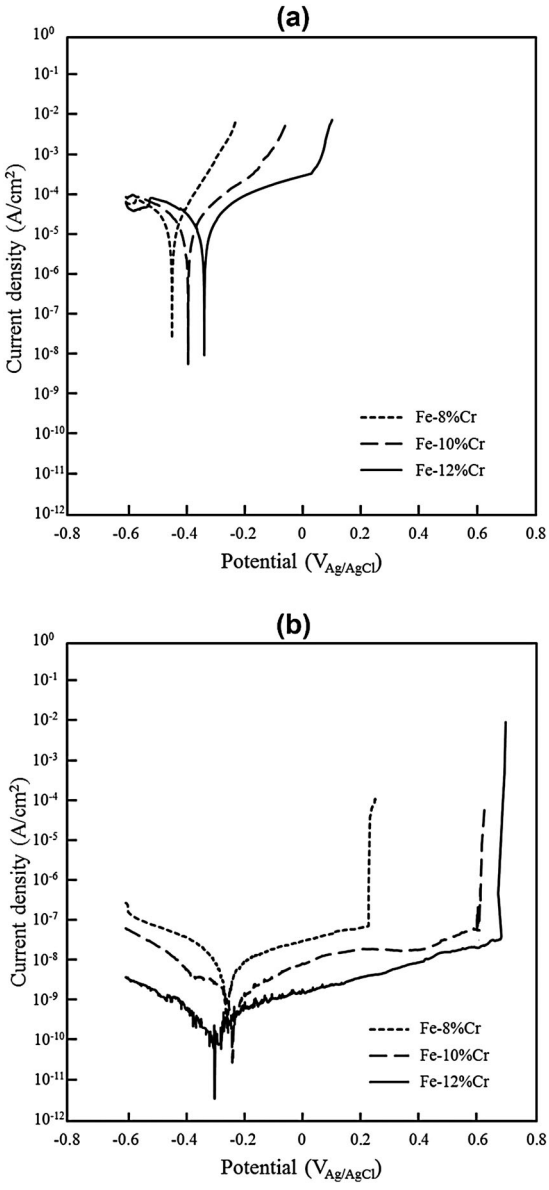

Figure 49. Dynamic polarization curves in 3.5% NaCl solutions for (a) coarse-grained and (b) ultrafine-grained Fe-Cr alloys [936,940].

various metals, but the material is known as having relatively low strength properties. The earliest attempts on nanostructuring CP-Ti were performed with the aim to develop the material in the form of long-length rods with superior mechanical and biomedical properties for the fabrication of dental implants [946]. After combined ECAP and thermo-mechanical treatment, a large reduction in grain size was observed from 25 μm in the initial CP-Ti rods to 150 nm in the SPD-processed one, as in Figures 50(a–c). Later, a continuous ECAP-conform method combined with further drawing was employed to produce long rods [947–949]. Table 5 illustrates mechanical property benefits of CP-Ti after nanostructuring by ECAP and thermo-mechanical treatment. As is seen, the nanostructured titanium has two times higher strength than the conventional CP-Ti without any drastic ductility reduction (below 10% elongation to failure), which is usually observed after rolling or drawing. It also has better properties compared to the Ti-6Al-4%V (wt%) alloy [946].

During the last decade, a number of studies were also performed aiming at increasing mechanical and functional properties of titanium alloys using their nanostructuring [322]. Special interest is currently attracted to use the SPD approach as a promising way to fabricate nanocrystalline β-Ti alloys from the Ti-Mo and Ti-Nb systems that can have simultaneously high strength, low elastic modulus and excellent biocompatibility [948–951]. Austenitic stainless steels, which are promising for medical purposes, are also readily strengthened by SPD processing (see e.g. [322]). Regarding SPD processing of magnesium alloys, the most curious aspect of recent research is modifying their strength, ductility, and corrosion behavior to suit them for biomedical applications, especially for stents [322,952–954].

The superior mechanical properties of nanostructured metals enable the improvement of the design for medical implants [955–960]. Recently, two exciting examples of making and using the implants from nanostructured titanium with the premium design for dentistry and orthopedics have been presented [940]. Figure 50(d) shows a dental implant and Figure 50(e) shows a medical mini-sheet fabricated from nanostructured titanium [955,960]. Surface modification of nanometals and their surface properties are important aspects of an implant design to ensure effective osseointegration. For example, extensive studies have shown that grain refinement down to the nanoscale in CP-Ti can stimulate various bone-forming cell types to adhere and proliferate with the increased efficiency [949,957]. Additional surface modification by chemical etching or deposition of bioactive coatings can further improve bioactivity of implants made from nanometals [949,958,959]. All these results introduce nanostructured metals as attractive materials for manufacturing implants, as discussed in detail recently [955,959,960]. Nevertheless, additional biological in-vitro and in-vivo studies are necessary to clarify more the clinical significance of these research results.

11. Commercialization of severe plastic deformation

The SPD-processed materials demonstrate outstanding combinations of multifunctional or superfunctional properties that are attractive for industrial applications.

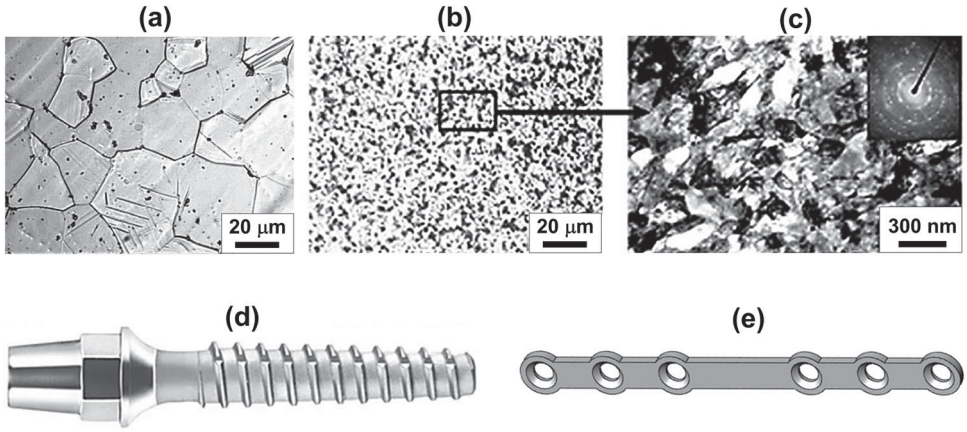

Figure 50. (a-c) Microstructure of commercially pure grade 4 titanium: (a) optical micrograph of initial coarse-grained rod, (b) optical and (c) transmission electron micrograph of nanograined titanium processed by equal-channel angular pressing and thermo-mechanical treatment [955]. (d) Dental implant [960,961] and (e) medical mini-sheet fabricated from nanograined titanium [955,956].

Table 5. Mechanical properties of conventional titanium and Ti-6Al-4V (wt%) alloy compared with nanostructured titanium (commercially pure grade 4) processed by equal-channel angular pressing (ECAP) and thermo-mechanical treatment (TMT) [946].

Material	Processing	UTS, MPa	YS, MPa	Elongation, %	Reduction area, %	Fatigue strength at 10^6 cycles
Ti	Conventional (As-received)	700	530	25	52	340
Ti	ECAP + TMT	1240	1200	12	42	620
Ti-6Al-4V	Annealed	940	840	16	45	530

Note: UTS any YS refers to ultimate tensile strength and yield tress, respectively.

However, commercialization of nanostructured materials also requires bridging between the systematic scientific knowledge and effective manufacturing and processing technologies to be put forward to the markets. Several examples of the recent advances in commercial potential of nanostructured materials were featured in a recent review paper [112]. Among the others, the most significant progress has been achieved for the SPD-processed titanium to be used for manufacturing dental implants by the Timplant Company established in the Czech Republic. The enhanced biocompatibility and mechanical performance of the SPD-processed titanium allow to design and produce optimized dental implants with the reduced diameter [961]. The miniaturized nano-titanium implants show good clinical performance and have an advantage to be placed within the small margins of bone tissues for front teeth area, which is not possible for implants traditionally fabricated from the coarse-grained titanium [949]. Another example of commercializing nanostructured metallic materials is associated with the approaches developed by the NanoSteel Company, Inc. (U.S.A.) to form nanomodal structures in the third generation advanced high-strength steels via a complex processing route including heavy cold straining and thermal treatment [112,962]. Another success in commercialization is the use of UFG thin strips of stainless steels for bio-tools (end of forceps, endoscopes, etc.) and orifice plate of gasoline injector in automobile engine. The processing of these steels is carried out in a few Japanese companies including, Tokkin [963] and Komatsuseiki [964]. The main reason for the success of this commercialization is excellent formability and precise shapes of UFG steels in micro-forming (e.g. making micro-size holes). Intensive cold drawing is also used to fabricate UFG wires from the pearlitic steels for long bridges such as the Akashi bridge in Kobe, Japan [965].

Although the innovation potential of SPD-processed materials is great, but it is yet to be explored for promotion to the market. There are several major challenges on this way: upscaling and improving productivity of SPD technologies to manufacture bulk billets for mass production; improving thermal and time stability of nanostructures; reducing costs of the final products; developing new standards regulating application of nanostructured materials; developing robust characterization techniques for the industrial quality control; and overcoming the psychological barriers of customers on the way of accepting novel approaches. As already attempted in many other fields, tailoring the composition and structural features of materials for a special SPD process to achieve exceptional properties can be an effective strategy to move from the laboratory scale to commercialization. Taken altogether, the offers on SPD-related innovative solutions are growing, and this will

facilitate the further progress in using the SPD-processed nanostructured materials into commercial products.

12. Concluding remarks and outlook

The science and art of production of advanced nanomaterials by severe plastic deformation (SPD) and examination of the relation between the mechanical/functional properties of these materials with their nanostructural features is known as the NanoSPD field. Despite the long history of this field, the importance of SPD processes for producing nanomaterials with exceptional mechanical and functional properties has been recognized only in recent decades. The current article covers some critical issues regarding the historical development and recent trends in the NanoSPD field including the terminological aspects (Section 2), history (Section 3), processing methods (Section 4), materials (Section 5), microstructural features (Section 6), phase transformations (Section 7), synthesis capability (Section 8), mechanical properties (Section 9), functional properties (Section 10) and current state of commercialization (Section 11).

Nanomaterials processed by SPD have an average grain size below 1 μm and they are usually produced at large enough strains for generating of large fractions of high-angle grain boundaries. The history of SPD methods goes back to the ancient time, when repeated hammering and folding was used to produce metallic weapons including Damascus swords. The SPD approach was applied to a wider range of materials in the 1930s by introducing the principles of the high-pressure torsion method. The SPD process was later used as an effective technology to produce nanomaterials with exceptional properties, and this technology became popular worldwide since 2000. High-pressure torsion, equal-channel angular pressing, accumulative roll-bonding, twist extrusion and multi-directional forging are the most popular SPD methods, but many processes are now available to induce SPD or surface-SPD in samples with different shapes and sizes in a continuous or semicontinuous way, as reviewed in Section 4. Metals and metallic alloys are the first kinds of materials which were processed by SPD, but there is now a wide range of processed materials including composites, glasses, semiconductors, ceramics, and polymers (Section 5). As discussed in Section 6, the formation of ultrafine grains with various kinds of lattice defects including dislocations, twins, stacking faults, vacancies, and segregated regions as well as texture are common microstructural features of materials process by SPD. Controlling phase transformation and synthesis of new nanostructured materials are other well-known benefits of SPD methods (Sections 7 and 8). All these structural and microstructural features lead to exceptional mechanical properties as well as to interesting multifunctional and superfunctional properties, as reviewed in Sections 9 and 10.

Since a wide range of materials can be processed by SPD methods, it is possible to achieve enhanced properties for various applications by careful selection of the materials and processing technique. As discussed in this article, most materials studied for SPD processing are pure metals, alloys and compounds which are already used technically in the coarse-grained form and their compositions and microstructures were optimized for conventional processing methods. Although SPD allows the generation of new nanostructural features, optimization of the chemical compositions for the SPD processing condition is required to take full advantage of SPD. As discussed in Section 11, the SPD-processed materials have been commercialized for biomedical applications, and it is expected that this application to be further developed due to an increase in the life expectancy and the need for advanced biomaterials. Moreover, by considering the global demands to realize carbon-neutral energy and to reduce the CO_2 emission, it is expected that the NanoSPD field will contribute to the energy-related issues in the future, particularly because of promising energy-related properties reported for the SPD-processed materials. Combinations of materials science, chemistry/physics and theoretical calculations together with the development of SPD methods at the industrial scale are still necessary for such innovative applications.

Disclosure statement

No potential conflict of interest was reported by the author(s).

Funding

K. Edalati thanks the Ministry of Education, Culture, Sports, Science and Technology of Japan (MEXT) for Grants-in-Aid for Scientific Research [grant numbers JP19H05176 and JP21H00150]. W.J. Botta acknowledges the financial support from the Brazilian agencies CAPES, CNPq and FAPESP. S. Divinski acknowledges financial support by the German Research Foundation (DFG) [Research Grant DI 1419/16-1]. N.A. Enikeev acknowledges the support by the 'Metals and Alloys under Extreme Impacts' Laboratory of Eurasian Center of Excellence (Ufa, Russia) via a state asignment [No. 0.75-03-2021-014/4] by the Ministry of Education and Science of the Russian Federation. T. Grosdidier acknowledges the French State through the program "Investment in the Future" operated by the National Research Agency (ANR) and referenced by ANR-11-LABX-0008-01 (LabEx DAMAS). Z. Horita thanks the Ministry of Education, Culture, Sports, Science and Technology of Japan (MEXT) for Grants-in-Aid for Scientific Research [grant numbers JP19H00830 and JP20H00312]. Y. Ikoma thanks the Ministry of Education, Culture, Sports,

Science and Technology of Japan (MEXT) for a Grant-in-Aid for Scientific Research [grant number JP18H01384]. M. Kawasaki acknowledges the support from the National Science Foundation of the United States [grant number DMR-1810343]. D.R. Leiva acknowledges the financial support from the Brazilian agencies CAPES, CNPq and FAPESP. V.I. Levitas appreciates support from National Science Foundation of the USA [grant numbers CMMI-1943710 and DMR-1904830], and Iowa State University (Vance Coffman Faculty Chair Professorship). V.V. Popov and E.N. Popova's contribution was carried out within the State Assignment of Russian Federation on themes 'Pressure' and 'Function'. B.B. Straumal acknowledges the support of the Russian Ministry of Science and Higher Education [Contract Number 075-15-2021-945 and grant number 13.2251.21.0013]. L.S. Toth acknowledges the French State through the program "Investment in the Future"operated by the National Research Agency (ANR) and referenced by ANR-11-LABX-0008-01 (LabEx DAMAS). N. Tsuji appreciates the financial supports from the Ministry of Education, Culture, Sports, Science and Technology of Japan (MEXT) through Elements Strategy Initiative for Structural Materials (ESISM, JPMXP0112101000), KAKENHI program of the Japan Society for the Promotion of Science (JSPS) [grant number JP20H00306] and CREST program of the Japan Science and Technology Agency (JST) [grant number JPMJCR1994]. R.Z. Valiev was supported by a grant of the Russian Science Foundation [grant number 20-63-47027]. G. Wilde acknowledges financial support by the German Research Foundation (DFG) [grant number WI 1899/32-1]. X. Zhu acknowledges financial support by the National Natural Science Foundation of China (NSFC) [grant numbers 51664033, 51561015 and 51501078].

ORCID

Kaveh Edalati http://orcid.org/0000-0003-3885-2121
Andrea Bachmaier http://orcid.org/0000-0001-7207-2917
Yan Beygelzimer http://orcid.org/0000-0002-1321-8565
Sergiy Divinski http://orcid.org/0000-0003-1935-9542
Nariman A. Enikeev http://orcid.org/0000-0002-7503-8949
Yuri Estrin http://orcid.org/0000-0001-7784-5704
Masayoshi Fuji http://orcid.org/0000-0003-3429-1435
Jenő Gubicza http://orcid.org/0000-0002-8938-7293
Anton Hohenwarter http://orcid.org/0000-0001-9827-9828
Yoshifumi Ikoma http://orcid.org/0000-0001-5483-464X
Megumi Kawasaki http://orcid.org/0000-0003-0028-3007
Terence G. Langdon http://orcid.org/0000-0003-3541-9250
Valery I. Levitas http://orcid.org/0000-0001-8556-4419
Terukazu Nishizaki http://orcid.org/0000-0002-5403-0585
Satyam Suwas http://orcid.org/0000-0002-1722-6650
Nobuhiro Tsuji http://orcid.org/0000-0002-2132-1327
Ruslan Z. Valiev http://orcid.org/0000-0003-4340-4067
Michael J. Zehetbauer http://orcid.org/0000-0001-8430-8587

References

[1] Valiev RZ, Islamgaliev RK, Alexandrov IV. Bulk nanostructured materials from severe plastic deformation. Prog Mater Sci. 2000;45:103–189.
[2] Valiev RZ, Estrin Y, Horita Z, et al. Producing bulk ultrafine-grained materials by severe plastic deformation. JOM. 2006;58:33–39.
[3] Segal VM. Review: modes and processes of severe plastic deformation (SPD). Materials. 2018;11:1175.
[4] Beloshenko V, Vozniak I, Beygelzimer Y, et al. Severe plastic deformation of polymers. Mater Trans. 2019;60:1192–1202.
[5] Edalati K. Review on recent advancement in severe plastic deformation of oxides by high-pressure torsion (HPT). Adv Eng Mater. 2019;21:1800272.
[6] Révész Á, Kovács Z. Severe plastic deformation of amorphous alloys. Mater Trans. 2019;60:1283–1293.
[7] Gao Y, Ma Y, An Q, et al. Shear driven formation of nano-diamonds at sub-gigapascals and 300 K. Carbon. 2019;146:364–368.
[8] Ikoma Y. Severe plastic deformation of semiconductor materials using high-pressure torsion. Mater Trans. 2019;60:1168–1176.
[9] Edalati K. Metallurgical alchemy by ultra-severe plastic deformation via high-pressure torsion process. Mater Trans. 2019;60:1221–1229.
[10] Durand-Charre M. La Microstructure des aciers et desfontes [Microstructure of steels and cast irons]. Paris: Gense et Interpretation Ed. SIRPE; 2003.
[11] Lapérouse J. Metallurgy: early metallurgy in Mesopotamia. In: Selin H, editor. Encyclopaedia of the history of science, technology, and medicine in non-western cultures 2nd ed. Berlin: Springer-Verlag; 2008. p. 1632.
[12] Durand-Charre M. Damascus and pattern-welded steels, forging blades since the iron age. Les Ulis: EDP Sciences; 2014.
[13] Bridgman PW. Studies in large plastic flow and fracture. New York (NY): McGraw-Hill; 1952.
[14] Erbel S. Mechanizm zmian własności metali poddanych wielkim odkształceniom [Mechanism of change of properties of metals subjected to large deformation]. Warszawa: Wydawnictwa PW; 1976.
[15] Sevillano J G, van Houtte P, Aernoudt E. Large strain work hardening and textures. Prog Mater Sci. 1981;25:69–412.
[16] Valiev RZ, Kaibyshev OA, Kuznetsov RI, et al. Low-temperature superplasticity of metallic materials. Dokl Akad Nauk SSSR. 1988;301:864–866.
[17] Gore A. An inconvenient truth: the planetary emergency of global warming and what we can do about it. New York (NY): Rodale Press; 2006.
[18] Horita Z, Edalati K. Severe plastic deformation for nanostructure controls. Mater Trans. 2020;61:2241–2247.
[19] Bridgman PW. Effects of high shearing stress combined with high hydrostatic pressure. Phys Rev. 1935;48:825–847.
[20] Segal VM, Reznikov VI, Drobyshevskiy AE, et al. Plastic working of metals by simple shear. Russ Metall. 1981;1:99–105.
[21] Saito Y, Tsuji N, Utsunomiya H, et al. Ultra-fine grained bulk aluminum produced by accumulative roll-bonding (ARB) process. Scr Mater. 1998;39:1221–1227.
[22] Beygelzimer YY, Varyukhin VN, Synkov SG, et al. New techniques for accumulating large plastic deformations

using hydroextrusion. Fizika and Tekhnika Vysokikh Davlenii. 1999;9:109–110.
[23] Valiahmetov OR, Galeyev RM, Salishchev GA. Mechanical properties of VT 8 Ti-alloy of submicrocrystalline structure. Fiz Met Metalloved. 1990;10:204–206.
[24] Wen M, Liu G, Gu JF, et al. Dislocation evolution in titanium during surface severe plastic deformation. Appl Surf Sci. 2009;255:6097–6102.
[25] Sachse M, Knighton P. Damascus steel myth, history, technology, applications. 3rd ed. Stahleisen: Düsseldorf Verl; 2008.
[26] Verhoeven JD. The mystery of Damascus blades. Sci Am. 2001;284:74–79.
[27] Reibold M, Paufler P, Levin AA, et al. Carbon nanotubes in an ancient Damascus sabre. Nature. 2006;444:286.
[28] Sanderson K. Sharpest cut from nanotube sword. Nature. 2006. https://doi.org/10.1038/news061113-11.
[29] Hjardar K, Vike V. Vikings at war. Oxford: Casemate Publishers; 2016.
[30] Fedrigo A, Grazzi F, Williams AR, et al. Extraction of archaeological information from metallic artefacts - a neutron diffraction study on Viking swords. J Archaeol Sci Rep. 2017;12:425–436.
[31] Sherby OD, Wadsworth J. Damascus steels. Sci Am. 1985;252:112–121.
[32] Wang JT. Historic retrospection and present status of severe plastic deformation in China. Mater Sci Forum. 2006;503-504:363–370.
[33] Weber M, Banaschak S, Rothschild MA. Sharp force trauma with two katana swords: identifying the murder weapon by comparing tool marks on the skull bone. Int J Legal Med. 2021;135:313–322.
[34] http://www.city.sakurai.lg.jp/yamato-travel/destination/area01/spot07/.
[35] Wadsworth J. Archeometallurgy related to swords. Mater Charact. 2015;99:1–7.
[36] Roberts WL. Cold rolling of steel. New York, Basel: Marcel Dekker Inc.; 1978.
[37] Benjamin EO. Rubber products and method of making the same. US Patent 1,409,275. 1922.
[38] Benjamin EO. Soft rubber product and method of making it. US Patent 1,493,062. 1924.
[39] Delbert MC, Heights N. Laminar electrode including hydrophobic and hydrophilic layers; methods of making; fuel cell therewith; and method of using fuel cell. US Patent 3,457,113. 1969.
[40] Bice HC, Bro MI, Dalton JR. Propellant grain with alternation layers of encapsulated fuel and oxidizer. US Patent 3,995,559. 1976.
[41] Avery DH, Backofen WA. A structural basis for superplasticity. Trans ASM. 1965;58:551–562.
[42] Przybysz JX, Ginsberg DM. Electronic thermal conductivity of superconducting lead-manganese and indium-manganese alloy films. Phys Rev B. 1976;14:1039–1044.
[43] Mrstik BJ, Ginsberg DM. Electron thermal conductivity of superconducting films of indium-gadolinium and lead-gadolinium alloys. Phys Rev B. 1973;7:4844–4850.
[44] Miura I. Introduction to the foil metallurgy; 1966.
[45] Kikuchi S, Kuwahara H, Mazaki N, et al. Mechanical properties of Ag-Ni super-laminates produced by rolling. Mater Sci Eng A. 1997;234-236:1114–1117.
[46] Metenier P, González-Doncel G, Ruano OA, et al. Superplastic behavior of a fine-grained two-phase Mg-9wt.%Li alloy. Mater Sci Eng A. 1990;125:195–202.
[47] Edalati K, Horita Z. A review on high-pressure torsion (HPT) from 1935 to 1988. Mater Sci Eng A. 2016;652:325–352.
[48] Smithsonian Institution Archives, Image # SIA2008-0025.
[49] Bridgman PW. Shearing phenomena at high pressures, particularly in inorganic compounds. Proc Am Acad Arts Sci. 1937;71:387–460.
[50] Bridgman PW. Flow phenomena in heavily stressed metals. J Appl Phys. 1937;8:328–336.
[51] Larsen ES, Bridgman PW. Shearing experiments on some selected minerals and mineral combinations. Am J Sci. 1938;36:81–94.
[52] Bridgman PW. The effect of pressure on several properties of the alloys of bismuth-tin and of bismuth-cadmium. Proc Am Acad Arts Sci. 1953;82:101–156.
[53] Bridgman PW. Shearing phenomena at high pressure of possible importance for geology. J Geol. 1936;44:653–669.
[54] Boyd J, Robertson BP. The friction properties of various lubricants at high pressures. Trans ASME. 1945;67:51–59.
[55] Vereshchagin FL, Shapochkin VA. Effect of hydrostatic pressure on the shear stress in solid state. Fiz Met Metalloved. 1960;9:258–264.
[56] Griggs DT, Turner EJ, Heard HC. Deformation of rocks at 500°C to 800°C. Geol Soc Am Mere. 1960;79:39–104.
[57] Riecker RE. New shear apparatus for temperatures of 1000°C and pressures of 50 kilobars. Rev Sci Instrum. 1964;35:596–599.
[58] Abey AE, Stromberg HD. 70 kilobar shear apparatus. Rev Sci Instrum. 1969;40:557–559.
[59] Aksenenkov VV, Blank VD, Konyayev YS, et al. Investigation of phase equilibria in a diamond chamber for shear at pressures up to 25.0 GPa. Phys Met Metallogr. 1984;57:159–162.
[60] Paterson MS, Olgaard DL. Rock deformation tests to large shear strains in torsion. J Struct Geol. 2000;22:1341–1358.
[61] Jesser WA, Kuhlmann-Wilsdorf D. The flow stress and dislocation structure of nickel deformed at very high pressure. Mater Sci Eng. 1972;9:111–117.
[62] Erbel S. Mechanical properties and structure of extremely strain-hardened copper. Met Technol. 1979;6:482–486.
[63] Saunders I, Nutting J. Deformation of metals to high strains using combination of torsion and compression. Met Sci. 1984;18:571–575.
[64] Zhorin VA, Shashkin DP, Enikolopian NS. Dynamics of solid solution formation in Cu-Ni mixture under plastic flow at high pressure. Phys Stat Sol A. 1985;8:437–442.
[65] Smirnova NA, Levit VI, Pilyugin VI, et al. Evolution of structure of fcc. sigle crystals during storing plastic deformation. Phys Met Metallogr. 1986;61:127–134.
[66] Smirnova NA, Levit VI, Pilyugin VI, et al. Low temperature recrystallization of nickel and copper. Phys Met Metallogr. 1986;62:140–144.

[67] Davudova LS, Degtiarev MV, Kuznetsov VI. Structure and properties of martensite structural steels under different straining. Phys Met Metallogr. 1986;61:339–347.
[68] Teplov VA, Pilugin VP, Kuznetsov VI. Phase f.c.c.-b.c.c. transition induced steady deformation under pressure in iron-nickel alloys. Phys Met Metallogr. 1987;64:93–100.
[69] Gil Sevillano J, Aernoudt E. Low energy dislocation structures in highly deformed materials. Mater Sci Eng. 1987;86:35–51.
[70] Aleksandrova MM, Blank VD, Golobokov AE, et al. Amorphisation of gallium antimonide under the conditions of shear deformation under pressure. Phys Stat Sol A. 1988;105:K29–K32.
[71] Teplov VA, Korshunov LG, Shabashov VA, et al. Structural transformations of high-manganese austenitic steels during deformation by shear under pressure. Phys Met Metallogr. 1988;66:135–143.
[72] Ivanov E, Neverov V, Jitnikov N, et al. Nucleation of phases in Ni-Al deformed in Bridgman anvils. Mater Lett. 1988;7:57–60.
[73] Valiev RZ, Mulyukov RR, Ovchinnikov VV. Direction of grain-boundary phase in submicrometre-grained iron. Philos Mag Lett. 1990;62:253–256.
[74] Abdulov RZ, Valiev RZ, Krasilnikov NA. Formation of submicrometre-grained structure in magnesium alloy due to high plastic strains. J Mater Sci Lett. 1990;9:1445–1447.
[75] Valiev RZ, Krasilnikov NA, Tsenev NK. Plastic deformation of alloys with submicron-grained structure. Mater Sci Eng A. 1991;137:35–40.
[76] Toews PJ. Doughnut machine. US Patent 2,207,560. 1940.
[77] Fisch RA. Curved extrusion process and apparatus. US Patent 2,728,104. 1955.
[78] Nolf CA. Spiral extrusion. US Patent 2,859,869. 1958.
[79] Aitchison L. A history of metals. London: Macdonald & Evans; 1960.
[80] Wright RN. Wire technology: process engineering and metallurgy. New York: Butterworth-Heinemann; 2014.
[81] Rigney DA. Dislocation content at large plastic strains. Scr Metall. 1979;13:353–354.
[82] Nutting J. Some aspects of structure property relationships in materials. In: Thomas G, Fulrath RM, Fisher RM, editors. Proceedings of the Electron Microscopy and Structure of Materials. Berkeley: University of California Press; 1971. p. 617–636.
[83] Segal VM. Methods of stress-strain analyses in metal forming [dissertation]. Minsk: Physical Technical Institute Academy of Sciences of Buelorussia;1974.
[84] Segal VM. Materials preparation for following processing. USSR Invention Certificate 575,892. 1977.
[85] Kopylov VI, Segal VM. A device for continuous pressing of metals. USSR Invention Certificate 575,151. 1977.
[86] Segal VM, Reznikov VI, Kopylov VI, et al. Processes of plastic structure formation in metals. Minsk: Nauka I Tehnika; 1994.
[87] Segal VM. Materials processing by simple shear. Mater Sci Eng A. 1995;197:157–164.
[88] Iwahashi Y, Wang J, Horita Z, et al. Principle of equal-channel angular pressing for the processing of ultra-fine grained materials. Scr Mater. 1996;35:143–146.
[89] Rigney DA, Naylor MGS, Divakar R, et al. Low energy dislocation structures caused by sliding and by particle impact. Mater Sci Eng. 1986;81:409–425.
[90] Kuo SM, Rigney DA. Sliding behavior of aluminum. Mater Sci Eng A. 1992;157:131–143.
[91] Lu K, Lu J. Surface nanocrystallization (SNC) of metallic materials-presentation of the concept behind a new approach. J Mater Sci Technol. 1999;15:193–197.
[92] Bryła K, Edalati K. Historical studies by polish scientist on ultrafine-grained materials by severe plastic deformation. Mater Trans. 2019;60:1553–1560.
[93] Wilde G, Ribbe J, Reglitz G, et al. Plasticity and grain boundary diffusion at small grain sizes. Adv Eng Mater. 2010;12:758–764.
[94] Kawasaki M, Figueiredo RB, Langdon TG. An investigation of hardness homogeneity throughout disks processed by high-pressure torsion. Acta Mater. 2011;59:308–316.
[95] Edalati K, Cubero-Sesin JM, Alhamidi A, et al. Influence of severe plastic deformation at cryogenic temperature on grain refinement and softening of pure metals: investigation using high-pressure torsion. Mater Sci Eng A. 2014;613:103–110.
[96] Chinh NQ, Szommer P, Horita Z, et al. Experimental evidence for grain-boundary sliding in ultrafine-grained aluminum processed by severe plastic deformation. Adv Mater. 2006;18:34–39.
[97] Schwartz AJ, Kumar M, Adams BL, et al. Electron backscatter diffraction in materials science. 2nd ed Boston: Springer; 2009.
[98] Chen YJ, Hjelen J, Roven HJ. Application of EBSD technique to ultrafine grained and nanostructured materials processed by severe plastic deformation: sample preparation, parameters optimization and analysis. Trans Nonferrous Met Soc China. 2012;22:1801–1809.
[99] Pippan R, Scheriau S, Taylor A, et al. Saturation of fragmentation during severe plastic deformation. Annu Rev Mater Res. 2010;40:319–343.
[100] Meyers MA, Mishra A, Benson DJ. The deformation physics of nanocrystalline metals: experiments, analysis, and computations. JOM. 2006;58:41–48.
[101] Popov VV, Stolbovkiy AV, Popova EN, et al. Structure and thermal stability of Cu after severe plastic deformation. Defect Diffus Forum. 2010;297-301:1312–1321.
[102] Edalati K, Hashiguchi Y, Iwaoka H, et al. Long-time stability of metals after severe plastic deformation: softening and hardening by self-annealing vursus thermal stability. Mater Sci Eng A. 2018;729:340–348.
[103] Kwon YJ, Shigematsu I, Saito N. Production of ultra-fine grained aluminum alloy by friction stir process. J Jpn Inst Met. 2002;66:1325–1332.
[104] Huang JY, Zhu YT, Jiang HG, et al. Microstructures and dislocation configurations in nanostructured Cu processed by repetitive corrugation and straightening. Acta Mater. 2001;49:1497–1505.
[105] Kurzydlowski KJ. Hydrostatic extrusion as a method of grain refinement in metallic materials. Mater Sci Forum. 2006;503-504:341–348.
[106] Richert J, Richert M, Zasadziński A, et al. A method of plastic processing of metals and alloys and a device

for plastic processing of metals and alloys. PL Patent 123,026. 1979.
[107] Korbel A, Bochniak W. Method of plastic forming of materials. US Patent 5,737,959. 1998.
[108] Shin DH, Park JJ, Kim YS, et al. Constrained groove pressing and its application to grain refinement of aluminum. Mater Sci Eng A. 2002;328:98–103.
[109] Fujioka T, Horita Z. Development of high-pressure sliding process for microstructural refinement of rectangular metallic sheets. Mater Trans. 2009;50:930–933.
[110] Estrin Y, Vinogradov A. Extreme grain refinement by severe plastic deformation: a wealth of challenging science. Acta Mater. 2013;61:782–817.
[111] Faraji G, Torabzadeh H. An overview on the continuous severe plastic deformation methods. Mater Trans. 2019;60:1316–1330.
[112] Lowe TC, Valiev RZ, Li X, et al. Commercialization of bulk nanostructured metals and alloys. MRS Bull. 2021;46:265–272.
[113] Zhilyaev AP, Langdon TG. Using high-pressure torsion for metal processing: fundamentals and applications. Prog Mater Sci. 2008;53:893–979.
[114] Edalati K, Uehiro R, Fujiwara K, et al. Ultra-severe plastic deformation: evolution of microstructure, phase transformation and hardness in immiscible magnesium-based systems. Mater Sci Eng A. 2017;701:158–166.
[115] Blank VD, Popov MY, Kulnitskiy BA. The effect of severe plastic deformations on phase transitions and structure of solids. Mater Trans. 2019;60:1500–1505.
[116] Xu C, Horita Z, Langdon TG. The evolution of homogeneity in an aluminum alloy processed using high-pressure torsion. Acta Mater. 2008;56:5168–5176.
[117] Pereira PHR, Figueiredo RB. Finite element modelling of high-pressure torsion: an overview. Mater Trans. 2019;60:1139–1150.
[118] Edalati K, Lee DJ, Nagaoka T, et al. Real hydrostatic pressure in high-pressure torsion measured by bismuth phase transformations and FEM simulations. Mater Trans. 2016;57:533–538.
[119] Figueiredo RB, Cetlin PR, Langdon TG. Using finite element modeling to examine the flow processes in quasi-constrained high-pressure torsion. Mater Sci Eng A. 2011;528:8198–8204.
[120] Kim HS. Finite element analysis of high-pressure torsion processing. J Mater Process Technol. 2001;113:617–621.
[121] Kamrani M, Levitas VI, Feng B. FEM simulation of large deformation of copper in the quasi-constrain high-pressure-torsion setup. Mater Sci Eng A. 2017;705:219–230.
[122] Hohenwarter A, Pippan R. Sample size and strain-rate-sensitivity effects on the homogeneity of high-pressure torsion deformed disks. Metall Mater Trans A. 2019;50:601–608.
[123] Sakai G, Nakamura K, Horita Z, et al. Developing high-pressure torsion for use with bulk samples. Mater Sci Eng A. 2005;406:268–273.
[124] Figueiredo RB, De Faria GCV, Cetlin P, et al. Three-dimensional analysis of plastic flow during high-pressure torsion. J Mater Sci. 2013;48:4524–4532.
[125] Cao Y, Wang YB, Alhajeri SN, et al. A visualization of shear strain in processing by high-pressure torsion. J Mater Sci. 2010;45:765–770.
[126] Cao Y, Kawasaki M, Wang YB, et al. Unusual macroscopic shearing patterns observed in metals processed by high-pressure torsion. J Mater Sci. 2010;45:4545–4553.
[127] Cao Y, Wang YB, Figueiredo RB, et al. Three-dimensional shear-strain patterns induced by high-pressure torsion and their impact on hardness evolution. Acta Mater. 2011;59:3903–3914.
[128] Jiang W, Zhou H, Cao Y, et al. On the heterogeneity of local shear strain induced by high-pressure torsion. Adv Eng Mater. 2020;22:1900477.
[129] Edalati K, Miresmaeili R, Horita Z, et al. Significance of temperature increase in processing by high-pressure torsion. Mater Sci Eng A. 2011;528:7301–7305.
[130] Figueiredo RB, Pereira PHR, Aguilar MTP, et al. Using finite element modeling to examine the temperature distribution in quasi-constrained high-pressure torsion. Acta Mater. 2012;60:3190–3198.
[131] Pereira PHR, Figueiredo RB, Huang Y, et al. Modeling the temperature rise in high-pressure torsion. Mater Sci Eng A. 2014;593:185–188.
[132] Saito Y, Utsunomiya H, Tsuji N, et al. Novel ultra-high straining process for bulk materials development of the accumulative roll-bonding (ARB) process. Acta Mater. 1999;47:579–583.
[133] Edalati K, Horita Z. Application of high-pressure torsion for consolidation of ceramic powders. Scr Mater. 2010;63:174–177.
[134] Razavi-Khosroshah H, Fuji M. Development of metal oxide high-pressure phases for photocatalytic properties by severe plastic deformation. Mater Trans. 2019;60:1203–1208.
[135] Edalati K, Horita Z. Scaling-up of high pressure torsion using ring shape. Mater Trans. 2009;50:92–95.
[136] Edalati K, Horita Z. Continuous high-pressure torsion. J Mater Sci. 2010;45:4578–4582.
[137] Edalati K, Lee S, Horita Z. Continuous high-pressure torsion using wires. J Mater Sci. 2012;47:473–478.
[138] Hohenwarter A. Incremental high pressure torsion as a novel severe plastic deformation process: processing features and application to copper. Mater Sci Eng A. 2015;626:80–85.
[139] Shigeno E, Komatsu T, Sumikawa K, et al. Combination of high-pressure torsion with incremental feeding for upsizing sample. Mater Trans. 2018;59:1009–1012.
[140] Ivanisenko Y, Kulagin R, Fedorov V, et al. High pressure torsion extrusion as a new severe plastic deformation process. Mater Sci Eng A. 2016;664:247–256.
[141] Takizawa Y, Sumikawa K, Watanabe K, et al. Incremental feeding high-pressure sliding for grain refinement of large-scale sheets: application to Inconel 718. Metall Mater Trans A. 2018;49:1830–1840.
[142] Vu VQ, Toth LS, Beygelzimer Y, et al. Microstructure, texture and mechanical properties in aluminum produced by friction-assisted lateral extrusion. Materials. 2021;14:2465.
[143] Horita Z, Tang Y, Masuda T, et al. Severe plastic deformation under high pressure: upsizing sample dimensions. Mater Trans. 2020;61:1177–1190.
[144] Masuda T, Horita Z. Grain refinement of AZ31 and AZ61 Mg alloys through room temperature processing

by up-scaled high-pressure torsion. Mater Trans. 2019;60:1104–1110.
[145] Toth LS, Arzaghi M, Fundenberger JJ, et al. Severe plastic deformation of metals by high-pressure tube twisting. Scr Mater. 2009;60:175–177.
[146] Bouaziz O, Estrin Y, Kim HS. A new technique for severe plastic deformation: the cone-cone method. Adv Eng Mater. 2009;11:982–985.
[147] Pougis A, Toth LS, Bouaziz O, et al. Stress and strain gradients in high-pressure tube twisting. Scr Mater. 2012;66:773–776.
[148] Wang JT, Li Z, Wang J, et al. Principles of severe plastic deformation using tube high-pressure shearing. Scr Mater. 2012;67:810–813.
[149] Pougis A. Affinement de microstructures de métaux par des déformations plastiques extremes [dissertation]. Lorraine University; 2013.
[150] Lapovok R, Qi Y, Ng HP, et al. Gradient structures in thin-walled metallic tubes produced by continuous high pressure tube shearing process. Adv Eng Mater. 2017;19:1700345.
[151] Gu CF, Toth LS, Arzaghi M, et al. Effect of strain path on grain refinement in severely plastically deformed copper. Scr Mater. 2011;64:284–287.
[152] Arzaghi M. New severe plastic deformation process for tubes [dissertation]. Metz: Paul Verlain University; 2010.
[153] Chen C. Textures and Microstructures in Al, Cu and Mg under Severe Plastic Deformation [dissertation]. France: Lorraine University; 2016.
[154] Arzaghi M, Fundenberger JJ, Toth LS, et al. Microstructure, texture and mechanical properties of aluminum processed by high-pressure tube twisting. Acta Mater. 2012;60:4393–4408.
[155] Li Z, Zhang PF, Yuan H, et al. Principle of one-step synthesis for multilayered structures using tube high-pressure shearing. Mater Sci Eng A. 2016;658:367–375.
[156] Toth LS, Chen C, Pougis A, et al. High pressure tube twisting for producing ultra fine grained materials: a review. Mater Trans. 2019;60:1177–1191.
[157] Blank VD, Konyaev YS, Kuznetsov AI, et al. Diamond chamber for examining the effects of shear deformation on the structure and properties of solids at pressures up to 43 GPa. Instrum Exper Tech New York. 1984;27:1240–1242.
[158] Weir CE, Lippincott ER, Van Valkenburg A, et al. Infrared studies in the 1- to I5-micron region to 30,000 atmospheres. J Res Nat Bur Stand Sect A. 1959;63:55–62.
[159] Blank VD, Churkin VD, Kulnitskiy BA, et al. Pressure-induced transformation of graphite and diamond to onions. Crystals. 2018;8:68.
[160] Blank VD, Denisov VN, Kirichenko AN, et al. High pressure transformation of single-crystal graphite to form molecular carbon-onions. Nanotechnology. 2007;18:345601.
[161] Valiev RZ, Langdon TG. Principles of equal-channel angular pressing as a processing tool for grain refinement. Prog Mater Sci. 2006;51:881–981.
[162] Beyerlein IJ, Tóth LS. Texture evolution in equal-channel angular extrusion. Prog Mater Sci. 2009;54:427–510.
[163] Skrotzki W, Scheerbaum N, Oertel CG, et al. Microstructure and texture gradient in ECAP copper deformed by equal channel angular pressing. Acta Mater. 2007;55:2013–2024.
[164] Skrotzki W, Scheerbaum N, Oertel CG, et al. Recrystallization of high-purity aluminum during equal channel angular pressing. Acta Mater. 2007;55:2211–2218.
[165] Kang F, Wang JT, Su YL, et al. Finite element analysis of the effect of back pressure during equal channel angular pressing. J Mater Sci. 2007;42:1491–1500.
[166] Frint S, Hockauf M, Frint P, et al. Scaling up segal's principle of equal channel angular pressing. Mater Des. 2016;97:502–511.
[167] Skrotzki W. Deformation heterogeneities in equal channel angular pressing. Mater Trans. 2019;60:1331–1343.
[168] Tsuji N, Saito Y, Utsunomiya H, et al. Ultra-fine grained bulk steel produced by accumulative roll-bonding (ARB) process. Scr Mater. 1999;40:795–800.
[169] Kamikawa N, Sakai T, Tsuji N. Effect of redundant shear strain on microstructure and texture evolution during accumulative roll-bonding in ultralow carbon IF steel. Acta Mater. 2007;55:5873–5888.
[170] Sato M, Tsuji N, Minamino Y, et al. Formation of nanocrystalline surface layers in various metallic materials by near surface severe plastic deformation. Sci. Technol. Adv Mater. 2004;5:145–152.
[171] Tylecote RF. The solid phase welding of metals. London: Edward Arnold; 1968.
[172] Lenard JG. Primer on fat rolling. Amsterdam: Elsevier; 2007. p. 252–267.
[173] Tsuji N. Accumulative roll-bonding. In: Buschow KHT, Cahn RW, Flemings MC, et al, editors. Encyclopedia of materials: science & technology. Amsterdam: Elsevier; 2011. p. 1–8.
[174] Sakai T, Saito Y, Hirano K, et al. Deformation and recrystallization behavior of low carbon steel in high speed hot rolling. ISIJ Int. 1988;28:1028–1035.
[175] Lee SH, Saito Y, Tsuji N, et al. Role of shear strain in ultragrain refinement by accumulative roll-bonding (ARB) process. Scr Mater. 2002;46:281–285.
[176] Huang X, Tsuji N, Hansen N, et al. Microstructural evolution during accumulative roll-bonding of commercial purity aluminum. Mater Sci Eng A. 2003;340:265–271.
[177] Tsuji N. Formation mechanisms of ultrafine grained structures in severe plastic deformation of metallic materials. Tetsu-to-Hagané. 2008;94:582–589.
[178] Tsuji N, Gholizadeh R, Ueji R, et al. Formation mechanism of ultrafine grained microstructures: various possibilities for fabricating bulk nanostructured metals and alloys. Mater Trans. 2019;60:1518–1532.
[179] Tsuji N, Ito Y, Saito Y, et al. Strength and ductility of ultrafine grained aluminum and iron produced by ARB and annealing. Scr Mater. 2002;47:893–899.
[180] Tsuji N, Okuno S, Koizumi Y, et al. Toughness of ultrafine grained ferritic steels fabricated by ARB and annealing process. Mater Trans. 2004;45:2272–2281.
[181] Tsuji N. Unique mechanical properties of nanostructured metals. J Nanosci Nanotechnol. 2007;7:3765–3770.
[182] Tsuji N. Ways to manage both strength and ductility in nanostructured steels. In: Weng Y, Dong H, Gan Y, editors. Advanced steels, the recent scenario in steel science and technology. Berlin/Heidelberg: Springer-Verlag/Metallurgical Industry Press; 2011. p. 119–130.

[183] Ohsaki S, Kato S, Tsuji N, et al. Bulk mechanical alloying of Cu-Ag and Cu/Zr two-phase microstructures by accumulative roll-bonding process. Acta Mater. 2007;55:2885–2895.
[184] Chen MC, Hsieh HC, Wu W. The evolution of microstructures and mechanical properties during accumulative roll bonding of Al/Mg composite. J Alloys Compd. 2006;416:169–172.
[185] Quadir MZ, Al-Buhamad O, Lau KD, et al. The effect of initial microstructure and processing temperature on microstructure and texture in multilayered Al/Al(Sc) ARB sheets. Int J Mater Res. 2009;100:1705–1714.
[186] Wu K, Chang H, Maawad E, et al. Microstructure and mechanical properties of the Mg/Al laminated composite fabricated by accumulative roll bonding (ARB). Mater Sci Eng A. 2010;527:3073–3078.
[187] Chekhonin P, Beausir B, Scharnweber J, et al. Confined recrystallization of high-purity aluminium during accumulative roll bonding of aluminium laminates. Acta Mater. 2012;60:4661–4671.
[188] Beyerlein IJ, Mara NA, Carpenter JS, et al. Interface-driven microstructure development and ultra high strength of bulk nanostructured Cu-Nb multilayers fabricated by severe plastic deformation. J Mater Res. 2013;28:1799–1812.
[189] Chekhonin P, Scharnweber J, Scharnweber M, et al. Mechanical properties of aluminium laminates produced by accumulative roll bonding. Cryst Res Technol. 2013;48:532–537.
[190] Koseki T, Inoue J, Nambu S. Development of multilayer steels for improved combinations of high strength and high ductility. Mater Trans. 2014;55:227–237.
[191] Quadir MZ, Najafzadeh N, Munroe PR. Variations in through-thickness recrystallization and grain growth textures in the Al layers in ARB-processed Al/Al(0.3% Sc) composite sheets. Mater Des. 2016;93:467–473.
[192] Ebrahimi SHS, Dehghani K, Aghazadeh J, et al. Investigation on microstructure and mechanical properties of Al/Al-Zn-Mg-Cu laminated composite fabricated by accumulative roll bonding (ARB) process. Mater Sci Eng A. 2018;718:311–320.
[193] Höppel HW, Westermeyer M, Kümmel F, et al. The role of interfaces on the deformation mechanisms in bimodal Al laminates produced by accumulative roll bonding. Adv Eng Mater. 2020;22:2000145.
[194] Zhu Y, Ameyama K, Anderson PM, et al. Heterostructured materials: superior properties from hetero-zone interaction. Mater Res Lett. 2021;9:1–31.
[195] Tsuji N. New routes for fabricating ultrafine-grained microstructures in bulky sheets without very-high strains. Adv Eng Mater. 2010;12:701–707.
[196] Tekko Shinbun, Newspaper, Japan. 2008 May 26.
[197] Beygelzimer Y, Orlov D, Varyukhin V. A new severe plastic deformation method: twist extrusion. In: Zhu YT, Langdon TG, Mishra RS, et al, editors. Seattle (WA): TMS Annual Meeting; 2002; p. 297–304.
[198] Beygelzimer Y, Varyukhin V, Orlov D, et al Microstructural evolution of titanium under twist extrusion. In: Zhu Y, Langdon T, Mishra R, et al, editors. Seattle (WA): TMS Annual Meeting; 2002; p. 43–46.
[199] Beygelzimer Y, Varyukhin V, Orlov D, et al. Twist extrusion-process for strain accumulation. Donetsk: TEAN; 2003.
[200] Beygelzimer Y, Kulagin R, Estrin Y, et al. Twist extrusion as a potent tool for obtaining advanced engineering materials: a review. Adv Eng Mater. 2017;19:1600873.
[201] Bagherpour E, Pardis N, Reihanian M, et al. An overview on severe plastic deformation: research status, techniques classification, microstructure evolution, and applications. Int J Adv Manuf Technol. 2019;100:1647–1694.
[202] Yalçinkaya T, Şimşek Ü, Miyamoto H, et al. Numerical analysis of a new nonlinear twist extrusion process. Metals. 2019;9:513.
[203] Macháčková A. Decade of twist channel angular pressing: a review. Materials. 2020;13:1725.
[204] Joudaki J, Safari M, Alhosseini SM. New die design configuration for grain refinement by hollow twist extrusion (HTE) process. Met Mater Int. 2021;27:667–675.
[205] Fouad DM, El-Garaihy WH, Ahmed MMZ, et al. Grain structure evolution and mechanical properties of multi-channel spiral twist extruded AA5083. Metals. 2021;11:1276.
[206] Özbeyaz K, Kaya H, Kentli A. Novel SPD method: twisted variable channel angular extrusion. Met Mater Int. 2022. Forthcoming. doi:10.1007/s12540-021-01086-4
[207] Wang C, Li F, Li Q, et al. A novel severe plastic deformation method for fabricating ultrafine grained pure copper. Mater Des. 2013;43:492–498.
[208] Beygelzimer Y, Kulagin R, Latypov MI, et al. Off-axis twist extrusion for uniform processing of round bars. Met Mater Int. 2015;21:734–740.
[209] Segal VM. Severe plastic deformation: simple shear versus pure shear. Mater Sci Eng A. 2002;338:331–344.
[210] Beygelzimer Y. Vortices and mixing in metals during severe plastic deformation. Mater Sci Forum. 2011;683:213–224.
[211] Nouri M, Mohammadian Semnani H, Emadoddin E. Computational and experimental studies on the effect back pressure on twist extrusion process. Met Mater Int. 2021;27:2910–2918.
[212] Beygelzimer Y, Varyukhin V, Synkov S. Shear, vortices, and mixing during twist extrusion. Int J Mater Form. 2008;1:443–446.
[213] Kulagin R, Latypov M, Kim HS, et al. Cross flow during twist extrusion: theory, experiment, and application. Metall Mater Trans A. 2013;44:3211–3220.
[214] Beygelzimer Y, Varyukhin V, Kulagin R, et al. Twist extrusion in severe plastic deformation technology. In: Rosochowski A, Scotland: Whittles Publishing; 2017. p. 202–234.
[215] Beygelzimer YE, Pavlenko DV, Synkov OS, et al. The efficiency of twist extrusion for compaction of powder materials. Powder Metall Met Ceram. 2019;58:7–12.
[216] Boguslaev VA, Kotsyuba V, Pavlenko DV. Modernisation of press equipment for realisation of severe plastic deformation technology for aviation alloys. Technol Syst. 2017;4:7–14.
[217] Pavlenko DV, Tkach DV, Kotsyuba VY, et al. Analysis of submicrocrystalline structure formation conditions in iron-nickel alloys with helical extrusion. Met Sci Heat Treat. 2017;59:272–277.

[218] Beygelzimer Y, Estrin Y, Kulagin R. Synthesis of hybrid materials by severe plastic deformation: a new paradigm of SPD processing. Adv Eng Mater. 2015;17:1853–1861.
[219] Prokofeva OV, Beigelzimer YE, Kulagin RY, et al. Producing of ultrafine grained composites with a large uniform elongation by twist extrusion: mathematical simulation. Russ Metall. 2017;3:226–230.
[220] Prokofeva OV, Beygelzimer YY, Usov VV, et al. Formation of a gradient structure in a material by twist extrusion. Russ Metall. 2020;5:573–578.
[221] Meyer GE, Henning HJ. Beryllium wrought products, defense metals information center. Battelle Memorial Institute; 1970.
[222] Salishchev G, Zaripova R, Galeev R, et al. Nanocrystalline structure formation during severe plastic deformation in metals and their deformation behaviour. Nanostruct Mater. 1995;6:913–916.
[223] Ghosh AK, Huang W. Severe deformation based process for grain subdivision and resulting microstructures. In: Lowe TC, Valiev RZ, editors. Investigations and applications of severe plastic deformation. Dordrecht: Springer; 2000. p. 29–36.
[224] Belyakov A, Sakai T, Miura H. Microstructure and deformation behaviour of submicrocrystalline 304 stainless steel produced by severe plastic deformation. Mater Sci Eng A. 2001;319:867–871.
[225] Sitdikov O, Sakai T, Goloborodko A, et al. Effect of pass strain on grain refinement in 7475 Al alloy during hot multidirectional forging. Mater Trans. 2004;45:2232–2238.
[226] Bing L, Teng BG, Luo DG. Effects of passes on microstructure evolution and mechanical properties of Mg-Gd-Y-Zn-Zr alloy during multidirectional forging. Acta Metall Sin Engl Lett. 2018;31:1009–1018.
[227] Lee JW, Park JJ. Numerical and experimental investigations of constrained groove pressing and rolling for grain refinement. J Mater Process Technol. 2002;130-131:208–213.
[228] Faraji G, Kim HS, Torabzadeh H. Severe plastic deformation: methods, processing and properties. Amsterdam: Elsevier; 2018.
[229] Zhong HS ZY, Kim TH, Holm EA, et al. Effects of constraint and strain path on evolution of ultrafine grained microstructure by multi-axial alternative forging. Mater Sci Forum. 2005;475-479:3471–3474.
[230] Montazeri-Pour M, Parsa MH, Khajezade A, et al. Multi-axial incremental forging and shearing as a new severe plastic deformation processing technique. Adv Eng Mater. 2015;17:1197–1207.
[231] Huang H, Zhang J. Microstructure and mechanical properties of AZ31 magnesium alloy processed by multidirectional forging at different temperatures. Mater Sci Eng A. 2016;674:52–58.
[232] Miura H, Iwama Y, Kobayashi M. Comparisons of microstructures and mechanical properties of heterogeneous nano-structure induced by heavy cold rolling and ultrafine-grained structure by multi-directional forging of Cu-Al alloy. Mater Trans. 2019;60:1111–1115.
[233] Miura H, Kobayashi M, Aoba T, et al. An approach for room-temperature multi-directional forging of pure titanium for strengthening. Mater Sci Eng A. 2018;731:603–608.
[234] Ito Y, Hoshi N, Hayakawa T, et al. Mechanical properties and biological responses of ultrafine-grained pure titanium fabricated by multi-directional forging. Mater Sci Eng B. 2019;245:30–36.
[235] Eskandarzade M, Masoumi A, Faraji G, et al. A new designed incremental high pressure torsion process for producing long nanostructured rod samples. J Alloys Compd. 2017;695:1539–1546.
[236] Faraji G, Kim HS. Review of principles and methods of severe plastic deformation for producing ultrafine-grained tubes. J Mater Sci Technol. 2017;33:905–923.
[237] Samadpour F, Faraji G, Babaie P, et al. Hydrostatic cyclic expansion extrusion (HCEE) as a novel severe plastic deformation process for producing long nanostructured metals. Mater Sci Eng A. 2018;718:412–417.
[238] Savarabadi MM, Faraji G, Zalnezhad E. Hydrostatic tube cyclic expansion extrusion (HTCEE) as a new severe plastic deformation method for producing long nanostructured tubes. J Alloys Compd. 2019;785:163–168.
[239] Chakkingal U, Suriadi AB, Thomson PF. Microstructure development during equal channel angular drawing of Al at room temperature. Scr Mater. 1998;39:677–684.
[240] Chakkingal U, Suriadi AB, Thomson PF. The development of microstructure and the influence of processing route during equal channel angular drawing of pure aluminum. Mater Sci Eng A. 1999;266:241–249.
[241] Pardis N, Chen C, Shahbaz M, et al. Development of new routes of severe plastic deformation through cyclic expansion-extrusion process. Mater Sci Eng A. 2014;613:357–364.
[242] Raab GJ, Valiev RZ, Lowe TC, et al. Continuous processing of ultrafine grained Al by ECAP-conform. Mater Sci Eng A. 2004;382:30–34.
[243] Lee JC, Seok HK, Han JH, et al. Controlling the textures of the metal strips via the continuous confined strip shearing (C2S2) process. Mater Res Bull. 2001;36:997–1004.
[244] Utsunomiya H, Hatsuda K, Sakai T, et al. Continuous grain refinement of aluminum strip by conshearing. Mater Sci Eng A. 2004;372:199–206.
[245] Faraji G, Kim HS, Kashi HT. Chapter 5, Severe plastic deformation for industrial applications. In: Faraji G, Kim HS, Kashi HT, editors. Severe plastic deformation. Amsterdam: Elsevier; 2018. p. 165–186.
[246] Huang Y, Prangnell PB. Continuous frictional angular extrusion and its application in the production of ultrafine-grained sheet metals. Scr Mater. 2007;56:333–336.
[247] Srinivasan R, Chaudhury P, Cherukuri B, et al. Continuous severe plastic deformation processing of aluminum alloys. Final Technical Report for DOE Award DE-FC36-01ID14022. Wright State University; 2006.
[248] Takayama MYY, Tozawa T, Kato H, et al. Microstructural control by means of continuous cyclic bending in a 5083 aluminum alloy. In: Sakai T, Suzuki HG, editors. Proceedings of the Fourth International Conference on Recrystallization and Related Phenomena. Sendai: Japan Institute of Metals; 1999. p. 321–326.
[249] Takayama Y, Miura T, Kato H, et al. Microstructural and textural evolution by continuous cyclic bending

and annealing in a high purity titanium. Mater Trans. 2004;45:2826–2831.
[250] Ji YH, Park JJ. Development of severe plastic deformation by various asymmetric rolling processes. Mater Sci Eng A. 2009;499:14–17.
[251] Lee T, Park CH, Lee SY, et al. Mechanisms of tensile improvement in caliber-rolled high-carbon steel. Met Mater Int. 2012;18:391–396.
[252] Mirsepasi A, Nili-Ahmadabadi M, Habibi-Parsa M, et al. Microstructure and mechanical behavior of martensitic steel severely deformed by the novel technique of repetitive corrugation and straightening by rolling. Mater Sci Eng A. 2012;551:32–39.
[253] Todaka Y, Umemoto M, Koichi T. Comparison of nanocrystalline surface layer in steels formed by air blast and ultrasonic shot peening. Mater Trans. 2004;45:376–379.
[254] Wang X, Li YS, Zhang Q, et al. Gradient structured copper by rotationally accelerated shot peening. J Mater Sci Technol. 2017;33:758–761.
[255] Lu K, Lu J. Nanostructured surface layer on metallic materials induced by surface mechanical attrition treatment. Mater Sci Eng A. 2004;375-377:38–45.
[256] Arifvianto B, Suyitno, Mahardika M, et al. Effect of surface mechanical attrition treatment (SMAT) on microhardness, surface roughness and wettability of AISI 316L. Mater Chem Phys. 2011;125:418–426.
[257] Alikhani Chamgordani S, Miresmaeili R, Aliofkhazraei M. Improvement in tribological behavior of commercial pure titanium (CP-Ti) by surface mechanical attrition treatment (SMAT). Tribol Int. 2018;119:744–752.
[258] Liu G, Lu J, Lu K. Surface nanocrystallization of 316L stainless steel induced by ultrasonic shot peening. Mater Sci Eng A. 2000;286:91–95.
[259] Tang T, Gao Y, Yao L, et al. Development of high-performance energy absorption component based on the structural design and nanocrystallization. Mater Des. 2018;137:214–225.
[260] Chan HL, Ruan HH, Chen AY, et al. Optimization of the strain rate to achieve exceptional mechanical properties of 304 stainless steel using high speed ultrasonic surface mechanical attrition treatment. Acta Mater. 2010;58:5086–5096.
[261] Badreddine J, Rouhaud E, Micoulaut M, et al. Simulation of shot dynamics for ultrasonic shot peening: effects of process parameters. Int J Mech Sci. 2014;82:179–190.
[262] Liu D, Liu DX, Zhang XH, et al. Surface nanocrystallization of 17-4 precipitation-hardening stainless steel subjected to ultrasonic surface rolling process. Mater Sci Eng A. 2018;726:69–81.
[263] Wang ZB, Lu J, Lu K. Fatigue behaviors of AISI 316L stainless steel with a gradient nanostructured surface layer. Acta Mater. 2015;87:150–160.
[264] Mordyuk BN, Prokopenko GI. Ultrasonic impact peening for the surface properties' management. J Sound Vib. 2007;308:855–866.
[265] Liu RY, Yuan S, Lin NM, et al. Application of ultrasonic nanocrystal surface modification (UNSM) technique for surface strengthening of titanium and titanium alloys: a mini review. J Mater Res Technol. 2021;11:351–377.
[266] Samih Y, Beausir B, Bolle B, et al. In-depth quantitative analysis of the microstructures produced by surface mechanical attrition treatment (SMAT). Mater Charact. 2013;83:129–138.
[267] Proust G, Retraint D, Chemkhi M, et al. Electron backscatter diffraction and transmission Kikuchi diffraction analysis of an austenitic stainless steel subjected to surface mechanical attrition treatment and plasma nitriding. Microsc Microanal. 2015;21:919–926.
[268] Liu W, Jin X, Zhang B, et al. A coupled EBSD/TEM analysis of the microstructure evolution of a gradient nanostructured ferritic/martensitic steel subjected to surface mechanical attrition treatment. Materials. 2019;12:140.
[269] Sun Y. Sliding wear behaviour of surface mechanical attrition treated AISI 304 stainless steel. Tribol Int. 2013;57:67–75.
[270] Roland T, Retraint D, Lu K, et al. Fatigue life improvement through surface nanostructuring of stainless steel by means of surface mechanical attrition treatment. Scr Mater. 2006;54:1949–1954.
[271] Chen XH, Lu J, Lu L, et al. Tensile properties of a nanocrystalline 316L austenitic stainless steel. Scr Mater. 2005;52:1039–1044.
[272] Wu XL, Yang MX, Yuan FP, et al. Combining gradient structure and TRIP effect to produce austenite stainless steel with high strength and ductility. Acta Mater. 2016;112:337–346.
[273] Waltz L, Retraint D, Roos A, et al. Combination of surface nanocrystallization and co-rolling: creating multilayer nanocrystalline composites. Scr Mater. 2009;60:21–24.
[274] Tao NR, Lu J, Lu K. Surface nanocrystallization by surface mechanical attrition treatment. Mater Sci Forum. 2008;579:91–108.
[275] Bagheri S, Guagliano M. Review of shot peening processes to obtain nanocrystalline surfaces in metal alloys. Surf Eng. 2009;25:3–14.
[276] Azadmanjiri J, Berndt CC, Kapoor A, et al. Development of surface nano-crystallization in alloys by surface mechanical attrition treatment (SMAT). Crit Rev Solid State Mater Sci. 2015;40:164–181.
[277] Grosdidier T, Novelli M. Recent developments in the application of surface mechanical attrition treatments for improved gradient structures: processing parameters and surface reactivity. Mater Trans. 2019;60:1344–1355.
[278] Olugbade TO, Lu J. Literature review on the mechanical properties of materials after surface mechanical attrition treatment (SMAT). Nano Mater Sci. 2020;2:3–31.
[279] Tong WP, Tao NR, Wang ZB, et al. Nitriding iron at lower temperature. Science. 2003;299:2002–2004.
[280] Balusamy T, Narayanan TSNS, Ravichandran K. Effect of surface mechanical attrition treatment (SMAT) on boronizing of EN8 steel. Surf Coat Technol. 2012;213:221–228.
[281] Si X, Lu B, Wang Z. Aluminizing low carbon steel at lower temperatures. J Mater Sci Technol. 2009;25:433–436.
[282] Guo S, Wang ZB, Wang LM, et al. Lower temperature aluminizing behaviors of a ferritic-martensitic steel processed by means of surface mechanical attrition treatment. Surf Coat Technol. 2014;258:329–336.

[283] Skripnyuk VM, Rabkin E, Estrin Y, et al. The effect of ball milling and equal channel angular pressing on the hydrogen absorption/desorption properties of Mg-4.95 wt% Zn-0.71 wt% Zr (ZK60) alloy. Acta Mater. 2004;52:405–414.
[284] Huot J, Skryabina NY, Fruchart D. Application of severe plastic deformation techniques to magnesium for enhanced hydrogen sorption properties. Metals. 2012;2:329–343.
[285] Schlapbach L, Seiler A, Stucki F, et al. Surface effects and the formation of metal hydrides. J Less-Common Met. 1980;73:145–160.
[286] Edalati K, Novelli M, Itano S, et al. Effect of gradient-structure versus uniform nanostructure on hydrogen storage of Ti-V-Cr alloys: investigation using ultrasonic SMAT and HPT processes. J Alloys Compd. 2018;737:337–346.
[287] Novelli M, Edalati K, Itano S, et al. Microstructural details of hydrogen diffusion and storage in Ti-V-Cr alloys activated through surface and bulk severe plastic deformation. Int J Hydrogen Energy. 2020;45:5326–5336.
[288] Ralston KD, Birbilis N. Effect of grain size on corrosion: a review. Corrosion. 2010;66:075005–075013.
[289] Liu L, Li Y, Wang F. Electrochemical corrosion behavior of nanocrystalline materials-a review. J Mater Sci Technol. 2010;26:1–14.
[290] Balusamy T, Narayanan TSNS, Ravichandran K, et al. Influence of surface mechanical attrition treatment (SMAT) on the corrosion behaviour of AISI 304 stainless steel. Corros Sci. 2013;74:332–344.
[291] Chen AY, Ruan HH, Wang J, et al. The influence of strain rate on the microstructure transition of 304 stainless steel. Acta Mater. 2011;59:3697–3709.
[292] Gatey AM, Hosmani SS, Singh RP. Surface mechanical attrition treated AISI 304L steel: role of processing parameters. Surf Eng. 2016;32:69–78.
[293] Darling KA, Tschopp MA, Roberts AJ, et al. Enhancing grain refinement in polycrystalline materials using surface mechanical attrition treatment at cryogenic temperatures. Scr Mater. 2013;69:461–464.
[294] Shen Y, Wen C, Yang X, et al. Ultrahigh strength copper obtained by surface mechanical attrition treatment at cryogenic temperature. J Mater Eng Perform. 2015;24:5058–5064.
[295] Cai B, Ma X, Moering J, et al. Enhanced mechanical properties in Cu-Zn alloys with a gradient structure by surface mechanical attrition treatment at cryogenic temperature. Mater Sci Eng A. 2015;626:144–149.
[296] Sun L, Cai B, Wen C, et al. The role of temperature in the strengthening of Cu-Al alloys processed by surface mechanical attrition treatment. J Mater Res. 2015;30:1670–1677.
[297] Murdoch H, Darling K, Roberts A, et al. Mechanical behavior of ultrafine gradient grain structures produced via ambient and cryogenic surface mechanical attrition treatment in iron. Metals. 2015;5:976–985.
[298] Novelli M, Fundenberger JJ, Bocher P, et al. On the effectiveness of surface severe plastic deformation by shot peening at cryogenic temperature. Appl Surf Sci. 2016;389:1169–1174.
[299] Novelli M, Bocher P, Grosdidier T. Effect of cryogenic temperatures and processing parameters on gradient-structure of a stainless steel treated by ultrasonic surface mechanical attrition treatment. Mater Charact. 2018;139:197–207.
[300] Fabijanic D, Ralston KD, Birbilis N, et al. Influence of surface mechanical attrition treatment attrition media on the surface contamination and corrosion of magnesium. Corrosion. 2012;69:527–535.
[301] Sun Q, Han Q, Liu X, et al. The effect of surface contamination on corrosion performance of ultrasonic shot peened 7150 Al alloy. Surf Coat Technol. 2017;328:469–479.
[302] Wen L, Wang Y, Zhou Y, et al. Iron-rich layer introduced by SMAT and its effect on corrosion resistance and wear behavior of 2024 Al alloy. Mater Chem Phys. 2011;126:301–309.
[303] Wen L, Wang Y, Jin Y, et al. Comparison of corrosion behaviour of nanocrystalline 2024-T4 Al alloy processed by surface mechanical attrition treatment with two different mediums. Corros Eng Sci Technol. 2014;50:425–432.
[304] Murdoch HA, Labukas JP, Roberts AJ, et al. Controlling surface chemistry to deconvolute corrosion benefits derived from SMAT processing. JOM. 2017;69:1170–1174.
[305] Maurel P, Weiss L, Bochet P, et al. Oxide dependant wear mechanisms of titanium against a steel counterface: influence of SMAT nanostructured surface. Wear. 2019;430-431:245–255.
[306] Gatey AM, Hosmani SS, Figueroa CA, et al. Role of surface mechanical attrition treatment and chemical etching on plasma nitriding behavior of AISI 304L steel. Surf Coat Technol. 2016;304:413–424.
[307] Samih Y, Novelli M, Thiriet T, et al. Plastic deformation to enhance plasma-assisted nitriding: on surface contamination induced by surface mechanical attrition treatment. IOP Conf Ser Mater Sci Eng. 2014;63:012020.
[308] Chemkhi M, Retraint D, Roos A, et al. Role and effect of mechanical polishing on the enhancement of the duplex mechanical attrition/plasma nitriding treatment of AISI 316L steel. Surf Coat Technol. 2017;325:454–461.
[309] Tian JW, Villegas JC, Yuan W, et al. A study of the effect of nanostructured surface layers on the fatigue behaviors of a C-2000 superalloy. Mater Sci Eng A. 2007;468-470:164–170.
[310] Kumar SA, Raman SGS, Narayanan TSNS. Influence of surface mechanical attrition treatment duration on fatigue lives of Ti-6Al-4V. Trans Indian Inst Met. 2014;67:137–141.
[311] Maurel P, Weiss L, Bochet P, et al. Effects of SMAT at cryogenic and room temperatures on the kink band and martensite formations with associated fatigue resistance in a beta-metastable titanium alloy. Mater Sci Eng A. 2021;803:140618.
[312] Pandey V, Chattopadhyay K, Srinivas NCS, et al. Role of ultrasonic shot peening on low cycle fatigue behavior of 7075 aluminium alloy. Int J Fatigue. 2017;103:426–435.
[313] Maurel P, Weiss L, Bochet P, et al. How does surface integrity of nanostructured surfaces induced by severe plastic deformation influence fatigue behaviors

of Al alloys with enhanced precipitation? Int J Fatigue. 2020;140:105792.
[314] Bagherifard S, Fernandez-Pariente I, Ghelichi R, et al. Effect of severe shot peening on microstructure and fatigue strenght of cast iron. Int J Fatigue. 2014;65: 64–70.
[315] Zhou J, Sun Z, Kanouté P, et al. Effect of surface mechanical attrition treatment on low cycle fatigue properties of an austenitic stainless steel. Int J Fatigue. 2017;103:309–317.
[316] Gao T, Sun Z, Xue H, et al. Effect of surface mechanical attrition treatment on the very high cycle fatigue behavior of TC11. MATEC Web Conf. 2018;165:09001.
[317] Wick A, Schulze V, Vöhringer O. Effects of warm peening on fatigue life and relaxation behaviour of residual stresses in AISI 4140 steel. Mater Sci Eng A. 2000;293:191–197.
[318] Harada Y, Mori K. Effect of processing temperature on warm shot peening of spring steel. J Mater Process Technol. 2005;162-163:498–503.
[319] Huang Y, Liu WC, Dong J. Surface characteristics and fatigue performance of warm shot peened wrought magnesium alloy Mg-9Gd-2Y. Mater Sci Technol. 2014;30: 1481–1487.
[320] Lapovok R, Estrin YS, Rundell S, et al. The influence of nano-scale surface roughness on bacterial adhesion to ultrafine-grained titanium. Biomaterials. 2010;31:3674–3683.
[321] Estrin Y, Ivanova EP, Michalska A, et al. Accelerated stem cell attachment to ultrafine grained titanium. Acta Biomater. 2011;7:900–906.
[322] Lowe TC, Valiev RZ. Advanced biomaterials and biodevices. In: Tiwari A, Nordin AN, editors. Beverly (MA): Wiley-Scrivener Publishing; 2014; p. 3–52.
[323] Bagherifard S, Hickey DJ, Fintova S, et al. Effects of nanofeatures induced by severe shot peening (SSP) on mechanical, corrosion and cytocompatibility properties of magnesium alloy AZ31. Acta Biomater. 2018;66:93–108.
[324] Acharya S, Suwas S, Chatterjee K. Review of recent developments in surface nanocrystallization of metallic biomaterials. Nanoscale. 2021;13:2286–2301.
[325] Maleki N, Fattahi NA, Unal O, et al. Mechanical characterization and interfacial enzymatic activity of AISI 316L stainless steel after surface nanocrstalliztaion. Surf Coat Technol. 2021;405:126729.
[326] Kraemer L, Champion Y, Pippan R. From powders to bulk metallic glass composites. Sci Rep. 2017;7:6651.
[327] Edalati K, Uehiro R, Ikeda Y, et al. Design and synthesis of a magnesium alloy for room temperature hydrogen storage. Acta Mater. 2018;149:88–96.
[328] Popova EN, Deryagina IL. Optimization of the micro structure of Nb_3Sn layers in superconducting composites. Phys Met Metallogr. 2018;119:1229–1236.
[329] Popova EN, Popov VV, Rodionova LA, et al. Effect of annealing and doping with Zr on the structure and properties of in situ Cu-Nb composite wire. Scr Mater. 2002;46:193–198.
[330] Popova EN, Popov VV. Dislocation and grain structure formation in Nb filaments of different geometry at fabrication of Nb_3Sn-based superconducting wires. Mater Charact. 2020;167:110488–110495.
[331] Popov VV, Popova EN, Stolbovskiy AV. Nanostructuring Nb by various techniques of severe plastic deformation. Mater Sci Eng A. 2012;539:22–29.
[332] Popova EN, Popov VV, Romanov EP, et al. Thermal stability of nanocrystalline Nb produced by severe plastic deformation. Phys Met Metallogr. 2006;101: 52–57.
[333] Popov VV, Popova EN, Stolbovskiy AV, et al. Thermal stability of nanocrystalline structure in niobium processed by high pressure torsion at cryogenic temperatures. Mater Sci Eng A. 2011;528:1491–1496.
[334] Popova EN, Popov VV, Romanov EP, et al. Effect of the degree of deformation on the structure and thermal stability of nanocrystalline niobium produced by high-pressure torsion. Phys Met Metallogr. 2007;103:407–413.
[335] Popov VV, Popova EN, Stolbovskiy AV, et al. Nanostructurization of Nb by high-pressure torsion in liquid nitrogen and the thermal stability of the structure obtained. Phys Met Metallogr. 2012;113:295–301.
[336] Popova EN, Popov VV, Romanov EP, et al. Effect of deformation and annealing on texture parameters of composite Cu-Nb wire. Scr Mater. 2004;51:727–731.
[337] Deryagina IL, Popova EN, Valova-Zaharevskaya EG, et al. Structure and thermal stability of high-strength Cu-18Nb composite depending on the degree of deformation. Phys Met Metallogr. 2018;119:92–102.
[338] Popova EN, Deryagina IL. Evolution of structure of Cu-Nb composite under high-pressure torsion and subsequent annealing. Phys Met Metallogr. 2020;121:1182–1187.
[339] Popov VV, Popova EN. Behavior of Nb and Cu-Nb composites under severe plastic deformation and annealing. Mater Trans. 2019;60:1209–1220.
[340] Yeh JW, Chen SK, Lin SJ, et al. Nanostructured high-entropy alloys with multiple principal elements: novel alloy design concepts and outcomes. Adv Eng Mater. 2004;6:299–303.
[341] Cantor B, Chang I, Knight P, et al. Microstructural development in equiatomic multicomponent alloys. Mater Sci Eng A. 2004;375:213–218.
[342] Miracle DB, Senkov ON. A critical review of high entropy alloys and related concepts. Acta Mater. 2017; 122:448–511.
[343] Li Z, Pradeep KG, Deng Y, et al. Metastable high-entropy dual-phase alloys overcome the strength-ductility tradeoff. Nature. 2016;534:227–230.
[344] Li W, Xie D, Li D, et al. Mechanical behavior of high-entropy alloys. Prog Mater Sci. 2021;118:100777.
[345] Hammond VH, Atwater MA, Darling KA, et al. Equal-channel angular extrusion of a low-density high-entropy alloy produced by high-energy cryogenic mechanical alloying. JOM. 2014;66:2021–2029.
[346] Schuh B, Mendez-Martin F, Völker B, et al. Mechanical properties, microstructure and thermal stability of a nanocrystalline CoCrFeMnNi high-entropy alloy after severe plastic deformation. Acta Mater. 2015;96:258–268.
[347] Shahmir H, He J, Lu Z, et al. Effect of annealing on mechanical properties of a nanocrystalline CoCrFeNiMn high-entropy alloy processed by high-pressure torsion. Mater Sci Eng A. 2016;676:294–303.

[348] Shahmir H, Mousavi T, He J, et al. Microstructure and properties of a CoCrFeNiMn high-entropy alloy processed by equal-channel angular pressing. Mater Sci Eng A. 2017;705:411–419.
[349] Gubicza J, Hung PT, Kawasaki M, et al. Influence of severe plastic deformation on the microstructure and hardness of a CoCrFeNi high-entropy alloy: A comparison with CoCrFeNiMn. Mater Charact. 2019;154:304–314.
[350] Skrotzki W, Pukenas A, Odor E, et al. Microstructure, texture, and strength development during high-pressure torsion of CrMnFeCoNi high-entropy alloy. Crystals. 2020;10:336.
[351] Lu Y, Mazilkin A, Boll T, et al. Influence of carbon on the mechanical behavior and microstructure evolution of CoCrFeMnNi processed by high pressure torsion. Materialia. 2021;16:101059.
[352] Kwon H, Asghari-Rad P, Park JM, et al. Synergetic strengthening from grain refinement and nano-scale precipitates in non-equiatomic CoCrFeNiMo medium-entropy alloy. Intermetallics. 2021;135:107212.
[353] Edalati P, Mohammadi A, Ketabchi M, et al. Microstructure and microhardness of dual-phase high-entropy alloy by high-pressure torsion: twins and stacking faults in FCC and dislocations in BCC. J Alloys Compd. 2022;894:162413.
[354] Tang QH, Huang Y, Huang YY, et al. Hardening of an $Al_{0.3}$CoCrFeNi high entropy alloy via high-pressure torsion and thermal annealing. Mater Lett. 2015;151:126–129.
[355] Tang QH, Huang Y, Cheng H, et al. The effect of grain size on the annealing-induced phase transformation in an $Al_{0.3}$CoCrFeNi high entropy alloy. Mater Des. 2016;105:381–385.
[356] Edalati P, Mohammadi A, Ketabchi M, et al. Ultrahigh hardness in nanostructured dual-phase high-entropy alloy AlCrFeCoNiNb developed by high-pressure torsion. J Alloys Compd. 2021;884:161101.
[357] Reddy TS, Wani IS, Bhattacharjee T, et al. Severe plastic deformation driven nanostructure and phase evolution in a $Al_{0.5}$CoCrFeMnNi dual phase high entropy alloy. Intermetallics. 2017;91:150–157.
[358] Edalati P, Floriano R, Tang Y, et al. Ultrahigh hardness and biocompatibility of high-entropy alloy TiAlFeCoNi processed by high-pressure torsion. Mater Sci Eng C. 2020;112:110908.
[359] Edalati P, Mohammadi A, Tang Y, et al. Phase transformation and microstructure evolution in ultrahard carbon-doped AlTiFeCoNi high-entropy alloy by high-pressure torsion. Mater Lett. 2021;302:130368.
[360] Shahmir H, Tabachnikova E, Podolskiy A, et al. Effect of carbon content and annealing on structure and hardness of $CrFe_2NiMnV_{0.25}$ high-entropy alloys processed by high-pressure torsion. J Mater Sci. 2018;53:11813–11822.
[361] Asghari-Rad P, Sathiyamoorthi P, Bae JW, et al. Effect of initial grain size on deformation mechanism during high-pressure torsion in $V_{10}Cr_{15}Mn_5Fe_{35}Co_{10}Ni_{25}$ high-entropy alloy. Adv Eng Mater. 2020;22:1900587.
[362] Asghari-Rad P, Sathiyamoorthi P, Nguyen NTC, et al. Fine-tuning of mechanical properties in $V_{10}Cr_{15}Mn_5Fe_{35}Co_{10}Ni_{25}$ high-entropy alloy through high-pressure torsion and annealing. Mater Sci Eng. 2020;771:138604.
[363] Edalati P, Floriano R, Mohammadi A, et al. Reversible room temperature hydrogen storage in high-entropy alloy TiZrCrMnFeNi. Scr. Mater. 2020;178:387–390.
[364] Asghari-Rad P, Sathiyamoorthi P, Nguyen NTC, et al. A powder-metallurgy-based fabrication route towards achieving high tensile strength with ultra-high ductility in high-entropy alloy. Scr Mater. 2021;190:69–74.
[365] Asghari-Rad P, Nguyen NTC, Kim Y, et al. TiC-reinforced CoCrFeMnNi composite processed by cold-consolidation and subsequent annealing. Mater Lett. 2021;303:130503.
[366] Karthik GM, Asghari-Rad P, Sathiyamoorthi P, et al. Architectured multi-metal CoCrFeMnNi-inconel 718 lamellar composite by high-pressure torsion. Scr Mater. 2021;195:113722.
[367] Kilmametov A, Kulagin R, Mazilkin A, et al. High-pressure torsion driven mechanical alloying of CoCrFeMnNi high entropy alloy. Scr Mater. 2019;158:29–33.
[368] González-Masís J, Cubero-Sesin JM, Campos-Quirós A, et al. Synthesis of biocompatible high-entropy alloy TiNbZrTaHf by high-pressure torsion. Mater Sci Eng A. 2021;825:141869.
[369] Oses C, Toher C, Curtarolo S. High-entropy ceramics. Nat Rev Mater. 2020;5:295–309.
[370] Akrami S, Edalati P, Edalati K, et al. High-entropy ceramics: review of principles, production and applications. Mater Sci Eng R. 2021;146:100644.
[371] de Marco MO, Li Y, Li HW, et al. Mechanical synthesis and hydrogen storage characterization of MgVCr and MgVTiCrFe high-entropy alloy. Adv Eng Mater. 2020;22:1901079.
[372] Edalati P, Wang Q, Razavi-Khosroshahi H, et al. Photocatalytic hydrogen evolution on a high-entropy oxide. J Mater Chem A. 2020;8:3814–3821.
[373] Akrami S, Murakami Y, Watanabe M, et al. Defective high-entropy oxide photocatalyst with high activity for CO_2 conversion. Appl Catal B. 2022;303:120896.
[374] Edalati P, Shen XF, Watanabe M, et al. Hih-entropy oxyitride as low-bandgap and stable photocatalyst for hydrogen production. J Mater Chem A. 2021;9:15076–15086.
[375] Bridgman PW, Simon I. Effects of very high pressures on glass. J Appl Phys. 1953;24:405–413.
[376] Sikka S, Mackenzie JD. High pressure effects on glass. J Non Cryst Solids. 1969;1:107–142.
[377] Sakata M, Aoki S. Torsional strength of glass under hydrostatic pressure. J Eng Mater Technol. 1973;95:83–86.
[378] Uhlmann DR. Densification of alkali silicate glasses at high pressure. J Non Cryst Solids. 1973;13:89–99.
[379] Edalati K, Fujita I, Sauvage X, et al. Microstructure and phase transformations of silica glass and vanadium oxide by severe plastic deformation via high-pressure torsion straining. J Alloys Compd. 2019;779:394–398.
[380] Inoue A. Stabilization of metallic supercooled liquid and bulk amorphous alloys. Acta Mater. 2000;48:279–306.
[381] Miracle DB, Egami T, Flores KM. Structural aspects of metallic glasses. MRS Bull. 2007;32:629–634.
[382] Trexler MM, Thadhani NN. Mechanical properties of bulk metallic glasses. Prog Mater Sci. 2010;55:759–839.

[383] Greer AL, Ma E. Bulk metallic glasses: at the cutting edge of metals research. MRS Bull. 2007;32:611–619.
[384] Schuh CA, Hufnagel TC, Ramamurty U. Mechanical behavior of amorphous alloys. Acta Mater. 2007;55: 4067–4109.
[385] Spaepen F. Homogeneous flow of metallic glasses: A free volume perspective. Scr Mater. 2006;54:363–367.
[386] Greer AL, Cheng YQ, Ma E. Shear bands in metallic glasses. Mater Sci Eng R. 2013;74:71–132.
[387] Chen H, He Y, Shiflet GJ, et al. Deformation-induced nanocrystal formation in shear bands of amorphous alloys. Nature. 1994;367:541–543.
[388] Zhang Y, Greer AL. Thickness of shear bands in metallic glasses. Appl Phys Lett. 2006;89:071907.
[389] Zhang Y, Wang WH, Greer AL. Making metallic glasses plastic by control of residual stress. Nat Mater. 2006;5:857–860.
[390] Liu YH, Wang G, Wang RJ, et al. Super plastic bulk metallic glasses at room temperature. Science. 2007;315:1385–1388.
[391] Xi XK, Zhao DQ, Pan MX, et al. Fracture of brittle metallic glasses: brittleness or plasticity. Phys Rev Lett. 2005;94:125510.
[392] Herbert RJ, Boucharat N, Perepezko JH, et al. Synthesis routes for controlling the microstructure in nanostructured $Al_{88}Y7Fe_5$ alloys. J Alloys Compd. 2007;434-435:252–254.
[393] Suzuki Y, Haimovich J, Egami T. Bond-orientational anisotropy in metallic glasses observed by x-ray diffraction. Phys Rev B. 1987;35:2162–2168.
[394] Poulsen HF, Wert JA, Neuefeind J, et al. Measuring strain distributions in amorphous materials. Nat Mater. 2005;4:33–36.
[395] Révész Á, Schafler E, Kovács Z. Structural anisotropy in a $Zr_{57}Ti_5Cu_{20}Al_{10}Ni_8$ bulk metallic glass deformed by high pressure torsion at room temperature. Appl Phys Lett. 2008;92:11910.
[396] Dmowski W, Yokoyama Y, Chuang A, et al. Structural rejuvenation in a bulk metallic glass induced by severe plastic deformation. Acta Mater. 2010;58:429–438.
[397] Blank VD, Kulnitskiy BA. Crystallogeometry of polymorphic transitions in silicon under pressure. High Press Res. 1996;37:31–42.
[398] Islamgaliev RK, Chmelik F, Gibadullin IF, et al. The nanocrystalline structure formation in germanium subjected to severe plastic deformation. Nanostruct Mater. 1994;4:387–395.
[399] Islamgaliev RK, Kuzel R, Obraztsova ED, et al. XRD and Raman scattering of germanium processed by severe deformation. Mater Sci Eng A. 1998;249:152–157.
[400] Islamgaliev RK, Kuzel R, Mikov SN, et al. Structure of silicon processed by severe plastic deformation. Mater Sci Eng A. 1999;266:205–210.
[401] Ikoma Y, Hayano K, Edalati K, et al. Phase transformation and nanograin refinement of silicon by processing through high-pressure torsion. Appl Phys Lett. 2012;101:121908.
[402] Ikoma Y, Hayano K, Edalati K, et al. Fabrication of nanograined silicon by high pressure torsion. J Mater Sci. 2014;49:6565–6569.
[403] Fukushima Y, Ikoma Y, Edalati K, et al. High-resolution transmission electron microscopy analysis of bulk nanograined silicon processed by high-pressure torsion. Mater Charact. 2017;129:163–168.
[404] Ikoma Y, Yamasaki T, Masuda T, et al. Synchrotron X-ray diffraction observation of phase transformation during annealing of Si processed by high-pressure torsion. Philos Mag Lett. 2021;101:223–231.
[405] Chon B, Ikoma Y, Kohno M, et al. Impact of metastable phases on electrical properties of Si with different doping concentrations after processing by high-pressure torsion. Scr Mater. 2018;157:120–123.
[406] Ikoma Y, Chon B, Yamasaki T, et al. Crystal and electronic structural changes during annealing in severely deformed Si containing metastable phases formed by high-pressure torsion. Appl Phys Lett. 2018;113:101904.
[407] Harish S, Tabara M, Ikoma Y, et al. Thermal conductivity reduction of crystalline silicon by high-pressure torsion. Nanoscale Res Lett. 2014;9:326.
[408] Shao C, Matsuda K, Ju S, et al. Phonon transport in multiphase nanostructured silicon fabricated by high-pressure torsion. J Appl Phys. 2021;129:085101.
[409] Ikoma Y, Toyota T, Ejiri Y, et al. Allotropic phase transformation and photoluminescence of germanium nanograins processed by high-pressure torsion. J Mater Sci. 2016;51:138–143.
[410] Ikoma Y, Kumano K, Edalati K, et al. High-resolution transmission electron microscopy analysis of nanograi ned germanium produced by high-pressure torsion. Mater Charact. 2017;132:132–138.
[411] Ikoma Y, Kumano K, Edalati K, et al. Phase transformation of germanium by processing through high-pressure torsion: strain and temperature effects. Philos Mag Lett. 2017;97:27–34.
[412] Ikoma Y, Yamasaki T, Shimizu T, et al. Formation of metastable bc8 phase from crystalline $Si_{0.5}Ge_{0.5}$ by high-pressure torsion. Mater Charact. 2020;169:110590.
[413] Ikoma Y, Ejiri Y, Hayano K, et al. Nanograin formation of GaAs by high-pressure torsion. Philos Mag Lett. 2014;94:1–8.
[414] Edalati K, Daio T, Ikoma Y, et al. Graphite to diamond-like carbon phase transformation by high-pressure torsion. Appl Phys Lett. 2013;103:034108.
[415] Ikoma Y. Production of nanograins and metastable phases in bulk Si and Ge semiconductors using severe plastic deformation under high pressure. Materia Japan. 2021;60:706–711.
[416] Boker R. The mechanics of plastic deformation in crystalline solids. Ver dtsch Ing Mitt Forsch. 1915;175: 1–51.
[417] Griggs DT. Deformation of rocks under high confining pressure. J Geol. 1937;44:541–577.
[418] Bates CH, White WB, Roy R. New high-pressure polymorph of zinc oxide. Science. 1963;137:993.
[419] Bell PM. Aluminum silicate system: experimental determination of the triple point. Science. 1963;139:1055–1056.
[420] Dachille F, Roy R. Effectiveness of shearing stresses in accelerating solid-phase reactions at low temperatures and high pressures. J Geol. 1964;72:243–247.
[421] Miller RO, Dachille FF, Roy R. High-pressure phase-equilibrium studies of CdS and MnS by static and dynamic methods. J Appl Phys. 1966;37:4913–4918.

[422] Vereshchagin LF, Zubova EV, Burdina KP, et al. Behavi our of oxides under the action of high pressure with simultaneous application of shear stresses. Dokl Akad Nauk SSSR. 1971;196:817–818.
[423] Morozova OS, Maksimov YV, Shashkin DP, et al. Carbon monoxide hydrogenation over iron oxide, subjected to shear deformation under high pressure: role of vacancies. Appl Catal. 1991;78:227–239.
[424] Morozova S, Ziborov AV, Kryukova GN, et al. Effect of shear deformation under high pressure on NiO structure transformation in reducing atmosphere. J Sol State Chem. 1992;101:353–355.
[425] Fujita I, Edalati K, Sauvage X, et al. Grain growth in nanograined aluminum oxide by high-pressure torsion: phase transformation and plastic strain effects. Scr Mater. 2018;152:11–14.
[426] Edalati K, Fujita I, Takechi S, et al. Photocatalytic activity of aluminum oxide by oxygen vacancy generation using high-pressure torsion straining. Scr Mater. 2019;173:120–124.
[427] Fujita I, Edalati K, Wang Q, et al. High-pressure torsion to induce oxygen vacancies in nanocrystals of magnesium oxide: enhanced light absorbance, photocatalysis and significance in geology. Materialia. 2020;11:100 670.
[428] Edalati K, Toh S, Ikoma Y, et al. Plastic deformation and allotropic phase transformations in zirconia ceramics during high-pressure torsion. Scr Mater. 2011;65:974–977.
[429] Wang Q, Edalati K, Koganemaru Y, et al. Photocatalytic hydrogen generation on low-bandgap black zirconia (ZrO_2) produced by high-pressure torsion. J Mater Chem A. 2020;8:3643–3650.
[430] Razavi-Khosroshahi H, Edalati K, Arita M, et al. Plastic strain and grain size effect on high-pressure phase transformations in nanostructured TiO_2 ceramics. Scr Mater. 2016;124:59–62.
[431] Razavi-Khosroshahi H, Edalati K, Hirayama M, et al. Visible-light-driven photocatalytic hydrogen generation on nanosized TiO_2-II stabilized by high-pressure torsion. ACS Catal. 2016;6:5103–5107.
[432] Wang Q, Watanabe M, Edalati K. Visible-light photocurrent in nanostructured high-pressure TiO_2-II (columbite) phase. J Phys Chem C. 2020;124:13930–13935.
[433] Akrami S, Watanabe M, Ling TH, et al. High-pressure TiO_2-II polymorph as an active photocatalyst for CO_2 to CO conversion. Appl Catal B. 2021;298: 120566.
[434] Edalati K, Wang Q, Razavi-Khosroshahi H, et al. Low-temperature anatase-to-rutile phase transformation and unusual grain coarsening in titanium oxide nanopowders by high-pressure torsion straining. Scr Mater. 2019;162:341–344.
[435] Edalati K, Wang Q, Eguchi H, et al. Impact of TiO_2-II phase stabilized in anatase matrix by high-pressure torsion on electrocatalytic hydrogen production. Mater Res Lett. 2019;7:334–339.
[436] Razavi-Khosroshahi H, Edalati K, Wu J, et al. High-pressure zinc oxide phase as visible-light-active photocatalyst with narrow band gap. J Mater Chem A. 2017;5:20298–20303.
[437] Wang Q, Edalati K, Fujita I, et al. High-pressure torsion of SiO_2 quartz sand: phase transformation, optical properties and significance in geology. J Am Ceram Soc. 2020;103:6594–6602.
[438] Razavi-Khosroshahi H, Edalati K, Emami H, et al. Optical properties of nanocrystalline monoclinic Y_2O_3 stabilized by grain size and plastic strain effects via high-pressure torsion. Inorg Chem. 2017;56:2576–2580.
[439] Fujita I, Edalati P, Wang Q, et al. Novel black bismuth oxide (Bi_2O_3) with enhanced photocurrent generation, produced by high-pressure torsion straining. Scr Mater. 2020;187:366–370.
[440] Edalati K, Arimura M, Ikoma Y, et al. Plastic deformation of $BaTiO_3$ ceramics by high-pressure torsion and changes in phase transformations, optical and dielectric properties. Mater Res Lett. 2015;3:216–221.
[441] Edalati K, Fujiwara K, Takechi S, et al. Improved photocatalytic hydrogen evolution on tantalate perovskites $CsTaO_3$ and $LiTaO_3$ by strain-induced vacancies. ACS Appl Energy Mater. 2020;3:1710–1718.
[442] Hidalgo-Jimenez J, Wang Q, Edalati K, et al. High-pressure torsion of TiO_2-ZnO composites: phase transformations, vacancy formation and changes in optical and photocatalytic properties. Int J Plasticity. 2020;124: 170–185.
[443] Edalati K, Uehiro R, Takechi S, et al. Enhanced photocatalytic hydrogen production on GaN-ZnO oxynitride by introduction of strain-induced nitrogen vacancy complexes. Acta Mater. 2020;185:149–156.
[444] Sena H. Stabilization of high-pressure phase semiconductors by plastic strain. J Soc Powder Technol Japan. 2021;58:66–72.
[445] Levitas VI, Shvedov LK. Low-pressure phase transformation from rhombohedral to cubic BN: experiment and theory. Phys Rev B. 2002;65:104109.
[446] Levitas VI, Javanbakht M. Phase transformations in nanograin materials under high pressure and plastic shear: nanoscale mechanisms. Nanoscale. 2014;6:162–166.
[447] Javanbakht M, Levitas VI. Phase field simulations of plastic strain-induced phase transformations under high pressure and large shear. Phys Rev B. 2016;94:214104.
[448] Ji C, Levitas VI, Zhu H, et al. Shear-induced phase transition of nanocrystalline hexagonal boron nitride to wurtzitic structure at room temperature and lower pressure. Proc Natl Acad Sci USA. 2012;109:19108–19112.
[449] Levitas VI, Ma Y, Hashemi J, et al. Strain-induced disorder, phase transformations and transformation induced plasticity in hexagonal boron nitride under compression and shear in a rotational diamond anvil cell: in-situ X-ray diffraction study and modeling. J Chem Phys. 2006;125:044507.
[450] Mohamed FA, Dheda SS. On the minimum grain size obtainable by high-pressure torsion. Mater Sci Eng A. 2012;558:59–63.
[451] Starink MJ, Cheng XC, Yang S. Hardening of pure metals by high-pressure torsion: a physically based model employing volume-averaged defect evolutions. Acta Mater. 2013;61:183–192.
[452] Setman D, Schafler E, Korznikova E, et al. The presence and nature of vacancy type defects in nanometals

detained by severe plastic deformation. Mater Sci Eng A. 2008;493:116–122.
[453] Oberdorfer B, Lorenzoni B, Unger K, et al. Absolute concentration of free volume-type defects in ultrafine-grained Fe prepared by high-pressure torsion. Scr Mater. 2010;63:452–455.
[454] Čížek J, Janeček M, Vlasák T, et al. The development of vacancies during severe plastic deformation. Mater Trans. 2019;60:1533–1542.
[455] Bridgman PW. Polymorphic transitions up to 50,000 Kg/cm^2 of several organic substances. Am Acad Arts Sci. 1938;72:227–268.
[456] Bridgman PW. The effect of high mechanical stress on certain solid explosives. J Chem Phys. 1947;15:311–313.
[457] Larsen HA, Drickamer HG. Chemical effects of plastic deformation at high pressure. J Phys Chem. 1957;61:1249–1252.
[458] Zhorin VA, Kissin YV, Luizo YV, et al. Structural changes in polyolefins due to the combination of high pressure and shear deformation. Polym Sci USSR. 1976;18:3057–3061.
[459] Zhorin VA, Maksimychev AV, Ponomarenko AT, et al. Electrophysical characteristics of several organic compounds at high pressures and high pressures combined with shearing strains. Bull Acad Sci USSR Div Chem Sci. 1979;28:2078–2082.
[460] Goldman AY, Demenchuk NP. Effect of hydrostatic pressure on mechanical properties of crystalline polymers under shear. Strength Mater. 1981;13:110–114.
[461] Zhorin VA, Kulakov VV, Nikolskii VG, et al. Homogenization of blends of polypropylene and ethylene-propylene rubber under shear in the presence of inorganic fillers. Polym Sci USSR. 1982;24:1081–1084.
[462] Enikolopov NS. Solid phase chemical reactions and new technologies. Russ Chem Rev. 1991;60:283–287.
[463] Zharov AA. Reaction ability of monomers and other organic compounds in solid state under high pressure and shear deformation. Vysokomoleculyarnya Soedineniya [Macromolecular Compounds]. 2004;46:1613–1637.
[464] Beloshenko V, Beygelzimer Y, Voznyak Y. Solid-state extrusion. In: Mark HF, editor. Encyclopedia of polymer science and technology. New York (NY): John Wiley & Sons; 2015. p. 1–16.
[465] Sue HJ, Li CKJ. Control of orientation of lamellar structure in linear low density polyethylene via equal channel angular extrusion process. J Mater Sci Lett. 1998;17:853–856.
[466] Sue HJ, Dilan H, Li CKY. Simple shear plastic deformation behavior of polycarbonate plate due to the equal channel angular extrusion process. I: finite element methods modeling. Polym Eng Sci. 1999;39:2505–2515.
[467] Beloshenko VA, Voznyak AV, Voznyak YV. Control of the mechanical and thermal properties of semicrystalline polymers via a new processing route of the equal channel multiple angular extrusion. Polym Eng Sci. 2014;54:531–539.
[468] Beloshenko VA, Voznyak AV, Voznyak YV. Effects of equal-channel, multiple-angular extrusion on the physical and mechanical properties of glassy polymers. J Appl Polym Sci. 2015;132:42180–42187.
[469] Beloshenko V, Voznyak Y, Voznyak A, et al. New approach to production of fiber reinforced polymer hybrid composites. Compos B. 2017;112:22–30.
[470] Beloshenko VA, Varyukhin VN, Voznyak AV, et al. New methods of solid-phase modification of polymers by simple-shear deformation. Dokl Phys Chem. 2009;426:81–83.
[471] Vozniak I, Beloshenko V, Savchenko B, et al. Improvement of mechanical properties of polylactide by equal channel multiple angular extrusion. J Appl Polym Sci. 2021;138:49720.
[472] Renk O, Pippan R. Saturation of grain refinement during severe plastic deformation of single phase materials: reconsiderations, current status and open questions. Mater Trans. 2019;60:1270–1282.
[473] Gubicza J. Lattice defects and their influence on the mechanical properties of bulk materials processed by severe plastic deformation. Mater Trans. 2019;60:1230–1242.
[474] Sauvage X, Enikeev N, Valiev R, et al. Atomic scale analysis of the segregation and precipitation mechanisms in a severely deformed Al-Mg alloy. Acta Mater. 2014;72:125–136.
[475] Tóth LS, Massion RA, Germain L, et al. Analysis of texture evolution in equal channel angular extrusion of copper using a new flow field. Acta Mater. 2004;52:1885–1898.
[476] Azzeddine H, Bradai D, Baudin T, et al. Texture evolution in high-pressure torsion processing. Prog Mater Sci. 2022;125:100886.
[477] Humphreys FJ, Hatherly M. Recrystallization and related annealing phenomena. Oxford: Pergamon; 1995.
[478] Tsuji N, Kamikawa N, Li B. Grain size saturation during severe plastic deformation. Mater Sci Forum. 2007;539-543:2837–2842.
[479] Hansen N, Hensen DJ. Development of microstructure in FCC metals during cold work. Phil Trans R Soc Lond A. 1999;357:1447–1469.
[480] Hansen N. New discoveries in deformed metals. Metall Mater Trans A. 2001;32:2917–2935.
[481] Huang X, Hansen N, Tsuji N. Hardening by annealing and softening by deformation in nanostructured metals. Science. 2006;312:249–251.
[482] Tian YZ, Gao S, Zhao LJ, et al. Remarkable transitions of yield behavior and Lüders deformation in pure Cu by changing grain sizes. Scr Mater. 2018;142:88–91.
[483] Tian YZ, Gao S, Zheng RX, et al. Two-stage Hall-Petch relationship in Cu with recrystallized structure. J Mater Sci Techol. 2020;48:31–35.
[484] Zheng R, Du JP, Gao S, et al. Transition of dominant deformation mode in bulk polycrystalline pure Mg by ultra-grain refinement down to sub-micrometer. Acta Mater. 2020;198:35–46.
[485] Terada D, Inoue M, Kitahara H, et al. Change in mechanical properties and microstructures of ARB processed Ti during annealing. Mater Trans. 2008;49:41–46.
[486] Saha R, Ueji R, Tsuji N. Fully recrystallized nanostructure fabricated without severe plastic deformation in high-Mn austenitic steel. Scr Mater. 2013;68:813–816.

[487] Bai Y, Tian Y, Gao S, et al. Hydrogen embrittlement behaviors of ultrafine-grained 22Mn-0.6C austenitic twinning induced plasticity steel. J Mater Res. 2017;32:4592–4604.
[488] Bai Y, Kitamura H, Gao S, et al. Unique transition of yielding mechanism and unexpected activation of deformation twinning in ultrafine grained Fe-31Mn-3Al-3Si alloy. Sci Rep. 2021;11:15870.
[489] Tian YZ, Zhao LJ, Chen S, et al. Significant contribution of stacking faults to the strain hardening behavior of Cu-15% Al alloy with different grain sizes. Sci Rep. 2015;5:16707.
[490] Zheng R, Bhattacharjee T, Shibata A, et al. Simultaneously enhanced strength and ductility of Mg-Zn-Zr-Ca alloy with fully recrystallized ultrafine grained structures. Scr Mater. 2017;131:1–5.
[491] Zheng RX, Bhattacharjee T, Gao S, et al. Change of deformation mechanisms leading to high strength and large ductility in Mg-Zn-Zr-Ca alloy with fully recrystallized ultrafine grained microstructures. Sci Rep. 2019;9:11702.
[492] Zhang B, Chong Y, Zheng R, et al. Enhanced mechanical properties in beta-Ti alloy aged from recrystallized ultrafine beta grains. Mater Des. 2020;195:109017.
[493] Yoshida Y, Ikeuchi T, Bhattacharjee T, et al. Effect of elemental combination on friction stress and Hall-Petch relationship in face-centered cubic high/medium entropy alloys. Acta Mater. 2019;171:201–215.
[494] Yoshida S, Bhattacharjee T, Bai Y, et al. Friction stress and Hall-Petch relationship in CoCrNi equi-atomic medium entropy alloy processed by severe plastic deformation and subsequent annealing. Scr Mater. 2017;134:33–36.
[495] Tsuji N, Ogata S, Inui H, et al. Strategy for managing both high strength and large ductility in structural materials - sequential nucleation of different deformation modes based in a concept of plaston. Scr Mater. 2020;181:35–42.
[496] Tsuji N, Ogata S, Inui H, et al. Corrigendum to 'strategy for managing both high strength and large ductility in structural materials - sequential nucleation of different deformation modes based on a concept of plaston'. Scr Mater. 2021;196:113755.
[497] Renk O, Hohenwarter A, Wurster S, et al. Direct evidence for grain boundary motion as the dominant restoration mechanism in the steady-state regime of extremely cold-rolled copper. Acta Mater. 2014;77:401–410.
[498] Yu T, Hansen N, Huang X, et al. Observation of a new mechanism balancing hardening and softening in metals. Mater Res Lett. 2014;2:160–165.
[499] Renk O, Pippan R. Transition from thermally assisted to mechanically driven boundary migration and related apparent activation energies. Scr Mater. 2018;154:212–215.
[500] Han J, Thomas SL, Srolovitz DJ. Grain-boundary kinetics: a unified approach. Prog Mater Sci. 2018;98:386–476.
[501] Rajabzadeh A, Legros M, Combe N, et al. Evidence of grain boundary dislocation step motion associated to shear-coupled grain boundary migration. Philos Mag. 2013;93:1299–1316.
[502] Rajabzadeh A, Mompiou F, Legros M, et al. Elementary mechanisms of shear-coupled grain boundary migration. Phys Rev Lett. 2013;110:265507.
[503] Kvashin N, Garcia-Müller PL, Anento N, et al. Atomic processes of shear-coupled migration in 112 twins and vicinal grain boundaries in bcc-Fe. Phys Rev Mater. 2020;4:073604.
[504] Kapp MW, Renk O, Leitner T, et al. Cyclically induced grain growth within shear bands investigated in UFG Ni by cyclic high pressure torsion. J Mater Res. 2017;32:4317–4326.
[505] Kapp MW, Renk O, Ghosh P, et al. Plastic strain triggers structural instabilities upon cyclic loading in ultrafine-grained nickel. Acta Mater. 2020;200:136–147.
[506] Renk O, Ghosh P, Pippan R. Generation of extreme grain aspect ratios in severely deformed tantalum at elevated temperatures. Scr Mater. 2017;137:60–63.
[507] Renk O, Ghosh P, Pippan R. From an understanding of structural restoration mechanisms towards a selective processing of extreme nanolamellar structures. IOP Conf Ser Mater Sci Eng. 2017;219:12037.
[508] Rathmayr GB, Pippan R. Influence of impurities and deformation temperature on the saturation microstructure and ductility of HPT-deformed nickel. Acta Mater. 2011;59:7228–7240.
[509] Zhang K, Alexandrov IV, Lu K. The X-ray diffraction study on a nanocrystalline Cu processed by equal-channel angular pressing. Nanostructured Mater. 1997;9:347–350.
[510] Chang JY, Kim GH, Moon IG. X-ray diffraction analysis of pure aluminum in the cyclic equal channel angular pressing. Scr Mater. 2001;44:331–336.
[511] Ungár T, Gubicza J, Hanák P, et al. Densities and character of dislocations and size-distribution of subgrains in deformed metals by X-ray diffraction profile analysis. Mater Sci Eng A. 2001;319-321:274–278.
[512] Gubicza J. X-ray line profile analysis in materials science. Hershey (PA): IGI-Global; 2014.
[513] Cízek J. Characterization of lattice defects in metallic materials by positron annihilation spectroscopy: a review. J Mater Sci Technol. 2018;34:577–598.
[514] Dalla Torre F, Lapovok R, Sandlin J, et al. Microstructures and properties of copper processed by equal channel angular extrusion for 1-16 passes. Acta Mater. 2004;52:4819–4832.
[515] Steiner EG, Korznikova E, Kerber M, et al. Lattice defect investigation of ECAP-Cu by means of X-ray line profile analysis, calorimetry and electrical resistometry. Mater Sci Eng A. 2005;410-411:169–173.
[516] Cizek J, Janecek M, Srba O, et al. Evolution of defects in copper deformed by high-pressure torsion. Acta Mater. 2011;59:2322–2329.
[517] Hegedűs Z, Gubicza J, Kawasaki M, et al. High temperature thermal stability of ultrafine-grained silver processed by equal-channel angular pressing. J Mater Sci. 2013;48:1675–1684.
[518] Gubicza J. Defect structure and properties of nanomaterials. Duxford: Woodhead Publishing; 2017.
[519] Heczel A, Kawasaki M, Lábár JL, et al. Defect structure and hardness in nanocrystalline CoCrFeMnNi high-entropy alloy processed by high-pressure torsion. J Alloys Compd. 2017;711:143–154.
[520] Kawasaki M, Horita Z, Langdon TG. Microstructural evolution in high purity aluminum processed by ECAP. Mater Sci Eng A. 2009;524:143–150.

[521] Xu C, Horita Z, Langdon TG. Microstructural evolution in an aluminum solid solution alloy processed by ECAP. Mater Sci Eng A. 2011;528:6059–6065.
[522] Tao J, Chen G, Jian W, et al. Anneal hardening of a nanostructured Cu-Al alloy processed by high-pressure torsion and rolling. Mater Sci Eng A. 2015;628:207–215.
[523] Gubicza J, Pereira PHR, Kapoor G, et al. Annealing-induced hardening in ultrafine-grained Ni-Mo alloys. Adv Eng Mater. 2018;20:1800184.
[524] Cao Y, Ni S, Liao X, et al. Structural evolutions of metallic materials processed by severe plastic deformation. Mater Sci Eng R. 2018;133:1–59.
[525] Hoffman A, Wen H, Islamgaliev R, et al. High-pressure torsion assisted segregation and precipitation in a Fe-18Cr-8Ni austenitic stainless steel. Mater Lett. 2019;243:116–119.
[526] Oh-ishi K, Edalati K, Kim HS, et al. High-pressure torsion for enhanced atomic diffusion and promoting solid-state reactions in the aluminum-copper system. Acta Mater. 2013;61:3482–3489.
[527] Čížek J, Melikhova O, Janeček M, et al. Homogeneity of ultrafine-grained copper deformed by high-pressure torsion characterized by positron annihilation and microhardness. Scr Mater. 2011;65:171–174.
[528] Čížek J, Melikhova O, Barnovská Z, et al. Vacancy clusters in ultra fine grained metals prepared by severe plastic deformation. J Phys Conf Series. 2013;443:012008.
[529] Sauvage X, Duchaussoy A, Zaher G. Strain induced segregations in severely deformed materials. Mater Trans. 2019;60:1151–1158.
[530] Sauvage X, Ganeev A, Ivanisenko Y, et al. Grain boundary segregation in UFG alloys processed by severe plastic deformation. Adv Eng Mater. 2012;14:968–974.
[531] Sauvage X, Wilde G, Divinsky S, et al. Grain boundaries in ultrafine grained materials processed by severe plastic deformation and related phenomena. Mater Sci Eng A. 2012;540:1–12.
[532] Zhang Y, Jin S, Trimby PW, et al. Dynamic precipitation, segregation and strengthening of an Al-Zn-Mg-Cu alloy (AA7075) processed by high-pressure torsion. Acta Mater. 2019;162:19–32.
[533] Sauvage X, Bobruk EV, Murashkin MY, et al. Optimization of electrical conductivity and strength combination by nanoscale structure design in an Al-Mg-Si alloy. Acta Mater. 2015;98:355–366.
[534] Masuda T, Sauvage X, Hirosawa S, et al. Achieving highly strengthened Al-Cu-Mg alloy by grain refinement and grain boundary segregation. Mater Sci Eng A. 2020;793:139668.
[535] Sauvage X, Cuvilly F, Russel A, et al. Understanding the role of Ca segregation on thermal stability, electrical resistivity and mechanical strength of nanostructured aluminum. Mater Sci Eng A. 2020;798:140108.
[536] Duchaussoy A, Sauvage X, Deschamps A, et al. Complex interactions between precipitation, grain growth and recrystallization in a severely deformed Al-Zn-Mg-Cu alloy and consequences on the mechanical behavior. Materialia. 2021;15:101028.
[537] Chinh NQ, Valiev RZ, Sauvage X, et al. Grain boundary segregation and unique plastic behaviour in an ultrafine-grained Al-Zn alloy processed by HPT. Adv Eng Mater. 2014;16:1000–1009.
[538] Nasedkina Y, Sauvage X, Bobruk EV, et al. Mechanisms of precipitation induced by large strains in the Al-Cu system. J Alloys Compd. 2017;710:736–747.
[539] Abramova MM, Enikeev NA, Valiev RZ, et al. Grain boundary segregation induced strengthening of an ultrafine-grained 316 stainless steel. Mater Lett. 2014;136:349–352.
[540] Semenova I, Salimgareeva G, Da Costa G, et al. Enhanced strength and ductility of ultrafine-grained Ti processed by severe plastic deformation. Adv Eng Mater. 2010;12:803–807.
[541] Sauvage X, Ivanisenko Y. The role of carbon segregation on nanocrystallisation of pearlitic steels processed by severe plastic deformation. J Mater Sci. 2007;42:1615–1621.
[542] Lefebvre-Ulrikson W, Vurpillot F, X. Sauvage, editors. Atom probe tomography: put theory into practice. 1st ed. Amsterdam: Elsevier; 2016.
[543] Sauvage X, Nasedkina Y. The role of grain boundaries and other defects on phase transformations induced by severe plastic deformation. In: Popov VV, Popova EN, editors. Diffusion Foundations, Vol. 5. Zurich: Trans Tech Publications; 2015; p. 77–92.
[544] Sauvage X, Murashkin MY, Straumal BB, et al. Ultrafine grained structures resulting from deformation induced phase transformation in Al-Zn alloys. Adv Eng Mater. 2015;17:1821–1827.
[545] Valiev RZ, Enikeev NA, Murashkin MY, et al. On the origin of the extremely high strength of ultrafine-grained Al alloys produced by severe plastic deformation. Scr Mater. 2010;63:949–952.
[546] Enikeev NA, Abramova MM, Lomakin IV, et al. Plasticity of an extra-strong nanocrystalline stainless steel controlled by the "dislocation-segregation interaction. Mater Lett. 2021;301:130235.
[547] Edalati K, Masuda T, Arita M, et al. Room-temperature superplasticity in an ultrafine-grained magnesium alloy. Sci Rep. 2017;7:2662.
[548] Bhowmik A, Biswas S, Suwas S, et al. Evolution of grain-boundary microstructure and texture in interstitial-free steel processed by equal-channel angular extrusion. Metall Mater Trans A. 2009;40:2729.
[549] Skrotzki W, Pukenas A, Joni B, et al. Microstructure and texture evolution during severe plastic deformation of CrMnFeCoNi high-entropy alloy. IOP Conf Ser Mater Sci Eng. 2017;194:012028.
[550] Nadammal N, Kailas SV, Szpunar J, et al. Microstructure and crystallographic texture evolution during the friction-stir processing of a precipitation-hardenable aluminum alloy. JOM. 2015;67:1014–1021.
[551] Edalati K, Hashiguchi Y, Pereira PHR, et al. Effect of temperature rise on microstructural evolution during high-pressure torsion. Mater Sci Eng A. 2018;714:167–171.
[552] Roy S, Singh S, Suwas S, et al. Microstructure and texture evolution during accumulative roll bonding of aluminium alloy AA5086. Mater Sci Eng A. 2011;528:8469–8478.
[553] Lim SCV, Rollett AD. Length scale effects on recrystallization and texture evolution in Cu layers of a roll-bonded Cu–Nb composite. Mater Sci Eng A. 2009;520:189–196.

[554] Suwas S, Mondal S. Texture evolution in severe plastic deformation processes. Mater Trans. 2019;60:1457–1461.
[555] Ivanisenko Y, Kilmametov A, Rösner H, et al. Evidence of $\alpha \rightarrow \omega$ phase transition in titanium after high pressure torsion. Int J Mater Res. 2008;99:36–41.
[556] Edalati K, Daio T, Arita M, et al. High-pressure torsion of titanium at cryogenic and room temperatures: grain size effect on allotropic phase transformations. Acta Mater. 2014;68:207–213.
[557] Edalati K, Horita Z, Yagi S, et al. Allotropic phase transformation of pure zirconium by high-pressure torsion. Mater Sci Eng A. 2009;523:277–281.
[558] Zhilyaev AP, Sabirov I, Gonzales-Doncel G, et al. Effect of Nb additions on the microstructure, thermal stability and mechanical behavior of high pressure Zr phases under ambient conditions. Mater Sci Eng A. 2011;528:3496–3505.
[559] Edalati K, Horita Z, Mine Y. High-pressure torsion of hafnium. Mater Sci Eng A. 2010;527:2136–2141.
[560] Cepeda-Jiménez CM, Beltrán JI, Hernando A, et al. Tuning the magnetic properties of pure hafnium by high pressure torsion. Acta Mater. 2017;123:206–2013.
[561] Sort J, Zhilyaev A, Zielinska M, et al. Microstructural effects and large microhardness in cobalt processed by high pressure torsion consolidation of ball milled powder. Acta Mater. 2003;51:6385–6393.
[562] Edalati K, Toh S, Arita M, et al. High-pressure torsion of pure cobalt: hcp-fcc phase transformations and twinning during severe plastic deformation. Appl Phys Lett. 2013;102:181902.
[563] Mazilkin A, Straumal B, Kilmametov A, et al. Phase transformations induced by severe plastic deformation, phase transformations induced by severe plastic deformation. Mater Trans. 2019;60:1489–1499.
[564] Edalati K, Kitabayashi K, Ikeda Y, et al. Bulk nanocrystalline gamma magnesium hydride with low dehydrogenation temperature stabilized by plastic straining via high-pressure torsion. Scr Mater. 2018;157:54–57.
[565] Kitabayashi K, Edalati K, Li HW, et al. Phase transformations in MgH_2-TiH_2 hydrogen storage system by high-pressure torsion process. Adv Eng Mater. 2020;22:1900027.
[566] Levitas VI. High-pressure phase transformations under severe plastic deformation by torsion in rotational anvils. Mater Trans. 2019;60:1294–1301.
[567] Azabou M, Makhlouf T, Saurin J, et al. A study of densification and phase transformations of nanocomposite Cu-Fe prepared by mechanical alloying and consolidation process. Int J Adv Manuf Technol. 2016;87:981–987.
[568] Straumal BB, Mazilkin AA, Baretzky B, et al. Accelerated diffusion and phase transformations in Co-Cu alloys driven by the severe plastic deformation. Mater Trans. 2012;53:63–71.
[569] Mazilkin AA, Straumal BB, Rabkin E, et al. Softening of nanostructured Al-Zn and Al-Mg alloys after severe plastic deformation. Acta Mater. 2006;54:3933–3939.
[570] Straumal B, Kilmametov AR, Kucheev YO, et al. Phase transitions during high pressure torsion of CuCo alloys. Mater Lett. 2014;118:111–114.
[571] Straumal BB, Kilmametov AR, Korneva A, et al. Phase transitions in Cu-based alloys under high pressure torsion. J Alloy Compd. 2017;707:20–26.
[572] Lugo N, Llorca N, Cabrera JM, et al. Microstructures and mechanical properties of pure copper deformed severely by equal-channel angular pressing and high pressure torsion. Mater Sci Eng A. 2008;477:366–371.
[573] Liao XZ, Zhao YH, Zhu YT, et al. Grain-size effect on the deformation mechanisms of nanostructured copper processed by high-pressure torsion. J Appl Phys. 2004;96:636–640.
[574] Shamsborhan M, Ebrahimi M. Production of nanostructure copper by planar twist channel angular extrusion process. J Alloys Compd. 2016;682:552–556.
[575] Tang CI, Li H, Li SY. Effect of processing route on grain refinement in pure copper processed by equal channel angular extrusion. Trans Nonferr Met Soc China. 2016;26:1736–1744.
[576] Mao ZN, Gu RC, Liu F, et al. Effect of equal channel angular pressing on the thermal-annealing-induced microstructure and texture evolution of cold-rolled copper. Mater Sci Eng A. 2016;674:186–192.
[577] Bagherpour E, Qods F, Ebrahimi R, et al. Microstructure quantification of ultrafine grained pure copper fabricated by simple shear extrusion (SSE) technique. Mater Sci Eng A. 2016;674:221–231.
[578] Bagherpour E, Qods F, Ebrahimi R, et al. Microstructure evolution of pure copper during a single pass of simple shear extrusion (SSE): role of shear reversal. Mater Sci Eng A. 2016;666:324–338.
[579] Yadav PC, Sinhal A, Sahu S, et al. Microstructural inhomogeneity in constrained groove pressed Cu-Zn alloy sheet. J Mater Eng Perform. 2016;25:2604–2614.
[580] Blank VD, Estrin EI. Phase transitions in solids under high pressure. New York: CRC Press; 2014.
[581] Srinivasarao B, Zhilyaev AP, Perez-Prado MT. Orientation dependency of the alpha to omega plus beta transformation in commercially pure zirconium by high-pressure torsion. Scr Mater. 2011;65:241–244.
[582] Zharov A. The polymerization reactions of solid mono mers under deformation at high pressure. Usp Khim. 1984;53:236–250.
[583] Zharov A. Chapter 7- Reaction of solid monomers and polymers under shear deformation and high pressure. In: Kovarskii AL, Boca Raton: CRC Press; 1994. p. 267–301.
[584] Levitas VI, Ma Y, Selvi E, et al. High-density amorphous phase of silicon carbide obtained under large plastic shear and high pressure. Phys Rev B. 2012;85:054114.
[585] Levitas VI. Continuum mechanical fundamentals of mechanochemistry, In: Gogotsi Y, Domnich V, editors. High pressure surface science and engineering. Bristol: Inst. of Physics; 2004; p. 159–292.
[586] Levitas VI. High-pressure mechanochemistry: conceptual multiscale theory and interpretation of experiments. Phys Rev B. 2004;70:184118.
[587] Levitas VI. Phase transformations, fracture, and other structural changes in inelastic materials. Int J Plasticity. 2021;140:102914.
[588] Levitas VI. High pressure phase transformations revisited. J Phys Condens Matter. 2018;30:163001.

[589] Levitas VI. Phase transitions in elastoplastic materials: continuum thermomechanical theory and examples of control. part I. J Mech Phys Solids. 1997;45:923–947.
[590] Levitas VI. Phase transitions in elastoplastic materials: continuum thermomechanical theory and examples of control. part II. J Mech Phys Solids. 1997;45:1203–1222.
[591] Levitas VI, Chen H, Xiong L. Lattice instability during phase transformations under multiaxial stress: modified transformation work criterion. Phys Rev B. 2017;96:054118.
[592] Levitas VI, Chen H, Xiong L. Triaxial-stress-induced homogeneous hysteresis-free first-order phase transformations with stable intermediate phases. Phys Rev Lett. 2017;118:025701.
[593] Zarkevich NA, Chen H, Levitas VI, et al. Lattice instability during solid-solid structural transformations under general applied stress tensor: example of Si I → Si II with metallization. Phys Rev Lett. 2018;121:165701.
[594] Levitas VI, Javanbakht M. Phase field approach to interaction of phase transformation and dislocation evolution. Appl Phys Lett. 2013;102:251904.
[595] Javanbakht M, Levitas VI. Nanoscale mechanisms for high-pressure mechanochemistry: a phase field study. J Mater Sci. 2018;53:13343–13363.
[596] Chen H, Levitas VI, Xiong L. Amorphization induced by 60° shuffle dislocation pileup against different grain boundaries in silicon bicrystal under shear. Acta Mater. 2019;179:287–295.
[597] Babaei H, Levitas VI. Finite-strain scale-free phase-field approach to multivariant martensitic phase transformations with stress-dependent effective thresholds. J Mech Phys Solids. 2020;144:104114.
[598] Levitas VI, Esfahani SE, Ghamarian I. Scale-free modeling of coupled evolution of discrete dislocation bands and multivariant martensitic microstructure. Phys Rev Lett. 2018;121:205701.
[599] Esfahani SE, Ghamarian I, Levitas VI. Strain-induced multivariant martensitic transformations: A scale-inde pendent simulation of interaction between localized shear bands and microstructure. Acta Mater. 2020;196:430–443.
[600] Chen H, Levitas V, Xiong L. Slip of shuffle screw dislocations through tilt grain boundaries in silicon. Comput Mater Sci. 2019;157:132–135.
[601] Levitas VI, Zarechnyy OM. Kinetics of strain-induced structural changes under high pressure. J Phys Chem B. 2006;110:16035–16046.
[602] Levitas VI, Zarechnyy OM. Modeling and simulation of strain-induced phase transformations under compression in a diamond anvil cell. Phys Rev B. 2010;82:174123.
[603] Levitas VI, Zarechnyy OM. Modeling and simulation of strain-induced phase transformations under compression and torsion in a rotational diamond anvil cell. Phys Rev B. 2010;82:174124.
[604] Feng B, Levitas VI, Kamrani M. Coupled strain-induced alpha to omega phase transformation and plastic flow in zirconium under high pressure torsion in a rotational diamond anvil cell. Mater Sci Eng A. 2018;731:623–633.
[605] Levitas VI. Large deformation of materials with complex rheological properties at normal and high pressure. New York: Nova Science Publishers; 1996.
[606] Feng B, Levitas VI, Li W. FEM modeling of plastic flow and strain-induced phase transformation in BN under high pressure and large shear in a rotational diamond anvil cell. Int J Plasticity. 2019;113:236–254.
[607] Levitas VI. Phase field approach for stress- and tempera ture-induced phase transformations that satisfies lattice instability conditions. part 1. general theory. Int J Plasticity. 2018;106:164–185.
[608] Novikov NV, Polotnyak SB, Shvedov LK, et al. Regularities of phase transformations and plastic straining of materials in compression and shear in diamond anvils: experiments and theory. J Superhard Mater. 1999;21:36–48.
[609] Novikov NV, Shvedov LK, Krivosheya YN, et al. New automated shear cell with diamond anvils for in situ studies of materials using X-ray diffraction. J Superhard Mater. 2015;37:1–7.
[610] Ciezak-Jenkins JA, Jenkins TA. Optical cell for in situ vibrational spectroscopic measurements at high pressure and shear. Rev Sci Instrum. 2011;82:073905.
[611] Nomura R, Uesugi K, Azuma S, et al. High-pressure rotational deformation apparatus to 135 GPa. Rev Sci Instrum. 2017;88:044501.
[612] Zarechnyy OM, Levitas VI, Ma Y. Coupled plastic flow and phase transformation under compression of materials in a diamond anvil cell: effects of transformation kinetics and yield strength. J Appl Phys. 2012;111:023518.
[613] Blank VD, Buga SG. Automated optical installation with a shear diamond-anvil cell. Instrum Exp Tech. 1993;36:149–157.
[614] Pandey KK, Levitas VI. Displacement field measurements in traditional and rotational diamond anvil cells. J Appl Phys. 2021;129:115901.
[615] Levitas VI, Hashemi J, Ma Y. Strain-induced disorder and phase transformation in hexagonal boron nitride under quasi-homogeneous pressure: in-situ X-ray study in a rotational diamond anvil cell. Europhys Lett. 2004;68:550–556.
[616] Levitas VI, Ma Y, Hashemi J. Transformation-induced plasticity and cascading structural changes in hexagonal boron nitride under high pressure and shear. Appl Phys Lett. 2005;86:071912.
[617] Ma Y, Levitas VI, Hashemi J. X-ray diffraction measurements in a rotational diamond anvil cell. J Phys Chem Solids. 2006;67:2083–2090.
[618] Levitas VI. Resolving puzzles of the phase-transforma tion-based mechanism of the deep-focus earthquake; 2020; arXiv preprint arXiv:2110.10862.
[619] Ma Y, Selvi E, Levitas VI, et al. Effect of shear strain on the α–ε phase transition of iron: a new approach in the rotational diamond anvil cell. J Phys Condens Matter. 2006;18:1075–1082.
[620] Pandey KK, Levitas VI. In situ quantitative study of plastic strain-induced phase transformations under high pressure: example for ultra-pure Zr. Acta Mater. 2020;196:338–346.

[621] Popov M, Mordkovich V, Perfilov S, et al. Synthesis of ultrahard fullerite with a catalytic 3D polymerization reaction of C_{60}. Carbon. 2014;76:250–256.
[622] Ciezak-Jenkins JA, Jenkins TA. Mechanochemical indu ced structural changes in sucrose using the rotational diamond anvil cell. J Appl Phys. 2018;123:085901.
[623] Hsieh S, Bhattacharyya P, Zu C, et al. Imaging stress and magnetism at high pressures using a nanoscale quantum sensor. Science. 2019;366:1349–1354.
[624] Levitas VI, Kamrani M, Feng B. Tensorial stress-strain fields and large elastoplasticity as well as friction in diamond anvil cell up to 400 GPa. NPJ Comput. Mater. 2019;5:94.
[625] Li B, Ji C, Yang W, et al. Diamond anvil cell behavior up to 4 mbar. Proc Natl Acad Sci USA. 2018;115:1713–1717.
[626] Watanabe T. An approach to grain boundary design for strong and ductile polycrystals. Res Mech. 1984;11:47.
[627] Nazarov A, Romanov A, Valiev RZ. On the structure, stress fields and energy of nonequilibrium grain boundaries. Acta Metall Mater. 1993;41:1033–1040.
[628] Wilde G, Divinski S. Grain boundaries and diffusion phenomena in severely deformed materials. Mater Trans. 2019;60:1302–1315.
[629] Divinski SV, Reglitz G, Rösner H, et al. Self-diffusion in Ni prepared by severe plastic deformation: effect of non-equilibrium grain boundary state. Acta Mater. 2011;59:1974–1985.
[630] Raju KS, Sarma VS, Kauffmann A, et al. High strength and ductile ultrafine-grained Cu-Ag alloy through bimodal grain size, dislocation density and solute distribution. Acta Mater. 2013;61:228–238.
[631] Ibrahim N, Peterlechner M, Emeis F, et al. Mechanical alloying via high-pressure torsion of the immiscible $Cu_{50}Ta_{50}$ system. Mater Sci Eng A. 2017;685:19–30.
[632] Emeis F, Peterlechner M, Divinski SV, et al. Grain boundary engineering parameters for ultrafine grained microstructures: proof of principles by a systematic composition variation in the Cu-Ni system. Acta Mater. 2018;150:262–272.
[633] Divinski SV, Reglitz G, Golovin IS, et al. Effect of heat treatment on diffusion, internal friction, microstructure and mechanical properties of ultra-fine-grained nickel severely deformed by equal-channel angular pressing. Acta Mater. 2015;82:11–21.
[634] Fiebig J, Divinski SV, Rösner H, et al. Diffusion of Ag and Co in ultrafine-grained α-Ti deformed by equal channel angular pressing. J Appl Phys. 2011;110:083514.
[635] Taheriniya S, Davani FA, Hilke S, et al. High entropy alloy nanocomposites produced by high pressure torsion. Acta Mater. 2021;208:116714.
[636] Sauvage X, Chbihi A, Quelennec X. Severe plastic deformation and phase transformations. J Phys Conf Ser. 2010;240:012003.
[637] Straumal B, Korneva A, Zięba P. Phase transitions in metallic alloys driven by the high pressure torsion. Arch Civ Mech Eng. 2014;14:242–249.
[638] Prokoshkin SD, Khmelevskaya IY, Dobatkin SV, et al. Alloy composition, deformation temperature, pressure and post-deformation annealing effects in severely deformed Ti-Ni based shape memory alloys. Acta Mater. 2005;53:2703–2714.
[639] Kovács Z, Henits P, Zhilyaev AP, et al. Deformation induced primary crystallization in a thermally non-primary crystallizing amorphous $Al_{85}Ce_8Ni_5Co_2$ alloy. Scr Mater. 2006;54:1733–1737.
[640] Sauvage X, Jessner P, Vurpillot F, et al. Nanostructure and properties of a Cu-Cr composite processed by severe plastic deformation. Scr Mater. 2008;58:1125–1128.
[641] Bachmaier A, Kerber M, Setman D, et al. The formation of supersaturated solid solutions in Fe-Cu alloys deformed by high-pressure torsion. Acta Mater. 2012;60:860–871.
[642] Sauvage X, Wetscher F, Pareige P. Mechanical alloying of Cu and Fe induced by severe plastic deformation of a Cu-Fe composite. Acta Mater. 2005;53:2127–2135.
[643] Straumal B, Baretzky B, Mazilkin A, et al. Formation of nanograined structure and decomposition of supersaturated solid solution during high pressure torsion of Al-Zn and Al-Mg alloys. Acta Mater. 2004;52:4469–4478.
[644] Krämer L, Champion Y, Kormout KS, et al. Bulk metallic dual phase glasses by severe plastic deformation. Intermetallics. 2018;94:172–178.
[645] Sun Y F, Nakamura T, Todaka Y, et al. Fabrication of CuZr(Al) bulk metallic glasses by high pressure torsion. Intermetallics. 2009;17:256–261.
[646] Jiang QK, Wang XD, Nie XP, et al. Zr-(Cu,Ag)-Al bulk metallic glasses. Acta Mater. 2008;56:1785–1796.
[647] Men H, Fu J, Ma C, et al. Bulk glass formation in ternary Cu-Zr-Ti system. J Univ Sci Technol Beijing Miner Metall Mater (Eng Ed). 2007;14:19–22.
[648] Wang Q, Wang YM, Qiang JB, et al. Composition optimization of the Cu-based Cu-Zr-Al alloys. Intermetallics. 2004;12:1229–1232.
[649] Wang YL, Xu J. Ti (Zr)-Cu-Ni bulk metallic glasses with optimal glass-forming ability and their compressive properties. Metall Mater Trans A. 2008;39:2990–2997.
[650] Chen W, Wang Y, Qiang J, et al. Bulk metallic glasses in the Zr-Al-Ni-Cu system. Acta Mater. 2003;51:1899–1907.
[651] He Q, Xu J. Locating malleable bulk metallic glasses in Zr-Ti-Cu-Al alloys with calorimetric glass transition temperature as an indicator. J Mater Sci Technol. 2012;28:1109–1122.
[652] Wiest A, Duan G, Demetriou MD, et al. Zr-Ti-based Be-bearing glasses optimized for high thermal stability and thermoplastic formability. Acta Mater. 2008;56:2625–2630.
[653] Umetsu RY, Tu R, Goto T. Thermal and electrical transport properties of Zr-based bulk metallic glassy alloys with high glass-forming ability. Mater Trans. 2012;53:2–6.
[654] Xu Y, Zhang Y, Li J, et al. Enhanced thermal stability and hardness of $Zr_{46}Cu_{39.2}Ag_{7.8}Al_7$ bulk metallic glass with Fe addition. Mater Sci Eng A. 2010;527:1444–1447.
[655] Caron A, Wunderlich R, Gu L, et al. Structurally enhanced anelasticity in Zr-based bulk metallic glasses. Scr Mater. 2012;64:946–949.
[656] Kim CP, Suh J, Wiest A, et al. Fracture toughness study of new Zr-based Be-bearing bulk metallic glasses. Scr Mater. 2009;60:80–83.

[657] Liu JW, Cao QP, Chen LY, et al. Shear band evolution and hardness change in cold-rolled bulk metallic glasses. Acta Mater. 2010;58:4827–4840.
[658] Liu XJ, Li X, Xu Y, et al. Atomic packing symmetry in the metallic liquid and glass states. Acta Mater. 2011;59:6480–6488.
[659] Ma D, Stoica AD, Yang L, et al. Nearest-neighbor coordination and chemical ordering in multicomponent bulk metallic glasses. Appl Phys Lett. 2007;90:6–9.
[660] Vo NQ, Zhou J, Ashkenazy Y, et al. Atomic mixing in metals under shear deformation. JOM. 2013;65:382–389.
[661] Raabe D, Ohsaki S, Hono K. Mechanical alloying and amorphization in Cu-Nb-Ag in situ composite wires studied by transmission electron microscopy and atom probe tomograph. Acta Mater. 2009;57:5254–5263.
[662] Kormout KS, Pippan R, Bachmaier A. Deformation-induced supersaturation in immiscible material systems during high-pressure torsion. Adv Eng Mater. 2017;19:1600675.
[663] Wilde G, Rösner H. Stability aspects of bulk nanostructured metals and composites. J Mater Sci. 2007;42:1772–1781.
[664] Bachmaier A, Pippan R. High-pressure torsion deformation induced phase transformations and formations: new material combinations and advanced properties. Mater Trans. 2019;60:1256–1269.
[665] Peng XK, Wuhrer R, Heness G, et al. On the interface development and fracture behaviour of roll bonded copper/aluminium metal laminates. J Mater Sci. 1999;34:2029–2038.
[666] Zhang XP, Yang TH, Castagne S, et al. Microstructure; bonding strength and thickness ratio of Al/Mg/Al alloy laminated composites prepared by hot rolling. Mater Sci Eng A. 2011;528:1954–1960.
[667] Macwan A, Jiang XQ, Li C, et al. Effect of annealing on interface microstructure and tensile properties of rolled Al/Mg/Al tri-layer clad sheets. Mater Sci Eng A. 2013;587:344–351.
[668] Lee KS, Lee YS, Kwon YN. Influence of secondary warm rolling on the interface microstructure and mechanical properties of a roll-bonded three-ply Al/Mg/Al sheet. Mater Sci Eng A. 2014;606:205–213.
[669] Eizadjou M, Talachi AK, Manesh HD, et al. Investigation of structure and mechanical properties of multi-layered Al/Cu composite produced by accumulative roll bonding (ARB) process. Comp Sci Technol. 2008;68:2003–2009.
[670] Chen MC, Kuo CW, Chang CM, et al. Diffusion and formation of intermetallic compounds during accumulative roll-bonding of Al/Mg alloys. Mater Trans. 2007;48:2595–2598.
[671] Chang H, Zheng MY, Xu C, et al. Microstructure and mechanical properties of the Mg/Al multilayer fabricated by accumulative roll bonding (ARB) at ambient temperature. Mater Sci Eng A. 2012;543:249–256.
[672] Dehsorkhi RN, Qods F, Tajally M. Investigation on microstructure and mechanical properties of Al-Zn composite during accumulative roll bonding (ARB) process. Mater Sci Eng A. 2011;530:63–72.
[673] Ghalandari L, Moshksar MM. High-strength and high-conductive Cu/Ag multilayer produced by ARB. J Alloys Compd. 2010;506:172–178.
[674] Tayyebi M, Eghbali B. Study on the microstructure and mechanical properties of multilayer Cu/Ni composite processed by accumulative roll bonding. Mater Sci Eng A. 2013;559:759–764.
[675] Ghalandari L, Mahdavian MM, Reihanian M. Micro structure evolution and mechanical properties of Cu/Zn multilayer processed by accumulative roll bonding (ARB). Mater Sci Eng A. 2014;593:145–152.
[676] Beausir B, Scharnweber J, Jaschinski J, et al. Plastic anisotropy of ultrafine grained aluminium alloys produced by accumulative roll bonding. Mater Sci Eng A. 2010;527:3271–3278.
[677] Sato YS, Park SC, Michiuchi M, et al. Constitutional liquation during dissimilar friction stir welding of Al and Mg alloys. Scr Mater. 2004;50:1233–1236.
[678] Bouaziz O, Kim HS, Estrin Y. Architecturing of metal-based composites with concurrent nanostructuring, a new paradigm of materials design. Adv Eng Mater. 2013;15:336–340.
[679] Ahn B, Zhilyaev AP, Lee HJ, et al. Rapid synthesis of an extra hard metal matrix nanocomposite at ambient temperature. Mater Sci Eng A. 2015;635:109–117.
[680] Han JK, Herndon T, Jang JI, et al. Synthesis of hybrid nanocrystalline alloys by mechanical bonding through high-pressure torsion. Adv Eng Mater. 2020;22:1901289.
[681] Han JK, Liss KD, Langdon TG, et al. Synthesis of a bulk nanostructured metastable Al alloy with extreme supersaturation of Mg. Sci Rep. 2019;9:17186.
[682] Han JK, Liss KD, Langdon TG, et al. Mechanical properties and structural stability of a bulk nanostructured metastable aluminum-magnesium system. Mater Sci Eng A. 2020;796:140050.
[683] Han JK, Jang JI, Langdon TG, et al. Bulk-state reactions and improving the mechanical properties of metals through high-pressure torsion. Mater Trans. 2019;60:1131–1138.
[684] Edalati K, Horita Z. High-pressure torsion of pure metals: influence of atomic bond parameters and stacking fault energy on grain size and correlation with hardness. Acta Mater. 2011;59:6831–6836.
[685] Sevillano J G. Dynamic steady state by unlimited unidirectional plastic deformation of crystalline materials deforming by dislocation glide at low to moderate temperatures. Metals. 2020;10:66.
[686] Edalati K, Daio T, Lee S, et al. High strength and superconductivity in nanostructured niobium-titanium alloy by high-pressure torsion and annealing: significance of elemental decomposition and supersaturation. Acta Mater. 2014;80:149–158.
[687] Edalati K, Shao H, Emami H, et al. Activation of titanium-vanadium alloy for hydrogen storage by introduction of nanograins and edge dislocations using high-pressure torsion. Int J Hydrogen Energy. 2016;41:8917–8924.
[688] Campos-Quirós A, Cubero-Sesín JM, Edalati K. Synthesis of nanostructured biomaterials by high-pressure torsion: effect of niobium content on microstructure and

mechanical properties of Ti-Nb alloys. Mater Sci Eng A. 2020;795:139972.
[689] Edalati K, Toh S, Watanabe M, et al. In-situ production of bulk intermetallic-based nanocomposites and nanostructured intermetallics by high-pressure torsion. Scr Mater. 2012;66:386–389.
[690] Edalati K, Toh S, Iwaoka H, et al. Ultrahigh strength and high plasticity in TiAl intermetallics with bimodal grain structure and nanotwins. Scr Mater. 2012;67:814–817.
[691] Lee S, Edalati K, Iwaoka H, et al. Formation of FeNi with L10-ordered structure using high-pressure torsion. Philos Mag Lett. 2014;94:639–646.
[692] Edalati K, Daio T, Horita Z, et al. Evolution of lattice defects, disordered/ordered phase transformations and mechanical properties in Ni-Al-Ti intermetallics by high-pressure torsion. J Alloys Compd. 2013;563:221–228.
[693] Edalati K, Emami H, Staykov A, et al. Formation of metastable phases in magnesium-titanium system by high-pressure torsion and their hydrogen storage performance. Acta Mater. 2015;99:150–156.
[694] Bachmaier A, Schmauch J, Aboulfadl H, et al. On the process of co-deformation and phase dissolution in a hard-soft immiscible Cu-Co alloy system during high-pressure torsion deformation. Acta Mater. 2016;115:333–346.
[695] Edalati K, Emami H, Ikeda Y, et al. New nanostructured phases with reversible hydrogen storage capability in immiscible magnesium-zirconium system produced by high-pressure torsion. Acta Mater. 2016;108:293–303.
[696] Lopez-Gomez EI, Edalati K, Coimbroo DD, et al. FCC phase formation in immiscible Mg-Hf (magnesium-hafnium) system by high-pressure torsion. AIP Adv. 2020;10:055222.
[697] Fujiwara K, Uehiro R, Edalati K, et al. New Mg-V-Cr BCC alloys synthesized by high-pressure torsion and ball milling. Mater Trans. 2018;59:741–746.
[698] Duchaussoy A, Sauvage X, Edalati K, et al. Structure and mechanical behavior of ultrafine-grained aluminum-iron alloy stabilized by nanoscaled intermetallic particles. Acta Mater. 2019;167:89–102.
[699] Edalati K, Horita Z, Valiev RZ. Transition from poor ductility to room-temperature superplasticity in a nanostructured aluminum alloy. Sci Rep. 2018;8:6740.
[700] Mohammadi A, Enikeev NA, Murashkin MY, et al. Developing age-hardenable Al-Zr alloy by ultra-severe plastic deformation: significance of supersaturation, segregation and precipitation on hardening and electrical conductivity. Acta Mater. 2021;203:116503.
[701] Mohammadi A, Enikeev NA, Murashkin MY, et al. Examination of inverse Hall-Petch relation in nanostructured aluminum alloys by ultra-severe plastic deformation. J Mater Sci Technol. 2021;91:78–89.
[702] Edalati K, Akiba E, Horita Z. High-pressure torsion for new hydrogen storage materials. Sci Technol Adv Mater. 2018;19:185–193.
[703] Edalati K, Li HW, Kilmametov A, et al. High-pressure torsion for synthesis of high-entropy alloys. Metals. 2021;11:1263.
[704] Bulffingeri GB. De solidorum resistentia specimen [The resistance of solids]. Commentarii Academiae Scientiarum Imperialis Petropolitanae. 1735;4:164–181.
[705] Hollomon JH. Tensile deformation. Trans AIME. 1945;162:268–290.
[706] Langdon TG. Twenty-five years of ultrafine-grained materials: achieving exceptional properties through grain refinement. Acta Mater. 2013;61:7035–7059.
[707] Edalati K, Horita Z. Significance of homologous temperature in softening behavior and grain size of pure metals processed by high-pressure torsion. Mater Sci Eng A. 2011;528:7514–7523.
[708] Kawasaki M. Different models of hardness evolution in ultrafine-grained materials processed by high-pressure torsion. J Mater Sci. 2014;49:18–34.
[709] Ito Y, Edalati K, Horita Z. High-pressure torsion of aluminum with ultrahigh purity (99.9999%) and occurrence of inverse Hall-Petch relationship. Mater Sci Eng A. 2017;679:428–434.
[710] Valiev RZ, Alexandrov IV, Zhu YT, et al. Paradox of strength and ductility in metals processed by severe plastic deformation. J Mater Res. 2002;17:5–8.
[711] Ovid'ko IA, Valiev RZ, Zhu YT. Review on superior strength and enhanced ductility of metallic nanomaterials. Prog Mater Sci. 2018;94:462–540.
[712] Demirtas M, Purcek G. Room temperature superplasticity in fine/ultrafine grained materials subjected to severe plastic deformation. Mater Trans. 2019;60:1159–1167.
[713] Pippan R, Hohenwarter A. The importance of fracture toughness in ultrafine and nanocrystalline bulk materials. Mater Res Lett. 2016;4:127–136.
[714] Wang CT, Gao N, Gee MG, et al. Effect of grain size on the micro-tribological behavior of pure titanium processed by high-pressure torsion. Wear. 2012;280-281:28–35.
[715] Khatibi G, Horky J, Weiss B, et al. High cycle fatigue behaviour of copper deformed by high pressure torsion. Int J Fatigue. 2010;32:269–278.
[716] Kral P, Dvorak J, Sklenicka V, et al. The characteristics of creep in metallic materials processed by severe plastic deformation. Mater Trans. 2019;60:1506–1517.
[717] Lu L, Chen X, Huang X, et al. Revealing the maximum strength in nanotwinned copper. Science. 2009;323:607–610.
[718] Jian WW, Cheng GM, Xu WZ, et al. Ultrastrong Mg alloy via nano-spaced stacking faults. Mater Res Lett. 2013;1:61–66.
[719] Wang Y, Chen M, Zhou F, et al. High tensile ductility in a nanostructured metal. Nature. 2002;419:912–915.
[720] Horita Z, Ohashi K, Fujita T, et al. Achieving high strength and high ductility in precipitation-hardened alloys. Adv Mater. 2005;17:1599–1602.
[721] Valiev RZ. On grain boundary engineering of UFG metals and alloys for enhancing their properties. Mater Sci Forum. 2008;584-586:22–28.
[722] Saito T, Furuta T, Hwang JH, et al. Multifunctional alloys obtained via a dislocation-free plastic deformation mechanism. Science. 2003;300:464–467.
[723] Cheng Z, Zhou H, Lu Q, et al. Extra strengthening and work hardening in gradient nanotwinned metals. Science. 2018;362. doi:10.1126/science.aau1925.
[724] Kuramoto S, Furuta T. Severe plastic deformation to achieve high strength and high ductility in Fe-Ni based alloys with lattice softening. Mater Trans. 2019;60:1116–1122.

[725] Yang X, Pan H, Zhang J, et al. Progress in mechanical properties of gradient structured metallic materials induced by surface mechanical attrition treatment. Mater Trans. 2019;60:1543–1552.
[726] Kuramoto S, Furuta T, Nagasako N, et al. Lattice softening for producing ultrahigh strength of iron base nanocrystalline alloy. Appl Phys Lett. 2009;95:211 901.
[727] Furuta T, Kuramoto S, Osuna T, etal Bulk nanograined Fe-Ni-Co-Ti alloy processed by high pressure torsion: approaching ideal strength with improved ductility. In: Higashida K, Tsuji N, editors. Proceedings of the Second International Symposium on Steel Sciences. Kyoto: The Japan Institute of Metals; 2010; p. 151–154.
[728] Furuta T, Kuramoto S, Horibuchi K, et al. Ultrahigh strength of nanocrystalline iron-based alloys produced by high-pressure torsion. J Mater Sci. 2010;45:4745–4753.
[729] Edalati K, Toh S, Furuta T, et al. Development of ultrahigh strength and high ductility in nanostructured iron alloys with lattice softening and nanotwins. Scr Mater. 2012;67:511–514.
[730] Furuta T, Kuramoto S, Osuna T, et al. Die-hard plastic deformation behavior in an ultrahigh-strength Fe-Ni-Al-C alloy. Scr Mater. 2015;101:87–90.
[731] Edalati K, Furuta T, Daio T, et al. High strength and high uniform ductility in a severely deformed iron alloy by lattice softening and multimodal-structure formation. Mater Res Lett. 2015;3:197–202.
[732] Ma Y, Yang M, Jiang P, et al. Plastic deformation mechanisms in a severely deformed Fe-Ni-Al-C alloy with superior tensile properties. Sci Rep. 2017;7:15619.
[733] Miyazaki I, Furuta T, Oh-ishi K, et al. Overcoming the strength–ductility trade-off via the formation of a thermally stable and plastically unstable austenitic phase in cold-worked steel. Mater Sci Eng A. 2018;721:74–80.
[734] Furuta T, Miyazaki I, Oh-ishi K, et al. Characterization of cold-rolled heterogeneous microstructure formed by multimodal deformation in an Fe-Ni-Al-C alloy with lattice softening. Mater Des. 2018;153:166–176.
[735] Gleiter H. Nanostructured materials: basic concepts and microstructure. Acta Mater. 2000;48:1–29.
[736] Zhu YT, Liao X. Retaining ductility. Nat Mater. 2004;3:351.
[737] Wu X, Jiang P, Chen L, et al. Extraordinary strain hardening by gradient structure. Proc Natl Acad Sci. 2014;111:7197–7201.
[738] Zhang Y, Yang C, Zhou D, et al. Effect of stacking fault energy on microstructural feature and back stress hardening in Cu-Al alloys subjected to surface mechanical attrition treatment. Mater Sci Eng A. 2019;740-741:235–242.
[739] Yang X, Ma X, Moering J, et al. Influence of gradient structure volume fraction on the mechanical properties of pure copper. Mater Sci Eng A. 2015;645:280–285.
[740] Yin Z, Sun L, Yang J, et al. Mechanical behavior and deformation kinetics of gradient structured Cu-Al alloys with varying stacking fault energy. J Alloys Compd. 2016;687:152–160.
[741] Lin Y, Pan J, Zhou HF, et al. Mechanical properties and optimal grain size distribution profile of gradient grained nickel. Acta Mater. 2018;153:279–289.
[742] Meng LF, Zhang Z, Zhang YL, et al. The influence of stacking fault energy on mechanical properties of Cu-Al-Zn alloys processed by surface mechanical attrition treatment. Mater Sci Eng A. 2019;744:235–240.
[743] Qu S, An XH, Yang HJ, et al. Microstructural evolution and mechanical properties of Cu-Al alloys subjected to equal channel angular pressing. Acta Mater. 2009;57:1586–1601.
[744] Ferrasse S, Segal VM, Alford F, et al. Scale up and application of equal-channel angular extrusion for the electronics and aerospace industries. Mater Sci Eng A. 2008;493:130–140.
[745] Serra G, Morais L, Elias CN, et al. Nanostructured severe plastic deformation processed titanium for orthodontic mini-implants. Mater Sci Eng C. 2013;33:4197–4202.
[746] Valiev RZ, Murashkin MY, Sabirov I. A nanostructural design to produce high-strength Al alloys with enhanced electrical conductivity. Scr Mater. 2014;76:13–16.
[747] Hertzberg RW. Deformation and fracture mechanics of engineering materials. 4th ed New York: Wiley; 1996.
[748] Hübner P, Kiessling R, Biermann H, et al. Fracture behaviour of ultrafine-grained materials under static and cyclic loading. Int J Mater Res. 2006;97:1566–1570.
[749] Kimura Y, Inoue T, Yin F, et al. Inverse temperature dependence of toughness in an ultrafine grain-structure steel. Science. 2008;320:1057–1060.
[750] Hohenwarter A, Kammerhofer C, Pippan R. The ductile to brittle transition of ultrafine-grained Armco iron: an experimental study. J Mater Sci. 2010;45:4805–4812.
[751] Gizynski M, Pakiela Z, Chrominski W, et al. The low temperature fracture behaviour of hydrostatically extruded ultra-fine grained Armco iron. Mater Sci Eng A. 2015;632:35–42.
[752] Semenova IP, Modina JM, Polyakov AV, et al. A fracture toughness at cryogenic temperatures of ultra fi negrained Ti-6Al-4V alloy processed by ECAP. Mater Sci Eng A. 2018;716:260–267.
[753] Rybalchenko OV, Prosvirnin DV, Tokar AA, et al. Effect of ECAP on structural, mechanical and functional characteristics of the austenitic Cr-Ni-Ti steels. J Phys Conf Ser. 2018;1134:012049.
[754] Hohenwarter A, Pippan R. Fracture of ECAP-deformed iron and the role of extrinsic toughening mechanisms. Acta Mater. 2013;61:2973–2983.
[755] Hohenwarter A, Pippan R. Anisotropic fracture behavior of ultrafine-grained iron. Mater Sci Eng A. 2010;527:2649–2656.
[756] Hohenwarter A. Unpublished work; 2021.
[757] Hohenwarter A, Pippan R. Fracture toughness evaluation of ultrafine-grained nickel. Scr Mater. 2011;64:982–985.
[758] Hohenwarter A, Völker B, Kapp MW, et al. Ultrastrong and damage tolerant metallic bulk materials: a lesson from nanostructured pearlitic steel wires. Sci Rep. 2016;6:33228.
[759] Ashby MF, Easterling KE, Harrysson R, et al. The fracture and toughness of woods. Proc R Soc Lond A Math Phys Sci. 1985;398:261–280.

[760] Langdon TG. Seventy-five years of superplasticity: historic developments and new opportunities. J Mater Sci. 2009;44:5998–6010.
[761] Pearson CE. The viscous properties of extruded eutectic alloys of lead-tin and bismuth-tin. J Inst Metals. 1934;54:111–124.
[762] Wang CT, He Y, Langdon TG. The significance of strain weakening and self-annealing in a superplastic Bi-Sn eutectic alloy processed by high-pressure torsion. Acta Mater. 2020;185:245–256.
[763] Langdon TG. The mechanical properties of superplastic materials. Metall Trans A. 1982;13:689–701.
[764] Langdon TG. The background to superplastic forming and opportunities arising from new developments. Solid State Phenom. 2020;306:1–8.
[765] Valiev RZ, Salimonenko DA, Tsenev NK, et al. Observations of high strain rate superplasticity in commercial aluminum alloys with ultrafine grain sizes. Scr Mater. 1997;37:1945–1950.
[766] Figueiredo RB, Langdon TG. Record superplastic ductility in a magnesium alloy processed by equal-channel angular pressing. Adv Eng Mater. 2008;10:37–40.
[767] Horita Z, Furukawa M, Nemoto M, et al. Superplastic forming at high strain rates after severe plastic deformation. Acta Mater. 2000;48:1633–1640.
[768] Kawasaki M, Langdon TG. Review: achieving superplastic properties in ultrafine-grained materials at high temperatures. J Mater Sci. 2016;51:19–32.
[769] Kawasaki M, Langdon TG. The contribution of severe plastic deformation to research on superplasticity. Mater Trans. 2019;60:1123–1130.
[770] Lin K, Li Z, Liu Y, et al. Exploiting tube high-pressure shearing to prepare a microstructure in Pb-Sn alloys for unprecedented superplasticity. Scr Mater. 2022;209:114390.
[771] Ha TK, Chang YW. Effects of temperature and micro structure on the superplasticity in microduplex Pb-Sn alloys. Mater Sci Forum. 2001;357-359:159–164.
[772] Padmanabhan KA, Davies GJ. Superplasticity, mechanical and structural aspects, environmental effects, fundamentals and applications. Berlin (NY): Springer-Verlag; 1980.
[773] Langdon TG. Recent developments in high strain rate superplasticity. Mater Trans JIM. 1999;40:716–722.
[774] Komura S, Horita Z, Furukawa M, et al. Influence of scandium on superplastic ductilities in an Al-Mg-Sc alloy. J Mater Res. 2000;15:2571–2576.
[775] Langdon TG. A unified approach to grain boundary sliding in creep and superplasticity. Acta Metall Mater. 1994;42:2437–2443.
[776] Kawasaki M, Langdon TG. Principles of superplasticity in ultrafine-grained materials. Mater Sci. 2007;42:1782–1796.
[777] Tanaka T, Makii K, Ueda H, et al. Study on practical application of a new seismic damper using a Zn-Al alloy with a nanocrystalline microstructure. Int J Mech Sci. 2003;45:1599–1612.
[778] Tanaka T, Higashi K. Superplasticity at room temperature in Zn-22Al alloy processed by equal-channel-angular extrusion. Mater Trans. 2004;45:1261–1265.
[779] Tanaka T, Watanabe H, Higashi K. Microstructure in Zn-Al alloys after equal-channel-angular extrusion. Mater Trans. 2003;44:1891–1894.
[780] Huang Y, Langdon TG. Characterization of deformation processes in a Zn-22% Al alloy using atomic force microscopy. J Mater Sci. 2002;37:4993–4498.
[781] Yang CF, Pan JH, Chuang MC. Achieving high strain rate superplasticity via severe plastic deformation processing. J Mater Sci. 2008;43:6260–6266.
[782] Demirtas M, Yanar H, Purcek G. Optimization of RT superplasticity of UFG Zn-22Al alloy by applying ECAP at different temperatures and phase regions. IOP Conf Ser Mater Sci Eng. 2017;194:012033.
[783] Demirtas M, Purcek G, Yanar H, et al. Improvement of high strain rate and room temperature superplasticity in Zn-22Al alloy by two-step equal-channel angular pressing. Mater Sci Eng A. 2014;620:233–240.
[784] Xia SH, Wang J, Wang JT, et al. Improvement of room-temperature superplasticity in Zn-22 wt.%Al alloy. Mater Sci Eng A. 2008;493:111–115.
[785] Kumar P, Xu C, Langdon TG. Mechanical characteristics of a Zn-22% Al alloy processed to very high strains by ECAP. Mater Sci Eng A. 2006;429:324–328.
[786] Hirata T, Tanaka T, Chung SW, et al. Relationship between deformation behavior and microstructural evolution of friction stir processed Zn-22 wt.% Al alloy. Scr Mater. 2007;56:477–480.
[787] Demirtas M, Purcek G, Yanar H, et al. Achieving room temperature superplasticity in Zn-5Al alloy at high strain rates by equal-channel angular extrusion. J Alloys Compd. 2015;623:213–218.
[788] Demirtas M, Purcek G, Yanar H, et al. Effect of equal-channel angular pressing on room temperature superplasticity of quasi-single phase Zn-0.3Al alloy. Mater Sci Eng A. 2015;644:17–24.
[789] Mehrer H. Numerical data and functional relationship in science and technology, Diffusion in solid metals and alloys. Series 26, Berlin: Springer; 1990.
[790] Langen G, Schwitzgebel G, Ruppersberg H. Thermodynamic and diffusion studies on solid (Li,Mg) and (Li,Cd) alloys. Mater Res Bull. 1984;19:1141–1147.
[791] da Costa Andrade EN. On the viscous flow in metals, and allied phenomena. Proc R Soc London Series A. 1910;84:1–12.
[792] Čadek J. Creep in metallic materials. Amsterdam: Elsevier Science Publishers; 1988.
[793] Valiev RZ, Langdon TG. Achieving exceptional grain refinement through severe plastic deformation: new approaches for improving the processing technology. Metall Mater Trans A. 2011;42:2942–2951.
[794] Grabovetskaya GP, Ivanov KV, Kolobov YR. Creep features of nanostructured materials produced by severe plastic deformation. Ann Chim Sci Mater. 2002;27:89–98.
[795] Sklenicka V, Dvorak J, Svoboda M. Creep in ultrafine-grained aluminium. Mater Sci Eng A. 2004;387-389:696–701.
[796] Sklenicka V, Dvorak J, Kral P, et al. Creep processes in pure aluminium processed by equal-channel angular pressing. Mater Sci Eng A. 2005;410-411:408–412.
[797] Kostka A, Tak KG, Eggeler G. On the effect of equal-channel angular pressing on the creep of tempered

martensite ferritic steels. Mater Sci Eng A. 2008;481-482:723–726.
[798] Sklenicka V, Kral P, Dvorak J, et al. Effect of equal-channel angular pressing on the creep resistance of precipitation strengthened alloys. Mater Sci Forum. 2011;667-669:897–902.
[799] Kral P, Dvorak J, Sklenicka V, et al. The effect of ultrafine-grained microstructure on creep behaviour of 9%Cr steel. Materials. 2018;11:787.
[800] Waitz T, Antretter T, Fischer FD, et al. Size effects on the martensitic phase transformation of NiTi nanograins. J Mech Phys Solids. 2007;55:419–444.
[801] Kozhushko VV, Paltauf G, Krenn H, et al. Attenuation of ultrasound in severely plastically deformed nickel. NDT E Int. 2011;44:261–266.
[802] Mine Y, Tachibana K, Horita Z. Effect of hydrogen on tensile properties of ultrafine-grained type 310S austenitic stainless steel processed by high-pressure torsion. Metall Mater Trans A. 2011;42:1619–1629.
[803] Menumerov E, Gilroy KD, Hajfathalian M, et al. Plastically deformed Cu-based alloys as high-performance catalysts for the reduction of 4-nitrophenol. Catal Sci Technol. 2016;6:5737–5745.
[804] Chu F, Han B, Edalati K, et al. Severe plastic deformed Pd-based metallic glass for superior hydrogen evolution in both acidic and alkaline media. Scr Mater. 2021;204:114145.
[805] Wu K, Chu F, Meng Y, et al. Cathodic corrosion activated Fe-based nanoglass as a highly active and stable oxygen evolution catalyst for water splitting. J Mater Chem A. 2021;9:12152–12160.
[806] Straumal BB, Protasova SG, Mazilkin AA, et al. Effect of severe plastic deformation on the coercivity of Co-Cu alloys. Philos Mag Lett. 2009;89:649–654.
[807] Dobatkin SV, Gubicza J, Shangina DV, et al. High strength and good electrical conductivity in Cu-Cr alloys processed by severe plastic deformation. Mater Lett. 2015;153:5–9.
[808] Nishizaki T, Lee S, Horita Z, et al. Superconducting properties in bulk nanostructured niobium prepared by high-pressure torsion. Physica C. 2013;493:132–135.
[809] Rogl G, Setman D, Schafler E, et al. High-pressure torsion, a new processing route for thermoelectrics of high ZTs by means of severe plastic deformation. Acta Mater. 2012;60:2146–2157.
[810] Radiguet B, Etienne A, Pareige P, et al. Irradiation behavior of nanostructured 316 austenitic stainless steel. J Mater Sci. 2008;43:7338–7343.
[811] Gao JH, Guan SK, Ren ZW, et al. Homogeneous corrosion of high pressure torsion treated Mg-Zn-Ca alloy in simulated body fluid. Mater Lett. 2011;65:691–693.
[812] Faghihi S, Li D, Szpunar JA. Tribocorrosion behaviour of nanostructured titanium substrates processed by high-pressure torsion. Nanotechnolgy. 2010;21:485703.
[813] Nie FL, Zheng YF, Cheng Y, et al. In vitro corrosion and cytotoxicity on microcrystalline, nanocrystalline and amorphous NiTi alloy fabricated by high pressure torsion. Mater Lett. 2010;64:983–986.
[814] Hirscher M, Yartys VA, Baricco M, et al. Materials for hydrogen-based energy storage-past, recent progress and future outlook. J. Alloys Compd. 2020;827:153548.
[815] Shao H, He L, Lin H, et al. Progress and trends in magnesium-based materials for energy-storage research: a review. Energy Technol. 2018;6:445–458.
[816] Zaluski L, Zaluska A, Tessier P, et al. Catalytic effect of Pd on hydrogen absorption in mechanically alloyed Mg_2Ni, $LaNi_5$ and FeTi. J Alloys Compd. 1995;217:295–300.
[817] Liang G, Huot J, Boily S, et al. Catalytic effect of transition metals on hydrogen sorption in nanocrystalline ball milled MgH_2-Tm (Tm = Ti, V, Mn, Fe and Ni) systems. J Alloys Compd. 1999;292:247–252.
[818] Yavari AR, Moulec AL, de Castro FR, et al. Improvement in H-sorption kinetics of MgH_2 powders by using Fe nanoparticles generated by reactive FeF_3 addition. Scr Mater. 2005;52:719–724.
[819] de Castro JFR, Yavari AR, Moulec AL, et al. Improving sorption in MgH_2 powders by addition of nanoparticles of transition metal fluoride catalysts and mechanical alloying. J Alloys Compd. 2005;389:270–274.
[820] de Castro JFR, Santos SF, Costa ALM, et al. Structural characterization and dehydrogenation behavior of Mg-5at.%Nb nano-composite processed by reactive milling. J Alloys Compd. 2004;376:251–256.
[821] Leiva DR, de Souza Villela AC, Paiva-Santos CO, et al. High-yield direct synthesis of Mg_2FeH_6 from the elements by reactive milling. Solid State Phenom. 2011;170:259–262.
[822] Leiva DR, Jorge AM, Ishikawa TT, et al. Nanoscale grain refinement and H-sorption properties of MgH_2 processed by high-pressure torsion and other mechanical routes. Adv Eng Mater. 2010;12:786–792.
[823] Edalati K, Yamamoto A, Horita Z, et al. High-pressure torsion of pure magnesium: evolution of mechanical properties, microstructures and hydrogen storage capacity with equivalent strain. Scr Mater. 2011;64:880–883.
[824] Botta WJ, Jorge AM, Veron M, et al. H-sorption properties and structural evolution of Mg processed by severe plastic deformation. J Alloys Compd. 2013;580:S187–S191.
[825] Løken S, Solberg JK, Maehlen JP, et al. Nanostructured Mg-Mm-Ni hydrogen storage alloy: structure-properties relationship. J Alloys Compd. 2007;446-447:114–120.
[826] Skripnyuk VM, Buchman E, Rabkin E, et al. The effect of equal channel angular pressing on hydrogen storage properties of a eutectic Mg-Ni alloy. J Alloys Compd. 2007;436:99–106.
[827] Skripnyuk VM, Rabkin E, Bendersky LA, et al. Hydrogen storage properties of as-synthesized and severely deformed magnesium - multiwall carbon nanotubes composite. Int J Hydrogen Energy. 2010;35:5471–5478.
[828] Jorge Jr. AM, Prokofiev E, de Lima GF, et al. An investigation of hydrogen storage in magnesium-based alloys processed by equal-channel angular pressing. Int J Hydrogen Energy. 2013;38:8306–8312.
[829] Skryabina N, Aptukov V, Romanov P, et al. Microstructure optimization of Mg-alloys by the ECAP process including numerical simulation, SPD treatments, characterization, and hydrogen sorption properties. Molecules. 2019;24:89.
[830] de Rango P, Wen J, Skryabina N, et al. Hydrogen storage properties of Mg-Ni alloys processed by fast forging. Energies. 2020;13:3509.

[831] Skryabina N, Aptukov V, de Rango P, et al. Effect of temperature on fast forging process of Mg-Ni samples for fast formation of Mg_2Ni for hydrogen storage. Int J Hydrogen Energy. 2020;45:3008–3015.
[832] de Rango P, Fruchart D, Aptukov V, et al. Fast forging: a new SPD method to synthesize Mg-based alloys for hydrogen storage. Int J Hydrogen Energy. 2020;45:7912–7916.
[833] Leiva DR, Floriano R, Huot J, et al. Nanostructured MgH_2 prepared by cold rolling and cold forging. J Alloys Compd. 2011;509:S444–S448.
[834] Floriano R, Leiva DR, Carvalho JA, et al. Nanocrystalline Mg produced by cold rolling under inert atmosphere: a powerful tool for Mg activation. Int J Hydrogen Energy. 2014;39:4959–4965.
[835] Lima GF, Triques MRM, Kiminami CS, et al. Hydrogen storage properties of pure Mg after the combined processes of ECAP and cold-rolling. J Alloys Compd. 2014;586:S405–S408.
[836] Márquez JJ, Soyama J, Silva RA, et al. Processing of MgH_2 by extensive cold rolling under protective atmosphere. Int J Hydrogen Energy. 2017;42:2201–2208.
[837] Leiva DR, Jorge Jr. AM, Ishikawa TT, et al. Hydrogen storage in Mg and Mg-based alloys and composites processed by severe plastic deformation. Mater Trans. 2019;60:1561–1570.
[838] Asselli AAC, Leiva DR, Huot J, et al. Effects of equal-channel angular pressing and accumulative roll-bonding on hydrogen storage properties of a commercial ZK60 magnesium alloy. Int J Hydrogen Energy. 2015;40:16971–16976.
[839] Soyama J, Triques MRM, Leiva DR, et al. Hydrogen storage in heavily deformed ZK60 alloy modified with 2.5 wt.% Mm addition. Int J Hydrogen Energy. 2016;41:4177–4184.
[840] Révész Á, Gajdics M. High-pressure torsion of non-equilibrium hydrogen storage materials: a review. Energies. 2021;14:819.
[841] Edalati K, Matsuda J, Iwaoka H, et al. High-pressure torsion of TiFe intermetallics for activation of hydrogen storage at room temperature with heterogeneous nanostructure. Int J Hydrogen Energy. 2013;38:4622–4627.
[842] Edalati K, Matsuda J, Yanagida A, et al. Activation of TiFe for hydrogen storage by plastic deformation using groove rolling and high-pressure torsion: similarities and differences. Int J Hydrogen Energy. 2014;39:15589–15594.
[843] Edalati K, Matsuda J, Arita M, et al. Mechanism of activation of TiFe intermetallics for hydrogen storage by severe plastic deformation using high-pressure torsion. Appl Phys Lett. 2013;103:143902.
[844] Edalati K, Matsuo M, Emami H, et al. Impact of severe plastic deformation on microstructure and hydrogen storage of titanium-iron-manganese intermetallics. Scr Mater. 2016;124:108–111.
[845] Hongo T, Edalati K, Arita M, et al. Significance of grain boundaries and stacking faults on hydrogen storage properties of Mg_2Ni intermetallics processed by high-pressure torsion. Acta Mater. 2015;92:46–54.
[846] Gómez EIL, Edalati K, Antiqueira FJ, et al. Synthesis of nanostructured TiFe hydrogen storage material by mechanical alloying via high-pressure torsion. Adv Eng Mater. 2020;22:2000011.
[847] Zhang LT, Ito K, Vasudevan VK, et al. Hydrogen absorption and desorption in a B2 single-phase Ti-22Al-27Nb alloy before and after deformation. Acta Mater. 2001;49:751–758.
[848] Zhang LT, Ito K, Vasudevan VK, et al. Effects of cold-rolling on the hydrogen absorption/desorption behaviour of Ti-22Al-27Nb alloys. Mater Sci Eng A. 2002;329-331:362–366.
[849] Ueda TT, Tsukahara M, Kamiya Y, et al. Preparation and hydrogen storage properties of Mg-Ni-Mg_2Ni laminate composites. J Alloys Compd. 2005;386:253–257.
[850] Lang J, Huot J. A new approach to the processing of metal hydrides. J Alloys Compd. 2011;509:L18–L22.
[851] Huot J, Tousignant M. Effect of cold rolling on metal hydrides. Mater Trans. 2019;60:1571–1576.
[852] Huot J, Cuevas F, Deledda S, et al. Mechanochemistry of metal hydrides: recent advances. Materials. 2019;12:2778.
[853] Fujishima A, Honda K. Electrochemical photolysis of water at a semiconductor electrode. Nature. 1972;238:37–38.
[854] Bak T, Nowotny J, Rekas M, et al. Photo-electrochemical hydrogen generation from water using solar energy: materials-related aspects. Int J Hydrogen Energy. 2002;27:991–1022.
[855] Irie H, Watanabe Y, Hashimoto K. Carbon-doped anatase TiO_2 powders as a visible-light sensitive photocatalyst. Chem Lett. 2003;32:772–773.
[856] Asahi R, Ohwaki T, Aoki K, et al. Visible-light photocatalysis in nitrogen-doped titanium oxides. Science. 2001;293:269–271.
[857] Dachille F, Simons PY, Roy R. Pressure-temperature studies of anatase, brookite, rutile, and TiO_2-II. Am Mineral. 1968;53:1929–1939.
[858] Zhu T, Gao SP. The stability, electronic structure, and optical property of TiO_2 polymorphs. J Phys Chem C. 2014;118:11385–11396.
[859] de Gennes PG. Superconductivity of metals and alloys. New York (NY): Perseus Books Publishing, L.L.C.; 1999.
[860] Tinkham M. Introduction to superconductivity. Singapore: McGraw-Hill Inc.; 1996.
[861] Poole Jr. CP, Farach HA, Creswick RJ. Handbook of superconductivity. San Diego: Academic Press; 1995.
[862] Onnes K. The resistance of pure mercury at helium temperature. Commun. Phys Univ Leiden. 1911;120b:261–263.
[863] Onnes K. The disappearance of the resistance of mercury. Commun Phys Univ Leiden. 1911;122b:264–266.
[864] Onnes K. On the sudden change in the rate at which the resistance of mercury disappears. Commun Phys Univ Leiden. 1911;124c:267–271.
[865] Nishizaki T, Edalati K, Lee S, et al. Critical temperature in bulk ultrafine-grained superconductors of Nb, V, and Ta processed by high-pressure torsion. Mater Trans. 2019;60:1367–1376.
[866] Mito M, Shigeoka S, Kondo H, et al. Hydrostatic compression effects on fifth-group element superconductors V, Nb, and Ta subjected to high-pressure torsion. Mater Trans. 2019;60:1472–1483.

[867] Mito M, Matsui H, Tsuruta K, et al. Large enhancement of superconducting transition temperature in single-element superconducting rhenium by shear strain. Sci Rep. 2016;6:36337.
[868] Hulm JK, Goodman BB. Superconducting properties of rhenium, ruthenium, and osmium. Phys Rev. 1957;106:659–671.
[869] Jennings LD, Swenson CA. Pressure effects on Sn, In, Ta, Tl, and Hg. Phys Rev. 1958;112:31–43.
[870] Smith TF. Pressure dependence of the superconducting transition temperature for vanadium. J Phys F. 1972;2:946–956.
[871] Strongin M. Superconductivity in thin films and small particles. Physica. 1971;55:155–172.
[872] Smirnova NA, Levit VI, Pilyugin VI, et al. Evolution of the structure of fcc single crystals during strong plastic deformation. Fiz Met Metalloved. 1986;61:1170–1177.
[873] Harai Y, Ito Y, Horita Z. High-pressure torsion using ring specimens. Scr Mater. 2008;58:469–472.
[874] Schilling JC. High-pressure effects. In: Schrieffer JR, editor. Handbook of High-Temperature Superconductivity. New York: Springer; 2007. p. 427–462.
[875] Debessai M, Hamlin JJ, Schilling JS. Comparison of the pressure dependences of Tc in the trivalent d-electron superconductors Sc, Y, La, and Lu up to megabar pressures. Phys Rev B. 2008;78:064519.
[876] Mito M, Kitamura Y, Tajiri T, et al. Hydrostatic pressure effects on superconducting transition of nanostructured niobium highly strained by high-pressure torsion. J Appl Phys. 2019;125:125901.
[877] Rogl G, Rogl P, Bauer E, et al. Severe plastic deformation, a tool to enhance thermoelectric performance. In: Kuomoto K, Mori T, editors. Thermoelectric nanomaterials. Vol. 182. Heidelberg: Springer Series in Materials Science; 2013; p. 193–254.
[878] Rogl G, Zehetbauer MJ, Rogl PF. The effect of severe plastic deformation on thermoelectric performance of skutterudites, half-heuslers and Bi-tellurides. Mater Trans. 2019;60:2071–2085.
[879] Rogl G, Grytsiv A, Anbalagan R, et al. Direct SPD-processing to achieve high-ZT skutterudites. Acta Mater. 2018;159:352–363.
[880] Rogl G, Yubuta K, Kerber M, et al. Sustainable and simple processing technique for n-type skutterudites with high ZT and their analysis. Acta Mater. 2019;173:9–19.
[881] Rogl G, Ghosh S, Renk O, et al. HPT production of large bulk skutterudites. J Alloys Compd. 2021;854:156678.
[882] Rogl G, Gosh S, Renk O, et al. Influence of shear strain on HPT-processed n-type skutterudites yielding ZT = 2.1. J Alloys Compd. 2021;855:157409.
[883] Rogl G, Renk O, Ghosh S, et al. Properties of HPT-processed large bulks of p-type skutterudite $DD_{0.7}Fe_3CoSb_{12}$ with ZT > 1.3. ACS Appl Energy Mater. 2021;4:4831–4844.
[884] Rogl G, Grytsiv A, Rogl P, et al. . n-type skutterudites $(R,Ba,Yb)_yCo_4Sb_{12}$ (R = Sr, La, Mm, DD, SrMm, SrDD) approaching ZT ≈ 2.0. Acta Mater. 2014;63:30–43.
[885] Rogl G, Grytsiv A, Heinrich P, et al. New bulk p-type skutterudites $DD_{0.7}Fe_{2.7}Co_{1.3}Sb_{12-x}X_x$ (X = Ge, Sn) reaching ZT > 1.3. Acta Mater. 2015;91:227–238.
[886] Masuda S, Tsuchiya K, Qiang J, et al. Effect of high-pressure torsion on the microstructure and thermoelectric properties of Fe_2VAl-based compounds. J Appl Phys. 2018;124:035106–9.
[887] Rogl G, Ghosh S, Wang L, et al. Half-Heusler alloys: enhancement of ZT after severe plastic deformation. Acta Mater. 2020;183:285–300.
[888] Yan X, Falmbigl M, Rogl G, et al. High-pressure torsion to improve thermoelectric efficiency of clathrates. J Electron Mater. 2013;42:1330–1334.
[889] Poudel B, Hao Q, Ma Y, et al. High-thermoelectric performance of nanostructured bismuth antimony telluride bulk alloys. Science. 2008;320:634–637.
[890] Sun ZM, Hashimoto H, Keawprak N, et al. Effect of rotary-die equal channel angular pressing on the thermoelectric properties of a $(Bi,Sb)_2Te_3$ alloy. Mater Res. 2005;20:895–903.
[891] Ashida M, Sumida N, Hasezaki K, et al. Effects of low rotational speed on crystal orientation of Bi_2Te_3-based thermoelectric semiconductors deformed by high-pressure torsion. Mater Trans. 2012;53:588–591.
[892] Kim SI, Lee KH, Mun HA, et al. Dense dislocation arrays embedded in grain boundaries for high-performance bulk thermoelectrics. Science. 2015;348:109–114.
[893] Park JG, Lee YH. High thermoelectric performance of Bi-Te alloy: defect engineering strategy. Curr Appl Phys. 2016;16:1202–1215.
[894] Rogl G, Rogl P. How severe plastic deformation changes the mechanical properties of thermoelectric skutterudites and half-Heusler alloys. Front Mater. 2020;7:600261.
[895] Zinkle SJ, Was GS. Materials challenges in nuclear energy. Acta Mater. 2013;61:735–758.
[896] Odette GR, Alinger MJ, Wirth BD. Recent developments in irradiation-resistant steels. Annu Rev Mater Res. 2008;38:471–503.
[897] Rose M, Gorzawski G, Miehe G, et al. Phase stability of nanostructured materials under heavy ion irradiation. Nanostruct Mater. 1995;6:731–734.
[898] Rose M, Balogh AG, Hahn H. Instability of irradiation induced defects in nanostructured materials. Nucl Instr Meth Phys Res B. 1997;127:119–122.
[899] Chimi Y, Imase A, Ishikawa N, et al. Accumulation and recovery of defects in ion-irradiated nanocrystalline gold. J Nucl Mater. 2001;297:355–357.
[900] Samaras M, Derlet PM, Swygenhoven HV, et al. Computer simulation of displacement cascades in nanocrystalline Ni. Phys Rev Lett. 2002;88:125505.
[901] Voegeli W, Able K, Hahn H. Simulation of grain growth in nanocrystalline nickel induced by ion irradiation. Nucl Instr Meth Phys Res B. 2003;202:230–235.
[902] Beyerlein IJ, Caro A, Demkowicz MJ, et al. Radiation damage tolerant nanomaterials. Mater. Today. 2013;16:443–449.
[903] Zhang X, Hattar K, Chen Y, et al. Radiation damage in nanostructured materials. Prog Mater Sci. 2018;96:217–321.
[904] Sabirov I, Enikeev NA, Murashkin MY, et al. Bulk nanostructured materials with multifunctional properties. Cham: SpringerBriefs in Materials, Springer; 2015.

[905] Nita N, Schaeublin R, Victoria M. Impact of irradiation on the microstructure of nanocrystalline materials. J Nucl Mater B. 2004;329-333:953–957.
[906] Nita N, Schaeublin R, Victoria M, et al. Effects of irradiation on the microstructure and mechanical properties of nanostructured materials. Philos Mag. 2005;85:723–735.
[907] Kilmametov AR, Gunderov DV, Valiev RZ, et al. Enhanced ion irradiation resistance of bulk nanocrystalline TiNi alloy. Scr Mater. 2008;59:1027–1030.
[908] Pareige P, Etienne A, Radiguet B. Experimental atomic scale investigation of irradiation effects in CW 316SS and UFG-CW 316SS. J Nucl Mater. 2009;389:259–264.
[909] Rajan PBR, Monnet I, Hug E, et al. Irradiation resistance of a nanostructured 316 austenitic stainless steel. IOP Conf Ser Mater Sci Eng. 2014;63:012121.
[910] Hug E, Prasath Babu R, Monnet I, et al. Impact of the nanostructuration on the corrosion resistance and hardness of irradiated 316 austenitic stainless steels. Appl Surf Sci. 2017;392:1026–1035.
[911] Shen TD. Radiation tolerance in a nanostructure: is smaller better. Nucl Instr Methods Phys Res Sect B. 2008;266:921–925.
[912] Aydogan E, Chen T, Gigax JG, et al. Effect of self-ion irradiation on the microstructural changes of alloy EK-181 in annealed and severely deformed conditions. J Nucl Mater. 2017;487:96–104.
[913] Gigax JG, Kim H, Chen T, et al. Radiation instability of equal channel angular extruded T91 at ultra-high damage levels. Acta Mater. 2017;132:395–404.
[914] Song M, Wu YD, Chen D, et al. Response of equal channel angular extrusion processed ultrafine-grained T91 steel subjected to high temperature heavy ion irradiation. Acta Mater. 2014;74:285–295.
[915] Sun C, Zheng S, Wei CC, et al. Superior radiation-resistant nanoengineered austenitic 304L stainless steel for applications in extreme radiation environments. Sci Rep. 2015;5:7801.
[916] Han W, Demkowicz MJ, Mara NA, et al. Design of radiation tolerant materials via interface engineering. Adv Mater. 2013;25:6975–6979.
[917] Wurmshuber M, Frazer D, Bachmaier A, et al. Impact of interfaces on the radiation response and underlying defect recovery mechanisms in nanostructured Cu-Fe-Ag. Mater Des. 2018;160:1148–1157.
[918] Shamardin VK, Goncharenko YD, Bulanova TM, et al. Effect of neutron irradiation on microstructure and properties of austenitic AISI 321 steel, subjected to equal-channel angular pressing. Rev Adv Mater Sci. 2012;31:167–173.
[919] Alsabbagh A, Sarkar A, Miller B, et al. Microstructure and mechanical behavior of neutron irradiated ultrafine grained ferritic steel. Mater Sci Eng A. 2014;615:128–138.
[920] Maksimkin OP, Gusev MN, Tsai KV, et al. Effect of neutron irradiation on the microstructure and the mechanical and corrosion properties of the ultrafine grained stainless Cr-Ni steel. Phys Met Metallogr. 2015;116:1270–1278.
[921] Shamardin VK, Abramova MM, Bulanova TM, et al. Stability of the structure and properties of an ultrafine-grained Cr-Ni steel irradiated with neutrons in nuclear reactor core conditions. Mater Sci Eng A. 2018;712:365–372.
[922] Mazilkin A, Ivanisenko Y, Sauvage X, et al. Nanostructured Fe-Cr-W steel exhibits enhanced resistance to self-ion irradiation. Adv Eng Mater. 2020;22:1901333.
[923] Hoffman A, Arivu M, Wen H, et al. Enhanced resistance to irradiation induced ferritic transformation in nanostructured austenitic steels. Materialia. 2020;13:100806.
[924] Shamardin VK, Bulanova TM, Fedoseev AE, et al. The effect of neutron irradiation on the impact toughness of austenitic stainless steel in ultrafine-grained state. J Nucl Mater. 2021;544:152680.
[925] Enikeev NA, Shamardin VK, Radiguet B. Radiation tolerance of ultrafine-grained materials fabricated by severe plastic deformation. Mater Trans. 2019;60:1723–1731.
[926] Foroulis ZA, Uhlig HH. Effect of cold-work on corrosion of iron and steel in hydrochloric acid. J Electrochem Soc. 1964;111:522–528.
[927] Vinogradov A, Mimaki T, Hashimoto S, et al. On the corrosion behavior of ultra-fine grain copper. Scr Mater. 1999;41:319–326.
[928] Fattah-Alhosseini A, Imantalab O. Effect of accumulative roll bonding process on the electrochemical behavior of pure copper. J Alloys Compd. 2015;632:48–52.
[929] Nie M, Wang CT, Qu M, et al. The corrosion behaviour of commercial purity titanium processed by high-pressure torsion. J Mater Sci. 2014;49:2824–2831.
[930] Pisarek M, Kedzierzawski P, Janik-Czachor M, et al. Effect of hydrostatic extrusion on the corrosion resistance of type316 stainless steel. Corrosion. 2008;64:131–137.
[931] Kim HS, Kim WJ. Annealing effects on the corrosion resistance of ultrafine-grained pure titanium. Corr Sci. 2014;89:331–337.
[932] Balusamy T, Kumar S, Narayanan TSNS. Effect of surface nanocrystallization on the corrosion behaviour of AISI 409 stainless steel. Corr Sci. 2010;52:3826–3834.
[933] Fattah-Alhosseini A, Attarzadeh FR, Vakili-Azghandi M. Effect of multi-pass friction stir processing on the electrochemical and corrosion behavior of pure titanium in strongly acidic solutions. Metall Mater Trans A. 2017;48:403–411.
[934] Noel JN. Effects of metallurgical variables on aqueous corrosion. In: Cramer SD, Covino BSJ, editors. ASM Handbook. Vol. 13A, Corrosion: fundamentals, testing, and protection. Materials Park, OH: ASM International; 2003. p. 258.
[935] Miyamoto H, Harada K, Mimaki T, et al. Corrosion of ultra-fine grained copper fabricated by equal-channel angular pressing. Corr Sci. 2008;50:1215–1220.
[936] Miyamoto H. Corrosion of ultrafine grained materials by severe plastic deformation, an overview. Mater Trans. 2016;57:559–572.
[937] Ralston KD, Birbilis N, Davies CHJ. Revealing the relationship between grain size and corrosion rate of metals. Scr Mater. 2010;63:1201–1204.
[938] Rifai M, Bagherpour E, Yamamoto G, et al. Transition of dislocation structures in severe plastic deformation and its effect on dissolution in dislocation etchant. Adv Mater Sci Eng. 2018;2018:4254156.

[939] Rifai M, Miyamoto H, Fujiwara H. Effects of strain energy and grain size on corrosion resistance of ultrafine grained Fe-20%Cr steels with extremely low C and N fabricated by ECAP. Int J Corr. 2015;2015: 386865.
[940] Rifai M, Yuasa M, Miyamoto H. Enhanced corrosion resistance of ultrafine-grained Fe-Cr alloys with subcritical Cr contents for passivity. Metals. 2018;8:149.
[941] Rifai M, Yuasa M, Miyamoto H. Effect of deformation structure and annealing temperature on corrosion of ultrafine-grained Fe-Cr alloy prepared by equal channel angular pressing. Int J Corr. 2018;2018:4853175.
[942] Sieradzki K, Newman RC. A percolation model for passivation in stainless steels. J Electrochem Soc. 1986;133:1979–1980.
[943] Miyamoto H, Yuasa M, Rifai M, et al. Corrosion behavior of severely deformed pure and single-phase materials. Mater Trans. 2019;60:1243–1255.
[944] Hanawa T. Metals for biomedical devices. Oxford: Woodhead Publishing Limited; 2010.
[945] Froes FH, Qian M. Titanium in medical and dental applications. Duxford: Woodhead Publishing; 2018.
[946] Valiev RZ, Semenova IP, Latysh VV, et al. Nanostructured titanium for biomedical applications. Adv Eng Mater. 2008;10:B15–B17.
[947] Gunderov DV, Polyakov AV, Semenova IP, et al. Evolution of microstructure, macrotexture and mechanical properties of commercially pure Ti during ECAP-conform processing and drawing. Mater Sci Eng A. 2013;562:128–136.
[948] Xu W, Wu X, Figueiredo RB, et al. Nanocrystalline body-centred cubic beta-titanium alloy processed by high-pressure torsion. Int J Mater Res. 2009;100:1662–1667.
[949] Valiev RZ, Sabirov I, Zemtsova EG, et al. Titanium in medical and dental applications. In: Froes F, Qian M, editors. Duxford, UK: Woodhead Publishing; 2018; p. 393–418.
[950] Yilmazer H, Niinomi M, Nakai M, et al. Mechanical properties of a medical β-type titanium alloy with specific microstructural evolution through high-pressure torsion. Mater Sci Eng C. 2013;33:2499–2507.
[951] Stráský J, Janeček M, Semenova I, et al. Titanium in medical and dental applications. In: Froes F, Qian M, Duxford: Woodhead Publishing; 2018. p. 455–475.
[952] Yang J, Cui F, Lee IS. Surface modifications of magnesium alloys for biomedical applications. Ann Biomed Eng. 2011;39:1857–1871.
[953] Dobatkin SV, Lukyanova EA, Martynenko NS, et al. Strength, corrosion resistance, and biocompatibility of ultrafine-grained Mg alloys after different modes of severe plastic deformation. IOP Conf Ser Mater Sci Eng. 2017;194:012004.
[954] Parfenov EV, Kulyasova OB, Mukaeva VR, et al. Influence of ultra-fine grain structure on corrosion behaviour of biodegradable Mg-1Ca alloy. Corr Sci. 2020;163:108303.
[955] Valiev RZ, Parfenov EV, Parfenova LV. Developing nanostructured metals for manufacturing of medical implants with improved design and biofunctionality. Mater Trans. 2019;60:1356–1366.
[956] Semenova IP, Klevtsov GV, Klevtsova NA, et al. Nanostructured titanium for maxillofacial mini-implants. Adv Eng Mater. 2016;18:12161224.
[957] Estrin Y, Lapovok R, Medvedev AE, et al. Titanium in medical and dental applications. In: Froes F, Qian M, Duxford: Woodhead Publishing; 2018. p. 419–454.
[958] Parfenov EV, Parfenova LV, Dyakonov GS, et al. Surface functionalization via PEO coating and RGD peptide for nanostructured titanium implants and their in vitro assessment. Surf Coat Technol. 2019;357:669–683.
[959] Balasubramanian R, Nagumothu R, Parfenov E, et al. Development of nanostructured titanium implants for biomedical implants - a short review. Mater Today Proc. 2021;46:1195–1200.
[960] Valiev RZ, Sabirov I, Zhilyaev AP, et al. Bulk nanostructured metals for innovative applications. JOM. 2012;64:1134–1142.
[961] Polyakov AV, Dluhoš L, Dyakonov GS, et al. Recent advances in processing and application of nanostructured titanium for dental implants. Adv Eng Mater. 2015;17:1869–1875.
[962] Branagan D, Frerichs A, Meacham B, et al. New mechanisms, enabling structures, and advanced properties resulting in a new class of 3rd generation AHSS sheet. SAE Technical Paper. 2014; No. 2014-01-0989.
[963] https://www.tokkin.com/materials/high_parformance/ufgs.
[964] https://www.komatsuseiki.co.jp/nanosus/.
[965] Ono K. Size effects of high strength steel wires. Metals. 2019;9:240.